Positrons, Antiprotons, and Interactions for Cold Antihydrogen

A thesis presented

by

David Sumner Hall

to
The Department of Physics
in partial fulfillment of the requirements
for the degree of
Doctor of Philosophy
in the subject of
Physics

Harvard University
Cambridge, Massachusetts

July 1997

Abstract

Three advances are made toward the production of low-energy antihydrogen for spectroscopic and gravitational studies. First, electrons and protons interact within the confines of an electromagnetic (Penning) trap. The electrons cool the protons to a point at which the two species have very low relative velocities and recombination is predicted to be most rapid. Second, a new positron accumulation technique is demonstrated, in which one million cryogenic positrons are accumulated from a 5 mCi ^{22}Na source at rates exceeding 10 e^+/sec. Finally, cold positrons and antiprotons are simultaneously confined in the overlapping region of a nested Penning trap. An interaction is observed in which the antiprotons heat the positrons.

Contents

Acknowledgments

My greatest appreciation and thanks are extended to my advisor, Gerald Gabrielse, for allowing me the opportunity to participate in an enjoyable and fulfilling project, and for his consistent support throughout my time at Harvard. Thanks as well to Dr. W. Quint for letting me play on the apparatus as a youngster, and to Dr. K. Abdullah for straightening me out when I got confused. I am especially thankful to my co-workers Dr. T. Roach and P. Yesley for their extraordinary work and effort over the past two years; without them this project could never have left the ground. I am also indebted to Dr. H. Kalinowsky, Dr. W. Jhe, A. Khabbaz, C. Heimann, and J. Estrada for their hard work and enthusiasm in the final days of LEAR and the TRAP collaboration.

I wish to thank A. Khabbaz and C. Heimann again for the opportunity to work with them on the proton/antiproton mass measurement, a project I enjoyed nearly as much as my own. L. Haarsma provided much wisdom about positrons and gave us the target to beat, and D. Phillips always had a good story to tell about protons and antiprotons. C.-H. Tseng rounded off my education on electrons, and Dr. M. Schneider made sure I didn't escape without knowing a little bit about nuclear physics and a lot more about particle detectors.

Without the support of C. Black, T. de Swiet, J. Edwards, L. Kaplan, J. Katine, D. Kestenbaum, G. Michail, and S. Osofsky, I would undoubtedly still be stranded in coursework. L. Defeo, R. Anderson, D. Osier, P. Crevoiserat, and S. Cotreau built components which outlasted all of the abuse I could inflict on them, and S. Paula and F. Osborne helped with radiation safety issues. Thanks to the staff of the Harvard Cyclotron for their assistance in the ^{19}Ne studies, and to the staff of LEAR for the delivery of high-quality antiprotons. Thanks, too, to J. Ragusa for her kindness, assistance, and patience over the years.

Finally, I have benefited enormously over the years by interaction with my fellow laboratory members: J. Tan, D. Enzer, L. Lapidus, S. Peil, C. Levy, P. Janzen, A. Tuchman, T. Fairfield, and C. Hornby. Thanks to you all; I wish you the best.

Financial support for these experiments came from the AFOSR, ONR, and NSF of the United States, the German BMFT, and the Korean KOSEF.

Publications

1. "(Anti)hydrogen Recombination Studies in a Nested Penning Trap," W. Quint, R. Kaiser, D. Hall, and G. Gabrielse, Hyp. Int. **76**, 181 (1993).

2. "Electron Cooling of Protons in a Nested Penning Trap," D. S. Hall and G. Gabrielse, Phys. Rev. Lett. **77**, 1962 (1996).

3. "Comparing the Antiproton and Proton and Progress toward Cold Antihydrogen," G. Gabrielse, D. S. Hall, A. Khabbaz, T. Roach, P. Yesley, C. Heimann, H. Kalinowsky, W. Jhe, and B. Brown, in *Proceedings of the Fifteenth International Conference on Atomic Physics,* University of Amsterdam, August 5–9, 1996.

4. "Comparing the Antiproton and Proton and Progress toward Cold Antihydrogen," G. Gabrielse, D. S. Hall, A. Khabbaz, T. Roach, P. Yesley, C. Heimann, H. Kalinowsky, W. Jhe, and B. Brown, in *Proceedings of the LEAP96 Conference,* Dinkelsbühl, Germany, August 27–31, 1996.

List of Tables

List of Figures

Chapter 1

Introduction

Antihydrogen ($\bar{\mathrm{H}}$) is the bound state of an antiproton ($\bar{p}$) and a positron (e^+). It is the simplest system of atomic antimatter, and has been much anticipated as a vehicle for precision tests of *CPT* and gravity.

In this work, several significant contributions are made toward the production and study of antihydrogen at energies suitable for spectroscopy (*i.e.*, *cold* antihydrogen), namely:

- An interaction is demonstrated between electrons and protons in which the electrons cool the protons to a point at which recombination is predicted to be most favorable [1]. This is the first demonstration of cooling by particles of opposite sign in a nested Penning trap. (Chs. 2, 3, and 4)
- One million positrons are accumulated in a cryogenic Penning trap at rates exceeding 10 e^+/sec. This is the largest number of positrons accumulated under conditions compatible with the long-term confinement of antiprotons. (Ch. 5)
- Positrons and antiprotons are, for the first time, simultaneously confined in the same apparatus. The positrons are heated by the antiprotons. (Ch. 6)

These advances synthesize and extend previous work on the trapping and cooling

of antiprotons [2, 3] and positrons [4] and the preliminary recombination studies in a nested Penning trap [5].

Nine antihydrogen atoms were recently produced at relativistic energies [6] by passing 1.2 GeV antiprotons from the Low Energy Antiproton Ring (LEAR) at the European Laboratory for Particle Physics (CERN) through a xenon gas target. The antiprotons produce electron-positron pairs as they encounter the heavy nuclei, and occasionally one of the positrons is captured to form an atom of antihydrogen. Highly-relativistic antihydrogen is difficult to detect and its properties difficult to determine, however, and precise measurements on antihydrogen await its production, trapping, and interrogation at lower energies.

1.1 Motivations

There are two principal motivations for the production of antihydrogen. The first involves comparing the properties of particles with those of their conjugate antiparticles (tests of the *CPT* theorem) to examine the underlying assumptions of quantum field theories. Antihydrogen production may also permit tests on the nature of gravity as it relates to the Weak Equivalence Principle (WEP) for antimatter.

1.1.1 Tests of Symmetry: *CPT*

Parity is the discrete symmetry which takes a state into a mirror image of itself. This is often written as the operation of a parity operator P on a state $\psi(\mathbf{x})$

$$P\psi(\mathbf{x}) = \psi(-\mathbf{x}). \tag{1.1}$$

Eigenstates of the parity operator have eigenvalues ± 1; those with eigenvalue $+1$ (-1) are known as even (odd) parity states. Prior to 1956, it was believed that the parity of a state is conserved under all physical processes. In that year it was pointed out [7] that the weak interaction had never been explicitly tested for parity invariance. A subsequent experiment [8] involving the beta decay of polarized ^{60}Co nuclei found that the electrons were emitted preferentially in the direction opposite to the nuclear spin. This result betrays a violation of parity, since spin (a pseudovector) is even under a parity transformation, but the emitted electron direction (an axial vector) is odd; in the parity-transformed version of the experiment, therefore, the electrons would be emitted preferentially in the same direction as the nuclear spin. (A parity-conserving result would have found no preference in the direction of the emitted electrons.) Subsequent experiments have shown that parity violation is endemic to the weak interaction; for instance, all neutrinos (ν) have negative helicity (spin antiparallel to direction of motion), and all antineutrinos ($\bar{\nu}$) have positive helicity (spin parallel to the direction of motion).

Following the discovery of P-violation in the weak interaction, a new theorem was devised which replaced simple P-invariance with invariance under both parity and charge-conjugation [9]. Charge-conjugation (C) is the operation which turns a particle into its antiparticle, *e.g.*,

$$C|\nu\rangle = |\bar{\nu}\rangle. \tag{1.2}$$

Conservation of the product CP (rather than P alone) neatly restored symmetry to systems such the neutrino by transforming a negative helicity neutrino into a positive helicity antineutrino (and *vice versa*). (Similarly, $^{60}\overline{\text{Co}}$ decay by positron emission should yield a preference for positrons emitted in the direction of the nuclear spin,

although experimental verification of this point has not yet been attempted.)

The pseudoscalar kaons (K^0 and $\bar{K}^0$) are mixed by charged weak currents [10]. Although these two particles are not eigenstates of CP, the combinations

$$|K_1^0\rangle = \frac{1}{\sqrt{2}}\left(|K^0\rangle - |\bar{K}^0\rangle\right) \tag{1.3}$$

and

$$|K_2^0\rangle = \frac{1}{\sqrt{2}}\left(|K^0\rangle + |\bar{K}^0\rangle\right), \tag{1.4}$$

are eigenstates of CP with eigenvalues $+1$ and -1, respectively. Each of the two states is therefore expected to decay to another CP eigenstate with the same eigenvalue. In 1964, the branching ratio for the decay $K_2^0 \to 2\pi$ was discovered to be nonzero [11]. This implies CP-violation, since the final state is an eigenstate of CP with eigenvalue $+1$, and the initial eigenstate has eigenvalue -1. This is the only test to date which has revealed CP-violation.

The discovery of CP-violation led to the inclusion of a third discrete symmetry, time- (or motion-) reversal symmetry T. Together, these three operations for the basis of the CPT theorem, which asserts that any interaction is invariant under the combined operations of C, P, and T, taken in any order. The CPT theorem is a fundamental consequence of any local, Lorentz-invariant quantum field theory which possesses a hermitian, Lorentz-invariant Lagrange density [12]. Almost all quantum field theories, therefore, respect CPT. In light of the previous revelations involving P and CP, however, one may rightly question whether this implicit theoretical confidence is well-placed.

The CPT theorem predicts that particle and antiparticle should have the same mass, mean lifetime, charge, and magnetic moment (up to a sign in the last two

quantities). Tests of these particle-antiparticle relationships are, therefore, tests of *CPT* and the underlying assumptions of quantum field theories.

Many experimental tests of *CPT*-invariance have been conducted (Fig. 1.1), the most precise of which is the mass comparison of the neutral kaon system at a fractional precision of a few parts in 10^{18} [13]. The next most accurate comparisons are, in leptons, the electron/positron magnetic moment (two parts in 10^{12} [14]) and, in baryons, the proton/antiproton mass (one part in 10^9 [15]). Comparing the properties of antihydrogen with those of hydrogen would constitute additional, extremely precise tests of *CPT*. For instance, the $1S$–$2S$ transition in hydrogen can currently be measured at a precision of 1 part in 10^{11} [16] — almost 5 orders of magnitude less than the precision dictated by the natural linewidth, which may itself (someday) be split by another factor of 100. Measurement of the transition in both hydrogen and antihydrogen could therefore test the *CPT* theorem to the same level of precision as the kaon test, and would be the most precise test involving baryons and leptons.

1.1.2 Tests of Gravity: WEP

The Weak Equivalence Principle (WEP) asserts that all bodies in a gravitational field fall with the same acceleration. WEP is well-established experimentally by Eötvös-type experiments for matter, but no direct tests exist for antimatter.

It is suggested in certain theories of quantum gravity that matter and antimatter may experience different gravitational forces. The origin of this difference arises through the possible existence of massive scalar and vector gravitational couplings (in addition to the "usual" tensor coupling) which arise from dimensional reduction of higher-dimensional theories [17, 18]. The scalar (and tensor) couplings produce

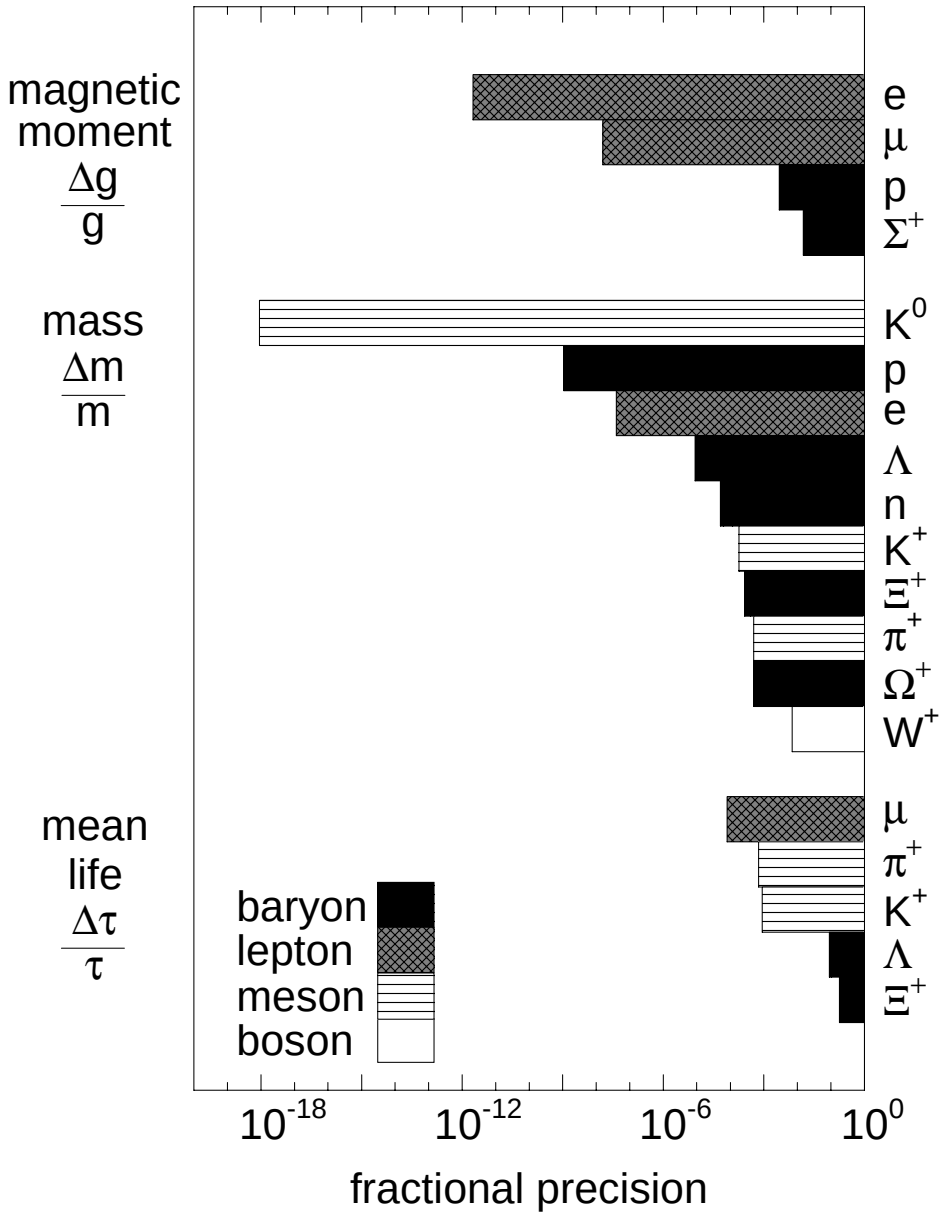

Figure 1.1: Tests of *CPT* symmetry. Charge-to-mass comparisons are listed as mass comparisons.

attractive forces between all particles, whereas the vector coupling is repulsive between like particles and attractive between conjugate particles. In matter-matter interactions, the scalar and vector contributions to the gravitational force could cancel one another precisely and remain undetected; for antimatter-matter interactions, however, the vector coupling would lead to an additional attractive force and no cancellation could occur. In this model, antimatter would be expected to experience a greater gravitational acceleration g than matter (at, say, the surface of the Earth).

Experiments to detect the gravitational acceleration of antimatter are notoriously difficult, since most of the readily-available antimatter is charged and the strength of the electric coupling to a charged particle is many orders of magnitude larger than that of the gravitational coupling. Stray electric fields interfere with the experiments, as observed in a measurement of the gravitational acceleration on electrons [19]. A proposed experiment along the same lines for antiprotons [20] would be less susceptible to such effects, but has also proved more challenging than originally anticipated.

Antihydrogen, being neutral, is not affected (to first order) by stray electric fields, and thus offers a number of possibilities for measuring the gravitational force on antimatter. For instance, the effect of gravity upon the spatial distribution of trapped antihydrogen atoms could be measured [21]. Alternatively, antihydrogen could be launched (in an atomic fountain) or dropped from a trap to measure g by time-of-flight methods. Atomic interferometry in cesium has recently permitted a measurement of g to a part in 10^9 [22]; a result at this precision in antihydrogen, although extremely challenging, would be a compelling gravitational test of WEP for antimatter.

Although direct tests of the gravitational acceleration of antimatter have not

been performed, there exist indirect tests which already place a stringent (up to a part in 10^6) limit on the scalar and vector contributions to the gravitational force [23]. No immediate surprises are expected in the direct tests (such as the possibility that antihydrogen falls *upward*), but the experiment remains to be done.

1.2 Cold Antihydrogen Production[1]

Several approaches have been identified for the production of cold antihydrogen. Two of the most promising will be considered here. The first merges cold plasmas of antiprotons and positrons, and the second impinges positronium atoms on a cold antiproton plasma.

The most conceptually straightforward approach to the production of antihydrogen is the merging of cold, trapped plasmas of antiprotons and positrons. The particles "recombine" to form atoms through a complicated combination of collisional and radiative processes. The recombination rate coefficient α is traditionally defined by the relation [25]

$$\frac{dn_p}{dt} = -\alpha n_e n_p \tag{1.5}$$

where n_e and n_p refer to the number densities of positrons and antiprotons, respectively, and the left-hand side of Eq. 1.5 represents the rate at which antiprotons are lost from the plasma due to recombination. A more widely used parameter for comparison of the various recombination strategies is the normalized recombination rate per antiproton Γ, which is defined by dividing both sides of Eq. 1.5 by the antiproton density. This gives

$$\Gamma = \alpha n_e = n_e \sigma v \tag{1.6}$$

[1]The material in this section draws heavily on Ref. [24].

where σ is the cross section for the recombination process and v is the relative velocity of the particles in the two plasmas.

For sufficiently tenuous plasmas, the dominant recombinative process is radiative recombination, in which the antihydrogen binding energy is released in the form of a photon as the positron jumps from the continuum into a bound state:

$$\bar{p} + e^+ \rightarrow \bar{\mathrm{H}} + h\nu. \tag{1.7}$$

Such recombination occurs preferentially into low-lying states with a rate that scales approximately as $T^{-1/2}$ [25, 26]. The value for the rate coefficient is [26]

$$\Gamma_{\mathrm{rad}} = 1.55 \times 10^{-10}\ T[\mathrm{K}]^{-0.63} n_e[\mathrm{cm}^{-3}]\ \mathrm{sec}^{-1}. \tag{1.8}$$

Substantial gains may be realized by driving the radiative transition with a laser in the stimulated process

$$\bar{p} + e^+ + h\nu \rightarrow \bar{\mathrm{H}} + 2h\nu \tag{1.9}$$

whereupon the recombination rate increases to

$$\Gamma_{\mathrm{stim}} = (1 + G)\Gamma_{\mathrm{rad}}. \tag{1.10}$$

The gain G may be expressed, for temperatures T and transitions to quantum levels n such that $k_B T \ll R_\infty/n^2$, by [27]

$$G = \frac{I\pi^2 n^5}{k_B c T}\left(\frac{\hbar c}{R_\infty}\right)^3 = 7.3 \times 10^{-5}\ \frac{n^5 I[\mathrm{W/cm}^2]}{T[\mathrm{K}]} \tag{1.11}$$

where R_∞ is the Rydberg, I is the laser intensity, k_B is the Boltzmann constant, and c is the speed of light.

For higher positron densities, the collisional three-body process

$$\bar{p} + e^+ + e^+ \rightarrow \bar{\mathrm{H}} + e^+ \tag{1.12}$$

may be much more favorable than pure radiative recombination. At low temperatures this process tends to be effective in producing high-Rydberg antihydrogen levels (within a few $k_B T$ of the ionization limit), which subsequently cascade to lower-lying states by spontaneous emission. The collisional recombination rate is calculated to be [26]

$$\Gamma_{\mathrm{coll}} = 3.8 \times 10^{-9}\ n_e[\mathrm{cm}^{-3}]^2\, T[\mathrm{K}]^{-9/2}\ \mathrm{sec}^{-1}. \tag{1.13}$$

This rate depends steeply on the relative temperatures of the two plasmas, as can be seen by considering the relevant length and time scales of the process [24]. A simple variation of this scheme involves a combined antiproton/electron plasma which is merged with a positron plasma, involving the three-body reaction

$$\bar{p} + e^+ + e^- \rightarrow \bar{\mathrm{H}} + e^-. \tag{1.14}$$

In general, $\Gamma_{\mathrm{tot}} \geq \Gamma_{\mathrm{rad}} + \Gamma_{\mathrm{coll}}$ since the collisional and radiative recombination processes are entangled in a complicated fashion. The net rate Γ_{tot} may be better approximated by the inclusion of an empirically-derived third term [26], such that

$$\Gamma_{\mathrm{tot}} = \Gamma_{\mathrm{rad}} + \Gamma_{\mathrm{coll}} + 6.0 \times 10^{-9}\ T[\mathrm{K}]^{-2.18}\, n_e[\mathrm{cm}^{-3}]^{1.37}\ \mathrm{sec}^{-1}. \tag{1.15}$$

A number of different ion-trap schemes have been considered to take advantage of these recombination mechanisms by confining and merging the cold positron and

antiproton plasmas. One possibility is to use a nested Penning trap [28], which uses static electric and magnetic fields to confine the particles in an overlapping region with a good degree of control [1]. Although the static confining fields permit cold plasma temperatures, a typical magnetic field used in such a trap (6 Tesla) has been calculated to reduce the collisional recombination rate by an order of magnitude [29], leading to a rate coefficient

$$\Gamma_{\rm mag} = 3.5 \times 10^{-10}\ n_e[{\rm cm}^{-3}]^2\, T[{\rm K}]^{-9/2}\ {\rm sec}^{-1}. \tag{1.16}$$

Antihydrogen production may be further inhibited if the atoms are field-ionized by the electrostatic trapping fields as they leave the positron plasma [30].

A Paul trap simultaneously confines the oppositely-charged plasmas in an overlapping region by the application of radiofrequency quadrupole fields, as has been demonstrated for the trapping of Tl^+ and I^- ions [31]. Unfortunately, the radiofrequency potential leads to "micromotion" heating of the particles, reducing the recombination rates by raising the plasma temperatures. The Paul trap would also require forces of very different strengths to confine the proton and electron plasmas in an overlapping region.

A third scheme [32] makes use of a combined trap, in which the antiprotons are confined by static fields (as in the Penning trap) and the positrons are confined by radiofrequency potentials (as in the Paul trap). This trapping configuration suffers from the disadvantages of the Penning and Paul traps (*i.e.*, reduction in recombination rates from the magnetic field and from micromotion heating) without offering any particular advantages.

Table 1.1 summarizes these three approaches to merging cold plasmas of positrons and antiprotons to produce antihydrogen. Given the temperature depen-

Table 1.1: Advantages and disadvantages for antihydrogen production in three classes of ion traps, each capable of confining particles of opposite signs of charge.

	advantages	disadvantages
Penning trap	cold controllable interaction	magnetic field field-ionization ?
Paul trap		micromotion heating
combined trap		micromotion heating magnetic field

dences of the recombination rates, the nested Penning trap currently affords the most promising approach to antihydrogen recombination in merged plasmas.

Another set of antihydrogen production schemes revolve about a charge-exchange process between positronium (Ps) and antiprotons trapped in an ion trap [33, 34], *e.g.*,

$$\bar{p} + \mathrm{Ps} \rightarrow \bar{\mathrm{H}} + e^- \tag{1.17}$$

with a rate given by

$$\Gamma_{\mathrm{Ps}} = F_0 \sigma_{\bar{\mathrm{H}}} \tag{1.18}$$

where F_0 is the incident flux of Ps atoms, and $\sigma_{\bar{\mathrm{H}}}$ is the charge-exchange cross section. Since $\sigma_{\bar{\mathrm{H}}} \approx 10^{-15}$ cm^2, and typical positronium beam fluxes might be only $F_0 \approx 10^7$ Ps/cm^2, this rate tends to be rather small ($\Gamma_{\mathrm{Ps}} \approx 10^{-8}$ sec^{-1}). (The charge-conjugate version of this reaction has recently been shown to yield hydrogen [35], and supports the theoretically predicted cross-sections for this process.) Enhancement of Γ_{Ps} may occur, however, as a result of exciting the positronium before it interacts with the antiprotons,

$$\bar{p} + \mathrm{Ps}^* \rightarrow \bar{\mathrm{H}}^* + e^- \tag{1.19}$$

This has the effect of increasing the effective cross-section by a factor of n^3 [36], where n is the principal quantum number; thus, excitation of the positronium to $n = 10$ before the interaction would increase the formation rate by a factor of 10^3 to $\Gamma_{\mathrm{Ps}^*} \approx 10^{-5}$ sec^{-1}.

To summarize the expected rates of antihydrogen production $N_p\Gamma$ for these approaches it is useful to evaluate the preceding expressions for typical experimental values of densities and temperatures. Positron densities $n_e \approx 10^8$ cm^{-3} at $T = 4$ K have been achieved, and up to $N_p = 0.4 \times 10^6$ antiprotons have been electron-cooled to about the same temperature. For laser-stimulated recombination, the laser is assumed to drive the transition from the continuum to $n = 3$ at an intensity of 10^5 W/cm^2. The antihydrogen production rates under these assumptions are given in Table 1.2.

1.3 Conclusions

One potentially fruitful approach to testing the *CPT* theorem uses antihydrogen to compare the properties of particle and antiparticle. Antihydrogen may also be used for tests of the effect of gravity on antimatter, which are notoriously difficult with

Table 1.2: Approximate cold antihydrogen production rates $N_p\Gamma$ for the processes considered in this work.

process	$N_p\Gamma$ (sec^{-1})
radiative	3×10^3
stimulated	1×10^5
collisional-radiative (c-r)	2×10^{10}
c-r + 6 T magnetic field	2×10^9
positronium	4×10^{-3}
excited-state positronium	4

the more common charged antiparticles. The most promising avenue for producing antihydrogen at energies suitable for these tests is to merge and recombine cold, confined plasmas of positrons and antiprotons. The collisional-radiative recombination rate is highest, but leaves atoms in highly excited states which are susceptible to field-ionization. A laser can be used to assist transitions to more tightly bound levels, or the positron plasma dimensions increased to give the atom more time to de-excite before experiencing the potentially-ionizing electrostatic trapping fields.

The remainder of this work addresses the experimental concerns associated with production of low-energy antihydrogen from cold, trapped plasmas of positrons and antiprotons in the context of a nested Penning trap, and is broadly divided into three sections. The first (Chs. 2, 3, and 4) describes work done in the charge conjugate system with electrons and protons. Chapter 5 discusses a novel method of positron accumulation into an environment suitable for antiproton storage. Finally, Ch. 6 describes the simultaneous confinement of positrons and antiprotons and some preliminary antimatter interaction studies. Some final thoughts are considered in the epilogue.

Chapter 2

Apparatus

Production of antihydrogen at energies suitable for spectroscopic studies requires that its constituents (antiprotons and positrons) are cold, can be trapped for extended periods, and can be made to interact with one another. A Penning trap environment satisfies these criteria. This chapter reviews the basic theory of the Penning trap and details common elements of the platform used for the experiments described in the subsequent chapters.

2.1 Penning Trap Theory

As shown in Sec. 1.2, the recombination rate possesses a strong dependence on the relative temperatures of the antiprotons and positrons. It is sensible to confine the particles with static fields, in order that the confining fields do not heat the particles.

A particle of charge e and mass m in a static, uniform magnetic field $\mathbf{B}$ will execute cyclotron motion about a magnetic field line at a frequency ν_c, given by

$$\nu_c = \frac{|e\mathbf{B}|}{2\pi mc} \tag{2.1}$$

where c is the speed of light. For a magnetic field $\mathbf{B} = B\hat{z}$ the radial motion is constrained to a field line (in the absence of other external forces) for particles of both signs of charge, and unconfined in z.

A Penning trap provides a restoring force in z by superposing a static electric field upon the uniform magnetic field $\mathbf{B}$. The electric field is generated by applying potentials to conducting surfaces surrounding the trapping region. In order to satisfy Laplace's equation for a charge-free region of space, the axially-confining electric field is inevitably accompanied by a radial electric field which is anticonfining, *i.e.*, the force it produces on a trapped particle is directed away from the center of the trap. The presence of this radial electric field makes the Penning trap unstable, since motion away from the trap axis will decrease the potential energy. The lifetime of trapped particles may still be quite long, however, and under typical experimental conditions is not limited by this instability [37].

An ideal Penning trap [37] superposes an electrostatic quadrupole potential

$$V(\rho, z) = V_0 \frac{z^2 - \rho^2/2}{2d^2} \tag{2.2}$$

(where V_0 is the applied trapping potential and d is a characteristic trap dimension) upon the magnetic field $\mathbf{B}$. This results in a linear restoring force in the z-direction and harmonic motion at a frequency ν_z, given by

$$\nu_z = \frac{1}{2\pi}\sqrt{\frac{eV_0}{md^2}}. \tag{2.3}$$

The radial electric field modifies the motion of a trapped particle in the xy-plane,

Table 2.1: Typical trapping parameters for the elementary particles considered in this work.

	electron positron	proton antiproton
magnetic field (B_0)	5.5 Tesla	
trapping potential (V_0)	$\pm$ 12 V	$\mp$ 32 V
cyclotron frequency (ν_c')	154 GHz	84 MHz
axial frequency (ν_z)	33 MHz	1.3 MHz
magnetron frequency (ν_m)	3 kHz	10 kHz

introducing a slow $\mathbf{E} \times \mathbf{B}$ drift motion at a frequency

$$\nu_m \approx \frac{\nu_z^2}{2\nu_c'} \tag{2.4}$$

where $\nu_c' = \nu_c - \nu_m$ is the modified cyclotron frequency. (Typical values for these frequencies are given in Table 2.1.) The frequencies observe the hierarchy

$$\nu_c' \gg \nu_z \gg \nu_m. \tag{2.5}$$

The motion of a particle in an ideal trap consists of epicyclic cyclotron and magnetron motions in x and y superposed upon harmonic oscillations in z (Fig. 2.1).

Axial confinement in the electrostatic potential well is limited to particles of a single sign of charge. A potential minimum for antiprotons, for example, is a potential maximum for positrons, which are therefore unbound. In order to confine particles of both signs of charge simultaneously, two trap wells may be placed adjacent to one another [Fig. 2.2(a)]. Of course, this will not be of much use for recombination, since the particles remain spatially separated. A nested Penning trap [28], as shown in Fig. 2.2(b), confines particles of both signs of charge in an

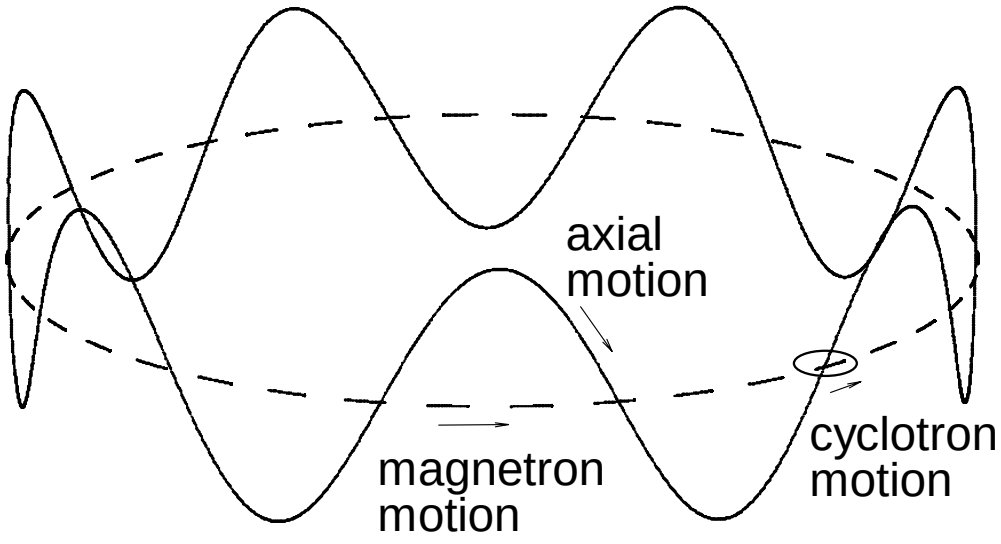

Figure 2.1: Particle motions in an ideal Penning trap.

overlapping region, provided the energy of the particles in the outer trap exceeds the height of the "hill" which constitutes the inner trap (less the space charge potential of any particles which may be confined there). If this condition is not met, the situation is actually one of *three* adjacent trapping regions. Experimental realization of the nested Penning trap is the subject of Sec. 4.3.

2.2 Penning Trap Design

An open-access Penning trap configuration [38] was chosen for these experiments. The uniform magnetic field (6 Tesla) is generated by a superconducting solenoid, and the electric potential is created by applying bias voltages to a series of hollow copper cylinders ("electrodes") aligned coaxial to the magnetic field. Particles may be injected into or extracted from the trap along the axis, or moved from region to region within the trap interior. The properties of the electrostatic potential produced by the cylinders are discussed in the following sections.

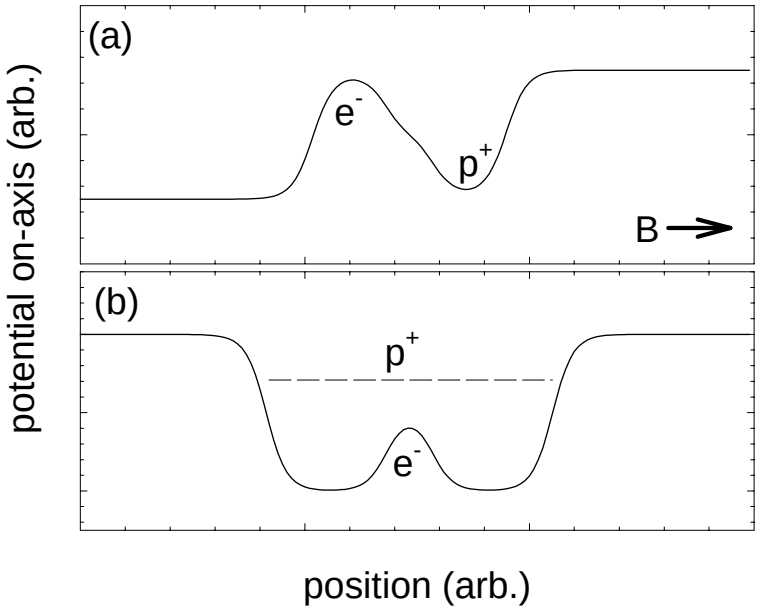

Figure 2.2: Electric potential on the axis of (a) two adjacent traps, and (b) two nested traps. The magnetic field is parallel to the z-axis.

The electric potential anywhere within a region bounded by conductors is determined by solving Laplace's equation under the appropriate boundary conditions. For cylinders of inner diameter ρ_0 and a stack length L, the solution may be expressed as an expansion in modified Bessel functions I_0 [39]:

$$V(\rho, z) = \sum_{n=1}^{\infty} A_n \sin(k_n z) I_0(k_n \rho) \tag{2.6}$$

where

$$k_n = \frac{n\pi}{L} \tag{2.7}$$

(n is a positive integer), and

$$A_n = \frac{2}{I_0(k_n \rho_0) L} \int_0^L V(\rho_0, z) \sin(k_n z)\, dz. \tag{2.8}$$

The additional assumption is made that the potential goes to zero at the ends of the outermost cylinders (*i.e.*, $V = 0$ at $z = 0$ and $z = L$).

In two regions of the trap the electrode geometry is chosen such that, with application of appropriate bias voltages, the electric potential near the centers of these regions closely approximates that of an ideal Penning trap (Eq. 2.2). The details of the calculations leading to the choice of geometry and potentials used for these regions are discussed elsewhere [38]; a summary is given below.

Each harmonic region consists of five electrodes (shown in section in Fig. 2.3): a ring electrode, two compensation electrodes, and two endcap electrodes. The expansion coefficients for this trap are calculated in the limit of long endcaps (drawn with dashed lines in Fig. 2.3); the tabulated values are therefore only approximately valid for the short endcap geometry (solid line) unless additional electrodes beyond these endcaps are also held at the endcap potential.

If the origin is taken at the center of the trap (location of the "+" in Fig. 2.3), the potential may be expanded in terms of Legendre polynomials

$$V(\rho,\theta) = \frac{1}{2}\sum_{k=0}^{\infty} C_k \left(\frac{\rho}{d}\right)^k P_k(\cos\theta) \tag{2.9}$$

where $d^2 = \frac{1}{2}(z_0^2 + \frac{1}{2}\rho_0^2)$, and the underlying azimuthal symmetry precludes any dependence on ϕ.

Neglecting an overall constant, there are four potentials which characterize this system of five electrodes. These are symmetrized as shown in Fig. 2.3, leading to

$$V(\rho,\theta) = V_0\phi_0 + V_C\phi_C + V_{E,A}\phi_{E,A} + V_{C,A}\phi_{C,A} \tag{2.10}$$

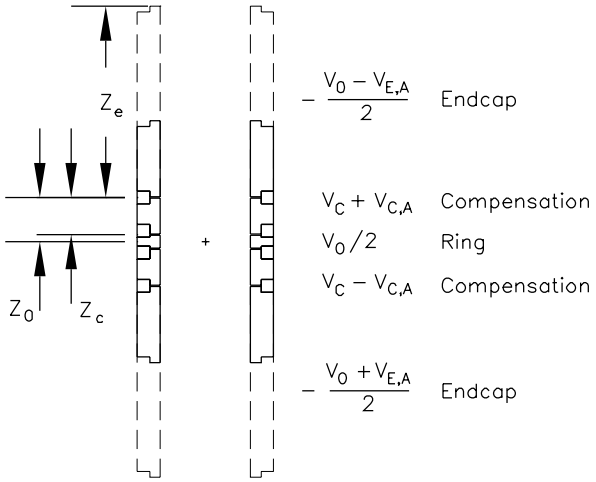

Figure 2.3: The compensated trap and boundary conditions for determining the expansion coefficients. The dashed line denotes the endcaps used in the calculation; the solid line, the actual trap endcaps.

where the symmetric solutions to Laplace's equation are contained in the functions

$$\phi_0 = \frac{1}{2}\sum_{\substack{k=0\\ \text{even}}}^{\infty} C_k^{(0)} \left(\frac{\rho}{d}\right)^k P_k(\cos\theta) \quad , \quad \phi_C = \frac{1}{2}\sum_{\substack{k=0\\ \text{even}}}^{\infty} D_k \left(\frac{\rho}{d}\right)^k P_k(\cos\theta) \tag{2.11}$$

and the antisymmetric solutions in

$$\phi_{E,A} = \frac{1}{2}\sum_{\substack{k=1\\ \text{odd}}}^{\infty} c_k \left(\frac{\rho}{z_0}\right)^k P_k(\cos\theta) \quad , \quad \phi_{C,A} = \frac{1}{2}\sum_{\substack{k=1\\ \text{odd}}}^{\infty} d_k \left(\frac{\rho}{z_0}\right)^k P_k(\cos\theta). \tag{2.12}$$

In terms of the expansion (Eq. 2.9),

$$C_k = C_k^{(0)} + \frac{V_C}{V_0} D_k + \frac{V_{E,A}}{V_0}\left(\frac{z_0}{d}\right)^k c_k + \frac{V_{C,A}}{V_0}\left(\frac{z_0}{d}\right)^k d_k. \tag{2.13}$$

In an ideal Penning trap, all of the terms except C_2 (and the unimportant constant C_0) are zero [37]. Electrode potentials and geometries can also be chosen such that

crucial higher-order terms in Eq. 2.13 are also zero. Requiring that the asymmetric potentials $V_{E,A}$ and $V_{C,A}$ are zero, for instance, insures that all of the odd terms vanish. The largest of the remaining terms is C_4, which can be tuned to zero by a suitable choice of V_C:

$$V_C = -\frac{C_4^{(0)}}{D_4} V_0. \tag{2.14}$$

Further geometrical selections yield a trap in which D_2 and C_6 also vanish [38].

The geometry chosen for the harmonic regions of the apparatus used here is given in Table 2.2, along with the values of the first few expansion coefficients. For this trap, $C_2 \neq 1$; thus, the axial frequency in Eq. 2.3 must be modified to read

$$\nu_z = \frac{1}{2\pi}\sqrt{\frac{C_2 e V_0}{m d^2}}. \tag{2.15}$$

By choosing $z_c = 0$, the preceding analysis may be applied to a trapping region consisting of only three electrodes (a ring electrode and two endcaps), as shown in Fig. 2.4. In particular, one of the ≈ 1 cm long electrodes (used as the endcaps in the five-cylinder compensated trap) may be used as a "ring" electrode in a three-electrode trap, resulting in a trapping region which is sufficiently harmonic to permit particle detection with the radiofrequency techniques of Sec. 3.2. While useful for relatively large clouds of particles, the three-electrode traps possess an (untunable) anharmonicity too great to permit precise measurements on smaller numbers; for the latter, a compensated, five-cylinder trap is required. The expansion coefficients for the three-electrode trap are included for completeness in Table 2.2.

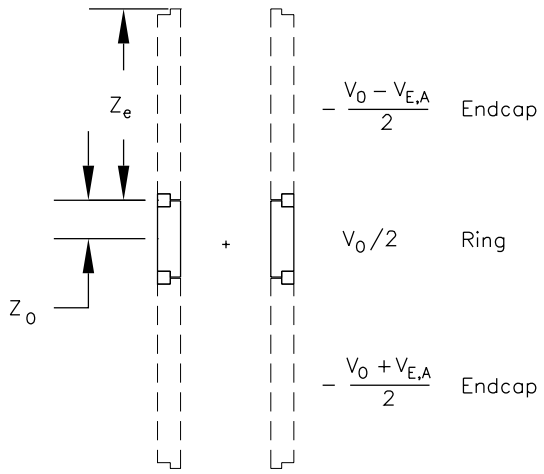

Figure 2.4: Three-electrode trap and boundary conditions for determining its expansion coefficients. The "ring" electrode shown is one of the ≈ 1 cm electrodes employed as an endcap in the five-electrode, compensated trap.

Table 2.2: Calculated electrostatic properties of common well configurations. Long endcaps are assumed.

electrode dimensions		5-cylinder	3-cylinder	
ρ_0	=	0.600	0.600	cm
z_0	=	0.586	0.512	cm
d	=	0.512	0.470	cm
z_c/z_0	=	0.8351	—	
V_C/V_0	=	0.3811	—	
expansion coefficients				
C_2	=	0.5449	0.5733	
D_2	=	0	—	
C_4	=	0	0.0137	
D_4	=	−0.5560	—	
C_6	=	0	−0.0486	
D_6	=	0.4300	—	
c_1	=	0.3346	0.3806	
c_3	=	0.2202	0.1605	
d_1	=	0.8994	—	
d_3	=	−0.8439	—	

Table 2.3: Determination of particle frequencies in the harmonic trapping region from the magnetic field B_0 and the trapping potential V_0.

freq.	protons, antiprotons	electrons, positrons
ν_c	15.24507 B_0[Tesla] MHz	27.99225 B_0[Tesla] GHz
ν_z	.22477$\sqrt{V_0[\text{Volt}]}$ MHz	9.63152$\sqrt{V_0[\text{Volt}]}$ MHz
ν_m	1.6570 V_0[Volt]/B_0[Tesla] kHz	

2.3 Apparatus Details

In addition to its electric and magnetic fields, a useful Penning trap requires a high vacuum (for long particle lifetimes) and systems for loading, manipulating, and detecting the confined particles. This section describes the the apparatus which supports the trap. Additional information on its design and construction may be found in Ref. [40].

The electrodes for the proton-electron ("recombination") apparatus are shown in section in Fig. 2.5. Most of the electrodes are machined of OFHC copper to minimize magnetic impurities and their associated magnetic field distortions. Copper leads are brazed to the electrodes in an hydrogen furnace, after which the electrodes are polished and gold-plated to minimize surface-charging effects. The electrodes are electrically insulated from one another by MACOR rings.

At the top of the electrode "stack" is an aluminum mirror electrode (MIR), designed to reflect light from radiative recombination of protons and electrons to the microchannel plates located below the trap (Sec. 2.5). Its surface is highly polished and coated with MgF_2 to maintain its vacuum ultraviolet (VUV, $\approx$ 100-200 nm) reflective properties [41]. At the other end is a long stainless-steel tube

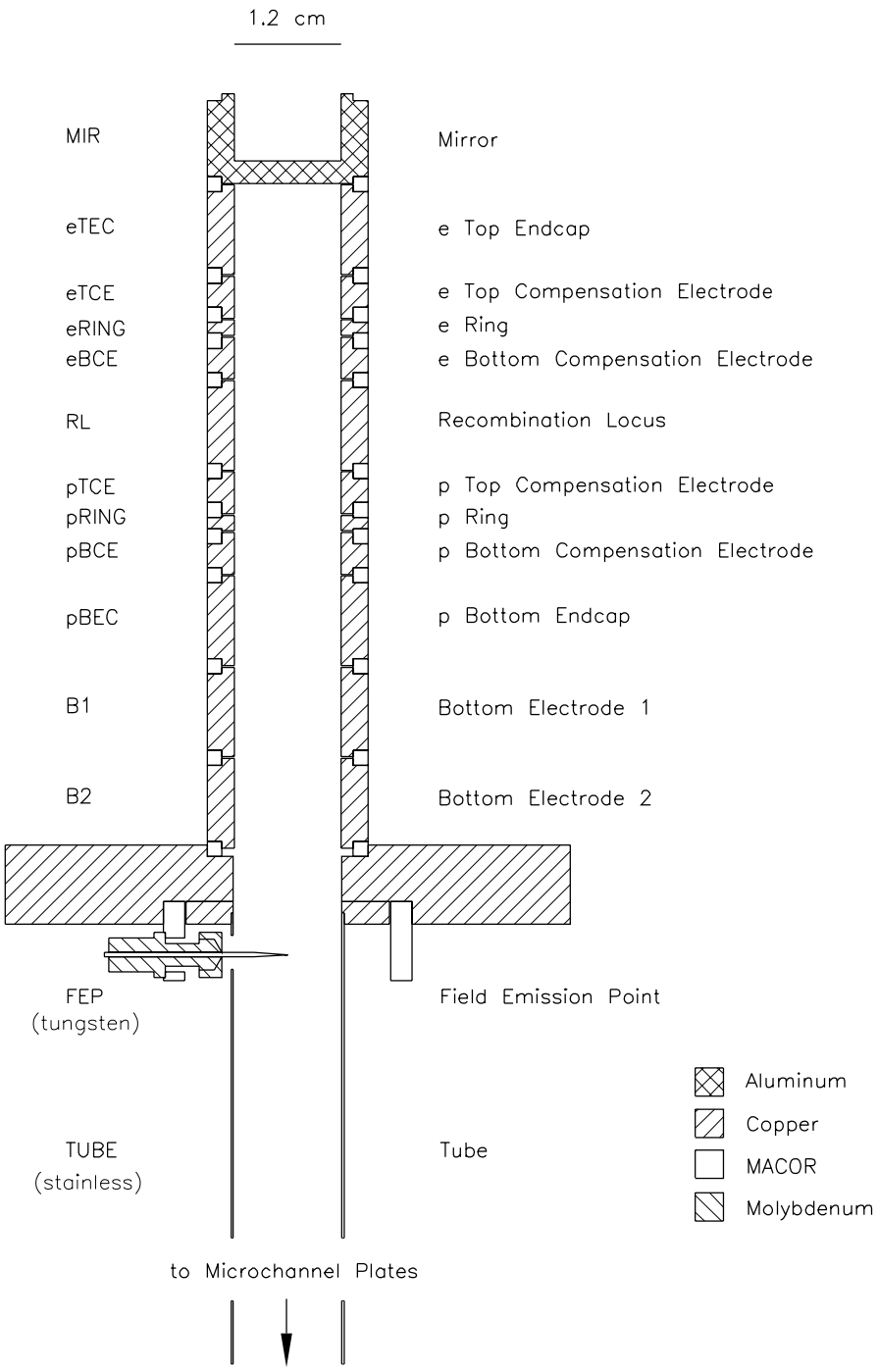

Figure 2.5: Electrodes and naming convention for the recombination apparatus.

(TUBE) which extends approximately 30 cm to the microchannel plates. Its interior is polished and gold-plated to improve reflectivity of VUV photons as well as to minimize surface-charging effects. Since it is quite long, the TUBE must be carefully aligned with the rest of the electrodes so as neither to touch the microchannel plate enclosure nor cross the magnetic field lines on the axis (see Sec. 2.5).

Jutting into the TUBE just below the last copper electrode are two field emission points (FEPs), held in place by molybdenum collets mounted on a MACOR ring. One end of each of these 0.5 mm diameter tungsten rods is electrochemically etched to a very sharp point, permitting a beam of electrons to tunnel from the point into the vacuum when the point is biased to -1 kV with respect to the TUBE (Sec. 3.1). One FEP is positioned so that its tip is as close as possible to the trap axis, and the other is placed ≈ 1 mm off-axis. Electrical connections are made by spot-welding small strips of constantan (CuNi) wire to the dull ends of the FEPs.

A good vacuum is essential for long-term particle confinement. The electrodes are, therefore, housed in their own OFHC copper trap vacuum enclosure ("trap can"), shown in section in Fig. 2.6. The body of the can is OFHC copper and mates with two OFHC copper flanges with indium O-ring seals. The upper flange ("pin-base") contains cryogenic feedthroughs which permit electrical access to the interior and provides support for the electrodes bolted to its interior surface. The bottom flange is connected to a long stainless steel tube which extends to the microchannel plate enclosure (Sec. 2.5). The trap can is evacuated to approximately 5×10^{-7} Torr at room temperature through a 3/8" OD copper tube which is then sealed using a pinch-off tool. Thermal contact with a reservoir of liquid helium (Fig. 2.7) cools the vacuum enclosure and its contents to 4.2 K, whereupon the vacuum improves to better than 5×10^{-17} Torr as determined by measurement of the lifetime of antiprotons in a similar apparatus [42, 43].

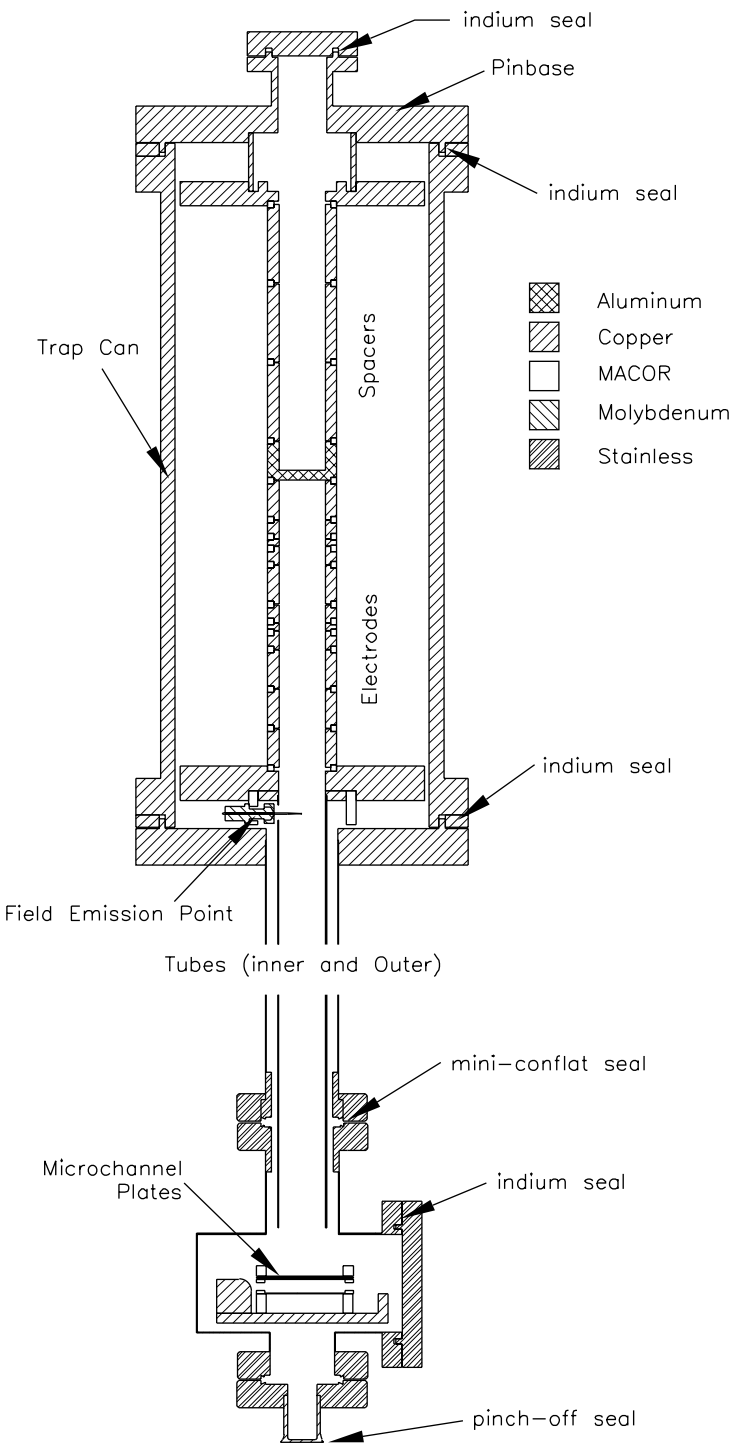

Figure 2.6: Trap vacuum enclosure (section). The stainless steel tubes extend approximately 30 cm below the bottom of the trap can.

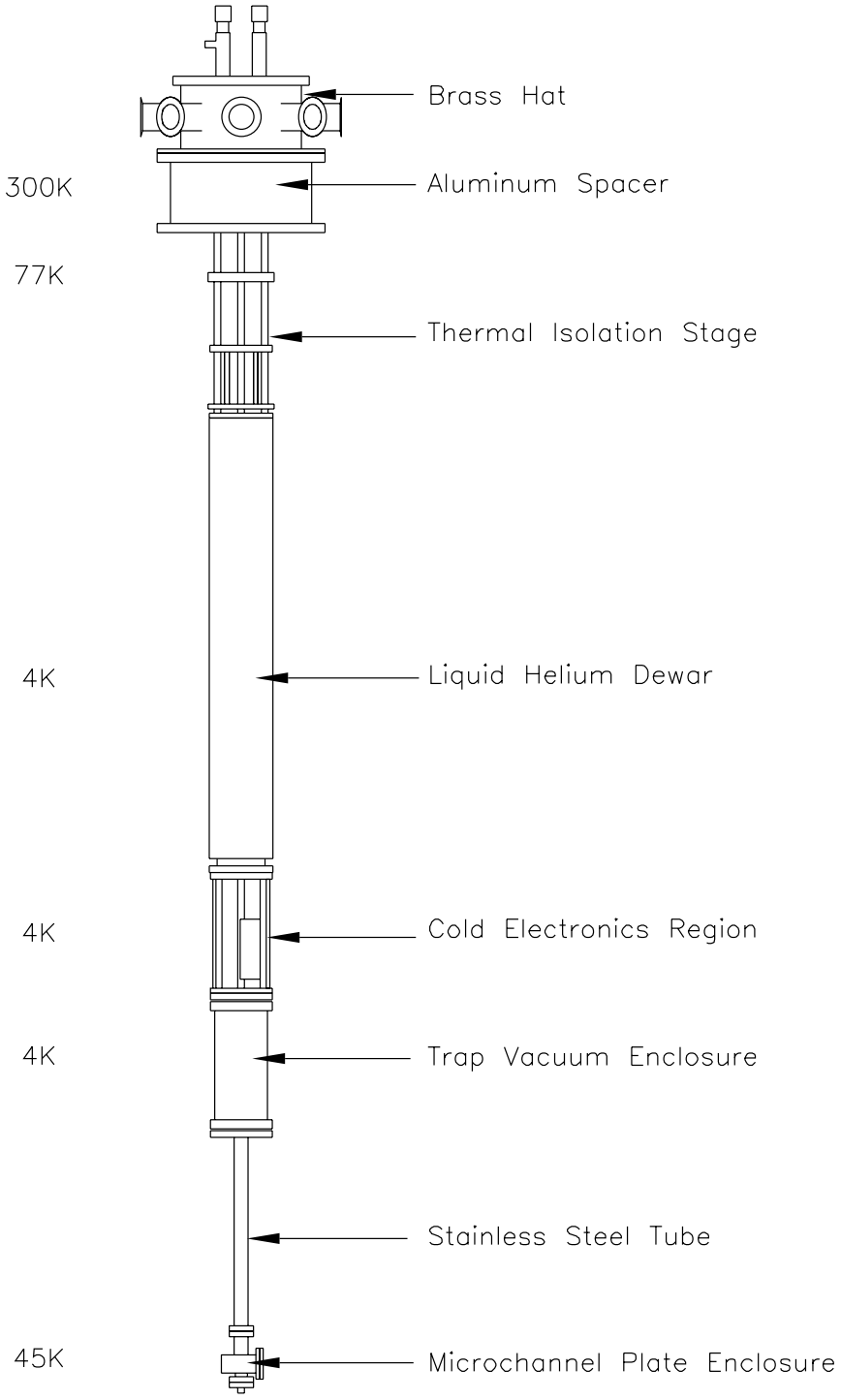

Figure 2.7: Trap vacuum enclosure and cryogenic support system. The radiation shields between the magnet bore and the apparatus are not shown.

The liquid helium reservoir is a hollow vessel constructed of OFHC copper with a volume of just over 3 liters and a hold time of about 2 days while the apparatus is operating. A number of tubes pass through the dewar to allow electrical and mechanical access to the stages below. An OFHC copper stage ("tripod") thermally connects the dewar to the trap vacuum enclosure and provides the necessary space for a set of helical resonators, FET amplifiers, and filters for the RF and DC connections to the trap electrodes (Sec. 2.4). These electrical circuits are mounted on a copper clad G-10 board situated just above the pinbase.

The helium dewar is insulated from the room temperature sections of the apparatus by a succession of copper plates joined by sections of thermally insulating G-10 epoxy-fiberglass (Fig. 2.7). The copper plates are heat-sunk to the gas-cooled helium dewar exhaust tube (a set of stainless-steel bellows). An aluminum radiation shield attached to the lowest copper plate surrounds the apparatus to the microchannel plate enclosure, minimizing the radiative heat load on the apparatus from the walls of the 77 K magnet bore. A copper radiation shield, in thermal contact with the magnet bore and the uppermost copper plate, surrounds the thermal isolation stage itself.

At the very top of the apparatus is the "brass hat," which provides an electrical interface to the magnet bore vacuum. Additional filters for the DC and RF circuits, as well as the first room-temperature gain stages for the signals originating in the apparatus, are located just outside the vacuum. An aluminum spacer for adjusting the vertical position of the apparatus with respect to the magnet field center is mounted between the hat and the top flange of the magnet bore.

Finally, the magnetic field of the Penning trap is produced by a 6 Tesla superconducting solenoid with a 4" diameter bore, into which the apparatus is inserted. The bore is subsequently pumped out and cooled to 77 K by thermal contact with

an reservoir of liquid nitrogen. Once filled, the apparatus liquid helium dewar cryopumps the bore and maintains a pressure better than 1×10^{-6} Torr.

2.4 Trap Wiring

The cold electronics and electrode wiring diagram for this apparatus is shown in Fig. 2.8. The circuits provide paths for DC biasing, RF drives, and particle detection. The remainder of this section will consider these three components in detail.

2.4.1 DC Bias Circuits

The bias potentials for the electrodes are derived from solid-state voltage sources. For the harmonic trapping regions, the voltage source is a Fluke 5440 series Direct Volts Calibrator, which generates a stable, high-resolution voltage over a range of $\pm$1000 V (although it is typically used below $\pm$100 V). The output of the calibrator is applied (after filtering) to a ring electrode (Fig. 2.9); the potentials for the associated compensation electrodes are derived from a Kelvin-Varley resistive divider. One calibrator (and divider) is used for each of the two harmonic trapping regions. The remaining electrodes are biased by amplified, filtered DAC channels (Joerger DAC-8 CAMAC modules), which have a range of $\pm$150 V and a resolution near 30 mV. All of the bias potentials are computer-controlled.

The DC bias lines are low-pass filtered at room temperature (1 ms time constant) and pass through vacuum feedthroughs at the brass hat into the magnet bore. Very thin constantan wires (minimizing thermal conduction) carry the potentials to the cold electronics region, where they are further filtered (1 ms time constant) before passing into the trap vacuum enclosure, where they are applied to the electrodes on OFHC copper straps. Care is taken to minimize the leakage current between the

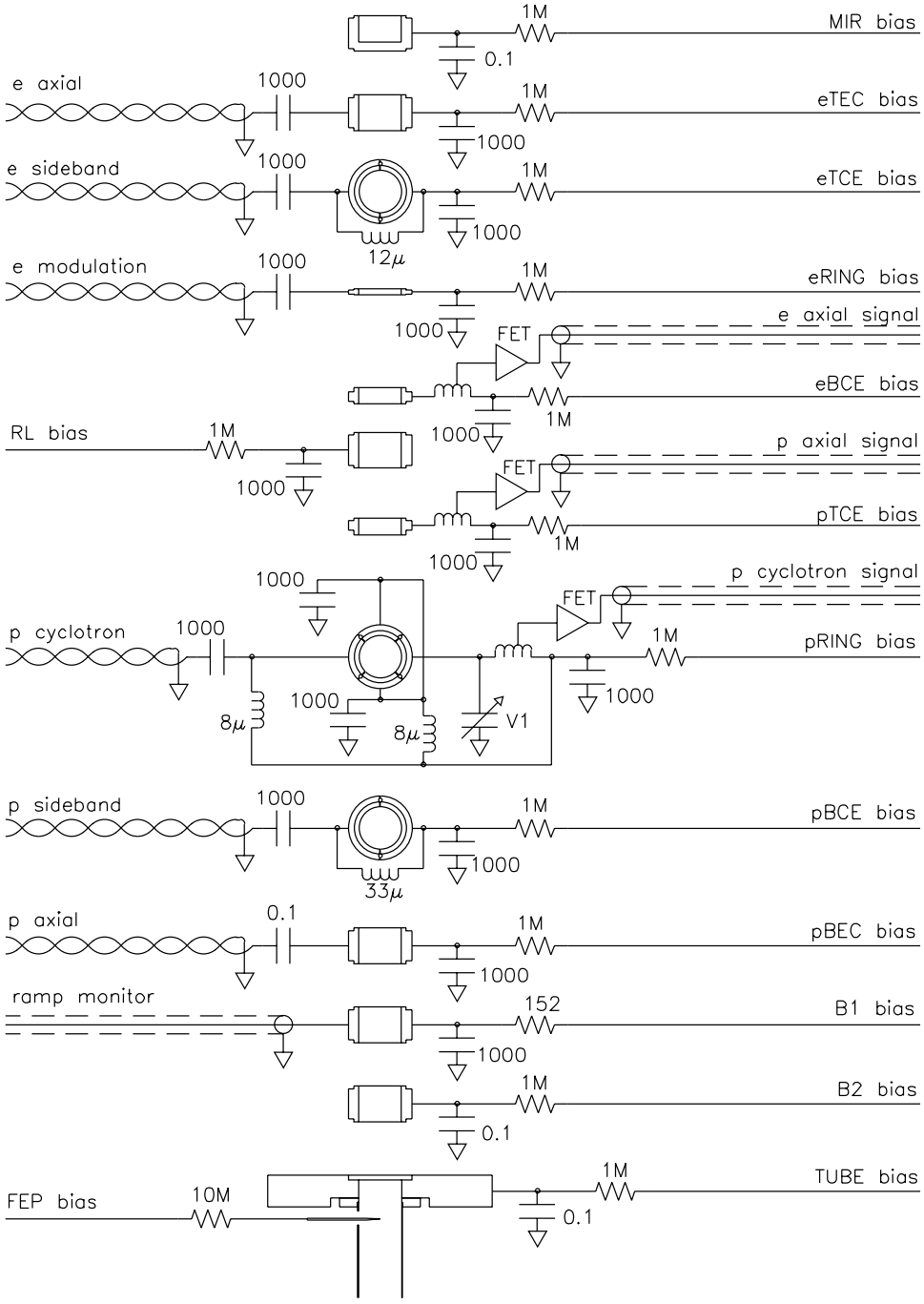

Figure 2.8: Trap wiring diagram for the recombination apparatus. Details of the amplifier (FET) and varactor (V1) circuits are shown in Figs. 2.12 and 2.14. Segmented electrodes are rotated 90° in the figure.

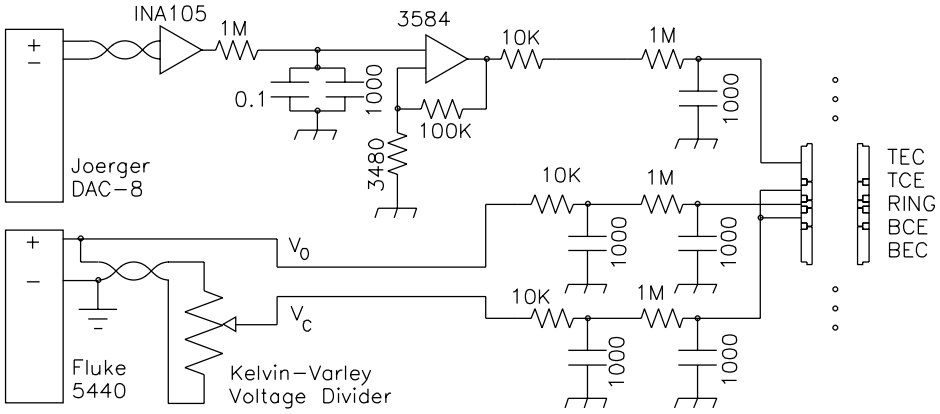

Figure 2.9: Room-temperature DC wiring schematic. Connections for only one of each type of voltage source is shown.

electrodes and ground, and the impedance looking into a typical DC bias line at the brass hat is typically greater than 5×10^{10} Ω.

The filter values on the B1 electrode are reduced to permit fast ramping of the applied potential. The fast ramp waveform is measured on the center conductor of a stainless steel microcoax line ("ramp monitor") which is DC-coupled to the B1 bias line at the pinbase feedthrough. The voltage appears on an SMA connector at the brass hat, where it is directed to a digital oscilloscope.

The segments of the three split electrodes (eTCE, pRING, and pBCE) are connected by inductors to maintain the DC bias on the entire electrode. The inductor value is chosen by the blocking frequency desired (Sec. 2.4.2) and is typically on the order of 10 μH.

2.4.2 Radiofrequency (Drive) Circuits

Radiofrequency drives are applied to excite and couple the motions of the particles in the trap. The drives are generated by frequency synthesizers and are filtered and

attenuated before passing into the apparatus. Twisted pairs of thin constantan wire form transmission lines between the brass hat and the cold electronics region, where one end of each twisted pair is grounded at the pinbase and the other is AC-coupled to the appropriate electrode bias line.

There are 6 drive lines in this apparatus, of which 4 (electron sideband, proton sideband, proton cyclotron, and proton axial) are used regularly (Fig. 2.10). The two "sideband" drives are used to reduce the radii of particle magnetron orbits (Sec. 3.3). These drives are applied to only one half of a split compensation electrode (pBCE or eTCE) in order to achieve the symmetry required to couple the axial and magnetron motions (Table 2.4). Inductors connected between the electrode halves block the drive frequencies but permit the DC bias to appear on the both segments. The proton cyclotron drive is used to excite the proton cyclotron motion and is applied to one quadrant of the split ring electrode (pRING); inductors are chosen to pass both DC and the proton magnetron frequency ($\approx$ 10 kHz). The proton axial drive is used to excite the axial motion of ions (other than protons) with the intent of driving them out of the trap. The drive is applied to an entire endcap electrode (pBEC) and is filtered so as to leave the protons undisturbed while exciting the axial motion of the other ions (Sec. 3.1). The two remaining drives (electron axial and electron modulation) are used for detection of small numbers of electrons and are discussed further in Sec. 3.4.2.

2.4.3 Radiofrequency (Detection) Circuits

Tuned LCr circuits are used to detect the particles in the harmonic regions of the trap. An inductor L (with associated internal losses r) is attached between two of the trap electrodes. In practice, one of the two electrodes is RF-grounded, as shown

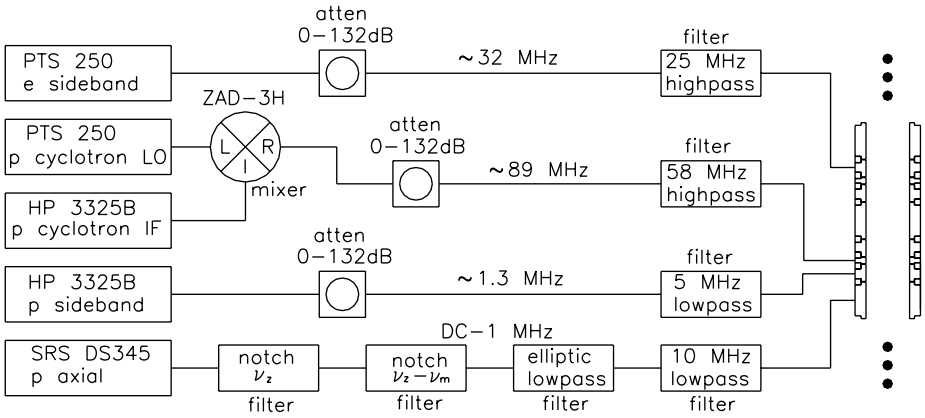

Figure 2.10: Block diagram of the "standard" RF drive configuration used in these experiments.

Table 2.4: Drive and detector symmetries for various particle motions and their corresponding electrodes.

drive	symmetry	electrode
ν_c'	x	1/4 ring
$\nu_c' \pm \nu_z$	xz	1/2 compensation
$\nu_c' \pm \nu_m$	x	1/4 ring
ν_z	z	endcap
$\nu_z \pm \nu_m$	xz	1/2 compensation
detect	**symmetry**	**electrode**
ν_c'	x	1/4 ring
ν_z	z	compensation

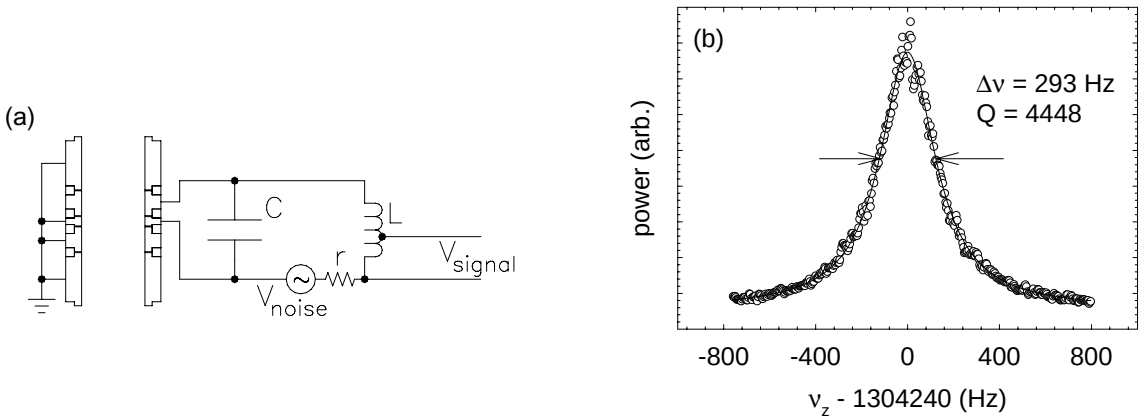

Figure 2.11: The tuned circuit detector. (a) Effective radiofrequency circuit schematic. (b) Johnson noise-driven resonance as seen by a spectrum analyzer.

in Fig. 2.11(a). The inductor forms a resonant *LCr* circuit with the capacitance C between the ungrounded electrode and its neighboring electrodes (typically 12–15 pF). A judicious choice of inductor yields a resonant frequency which is identical to that of the particle motion to be detected.

The inductors are helical resonators, consisting of a silver-plated copper coil wound in a helix within a grounded, gold-plated copper cylinder ("amplifier can"). The Q of the resulting tuned circuit is maximized by the choice of coil and can geometry [44], as well as by use of special "high-Q" capacitors.

The proton axial helical resonator, operating at 1.3 MHz, is exceptional in that it consists of an enameled NbTi wire coil wound about a teflon form within a NbTi can. The NbTi alloy is a type II superconductor at temperatures below 8 K, even in the magnetic field of the solenoid. As a result, resistive losses in the resonator are diminished and the Q increases dramatically [45, 46]. It is not yet known whether the higher-frequency resonator circuits would benefit from being constructed of the superconducting alloy.

Signal from the *LCr* circuit is coupled to an FET amplifier operating in the cold electronics region (Fig. 2.12). The FET is a dual-gate MESFET (Mitsubishi

Table 2.5: Typical operating parameters for the Mitsubishi MGF1100 MESFET.

V_{DS}	3.0 V
V_{G_1S}	≈ -2 V
V_{G_2S}	≈ 0 V
I_D	≈ 1 mA
P (dissipated)	≈ 3 mW
Z_{out}	≈ 6 kΩ

MGF1100) providing current gain (but little voltage gain); typical operating parameters are given in Table 2.5. The signal, taken from a tap on the helical resonator coil, is AC-coupled to gate 1 of the FET. After amplification it appears on the FET drain, where a pi-network circuit matches its impedance to that of a 50 Ω stainless-steel microcoaxial cable. The signal passes through the liquid helium dewar on the microcoax and emerges at an SMA connector at the brass hat, where it is decoupled from the drain DC bias by a bias-T network. It is subsequently amplified and filtered (Fig. 2.13) before being carried on a double-shielded coaxial cable to the signal-processing equipment in the experiment control area. For signals of bandwidth greater than 50 kHz the most commonly used measurement device is a wideband spectrum analyzer, such as the HP 8560A or HP 70000. Signals of narrow bandwidth are mixed down to $\approx$ 50 kHz and viewed with an FFT signal analyzer, such as the HP 3561A or SRS SR760. The LCr resonance of the proton axial amplifier, driven by the Johnson noise of the effective circuit resistance r, is shown after amplification and Fourier-transformation in Fig. 2.11(b). (The details of particle detection and signal interpretation are deferred to Sec. 3.2.)

The frequency of a particle's axial motion may be matched to the resonant frequency of the detector by a change of trapping potential (Eq. 2.3). This is almost always necessary, owing to variations in the tuned-circuit frequency introduced by

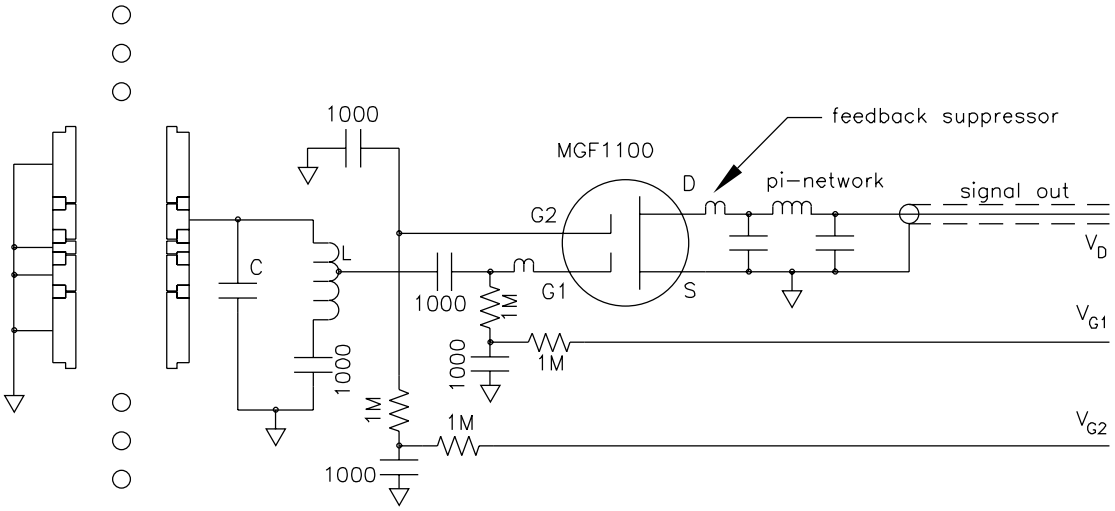

Figure 2.12: Typical FET circuit diagram showing connections to the helical resonator coil. The coil inductance L and effective trap capacitance C comprise the LCr resonant circuit, along with inductor losses r (not shown).

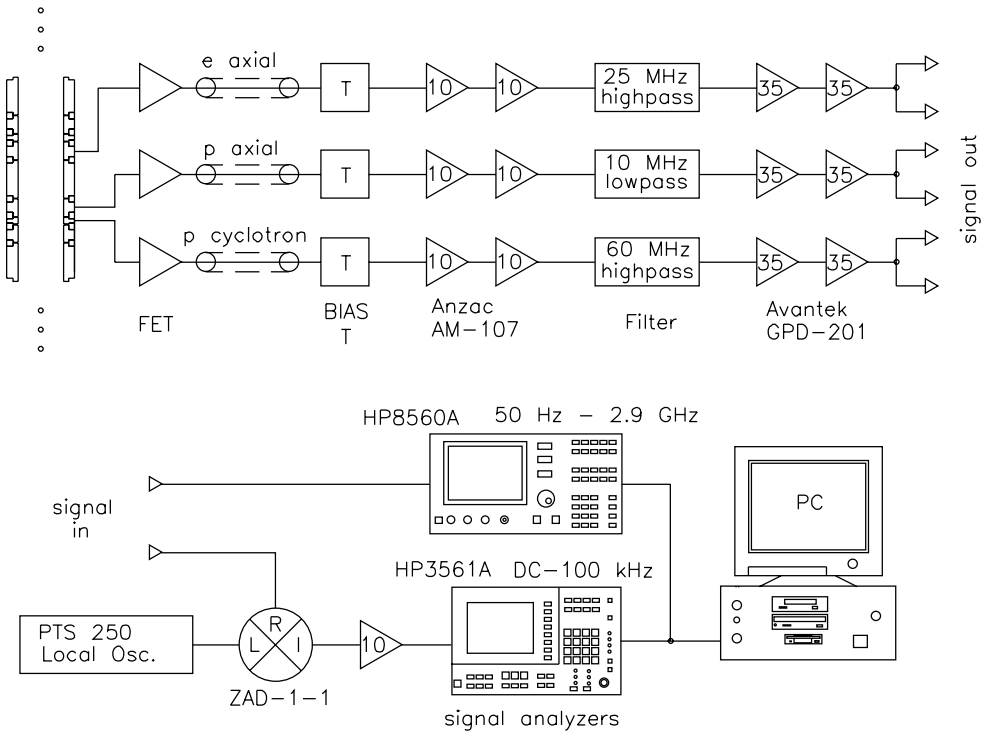

Figure 2.13: Standard RF detection circuits.

thermal contraction during cooldown. Changing the cyclotron frequency to match a detector frequency, however, can be much more cumbersome, since it involves the time-consuming (and somewhat risky) process of changing the magnetic field produced by the superconducting solenoid.[1] (Alternatively, there may be two particle species of interest with slightly different frequencies to be detected, as is the case in the recent antiproton/H^- ion mass comparison [47].) In such cases it may be easier to change the detector frequency rather than the particle frequency. This has been accomplished in the past [45] by tapping the helical resonator coil near the top, thereby increasing the coupling between the gate-source capacitance of the FET and the remainder of the tuned circuit. As the gate voltage of the FET is adjusted, the gate-source capacitance also varies, and the resonant frequency changes. Unfortunately, this method changes the operating point of the FET, and often permits only a limited tuning range.

In these experiments a GaAs varactor diode [48] capable of operation at 4 K is used to tune the detector frequency (Fig. 2.14). The capacitance of the varactor (MDT MV-2105) varies between 23 pF to $\approx$ 3 pF as a bias voltage between 0 V and 9 V is applied across the diode terminals. This range is too large for a circuit in which the effective trap capacitance is only 12–15 pF (even though the distributed capacitance in the helical resonator can add up to another 12 pF), so a small (1 pF) capacitor is placed in series with the diode to limit the tuning to a fraction of a pF. (Another capacitor of higher value is placed in series to block the varactor DC bias from the RF ground.) The resonant frequency of the detector circuit may then be easily changed to match the cyclotron frequency of the particles, without significantly affecting the operating point of the FET.

[1] Changing the axial frequency can also be difficult if the trapping potential is supplied from a battery.

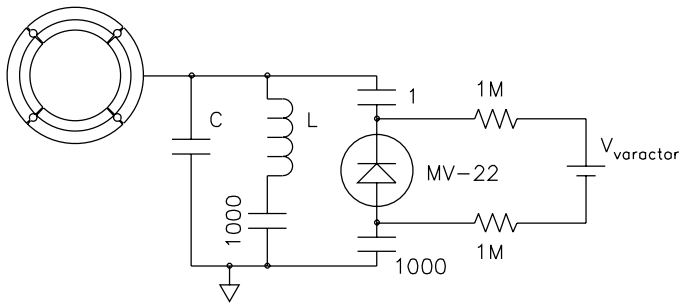

Figure 2.14: Circuit diagram for the varactor used to tune the resonant frequency of the proton axial amplifier. The amplifier circuit is omitted for clarity (see Fig. 2.12).

The results of outfitting the proton cyclotron detector with a varactor are shown in Fig. 2.15(a). At three temperatures a tuning of 400 kHz is achieved about a center frequency of roughly 83 MHz. The price for this relatively large tuning range is exacted in circuit Q at 4 K, as can be seen in Fig. 2.15(b). By reducing the value of the capacitor tuned by the varactor, one should be able to retain a high Q with a tuning range suitable for matching the detector and particle frequencies (typically 100–200 kHz).

2.5 Microchannel Plates

Microchannel plates (MCPs) for particle and ultraviolet light detection are housed in a stainless-steel enclosure connected to the trap can by a 3/4" diameter stainless-steel tube (Figs. 2.6 and 2.7). Since the trap region constitutes a rather severe environment for such detectors, the tube is approximately 30 cm long and permits operation of the plates at temperatures above 4 K in the 0.6 Tesla fringing field. Charged particle detection is generally unaffected by this choice of position, since particles ejected from the trap will be guided by the magnetic field lines until they strike the plates. On the other hand, the cross-section for detection of neutral

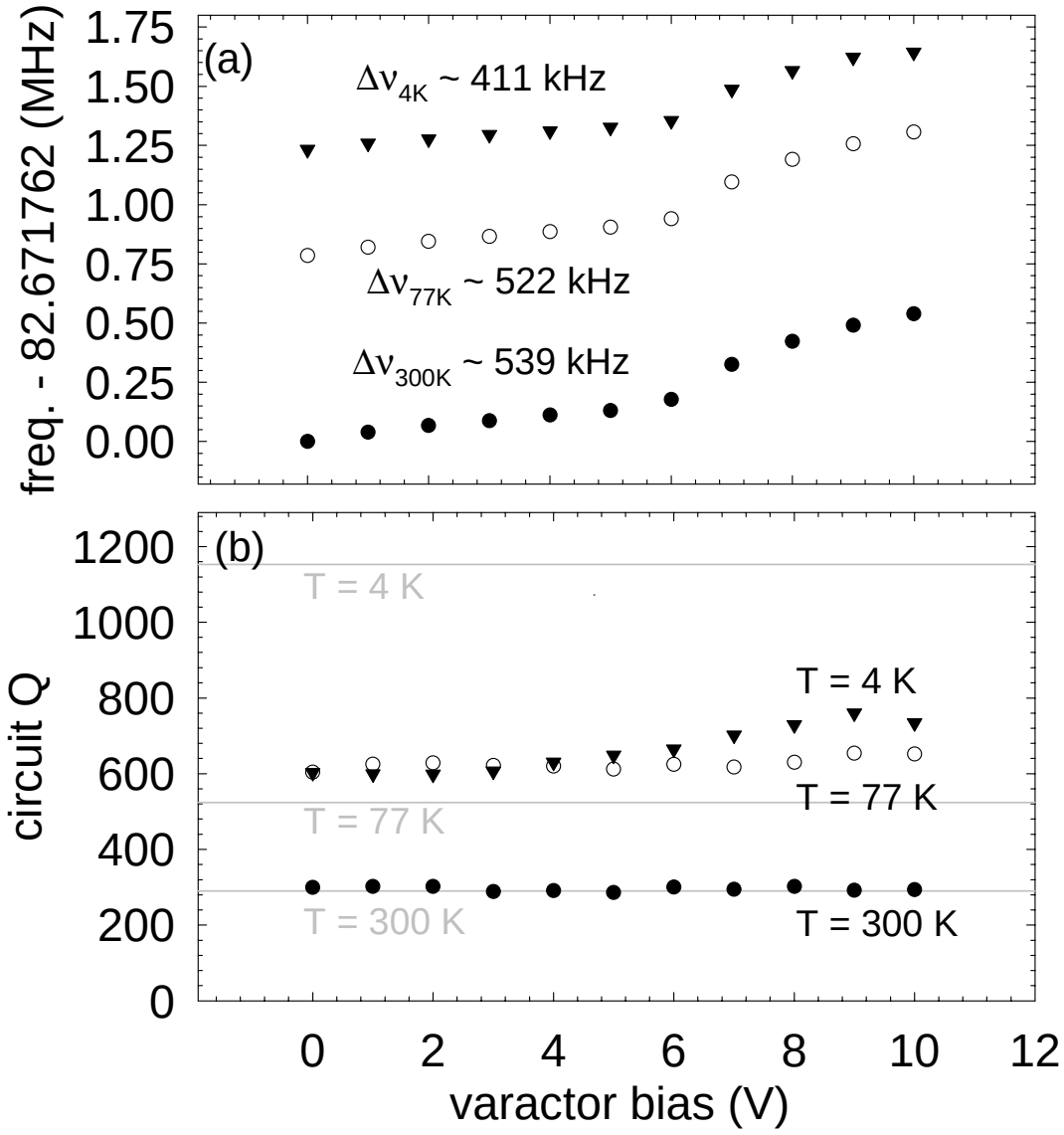

Figure 2.15: Variation of tuned circuit resonance (a) center frequency, and (b) Q (quality factor) as a function of applied varactor bias. Typical values for three different temperatures are shown; the gray lines indicate the quality factors of the circuit with the varactor absent.

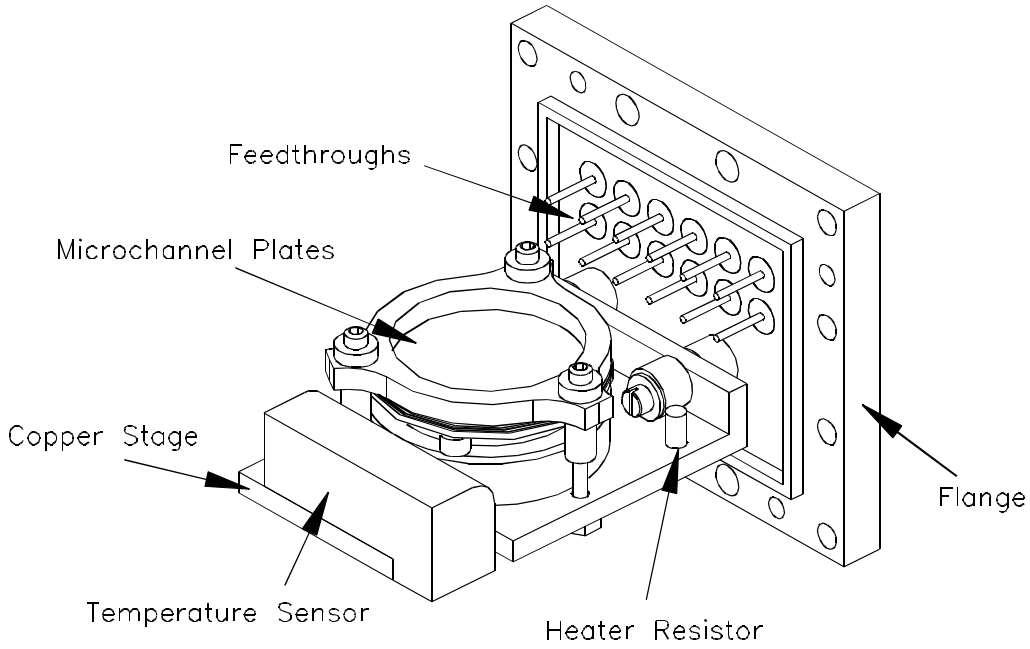

Figure 2.16: The microchannel plate assembly shown mounted to its flange.

particles (such as atoms or photons) is substantially reduced. The MIR and TUBE electrodes were installed, and the front MCP coated with CsI, to maximize the remaining detection sensitivity for UV photons.

The plates are mounted on a copper stage which is bolted to a rectangular flange on the side of the MCP enclosure (Fig. 2.16), facilitating easy removal of the the entire unit for servicing. The temperature of the plates is controlled by resistively heating the copper stage, and is monitored with a calibrated carbon-glass resistor. Electrical connections are made through the flange on feedthroughs constructed of epoxy [49] and wire.

Each microchannel plate consists of approximately 2 million tightly-packed lead glass tubes (channels), which are angled slightly from the vertical to prevent normally incident particles from passing through the plate undetected. When a bias voltage is applied across a channel (lengthwise) it becomes an electron multiplier

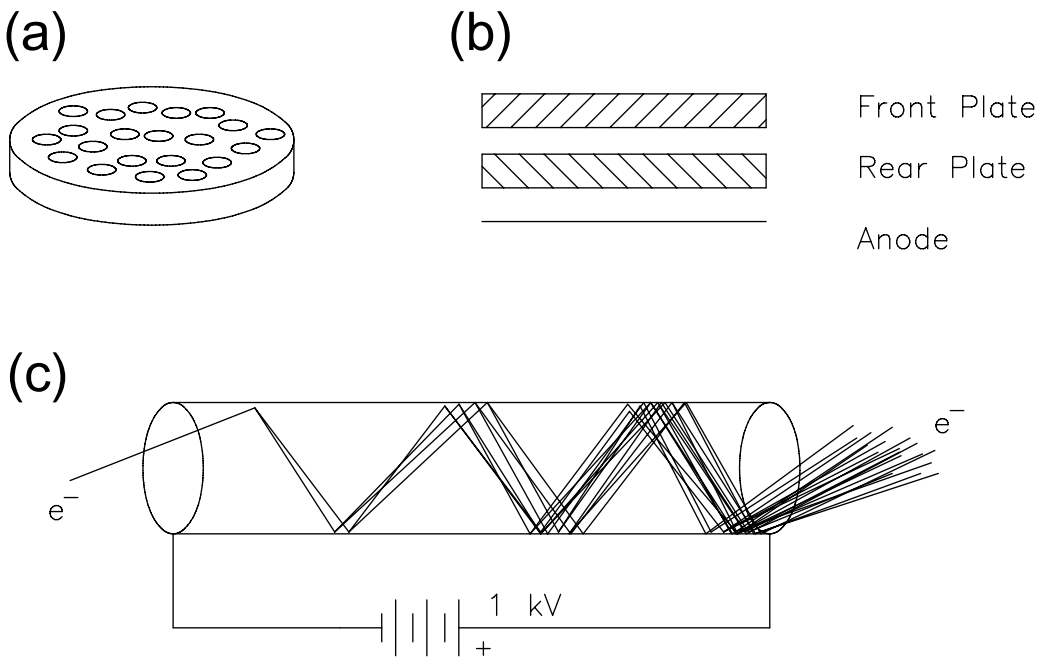

Figure 2.17: Microchannel plates, very schematically. (a) Exaggerated view of a microchannel plate. There are actually over 2 million channels on each of the plates. (b) Schematic of the chevron configuration, in which the bias angle is reversed at the interplate junction. (c) Electron multiplication process in a single channel.

very similar to a photomultiplier tube. An incident particle striking the channel wall ejects secondary electrons from the surface, which are then accelerated by the electric field until they too strike the channel walls, liberating additional secondaries, and so on [Fig. 2.17(c)]. If δ represents number of electrons emitted per incident (secondary) electron in each collision with the wall of the tube, then the gain will be $G = \delta^n$, where n is the number of times the process is repeated before the electrons exit the far side of the channel and are collected by the anode [50].

A crude kinematic model [50] may be derived for the gain of a single microchannel plate by making the assumption that secondary electrons are emitted perpendicular to the tube wall, and that the number of secondary electrons produced is proportional to the velocity of the particle which strikes the tube surface (*i.e.*, $\delta = \sqrt{E_c/E_1}$,

where the constant $E_1 \approx 25$ eV represents the energy required to liberate a single electron and E_c is the impact energy). The gain may then be expressed

$$G = \left(\frac{eV}{2\alpha\sqrt{E_1 E_2}} \right)^{\frac{4E_2\alpha^2}{eV}} \tag{2.16}$$

where V is the bias across the tube, α is the ratio of the length to the diameter of the tube, and $E_2 \approx 1$ eV is the initial energy of the secondary electron.

Due to onset of ion feedback, in which ions produced by the electron cascade find their way back to the plate input and excite additional channels, the gain of a typical straight-channel microchannel plate is limited to about 10^4 at a plate bias of 1 kV [50]. To achieve higher gains, two straight-channel plates with small bias angles are used in series with the channels oriented to form a "chevron," as depicted in Fig. 2.17(b). The electrons exit the first plate and enter the second, continuing the multiplication process, whereas ions are discouraged from returning to the input by the discontinuity in the channel direction. Gains of up to 10^7 may be realized. A chevron pair is usually operated in a saturated gain mode, in which enough electrons are liberated from the channel walls that their collective space charge prevents additional electrons from joining the cascade. The saturation gain for a single plate is estimated to be [51, 52]

$$G_{sat}^{(1)} = \frac{3\sqrt{3}}{2} \frac{\pi\epsilon_0}{e} D^2 \frac{V}{L} \tag{2.17}$$

where D is the channel diameter and L is the channel length.

The bias circuit for the microchannel plates (and the collector anode) used here is shown in Fig. 2.18; the currents passing through the plates ("strip currents") are monitored by measuring the voltage across 1 MΩ resistors. The voltage with respect

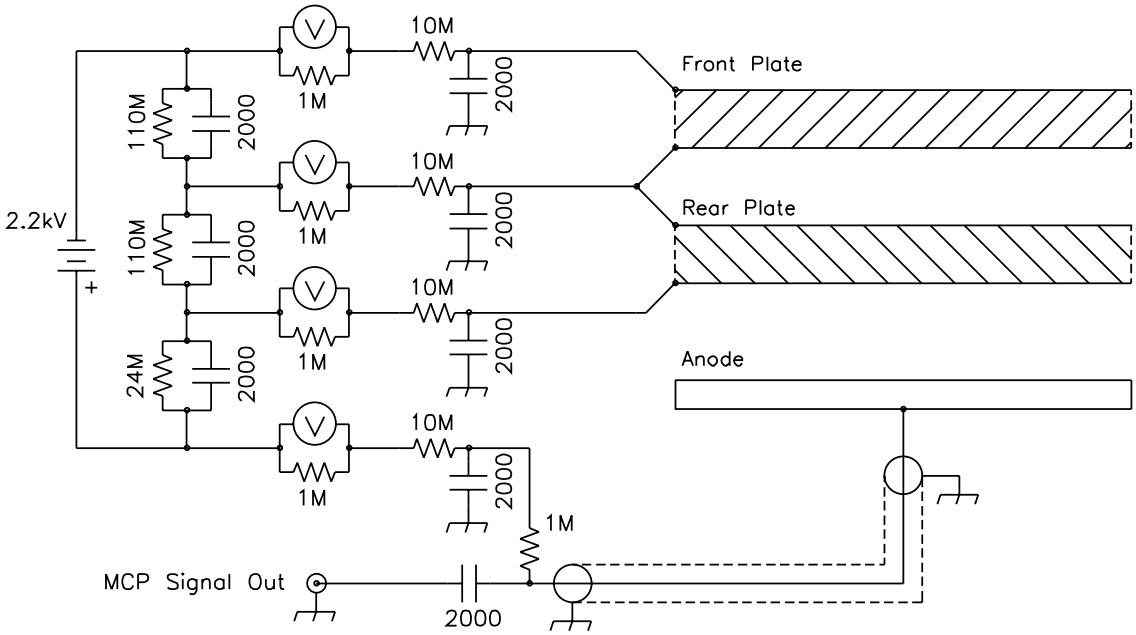

Figure 2.18: Microchannel plate bias circuit. The voltage on the surface of the front plate defines the absolute voltage for the remainder of the circuit, and can be set anywhere from +1 kV to −3 kV.

to ground of any part of the assembly is limited to ±3 kV by the dielectric strength of the feedthroughs on the MCP flange; thus, the front plate may be biased to −3 kV (with anode near −1 kV, for proton detection) or to +1 kV (with anode near +3 kV, for electron detection). Since the particles from the trap are ejected with very low energies (typically 100 eV or less), the front plate bias essentially determines the incident energy of the particles. The circuit was arranged so that any choice of front plate bias within the range −3 kV to +1 kV could be easily accommodated.

A pulse-height analysis circuit is used to assess the operating characteristics of the microchannel plate assembly (Fig. 2.19). Charge from the anode is quickly dumped onto the capacitor in the charge-sensitive preamplifier and slowly bled off by the resistor, leading to a fast-rising pulse with an exponential tail which is ideal

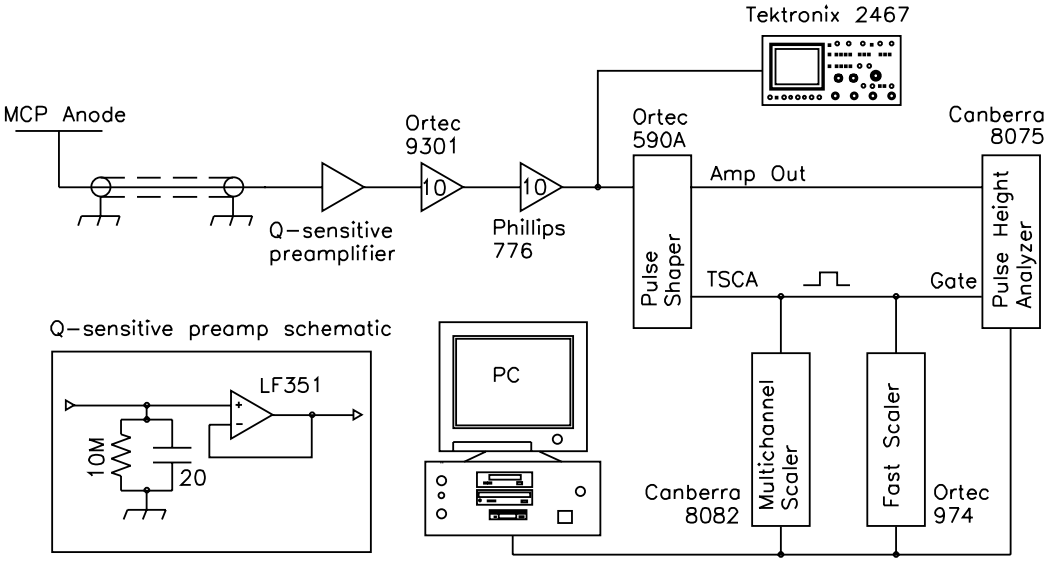

Figure 2.19: Detection electronics for pulse-height analysis of the microchannel plate signal.

for pulse-shaping. After the pulse is processed it is fed to a pulse-height analyzer, which accumulates the number of counts as a function of detected pulse height. A typical pulse-height spectrum for 1 keV incident electrons is shown in Fig. 2.20, illustrating the quasi-Gaussian saturated gain profile.

Once the plates are determined to be operating in a saturated-gain mode, the charge-sensitive preamplifier is removed and a the signal is discriminated using a Lecroy 821 discriminator, set just above the noise threshold. The discriminated signal is then passed to a series of fast scalers for counting (Sec. 4.2).

The model of Eq. 2.16 can be extended to examine the consequences of the 0.6 Tesla magnetic field (36 cm from the field center) on the microchannel plate gain. The relevant parameter in this case is the cyclotron radius r_c, given by

$$r_c = \frac{\sqrt{2mE_2}}{eB}. \tag{2.18}$$

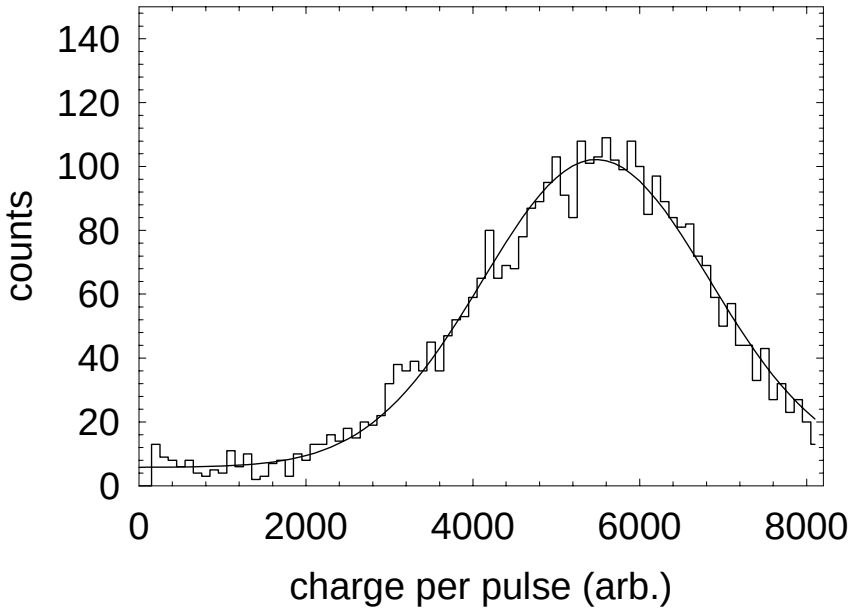

Figure 2.20: Pulse height spectrum for 1 keV incident electrons. The quasi-Gaussian profile is characteristic of chevron pairs operating in a saturated gain mode.

As B increases, the cyclotron radius decreases. When the cyclotron radius becomes comparable to the channel radius ($D/2$) the electrons will spiral into a channel wall in less time than they would in the absence of the magnetic field. They therefore travel a shorter distance along the channel axis (increasing the number of collisions n) and achieve a lower impact velocity (decreasing the multiplication factor δ). A crude estimate of the effects of a magnetic field on gain may be found by replacing the channel diameter D in Eqs. 2.16 and 2.17 with an effective channel diameter D^*, where

$$D^* = \begin{cases} D, & \text{if } r_c \gtrsim D/2; \\ 2r_c, & \text{otherwise.} \end{cases} \tag{2.19}$$

As the effective channel diameter decreases, the gain also decreases.

In an earlier version of this apparatus the microchannel plates were located closer to the trap can in a 1 Tesla magnetic field. The plates performed poorly, as explained

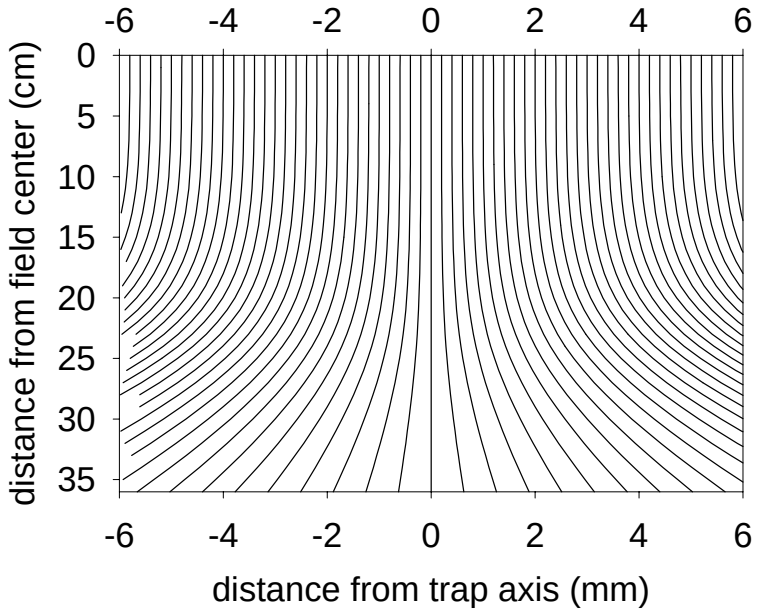

Figure 2.21: Magnetic field lines from the trap center to the MCP detector location. The field curvature restricts the effective area imaged by the plates to a disk of radius $\rho_m \approx 2$ mm. (Note the expanded horizontal scale.)

in the simple model by noting that the cyclotron radius for a 1 eV secondary electron in a 1 Tesla field is ≈ 3.5 microns — smaller than the channel radius (5 microns). The plate performance was improved by extending the stainless-steel tube and moving the plates slightly further away from the field center (to 0.6 Tesla), increasing the secondary electron cyclotron radius to 6 microns.

In addition to affecting the MCP gain, the magnetic field lines in the fringing field limit the region of the trap which can be imaged (Fig. 2.21). The maximum (orbital) radius at which a particle will be able to reach the plates (without striking the wall of the TUBE, for instance) is approximately 2 mm at the magnetic field center.

Once a MCP channel discharges, the charge expelled from the channel walls must be replenished before it can fire again. The characteristic channel-recharge time τ

is customarily defined by [50]

$$\tau = R_{\text{plate}} C_{\text{plate}} = \frac{V}{I_s(T)} C_{\text{plate}} \tag{2.20}$$

where $C_{\text{plate}}(R_{\text{plate}})$ is the effective capacitance (resistance) between the plate faces, and I_s is the strip current through the plate resulting from a bias V. At room temperature $\tau_{300\text{K}} \approx 10$ ms. The channel is assumed to recharge exponentially, and is therefore nearly recharged after 50 ms. The critical count rate per channel is inverse of this, *i.e.*, 20 Hz. This may seem rather small; in the context of a plate with 2 million uniformly-illuminated channels, however, a 40 MHz counting rate may be sustained with minimal gain degradation.

As the temperature decreases, the strip current also decreases (Fig. 2.22); the recharge time can therefore become quite long. At 45 K the strip current is on the order of 100 nA, and $\tau_{45\text{K}} \approx 1$ sec. The critical count rate per channel is now only 0.2 Hz, although under uniform illumination a relatively high counting rate may still be sustained (400 kHz). For detection of charged particles released from the Penning trap, however, the illumination is decidedly nonuniform. A cloud of electrons with the (relatively large) average magnetron radius of $\rho_m = 0.5$ mm would, when ejected to the plates, illuminate an area (after radial expansion in the fringing field) of about 0.1 cm^2 (see Fig. 2.21); this is only 1/30 of the active area of the plate. A more typical cloud may have on the order of 10^4 particles, which may be compressed into a radius $\rho_m \approx 0.1$ mm and released to the plates in under 1 ms, corresponding to a count rate per channel of more than 8 kHz! To compensate for these limitations the count rate must be reduced, the temperature increased, or the average magnetron radius of the cloud increased (Figs. 2.23 and 2.24).

The effect of exciting a channel that is not fully recharged is explored in Ref. [53].

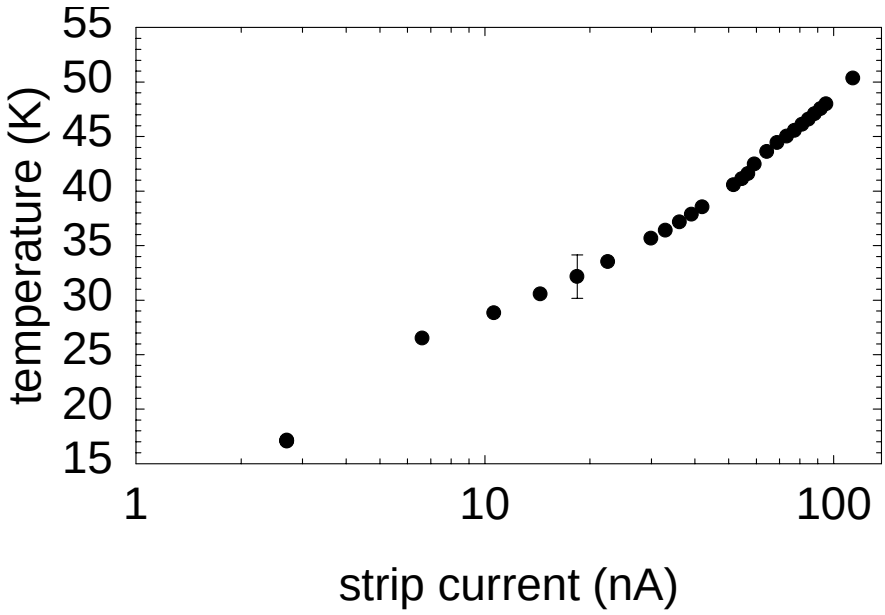

Figure 2.22: Microchannel plate strip current (rear plate) as a function of temperature. One typical error bar is shown.

Qualitatively, the gain decreases, since less charge is available to produce an output pulse. The quasi-Gaussian pulse-height distribution is distorted in the direction of lower energies (see Fig. 2.23 and Fig. 2 of Ref. [53]).

Dark counts are output pulses which appear in the absence of signal, and may be the result of background gas at the input stage, autoemission of electrons within the channel, ion feedback, or other similar processes. Microchannel plates have extraordinarily low dark count rates, typically below 3 $cm^{-2} \cdot sec^{-1}$ [50] at room temperature, generally improving for reduced temperatures. A dark count rate of 2 Hz is observed for the plates used in these experiments.

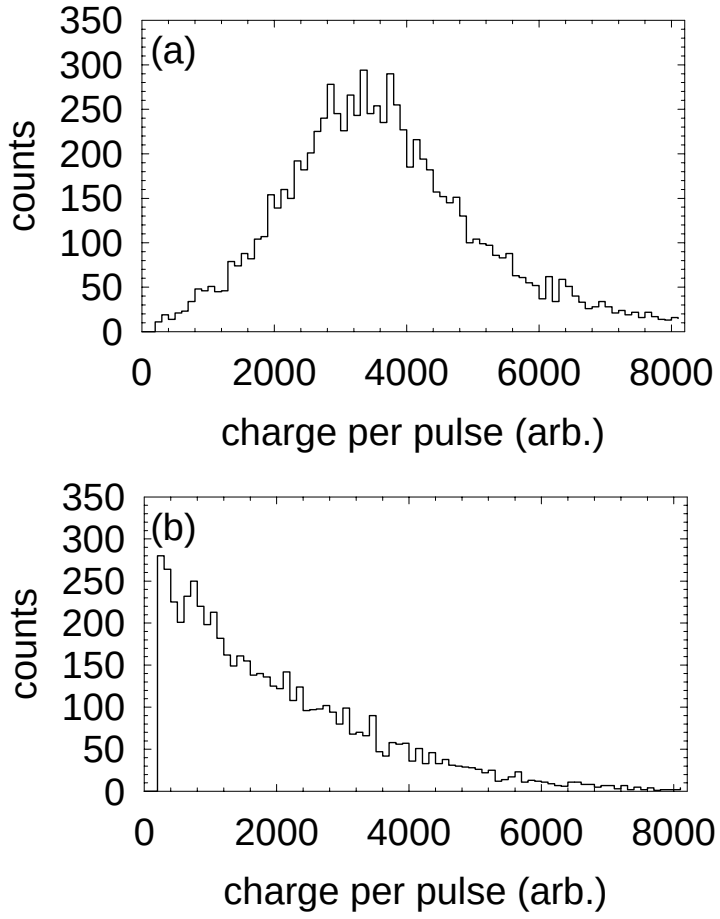

Figure 2.23: Microchannel plate gain as a function of illuminated area. Two clouds of roughly the same number of electrons (but different center-of-mass magnetron radii) are ejected to the plates under identical conditions. The large-radius cloud (a) displays the usual saturated gain, whereas the small-radius cloud shows a marked gain reduction. (T $\approx$ 20 K.)

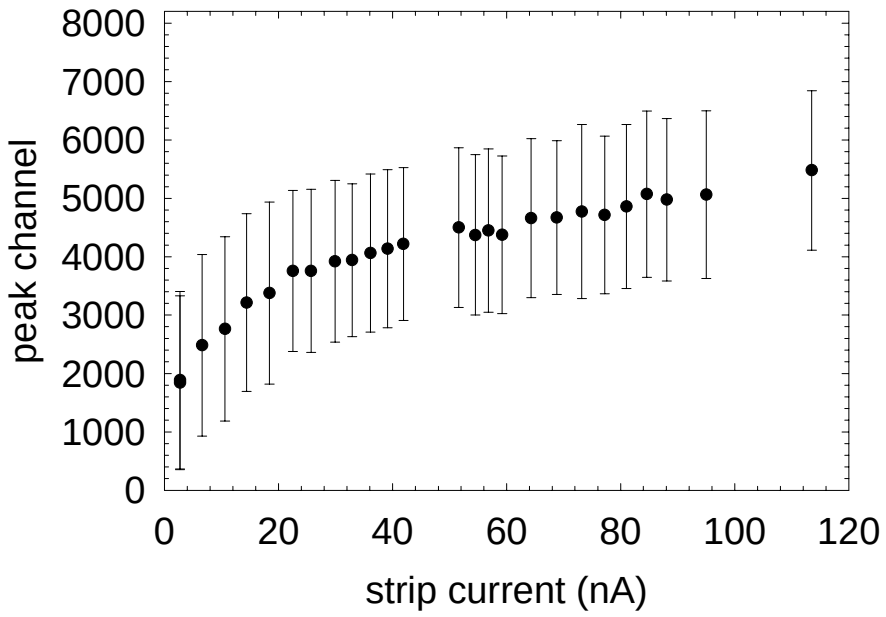

Figure 2.24: Microchannel plate gain as a function of strip current. Small-radius clouds of electrons are dumped at rates of $\approx$ 100 Hz to the plates. Even at this low counting rate some dependence on strip current (and therefore recharge time) is seen. (Error bars denote the FWHM of the gain peak.)

Table 2.6: Microchannel plate properties for the plates used in these experiments, as specified by their manufacturers.

Property	Front Plate (Galileo)	Rear Plate (Intevac)	Units
Outside Diameter	2.48	2.48	cm
Active Area (min.)	3.00	2.54	cm^2
Channel Diameter	10	10	μm
Center-to-Center	12	12	μm
Thickness	.043	.043	cm
L/D ratio (α)	40:1	40:1	
Bias Angle	5	5	$^\circ$
Open Area Ratio	66	60	%
Coating	CsI	none	

2.6 Control System

The experiment is run from an IBM-compatible PC running under MS-Windows 95. The computer is interfaced to the equipment via an IEEE-488 (GPIB) bus. A single CAMAC crate is attached via the GPIB, permitting modular expansion as well as access to the variety of counting and detecting systems which support the CAMAC standard.

The computer runs LabView 4.0 [54], which is a graphical programming language designed to interface well with GPIB systems. The greatest advantage of using LabView is the speed with which an intuitive data display can be adapted to changing experimental conditions. Labview is, however, a high-level language, and does not permit precise timing operations; for this reason, time-critical work is done exclusively in hardware.

2.7 Suggested Improvements

The trap support system has performed well over the years; accordingly, most of the improvements suggested here are related to the detection systems. A position-sensitive microchannel plate detection system would improve the understanding of the distribution of particles in the clouds; it could also facilitate alignment of the long tubes with the magnetic field axis. Mounting a MCP pre-amplifier just outside the MCP enclosure could help boost the signal further out of the noise and possibly enable timing information to be obtained. The addition of a superconducting axial amplifier for protons has greatly improved the ability to count and detect protons nondestructively; it is not yet known whether the higher-frequency detectors would benefit from being constructed of superconducting materials.

The greatest difficulty with the apparatus revolved about the ultraviolet-reflective coating on the MIR electrode, which proved susceptible to charging under electron bombardment from the field emission point. The charging introduced difficulties in manipulating particles close to the electrode, and occasional shifts in the trapping potentials. As a result, the MIR electrode has been removed from the apparatus for the next generation of experiments.

Chapter 3

Particle Detection and Manipulation

3.1 Loading and Cleaning Electrons and Protons

The key to loading protons and electrons is the on-axis field emission point (FEP), which is poked through a small hole in the TUBE electrode not far below the electrode stack (Fig. 2.6). An electron current of up to 100 nA is emitted from the high-field region at the tip of the FEP when a -1 kV bias is applied to the point (relative to the TUBE). The emitted electrons are radially constrained by the 6 Tesla magnetic field and travel along the trap axis in both directions; those which travel through the electrodes will strike the MIR electrode, dislodging secondary electrons, ions (including protons), and neutral "gas" atoms.

Low-energy secondary electrons from the MIR surface are trapped by biasing the electrodes as shown in Fig. 3.1(b). The trapping mechanism is likely collisional, involving secondaries scattering from each other, gas atoms, ions, or possibly electrons from the primary beam [55]. Electron trapping can be inhibited by biasing the

MIR electrode positive, which prevents the secondaries from reaching the trapping region, or strongly negative, which causes the electrons to pass through the trapping region with energies too high to trap.

Protons are trapped by ionizing hydrogen atoms liberated from the MIR surface by the FEP electron beam. Biasing the MIR electrode to -140 V creates (along with the FEP bias) a potential well for electrons, enhancing the yield of protons by increasing the number of ionizing electrons which pass through the proton trap [40]. [The well structure used for trapping protons is shown in Fig. 3.1(c).] Over time, the number of trapped protons declines as the MIR surface is scrubbed clean by the electron current.

The liberated hydrogen atoms are unconstrained by the magnetic field, so the number of atoms which reach the trapping region falls off as $1/z^2$, where z is the distance between the trapping region and the MIR surface. A slightly better trap design moves the proton trap closer to this surface (*e.g.*, interchanging the positions of the proton and electron traps). Ultimately, an additional proton source may be built into the apparatus to further improve the proton yield; for instance, a hydrogen-saturated metal foil (or a metal hydrogen cell with a palladium leak) should yield more protons under electron bombardment than does the MIR surface. Alternatively, the trap vacuum enclosure could be backfilled with a small pressure of hydrogen, which would be cryopumped to the electrode surfaces at low temperatures and provide a rich source of protons.

The MIR surface hosts adsorbed gases other than hydrogen, the most common of which are helium, carbon, oxygen, and nitrogen. These atoms are also liberated by the FEP beam, ionized within the trapping region, and trapped with the protons. Each of the ion species will have a different axial frequency, as determined by its particular charge-to-mass ratio (Eq. 2.15). The energy in the ion axial motion may

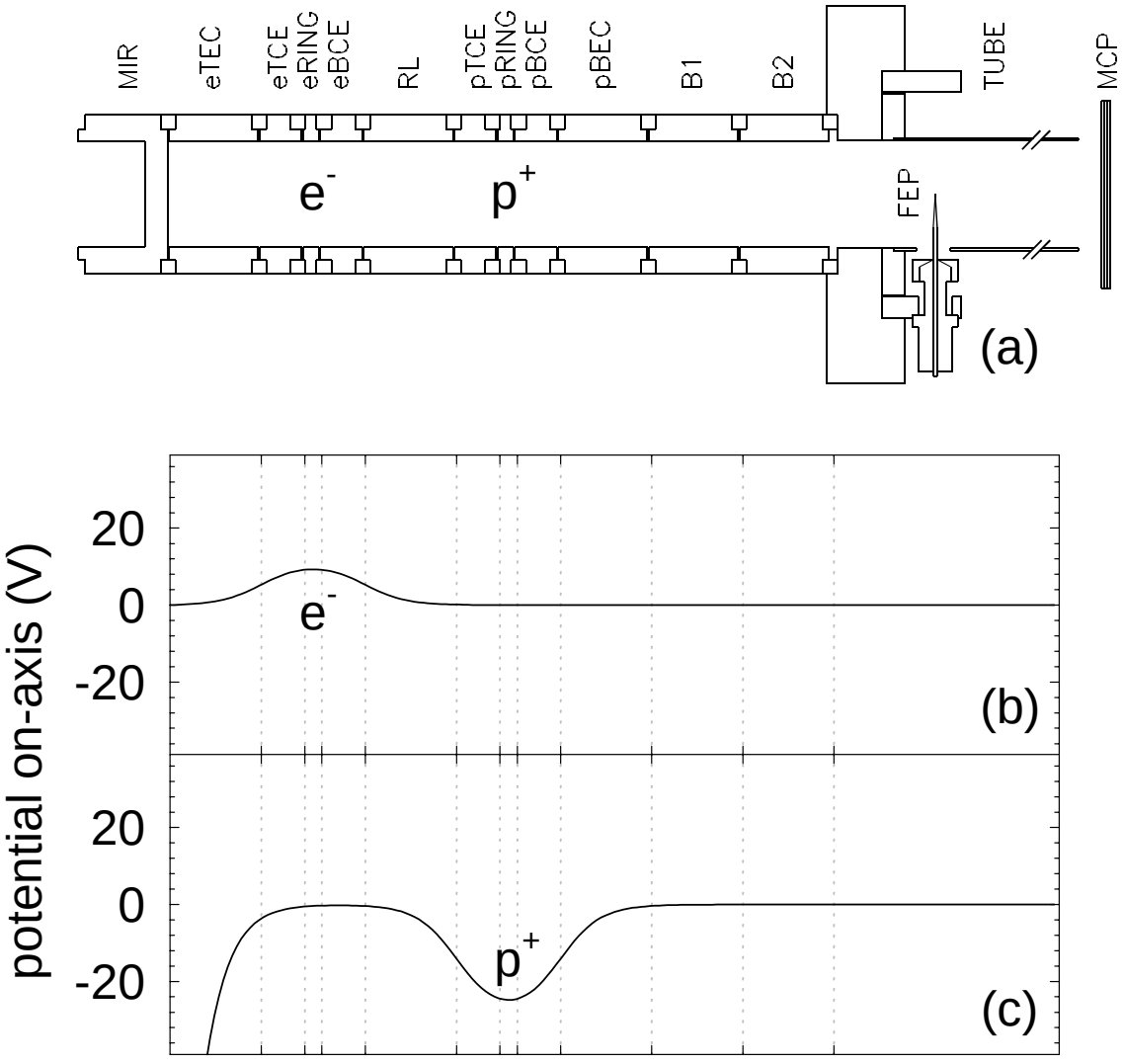

Figure 3.1: Axial potentials for loading particles. (a) Trap electrodes. (b) Potentials for loading electrons. (c) Potentials for loading protons. The effect of the field emission point bias is not shown.

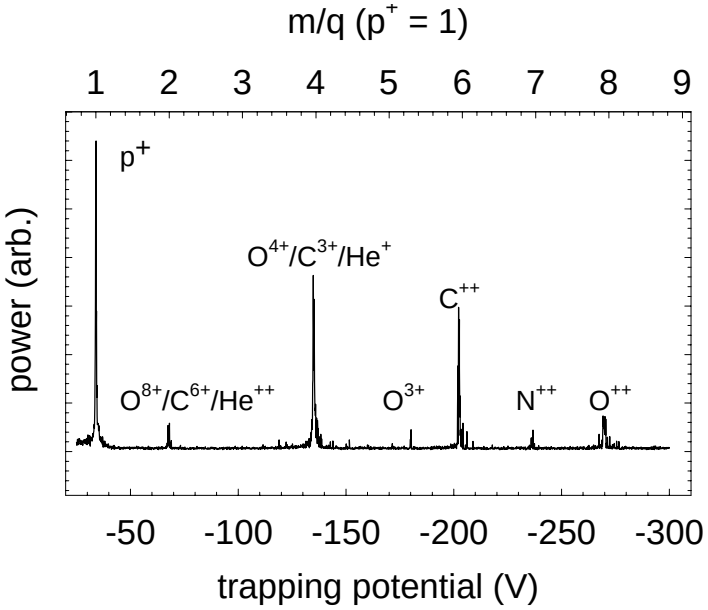

Figure 3.2: The variety of ions loaded into the trap is illustrated by varying the trapping potential to bring the ion axial motions into resonance with the proton axial tuned circuit.

be detected by varying the trapping potential and bringing the various ion species into resonance with a detection circuit. An example of such "mass spectroscopy" (Fig. 3.2) illustrates the typical assortment of trapped ions. (To protect the electrode filter capacitors, trapping potentials exceeding -300 V are not applied, and ions resonant at lower frequencies are not detected.) Details of the detection circuit are given in Sec. 3.2.

The mass spectrum of Fig. 3.2 is a very sensitive leak detector. If the trap vacuum enclosure has a leak, it will slowly fill with helium gas present in the magnet bore. The cold surfaces in the enclosure will pump up to a monolayer of helium effectively [56], after which a finite helium vapor pressure develops which is easily ionized by the 1 keV FEP electron beam. The resulting He^+ signal generally overwhelms the proton signal.

Three steps are taken to remove the undesirable contaminant ions from the trap. First, the axial motion of the trapped protons is damped as they are loaded into the trap by coupling it to a tuned circuit (Sec. 3.2). Once the FEP beam is turned off, a strong broadband drive (DC–1 MHz) excites the axial motion of the contaminant ions. The protons continue to be damped by the tuned circuit, and are further protected by their axial frequency, which is at least a factor of $\sqrt{2}$ greater than those of the closest ion species (fully stripped carbon, helium, oxygen, and nitrogen). Notch filters at the proton frequencies ν_z and $\nu_z - \nu_m$, as well as an elliptic low-pass filter with characteristic notch frequencies at ν_z and $2\nu_z$, provide an additional ≈ 100 dB of drive attenuation at ν_z. After 30 seconds the drive is turned off, and the trapping potential reduced to -2 V; the highly-excited ions escape the trap, leaving the axially-cooled protons behind. The trapping potential is then restored to bring the protons back into resonance with the detection circuit.

Electrons and protons may be trapped simultaneously by introducing an electron potential well just prior to termination of the FEP beam. The MIR must be briefly biased to 0 V, since electrons are not efficiently trapped at a bias of -140 V. The proton decontamination routine (as described above) is implemented after the FEP is switched off.

The electrons from the FEP can deposit their energy in a very small region on the microchannel plates (on the order of the square of the cyclotron radius, $\approx 10^{-5}$ cm^2). To prevent these electrons from damaging the plate channels, the entire plate assembly (including the anode) is biased to -1.3 kV while the point is fired. With no bias across the plates, the channels will not discharge even if struck by ions or gas atoms liberated by the electron beam.

3.2 Radiofrequency Detection

The heart of particle detection is an LCr resonant circuit [Fig. 3.3(a)], formed by attaching an inductor L between two of the trap electrodes (chosen by the symmetry of the particle motion to be detected). One of the two electrodes is typically RF-grounded; the effective capacitance C of the circuit is that between the ungrounded electrode and its neighbors (typically 12–15 pF). The resistance r is associated with (unavoidable) losses in the inductor, and drives the circuit with its Johnson noise

$$\langle V_{\text{noise}} \rangle = \sqrt{4k_B T(\Delta\nu)r} \tag{3.1}$$

where $\Delta\nu$ is the bandwidth and k_B is the Boltzmann constant. The resulting noise-driven signal is observed by coupling the circuit to the input of the FET amplifier; the detected power $P(\omega)$ is then the familiar Lorentzian

$$P(\omega) \propto \left(\frac{\omega_{LC}}{\Gamma}\right)^2 \frac{(\Gamma/2)^2}{(\omega_{LC}-\omega)^2 + (\Gamma/2)^2} \tag{3.2}$$

for $\omega \approx \omega_{LC}$, where

$$\omega_{LC} = \frac{1}{\sqrt{LC}} \tag{3.3}$$

is the resonant frequency of the tuned circuit, and $\Gamma = r/L$ is its full-width at half-maximum (FWHM). An example of the signal from the Johnson noise-driven resonance for the proton axial amplifier is shown in Fig. 3.3(b).

The circuit quality factor Q is defined as the ratio of energy stored in the circuit to the energy lost from the circuit [57]. Equivalently, this may be expressed as the ratio of the reactance (inductive or capacitive) to the resistance of the circuit on

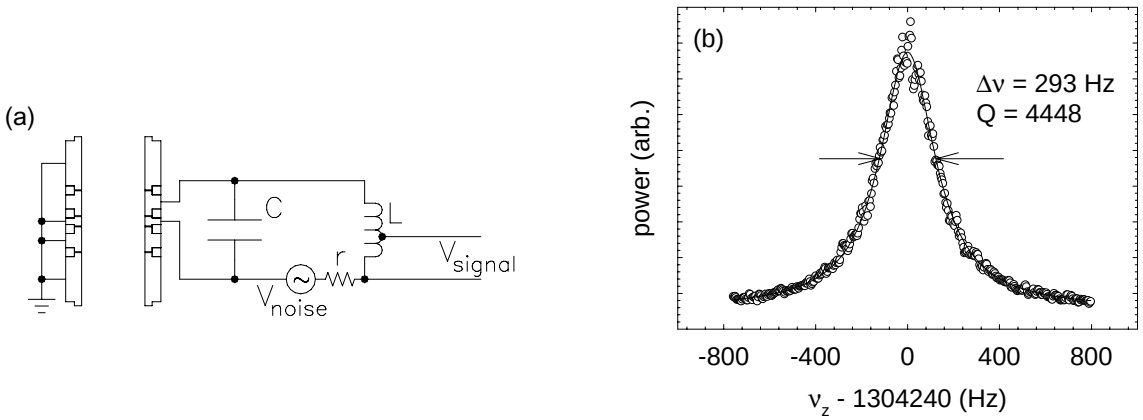

Figure 3.3: The tuned circuit detector. (a) Effective radiofrequency circuit schematic. (b) Johnson noise-driven resonance as seen by a spectrum analyzer.

resonance, *i.e.*,

$$Q \equiv \left.\frac{X_L}{r}\right|_{\omega=\omega_{LC}} = \frac{\omega_{LC}}{\Gamma} \tag{3.4}$$

The circuit Q is maximized to provide the best signal-to-noise ratio.

A simple model [58] is used to understand the interaction of a particle with the detection circuit. The particle oscillates with spring constant k inside the harmonic trap [Fig. 3.4(a)], inducing image charges in the surrounding electrodes. These charges will flow through the inductor as a current, given by [59, 60]

$$i = \frac{e\dot{z}}{2z_0}\alpha \tag{3.5}$$

where z_0 is the trap length defined in Table 2.2, and α represents a dimensionless geometrical factor of order unity ($\alpha = 1$ if the particle oscillates between two parallel conducting plates). Neglecting the (small) force of the image charges on the particle, the resulting equation of motion is

$$m\ddot{z} = -kz + \frac{\alpha eV}{2z_0} \tag{3.6}$$

where V is the voltage across the electrodes produced by the oscillation of the proton. By solving for V in terms of the current i, and identifying the spring constant $k = C_2 e V_0 / d^2$ (Eq. 2.15), Eq. 3.6 may be written as

$$V = \ell_{1p} \frac{di}{dt} + \frac{1}{c_{1p}} \int i \, dt \tag{3.7}$$

in which

$$\ell_{1p} = m \left(\frac{2 z_0}{e \alpha} \right)^2 \tag{3.8}$$

and

$$c_{1p} = \frac{1}{\ell_{1p} \omega_z^2} \tag{3.9}$$

where

$$\omega_z \equiv \frac{1}{\sqrt{\ell_p c_p}} = \sqrt{\frac{C_2 e V_0}{m d^2}} \tag{3.10}$$

is the resonant frequency of the particle motion. The equation of motion is therefore recast into an equation for a circuit, consisting of the inductor ℓ_{1p} and capacitor c_{1p} in series. The effect of having a particle in the trap is to add these two circuit elements to the LCr circuit, as shown in Fig. 3.4(b).

The preceding equations may be easily generalized to N particles by replacing ℓ_{1p} and c_{1p} with

$$\ell_p = \frac{m}{N} \left(\frac{2 z_0}{e \alpha} \right)^2 \tag{3.11}$$

and

$$c_p = \frac{N}{\ell_{1p} \omega_z^2} \tag{3.12}$$

where the circuit now represents the equation for the center-of-mass motion of the N particles. The geometric factor α is identified with the asymmetric expansion coefficient d_1 (Table 2.2) for an inductor attached to a compensation electrode.

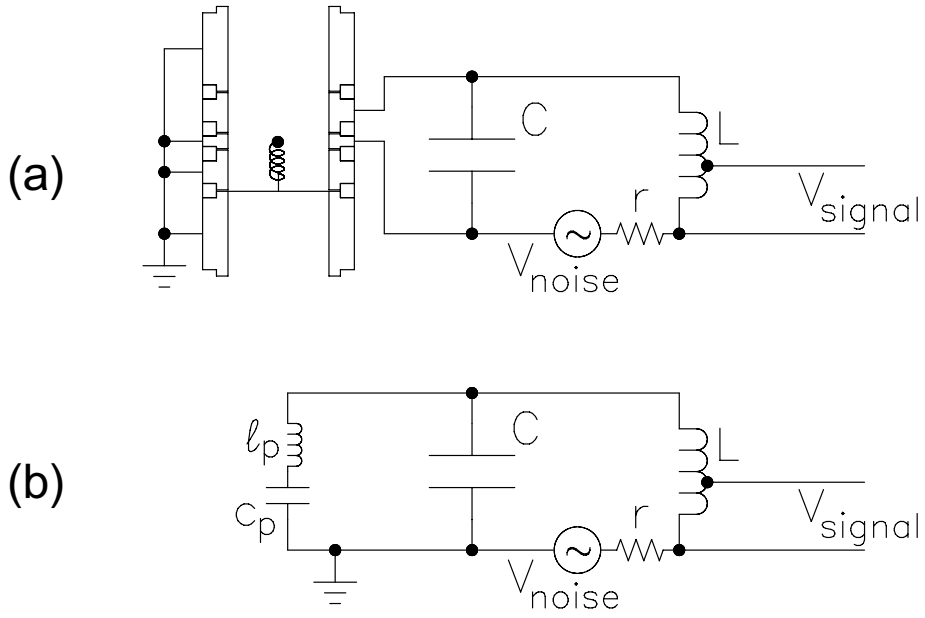

Figure 3.4: Model for particle detection. (a) Particles represented as oscillating charges on springs. (b) Equivalent lumped circuit representation.

Analysis of the complete circuit (for $\omega \approx \omega_{LC}$) yields a power spectrum

$$P(\omega) \propto \frac{\omega_{LC}^4(\omega_z^2 - \omega^2)^2}{[(\omega_z^2 - \omega^2)(\omega_{LC}^2 - \omega^2) - \omega^2 \Gamma N \gamma_z]^2 + \omega^2 \Gamma^2 [(\omega_z^2 - \omega^2) + \Gamma N \gamma_z]^2} \tag{3.13}$$

where γ_z is defined by

$$\gamma_z \equiv \left(\frac{d_1 e}{2 z_0}\right)^2 \frac{Q^2 r}{m}. \tag{3.14}$$

On resonance, the series resistance r of the LCr circuit may be written as a parallel resistance $R = Q^2 r$. A particle which drives an image current i (Eq. 3.5) through this resistance will dissipate energy at a rate given by $f\dot{z} = -i^2 R$. The particle experiences a force

$$f = -m\gamma_z \dot{z} \tag{3.15}$$

where γ_z (Eq. 3.14) is interpreted as the damping rate for a single particle of charge

e and mass m interacting with a tuned circuit at its resonant frequency ω_{LC}. Dissipation of particle energy in the tuned circuit causes the detected signal amplitude to increase, as seen in ion sweeps (Fig. 3.2), in sideband cooling responses (Fig. 3.7), and in cyclotron excitations (Fig. 3.8).

To determine the number of particles in the trap, the theoretical lineshape (Eq. 3.13) can be fit to the measured signal and the product $N\gamma_z$ extracted. Independent knowledge of γ_z (Sec. 3.4) makes this a measurement of N. For an empty trap ($N = 0$ and $\omega \approx \omega_{LC}$), Eq. 3.13 reduces to the Lorentzian of Eq. 3.2. For a small number of particles ($N\gamma_z \ll \Gamma$), it may be expressed

$$P(\omega) \propto \left[1 - \frac{(N\gamma_z/2)^2}{(\omega_z - \omega)^2 + (N\gamma_z/2)^2}\right]. \tag{3.16}$$

The particles short the Johnson noise generated by the effective circuit resistance r to form an inverted Lorentzian "dip" with a FWHM proportional to N [58]. In the opposite limit ($N\gamma_z \gg \Gamma$), the dip is braced by two peaks occurring at [61]

$$\omega_\pm = \omega_{LC} \pm \frac{1}{2}\sqrt{N\gamma_z\Gamma}. \tag{3.17}$$

The spacing between the peaks is therefore proportional to $\sqrt{N}$ [58]. The general case lies between these extremes, and Eq. 3.13 must be used. The agreement between theory and experiment is satisfying, as illustrated in the proton lineshapes of Fig. 3.5.

The preceding analysis applies equally well to other charged species (including antiprotons, positrons, and electrons). Figure 3.6 shows several million He^+ ions coupled to the proton axial detector which were trapped after firing the field emission point into a gas of helium which had entered the trapping region through a small leak in the vacuum enclosure.

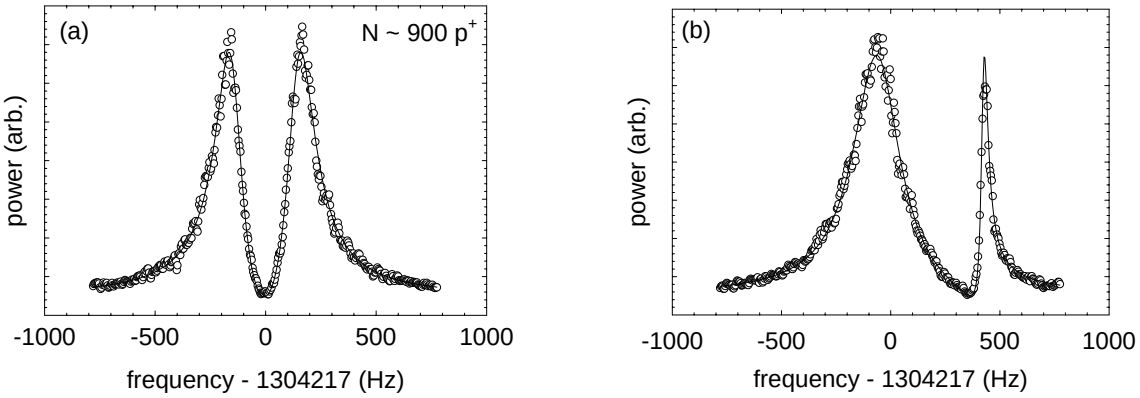

Figure 3.5: Proton "dips" formed by interaction with the tuned circuit. (a) Protons on resonance ($\omega_0 = \omega_{LC}$). (b) Protons detuned slightly ($\omega_0 > \omega_{LC}$). The line represents best fit to the experimental data (circles).

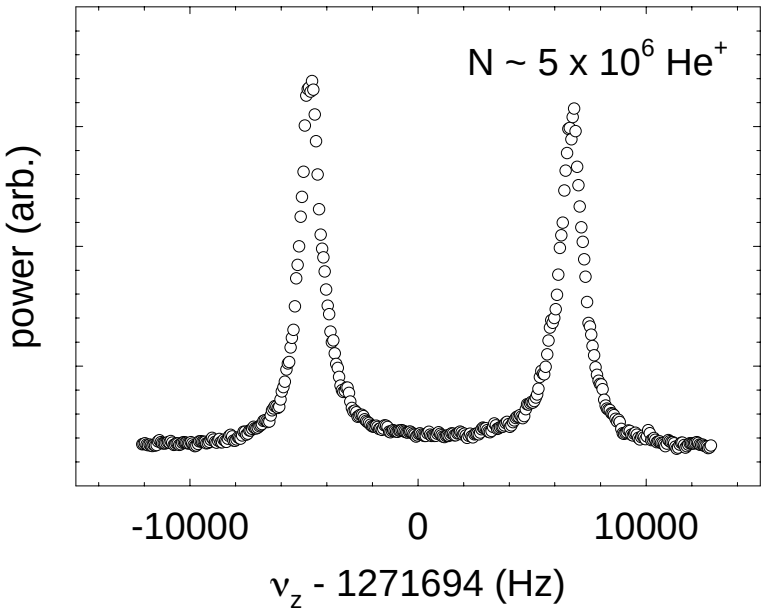

Figure 3.6: He^+ ions detected by their axial "dip." The large number is a result of a small leak in the trap vacuum enclosure.

The problems with ion contamination are not usually so dramatic. Weak, unstable proton dips are usually observed, however, if the steps outlined in Sec. 3.1 are not followed to clean the proton clouds. The weak dip can usually be maintained in the presence of a strong sideband drive (Sec. 3.3), but once the drive is removed the dip will rapidly drift (usually downwards) in frequency and disappear as the ions interfere with the axial motion. In one experiment, the dip from a cloud of several hundred positrons was irrevocably disrupted by deliberately adding ten protons.

3.3 Reducing the Magnetron Radius

The tip of the "on-axis" field emission point is inevitably misaligned with the central axis of the trap, resulting in trapped particles with sufficiently large magnetron orbits to sample a potential anharmonic enough to make radiofrequency detection and counting difficult. In order to reduce the magnetron radius a "sideband cooling" drive, applied at a frequency $\nu_d \approx \nu_z + \nu_m$, adds energy to both the axial and magnetron motions. The tuned circuit continuously damps the axial motion so that it remains cold; the magnetron motion, however, experiences a net gain in energy. Since the magnetron motion is unstable, this has the effect of reducing the radius of the magnetron orbit by nudging it up the radial potential "hill." (Driving the other sideband, $\nu_d \approx \nu_z - \nu_m$, achieves the opposite effect, and is therefore known as "sideband heating.") Due to a "stimulated emission" process, in which both the axial and magnetron motions lose energy (and the orbital radius increases), there is a limit to the efficacy of sideband cooling. This occurs when [37]

$$E_m = -\frac{\nu_m}{\nu_z} E_z. \tag{3.18}$$

A drive at (or near) $\nu_z + \nu_m$ is, in principle, all that is required to sideband cool a small cloud of particles ($N\gamma_z \ll \nu_m$). In practice, a cloud of particles can have a large center-of-mass magnetron orbit which shifts both its axial and magnetron frequencies. A drive at $\nu_z + \nu_m$ is not resonant with these particles, and sideband cooling is not effective. To compensate for these frequency shifts, a "sweepup" technique is used to center these clouds, in which the drive is applied at $\nu_z + \nu_m$ while the voltage is slowly ramped so that the sideband cooling resonance (for on-axis particles) approaches the fixed drive frequency from below. Particles oscillating at the (shifted) frequencies come into resonance with the drive and are cooled. The sweepup technique may also be used to sweep through the cooling resonance from above; care is required, however, not to drive either the axial or magnetron heating resonances directly.

A typical drive strength for the sweepup is -52 dBm (as applied at the brass hat); the voltage is swept over 0.1 V at a rate of 1 mV every 2 sec. A narrow cooling response spike is usually observed at $\nu_d - \nu_m$ (see Fig. 3.7). The amplitude of the response is an indication of the degree of cooling experienced by the particles, since it is the axial energy being deposited in (and being damped by) the tuned circuit. Other narrow responses are usually observed at the cooling harmonics $\nu_d - n\nu_m$ and the heating harmonics $\nu_d + n\nu_m$ (where n is a nonnegative integer).

For $N\gamma_z \approx \nu_m$ the axial resonance is wide enough to encroach upon (or even encompass) the magnetron cooling resonance. In order not to drive the axial resonance directly (which can drive the cloud into strange orbits from which recovery is difficult), the drive is detuned to a higher frequency by an additional amount ϵ. The best results are found when $\nu_z + \nu_m + \epsilon$ is just greater than the higher-frequency noise peak which frames the "dip." The sweepup procedure outlined above is followed at this new drive frequency.

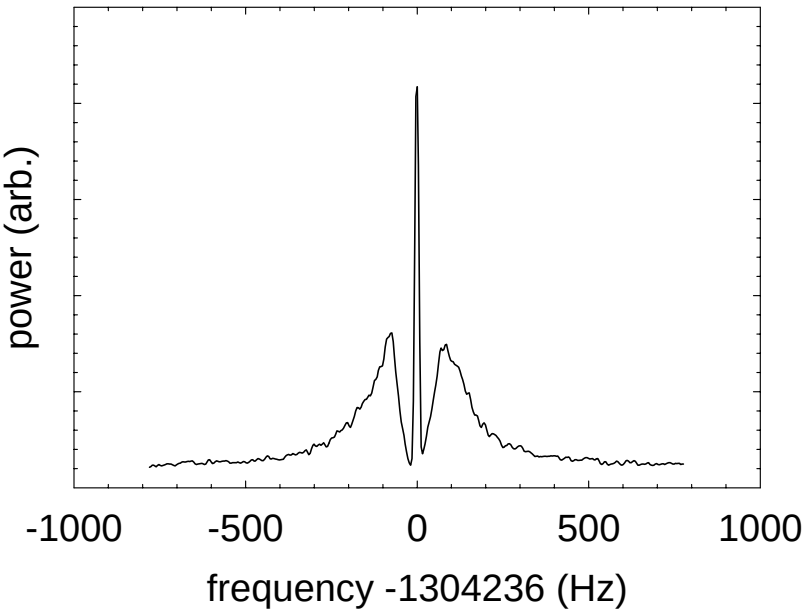

Figure 3.7: Sideband cooling response from a drive at $\nu_z + \nu_m$. The proton "dip" is clearly visible.

For larger clouds and large detunings ($\epsilon \gg \nu_m$) the magnetron heating and cooling resonances overlap and it becomes very difficult to cool the cloud. In this case, the most satisfactory solution is to place the drive far off-resonance ($\epsilon \approx 200$ kHz, or more) and to turn up the drive power (to +11 dBm, for instance).

In this trap, the rate at which protons are sideband cooled is limited by their narrow single-particle damping width γ_z, *i.e.*, the rate at which the energy supplied by the sideband cooling drive can be extracted from the axial motion. Electrons, on the other hand, have a larger damping width but a smaller magnetron frequency, such that for typical clouds $N\gamma_z \geq \nu_m$. As a consequence, only the smallest electron clouds can be cooled with a direct drive at $\nu_z + \nu_m$, whereas the larger electron clouds require strong, far-off-resonant drives.

3.4 Counting Particles and Measuring γ_z

The damping width per particle γ_z (Sec. 3.2) must be known in order to determine the number of particles N in the trap from a fit to the detected particle lineshape. In principle, γ_z may be calculated from knowledge of the trap constants d_1, z_0, and r in Eq. 3.14, although this yields a value which is usually only within a factor of two of the value obtained by measuring γ_z directly. Fortunately, N may be counted directly for small numbers of particles, such that extraction of $N\gamma_z$ from a fit to the lineshape (Eq. 3.13) determines γ_z.

3.4.1 Counting Protons

Small numbers of protons may be counted by observing their cyclotron motion. A strong drive (up to +13 dBm) is applied to one segment of the split ring electrode (pRING) and is swept down in frequency through the cyclotron resonance, transferring energy to the proton cyclotron motion. The cyclotron frequencies then shift due to the proton relativistic mass increase [15]. By transferring different amounts of energy to different protons, a series of "spikes" appears in the detected signal, each at its own (modified and relativistically-shifted) cyclotron frequency (Fig. 3.8). The spikes are then counted to determine the number of protons in the trap.

This counting method can be difficult to use for more than 10 protons, since the cyclotron frequencies often lock together and several protons may be represented by only a single spike. For smaller numbers, however, strongly and repeatedly driving the resonance insures that proton counting becomes purely a matter of the experimenter's patience.

Once the number of protons is known, the linewidth $N\gamma_z$ of their axial resonance must be measured. Changes in the trapping potential (near resonance) shift the pro-

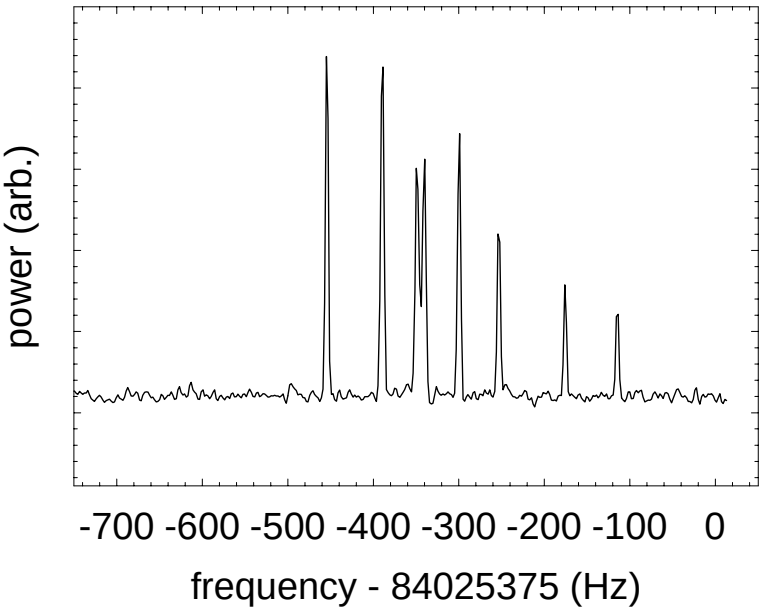

Figure 3.8: Eight protons, counted by their cyclotron signatures. The frequencies separate due to the relativistic mass increase accompanying the degree of excitation.

ton axial frequency by 19 Hz/mV; hence, voltage instabilities and noise on the trapping potential lead to undesirable frequency shifts $\Delta\omega$ which, when time-averaged, make the resonance appear broader and more shallow than $N\gamma_z$. This effect can reduced by requiring that $N\gamma_z/\Delta\omega \gg 1$. Since the single proton linewidth is only 0.4 Hz, every effort must be made to ensure the stability of the trapping potential. The trap wiring is modified [45] as shown in Fig. 3.9. A single voltage calibrator provides the trapping potential for the proton trap (including the trap endcaps), and all electrode potentials are referenced to its unique ground to avoid ground loops. Large (10 sec) filters are placed on the electrode bias lines to inhibit noise on the trapping potential. The remaining voltage sources (DACs) are disconnected from the trap, as are all nonessential support circuits (*e.g.*, ion gauges, level sensors, and flowmeters).

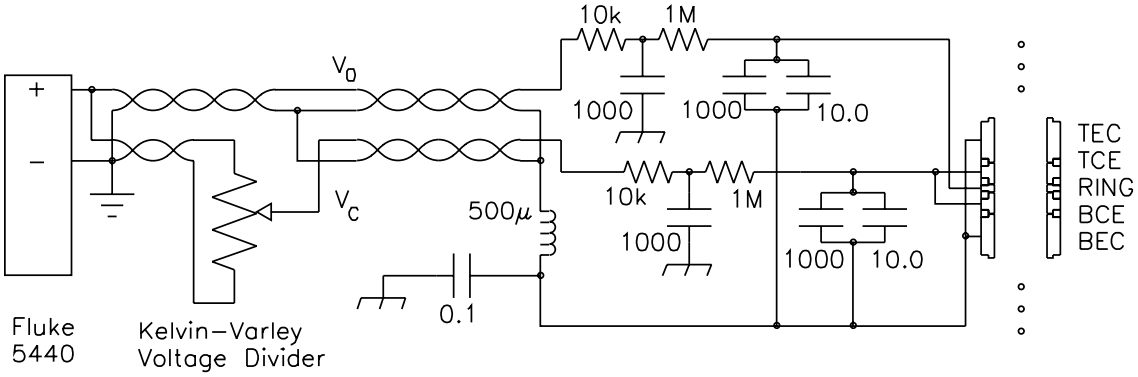

Figure 3.9: Circuit to supply the trapping potential for detecting small numbers of particles. The lines are heavily filtered and a common ground is introduced to avoid ground loops.

The resonance widths of two clouds of protons were repeatedly measured for this determination of γ_z. The first cloud was composed of 8 protons, counted with the cyclotron excitation technique; the second had 9. The measured widths are shown in Fig. 3.10. A straight-line fit to the data, constrained to pass through the origin, yields the damping width

$$\gamma_z(p^+) = 2\pi \cdot (0.38 \pm 0.02) \text{ Hz}. \tag{3.19}$$

Figure 3.11(a) shows the axial signal of a single proton, counted by observation of its cyclotron signal [Fig. 3.11(b)]. As mentioned above, the measured width of this heavily-averaged signal (≈ 14 minutes) is expected to be greater than that given in Eq. 3.19 due to fluctuations in the trapping potential; consequently, the single proton point is excluded from the measurement.

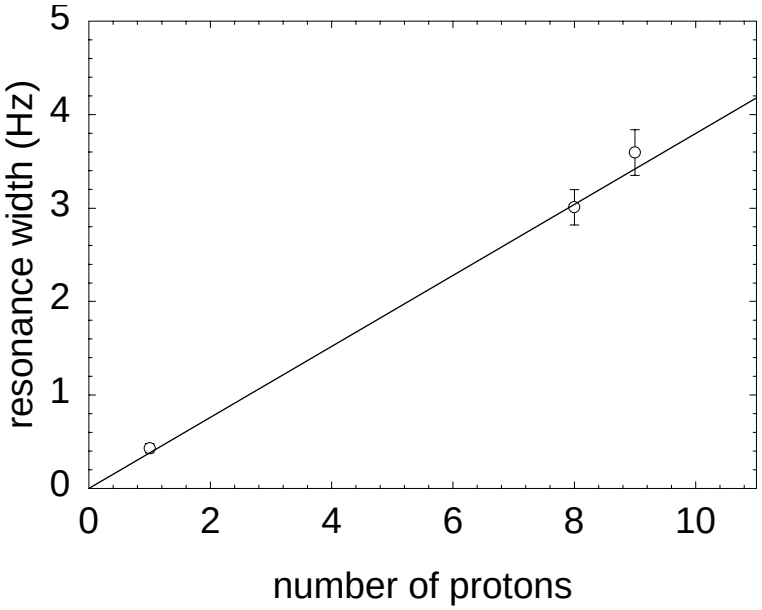

Figure 3.10: Proton damping width $N\gamma_z$ as a function of number. The line is a fit to the data, constrained to pass through the origin; its slope gives $\gamma_z(p^+) = 2\pi \cdot (0.38 \pm 0.02)$ Hz. The single proton point is shown for consistency and is not part of the measurement (see text).

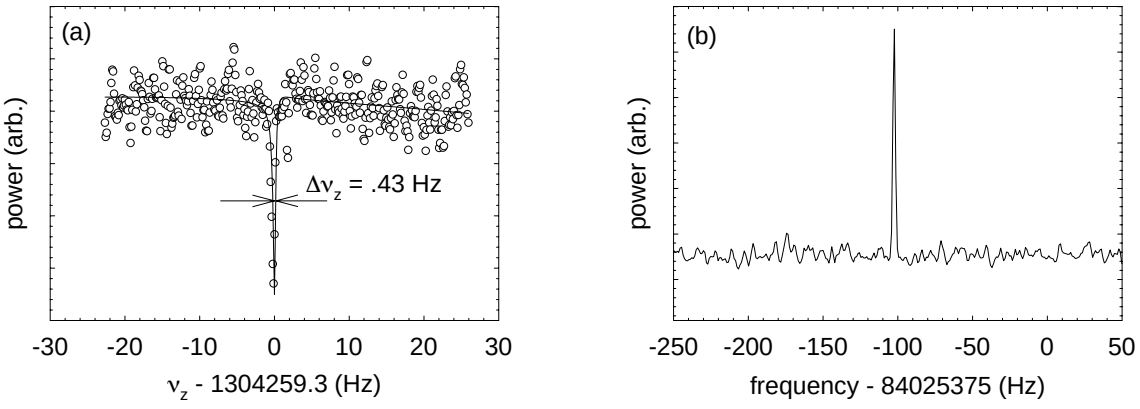

Figure 3.11: Observation of a single proton. (a) Axial motion (dip). (b) Cyclotron motion (spike).

3.4.2 Counting Electrons

The same general procedure is followed for electrons as for protons. A small number of electrons is loaded into the trap and counted; the lineshape is then fit to Eq. 3.13, and the number N is then divided from the fit parameter $N\gamma_z$ to yield the damping width γ_z. The details of the measurement, however, differ in a number of respects.

In a 6 Tesla magnetic field, the electron cyclotron frequency is in the microwave region (164 GHz), making direct cyclotron detection unsuitable for counting. Instead, the electron axial motion is driven and detected in a phase-sensitive detection scheme. The electrons are a damped, driven harmonic oscillator, and the measured signal $V_S(\omega)$ is given by [37]

$$V_S(\omega) = V_d(\omega)\frac{(N\gamma_z/2)^2\cos\phi + (N\gamma_z/2)(\omega-\omega_z)\sin\phi}{(\omega-\omega_z)^2 + (N\gamma_z/2)^2} \tag{3.20}$$

which for $\phi = 0$ and $\phi = \pi/2$ yields the familiar absorption and dispersion curves, respectively. With a detected phase $\phi = -\pi/2$, and the drive detuned such that $|\omega - \omega_z| \gg N\gamma_z/2$, the response becomes

$$V_S(\omega) \approx -\frac{V_d(\omega)}{\omega-\omega_z}\left(\frac{N\gamma_z}{2}\right)\left(1 - \mathcal{O}\left(\frac{N\gamma_z/2}{\omega-\omega_z}\right)^2\right) \tag{3.21}$$

which is proportional to N.

The signal from only a few trapped electrons is rather feeble. In order for the detector not to be swamped by direct feedthrough of the axial drive, the trapping potential is frequency-modulated at a frequency $\nu_{\rm mod} = 5$ MHz (Fig. 3.12) by applying a ≈ -9 dBm drive to the electron modulation drive line. The electron axial drive (also ≈ -9 dBm) is then swept through the resonance at the sideband $\nu_d \approx \nu_z - \nu_{\rm mod}$; an electron mixes the two frequencies together and responds as if a single drive were

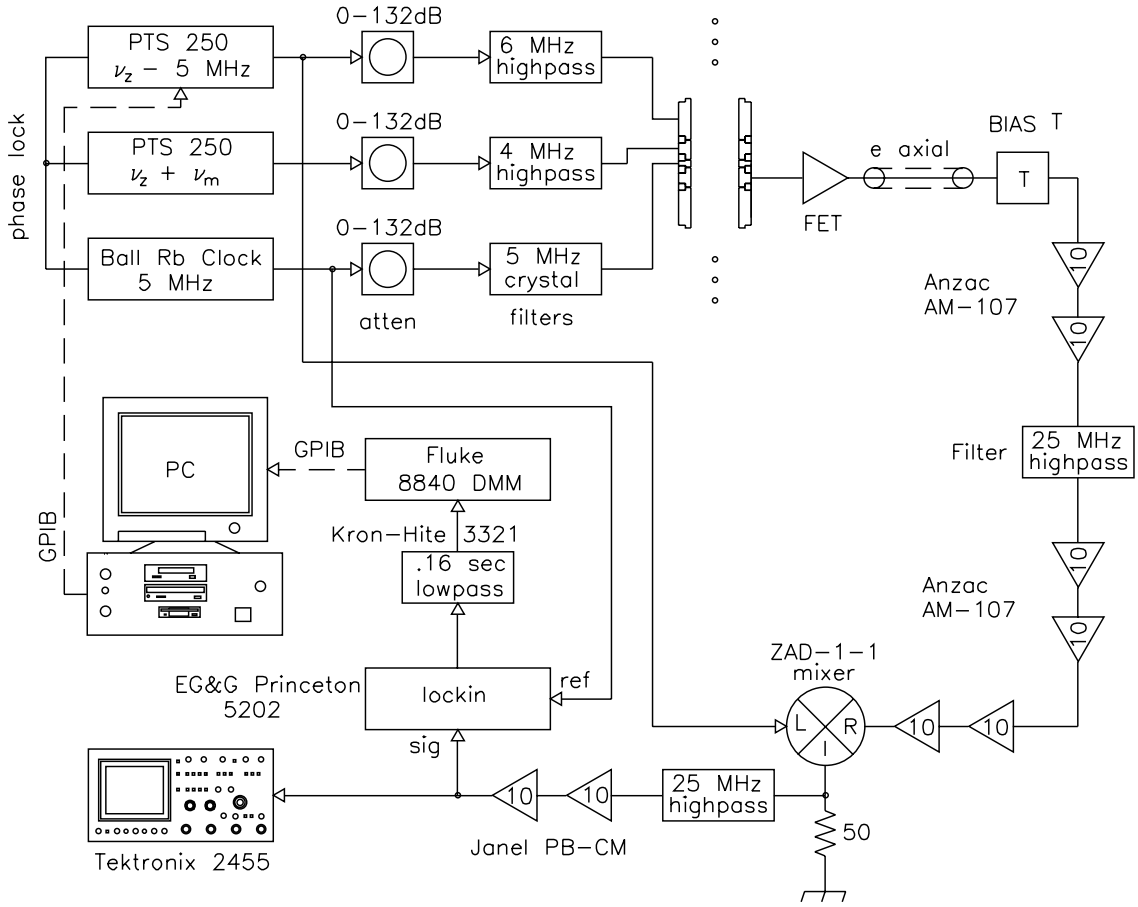

Figure 3.12: Radiofrequency drive and detection setup for small numbers of electrons.

operating at ν_d [37]. A lockin amplifier selects the phase of the output signal, and the signal amplitude is filtered and recorded by a digital multimeter.

Other experiments [61, 62] have used a similar phase-sensitive detection scheme to detect a "step" structure as the electrons load into the trap. Since the signal of Eq. 3.21 is proportional to N, and N is a whole number, the detected signal will exhibit series of discontinuous jumps in the signal level as additional electrons appear in the trap, making determination of the number of electrons in the trap relatively simple. In this apparatus, unfortunately, electrons are typically loaded too

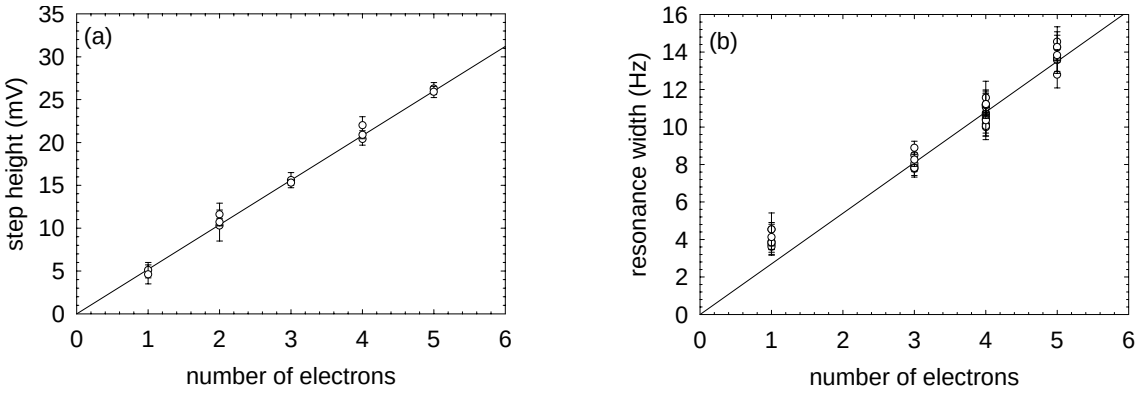

Figure 3.13: Determination of the damping width γ_z. (a) Height of the measured "step" as a function of particles. Each point on the graph represents the average of 5 steps taken with the same electrons. (b) Damping width as a function of the number of particles. The slope of the line yields $\gamma_z(e^-) = 2\pi \cdot (2.70 \pm 0.02)$ Hz. The single electron data illustrate the broadening associated with fluctuations of the trapping potential, and are not part of the measurement.

far from the trap axis to be driven and detected immediately. After sideband cooling, however, the electrons are shifted in and out of resonance with the tuned circuit by varying the trapping potential. The corresponding difference in the amplitude of the detected signal is the height of the "step" (Fig. 3.14).

Figure 3.13(a) shows the results of measuring the step height for 12 distinct electron clouds. The grouping appears at step height intervals of 5.2 mV. To increase the signal-to-noise, each cloud's step height was measured five times, and then averaged to produce the points shown. With the step height determined for a single electron, the step heights for other (small) electron clouds determine the number of electrons in those clouds.

Once the number of electrons in the trap is known, the cloud linewidth can be measured and fit using Eq. 3.13. In practice, the signal-to-noise is usually too poor to be able to determine the damping widths from the undriven axial motion [Fig. 3.14(a)]. Another phase-sensitive scheme is used to enhance the detected signal by sweeping the axial drive through the resonance at $\nu_z - \nu_{\rm mod}$ and detecting at $\phi = 0$

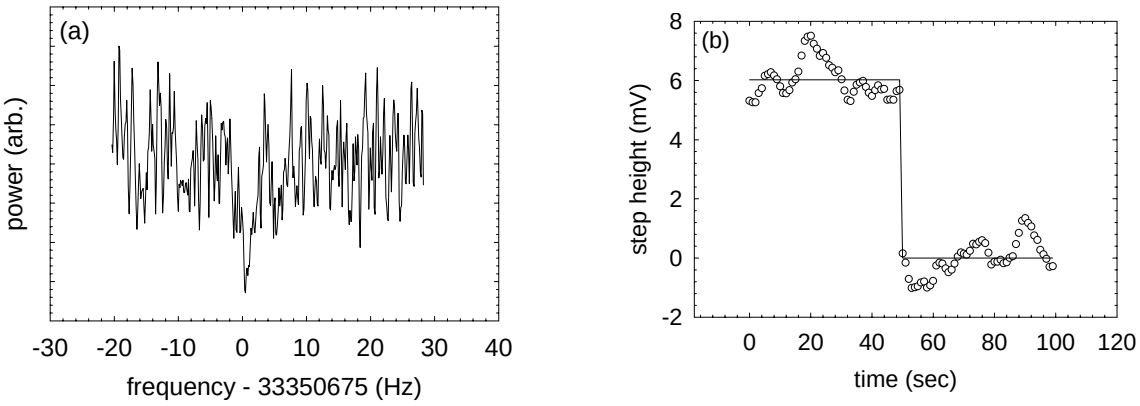

Figure 3.14: A single electron in the trap. (a) Single electron dip. The poor signal-to-noise makes it difficult to measure the width directly from the dip. (b) A single electron "step," illustrating the discontinuity in the response with the electron on- and off-resonance.

(Eq. 3.20). This technique yields a response which is a Lorentzian with FWHM equal to $N\gamma_z$. The widths measured using this driven technique are plotted as a function of electron number in Fig. 3.13(b); from the slope of the line, the measured value of the damping width is

$$\gamma_z(e^-) = 2\pi \cdot (2.70 \pm 0.02) \text{ Hz}. \tag{3.22}$$

Electrons are 100 times more sensitive than protons to variations in the trapping potential (1500 Hz/mV) but have a single-particle width which is only 10 times greater. The noise-reducing trapping potential scheme of Fig. 3.9 must therefore be implemented to reduce the systematic broadening of the measured widths. Single electrons dramatically fail to satisfy the requirement $N\gamma_z/\Delta\omega \gg 1$, and are therefore excluded from this measurement.

3.5 Microchannel Plate Detection

The microchannel plates constitute a destructive particle detection system wholly independent of the nondestructive RF detection system. It is interesting to see how

this detector agrees with the radiofrequency methods of Sec. 3.2. In this section, the absolute detection efficiency of the microchannel plates for protons and electrons is determined.

As discussed in Sec. 2.5, the effective gain of a microchannel plate is a function of its temperature and the incident count rate. For instance, when large, sideband-cooled electron clouds are dumped to the plates very quickly, the detection efficiency drops; values around 30% are often observed, although this may be even lower for very well-cooled clouds ramped out over a few milliseconds.

In order to divorce these effects from the "intrinsic" quantum efficiency of the plate, electron clouds of known number (as determined by the RF system) were ejected to the plates at rates not exceeding 100 Hz and compared to the number detected by the microchannel plates. The detection efficiency for 1 keV incident electrons at these low count rates is $(72 \pm 5)\%$, and is independent of temperature between 28 K and 45 K. This is consistent with a plate open-area ratio of 66%.

Figure 3.15 shows the measured absolute detection efficiency as a function of incident electron energy at the standard operating temperature ($T = 45$ K, 100 nA strip current). The detection efficiency is about 70% for electrons of incident energy above 0.4 keV, which is consistent with near unit efficiency of exciting the channels directly given a front plate open area ratio of 66%. The detection efficiency drops to near 50% at 0.02 keV; a clue as to this behavior is found in Fig. 3.16, which plots the gain peak as a function of incident energy. Very low energy incident electrons do not appear to drive the plates fully into saturation; some counts are doubtless lost as the curve shifts toward the noise.

Other groups [63, 64] have observed electron detection efficiencies which are very similar to those observed here. Some have even reported detection efficiencies which exceed the open area ratio of the plate. A simple model [65] serves to explain

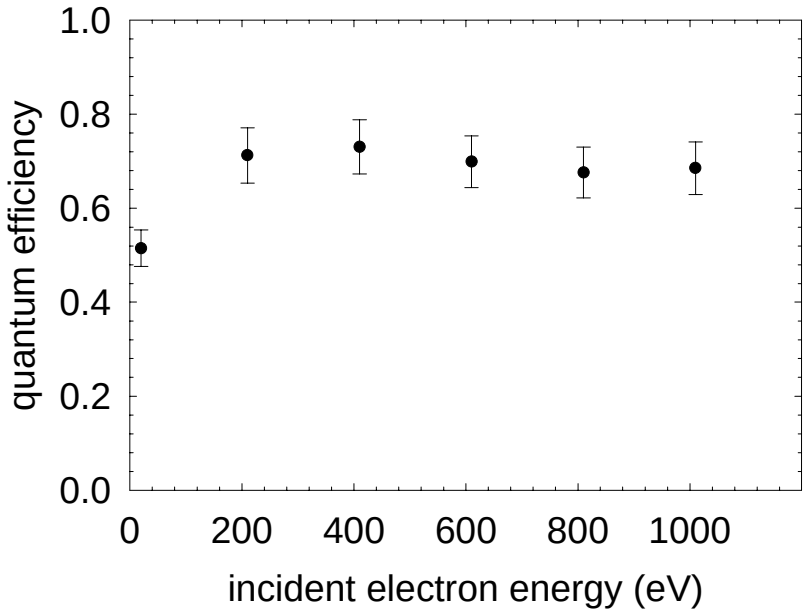

Figure 3.15: MCP quantum efficiency for electrons as a function of incident energy.

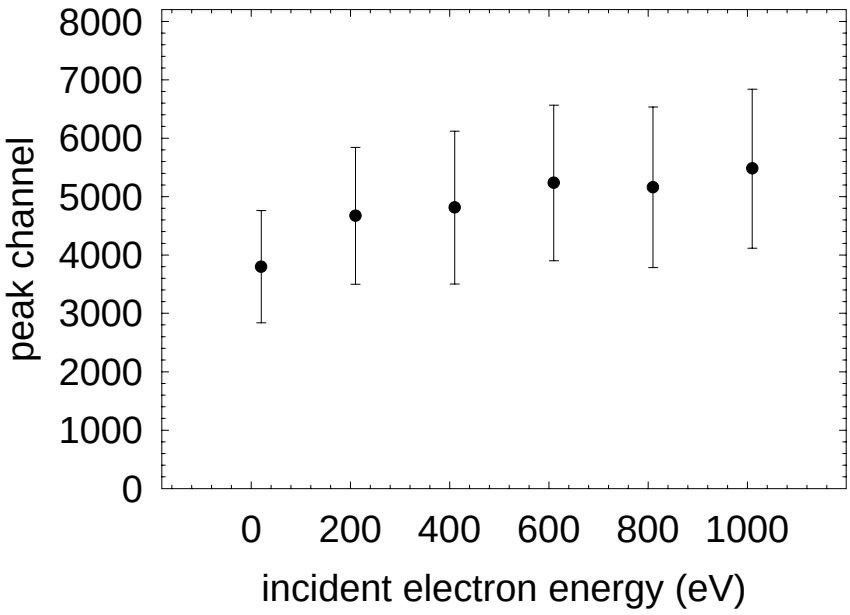

Figure 3.16: MCP peak gain as a function of incident energy. The error bars denote the FWHM of the quasi-Gaussian gain peak.

the latter behavior. The incident electrons are separated into two groups: those which enter a channel and excite it directly (in this case, 66%, given by the plate open area ratio) and those which miss the channels and strike the channel interstices instead (the remaining 34%). Electrons of the former group which strike the channel with enough energy to liberate at least one secondary (i.e., more than 25 eV or so) will be detected with near unit efficiency. Those electrons which miss the channels are also capable of liberating secondaries from the glass; these will, in general, be emitted away from the plate. If the front plate is biased positive with respect to the TUBE electrode, these secondary electrons will be drawn back to the front plate for an "additional" opportunity to excite a channel. When the plate is biased negative with respect to TUBE, however, the electrons do not return to the plate and this interstitial contribution to the electron detection efficiency vanishes. The presence of a magnetic field, however, may eliminate this potential improvement by preferentially returning the interstitial secondaries to their starting points and not to a nearby channel.

Proton detection is very similar to electron detection. The front plate is biased to -3 kV to increase the incident proton velocity; this maximizes the detection efficiency for those protons which strike a channel directly, but eliminates detection for protons which strike the plate interstices, since the interstitial secondary electrons from such events are cannot be returned to the plate. The detection efficiency therefore approaches the open area ratio of the plate.

No systematic study was conducted of the proton detection efficiency as a function of temperature and front plate bias voltage; the detection efficiency is measured directly at the operating temperatures to be $(61 \pm 4)\%$ by ejecting proton clouds of known number to the plates (Fig. 3.17). In the literature, proton detection is shown to peak between 1–3 keV incident energy [66, 67] at efficiencies approaching

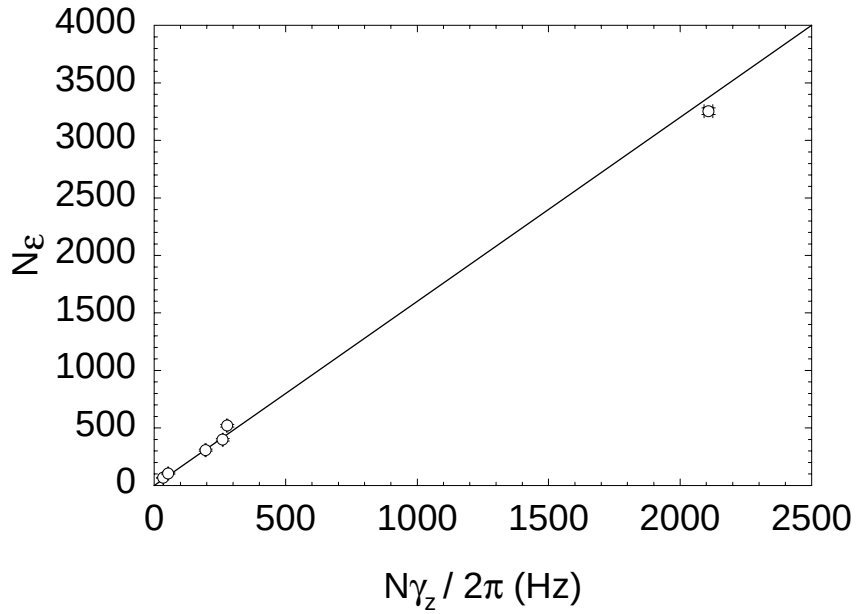

Figure 3.17: Measured MCP detection efficiency $N\epsilon$ as a function of dip width $N\gamma_z/2\pi$ for varying numbers of protons N. The slope of the line, multiplied by the independently measured single-particle width γ_z, determines the absolute detection efficiency of the plates for 3 keV incident protons: $(61 \pm 4)\%$.

the open area ratio of the plates. The proton detection efficiencies measured here are consistent with the latter observation.

3.6 Conclusion

Clean clouds of protons and electrons are trapped in separate harmonic trapping regions and sideband cooled to the trap axis. While in the trap they may be detected and counted using nondestructive radiofrequency techniques (Fig. 3.18). Using the nondestructive counting as a calibration, the detection efficiency for a set of microchannel plates is measured for electrons and protons, and is found to be consistent with the open-area ratio of the plates.

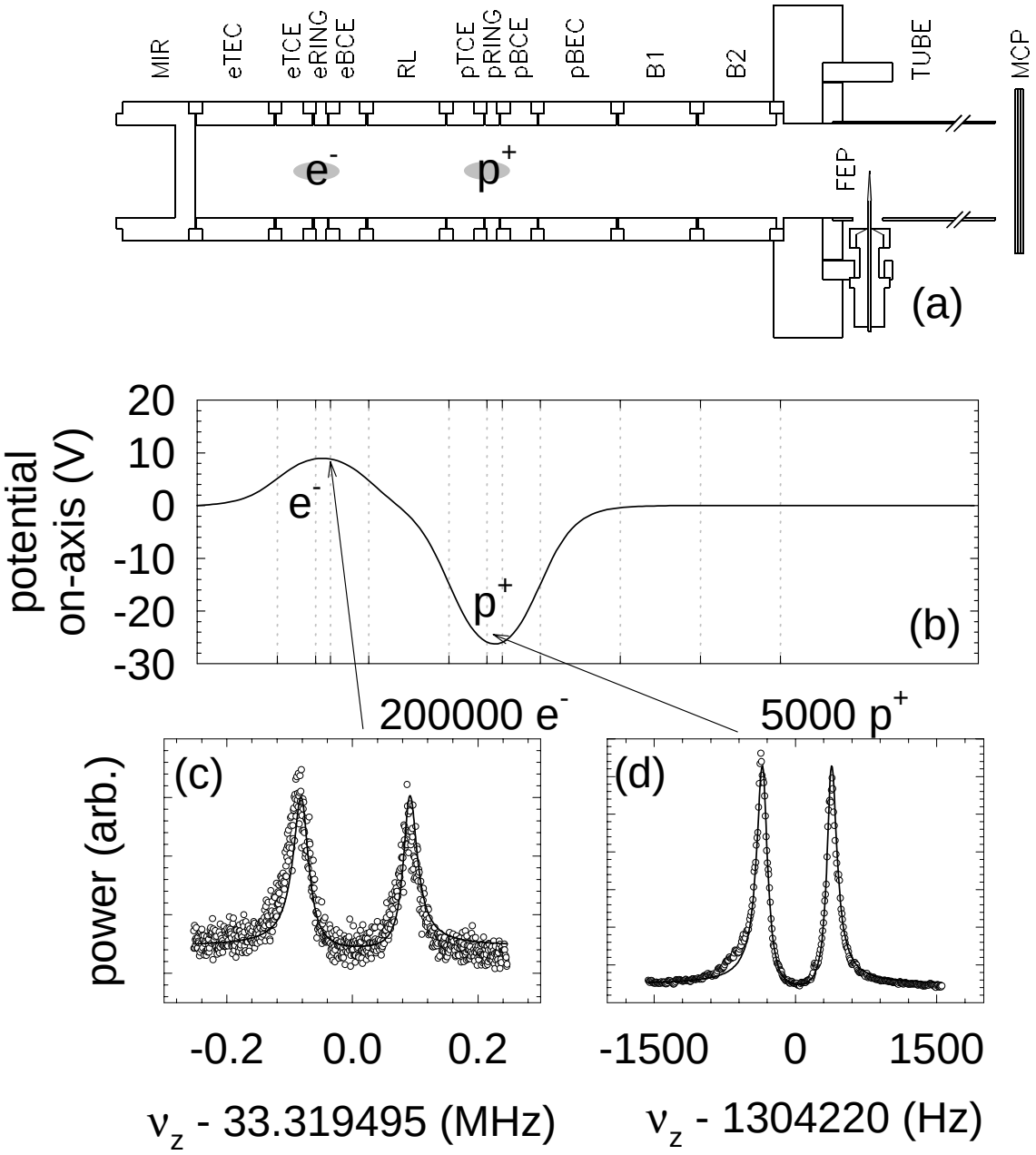

Figure 3.18: Electron and proton clouds in the trap simultaneously, as seen by the nondestructive RF detection technique.

Chapter 4

Electrons and Protons

4.1 Moving Particles about the Trap

Computer-controlled trapping potentials make it possible to move protons and electrons about the trap with the intent of bringing them together and encouraging them to interact. Transferring particles from one electrode to another is one of the simplest moving procedures. In the example shown (Fig. 4.1), particles trapped on the eTRAP electrode[1] are shifted to the RL electrode by biasing the latter to form a deeper well [Fig. 4.1(b)]. (Applying the same potential to both electrodes creates a "long well" and undesirable magnetron heating of the cloud, as discussed below.) The original eTRAP well is then eliminated [Fig. 4.1(c)], leaving the particles trapped on the RL electrode. The depth of this new well is usually reduced slightly to permit the process to be repeated [Fig. 4.1(d)].

"Long wells" are trapping regions in which the electrostatic confining fields vanish over a significant fraction of the trapping region. Torques exerted on the particles

[1]The bias potentials for the three interior electrodes of a compensated trap (RING, TCE, and BCE) are derived from a single voltage source (Sec. 2.4.1). For the purposes of this section, therefore, these sets of three electrodes are regarded as single electrodes: "eTRAP" and "pTRAP."

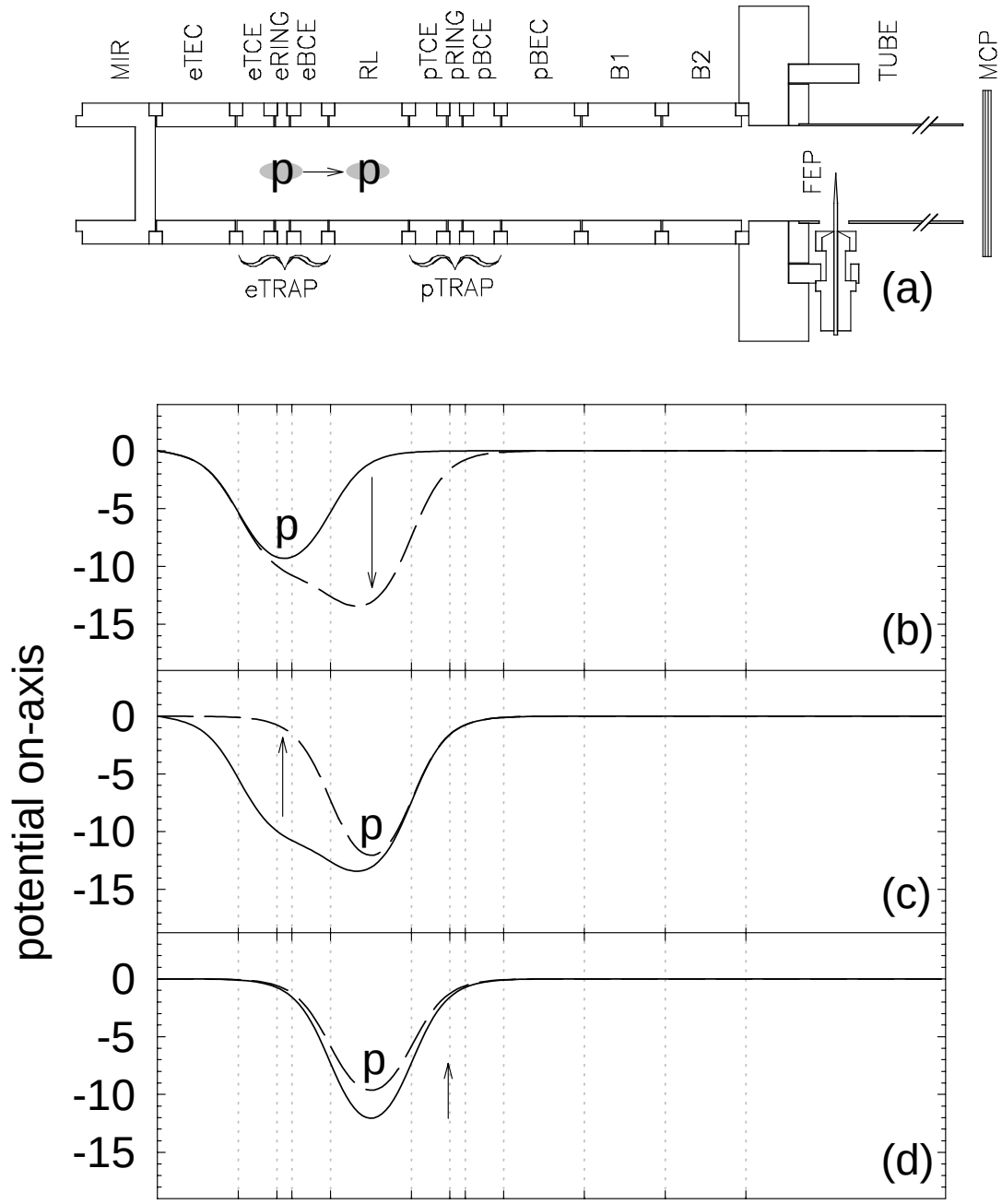

Figure 4.1: Moving particles from electrode to electrode. (a) Trap electrodes. Particles shift into the deeper well as it is created (b). The original well is then eliminated (c), and the potential of the new well adjusted (d) so that the process can be repeated.

(presumably due to residual electric fields) cause magnetron heating and loss from the trap within a few seconds.[2] Another group has also observed this "anomalous transport," with loss rates which scale as $(L/B)^2$ [68, 69] (where L is the length of the plasma column and B is the magnetic field). It is best to avoid long wells whenever possible in order to minimize particle losses.

A trivial variation of the electrode-to-electrode moving scheme described above avoids long wells by introducing a potential well on the adjacent electrode that is more *shallow* than the original well. The particles are pushed into this new well as the original, deep well is eliminated. The shallower-well moving procedure is often used in alternating conjunction with the deeper-well moving procedure to move particles across multiple electrodes, as illustrated in Fig. 4.2.

Particles which are confined in wells that are *too* shallow will also experience magnetron heating. This is (again) believed to be due to azimuthal field inhomogeneities, possibly arising from stray "patch" potentials which are comparable in magnitude to the (reduced) trapping potentials. Fortunately, magnetron heating is easily avoided by maintaining deeper potential wells (5 V or greater is sufficient for the ≈ 1 cm electrodes). The particle moving routines in these experiments typically use well depths of 12–15 V.

The deep and shallow moving procedures described above do not significantly change the particles' axial energy. It is possible to add energy to the axial motion, however, by "spilling" the particles from one electrode to another (Fig. 4.3). In this procedure, a deep well is introduced one electrode removed from the trapped particles [Fig. 4.3(b)], rather than on the adjacent electrode. The barrier between the two wells is then reduced, permitting the particles to spill from the original well

[2]Exception: particles with relatively high axial energies are less susceptible to magnetron heating and may survive for extended periods in a long well. This observation is employed to good advantage in Sec. 4.3.

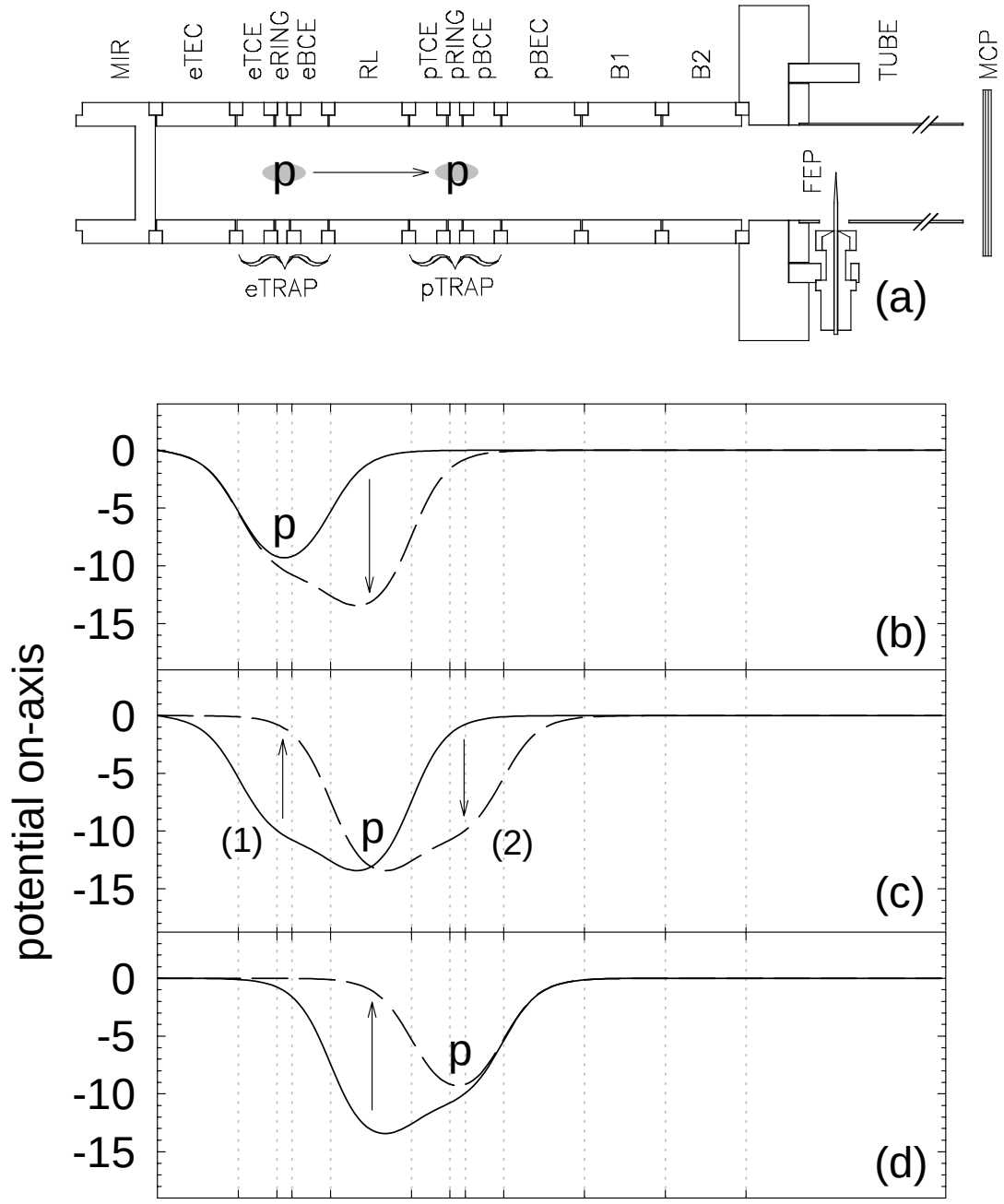

Figure 4.2: Moving particles across two electrodes. (a) Trap electrodes. Particles move into the deep well as it is created (b); the original well is then eliminated (c1), and a new (shallow) well is created on the opposite side (c2). The deep well is then removed, leaving particles in the remaining well two electrodes away (d).

(eTRAP) into the deeper well (pTRAP). As the particles enter the new well [barrier reduced to dash-dot line in Fig. 4.3(c)] their axial energy changes with respect to the potential minimum, which is now given by the depth of the new well. (This is quite unlike the previous moving procedures, in which the particles always sit at or near the potential minimum.) The original well is then eliminated and the barrier restored, leaving the particles in the new, deep well with additional axial energy.

The ultimate outcome of this "spilling" procedure depends critically on the ability of the particles involved to cool their axial motion. In a 6 Tesla magnetic field, electrons synchrotron-radiate (with a time constant $\tau_c \approx 0.1$ sec) until their cyclotron motion comes into thermal equilibrium with the 4 K environment. Electrons lose their axial energy by collisionally coupling it into cyclotron energy and settle into the bottoms of the potential wells into which they are introduced [indicated by the "e" in Fig. 4.3(d)]. Since the synchrotron-radiation time constant scales as m^3 [37], protons (and other heavy ions) are insignificantly damped by this mechanism and tend to maintain their axial energies [indicated by the "p" in Fig. 4.3(d)].

The time constant for collisional coupling between the electron cyclotron and axial motions is predicted to be greater than 100 sec at low temperatures (4 K) and high magnetic fields (6 Tesla) due to the presence of an adiabatic invariant [70]. Data [71] from slightly higher temperatures (10 K) in a similar magnetic field support the theory but indicate a time constant on the order of 1 ms, which is much less than τ_c. Other observations at experimental conditions similar to those reported here [72] suggest a time constant on the order of a few seconds, which is considerably shorter than the theoretically-predicted time.

In a final simple procedure, the contents of two potential wells (of the same sign) are combined (Fig. 4.4). One of the two wells (in this example, the well defined by the pTRAP electrode) is made deeper than the other, and the barrier between the

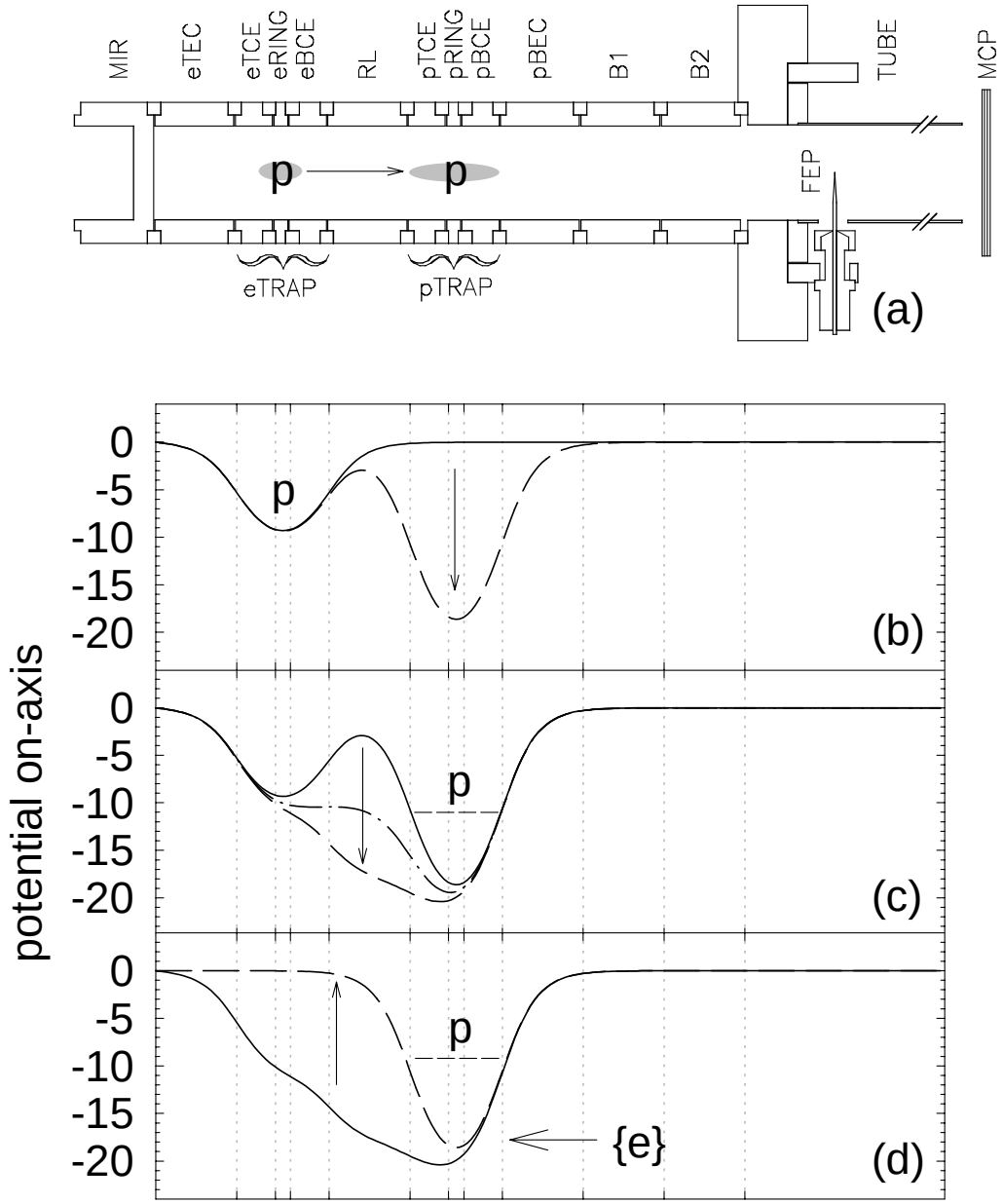

Figure 4.3: Adding axial energy. (a) Trap electrodes. A second, deeper well is introduced one electrode away from the original well (b). The barrier between the wells is reduced (c), permitting the particles to spill into the deep well. The barrier and original well are then eliminated (d). The final energy depends on the ability of the particles to cool themselves (see text).

two wells reduced to form an even deeper well, drawing into it particles from both of the original wells [Fig. 4.4(c)]. (Note that the particles originally trapped in the shallower well (eTRAP) undergo a "spilling" move and thus gain axial energy.) Such "combining" procedures are useful in the accumulation of positrons (Sec. 5.5.1), and may also permit experiments which study axial temperature relaxation times.

4.2 Measuring Particle Energies

The energy spectrum of particles confined in a potential well is measured using a simple experimental technique, illustrated in Fig. 4.5. The procedure begins as the computer triggers a (linear or exponential) voltage ramp on the B1 electrode, permitting particles to escape the trap as their axial energies exceed the (reduced) confining potential. The escaping particles are counted by a multichannel scaler as they reach the microchannel plates, and the ramp waveform is digitized by an oscilloscope connected to the B1 ramp monitor line (Fig. 2.8) and fit to the appropriate (linear or exponential) waveform to reduce the effects of digital noise. The resulting spectrum is expressed as the number of particles detected as a function of the voltage applied to the B1 electrode.

Figure 4.6 demonstrates this technique for the simple example of dumping protons from the B1 electrode to the microchannel plates. The voltage is ramped exponentially from -10 V to $+1$ V with a time constant of 0.1 sec; the oscilloscope waveform and microchannel scaler counts are shown in Fig. 4.6(c), and the resulting spectrum (after binning) is shown in Fig. 4.6(d).

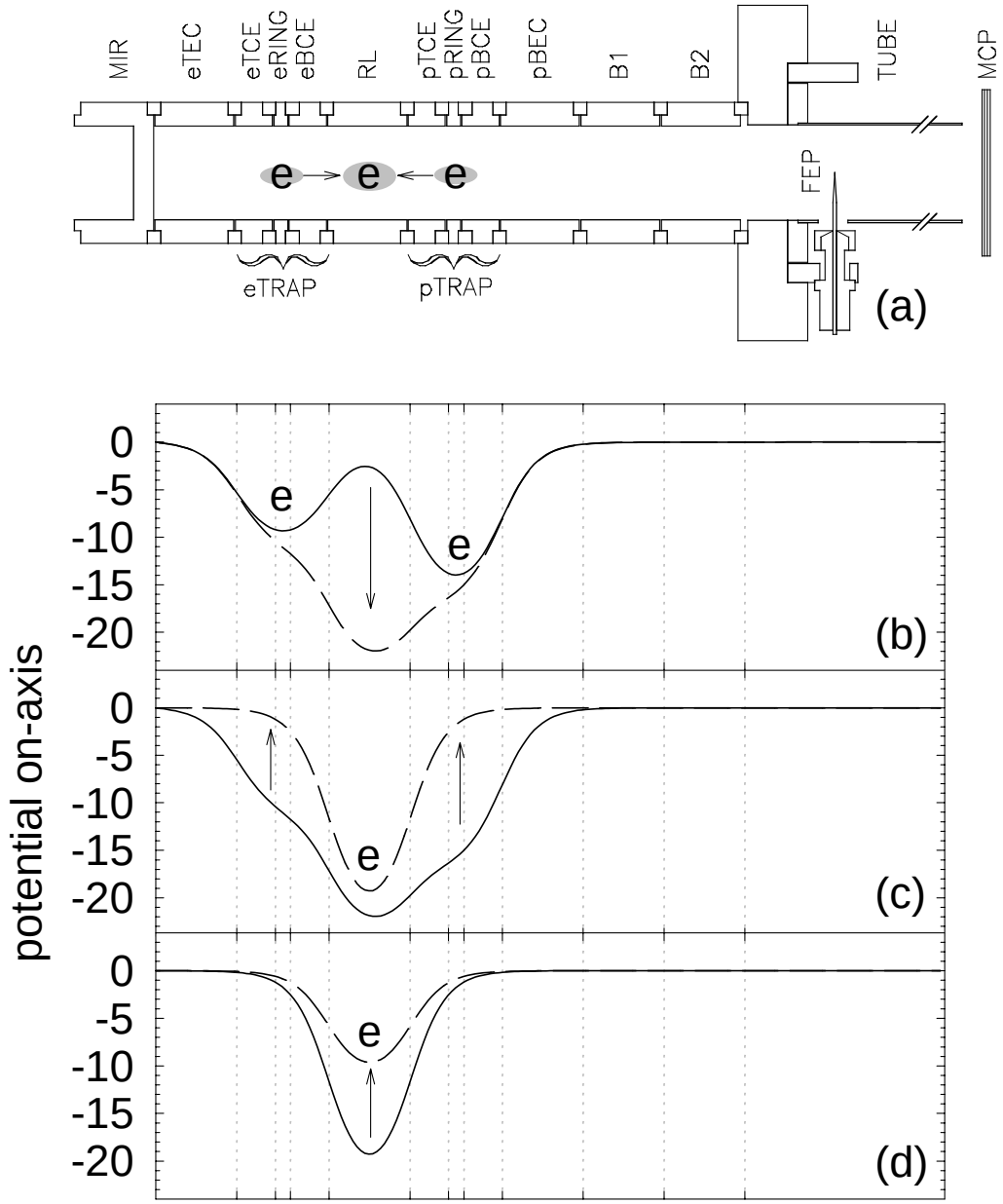

Figure 4.4: Combining the contents of two wells. (a) Trap electrodes. The potential barrier between the two wells is reduced to form a single well, deeper than either of the two initial wells (b). This is a heating move for particles in the left-hand well. The original wells are then eliminated (c) and the shallower potential may be restored (d) if the particles are capable of cooling their axial motion.

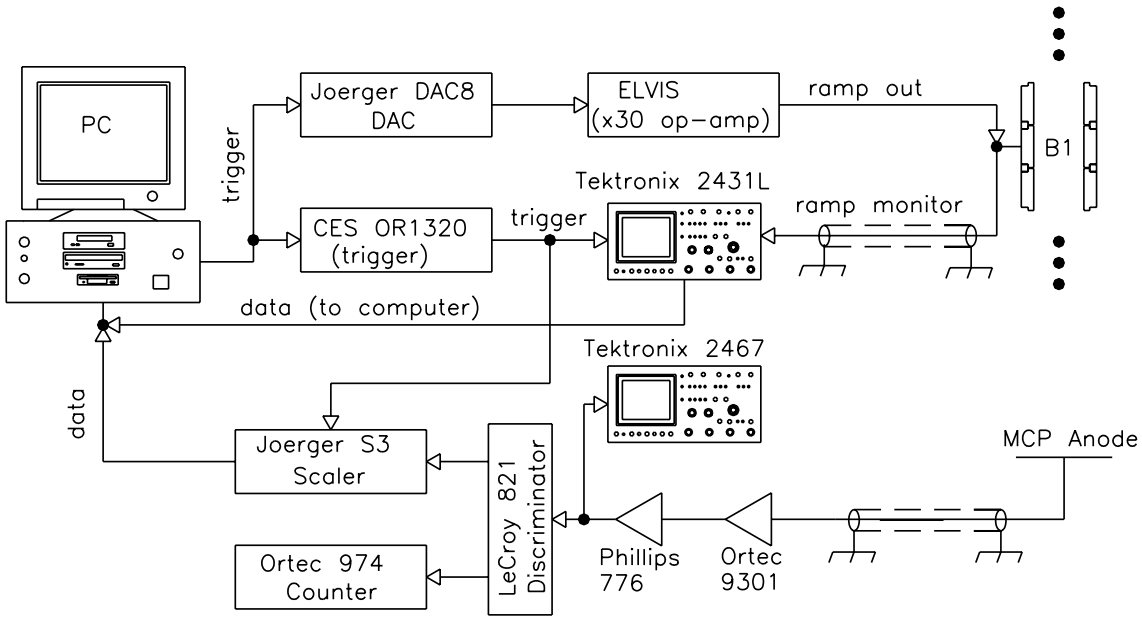

Figure 4.5: Equipment setup for measuring the energy spectrum of particles confined in a potential well. The computer triggers the ramp, digital oscilloscope, and multichannel scaler, and then takes the data to produce a plot of counts *vs.* applied potential.

4.3 Electron Cooling of Protons in a Nested Penning Trap

A nested Penning trap achieves confinement of particles of opposite sign of charge by "nesting" one potential well within another of the opposite sign. Significantly, its use was first suggested in 1988 [28] for the production of antihydrogen; it has subsequently been used in ion cyclotron resonance spectroscopy with oppositely-charged ions [73, 74] as well as in the initial studies in helium [5] which led to this work.

The techniques of Sec. 4.1 are used to inject protons into the outermost of the two nested traps. After cleaning and counting, protons are moved to the B2 electrode,

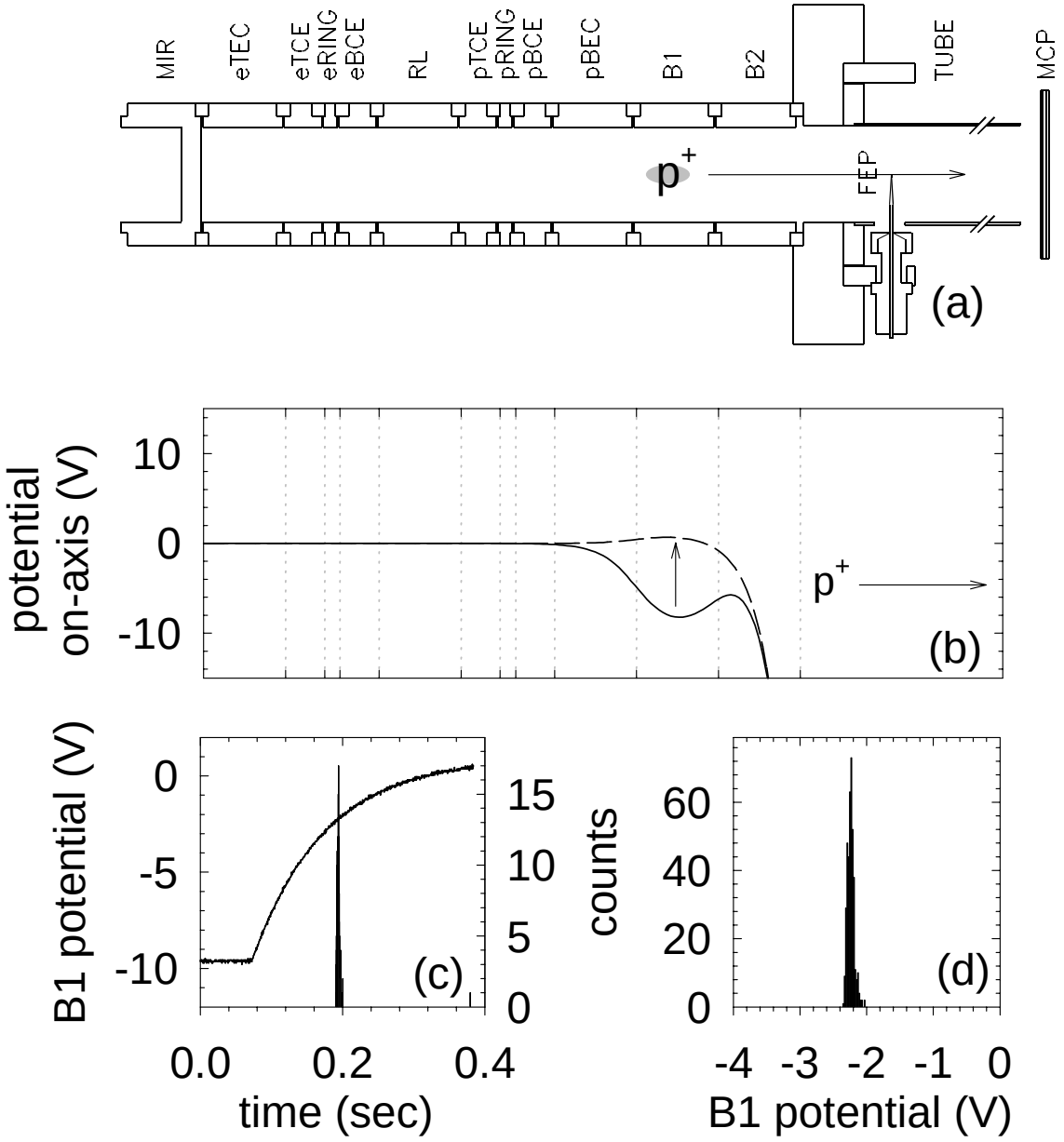

Figure 4.6: Measuring the energy of trapped protons. (a) Trap electrodes. The protons are initially trapped in a well formed by the B1 electrode. As the well depth is reduced (b), the particles escape to the microchannel plates. The measured ramp waveform is digitized (c) and synchronized with the counts on the plates to yield the number of counts as a function of the potential applied to B1 (d).

whereupon the trap electrodes are biased as shown in [Fig. 4.7(b)]. The protons perch above (and outside) the outer well, which is defined by the potentials on the B1 and MIR electrodes; a nested, inner well is defined by the voltage applied to the RL electrode. The potential is then reduced on B1, permitting the protons to spill into the outer trapping region with an axial energy given by the effective "height" of the B2 potential above the bottom of the outer well. The bias is subsequently restored on B1 [Fig. 4.7(c)], leaving the protons in the outer well of the nested trap.[3]

The trapping configuration described above is a nested trap only if the protons are injected into the outer well with enough energy to pass over the "hump" formed by the inner well. This requirement also insures that the protons have enough axial energy to avoid the magnetron heating associated with being trapped in long wells, as discussed in Sec. 4.1. Electrons are less suitable for use in the outer well, since their ability to cool themselves by synchrotron radiation will cause them to drop into the side wells. Protons, however, do not experience significant radiative damping, and remain in the outer well of the nested trap for extended periods.

The proton axial orbits in the nested trap are too anharmonic to permit effective use of the nondestructive radiofrequency detection techniques. Their energies may still be analyzed, however, since ramping the B1 bias through zero (after reducing the B2 and TUBE potentials to 0 V and -100 V, respectively) permits them to escape to the microchannel plates and be detected (Fig. 4.8).

The potential applied to the B1 electrode as the protons spill out is a good indicator of the proton energies in the long well, but it requires calibration to account for the fact that the potential applied to the B1 electrode and the confining potential

[3] Actually, only *most* of the protons are left in the outer well; some manage to sneak back onto the B2 electrode and get stuck there as the B1 potential is raised. An improved procedure (not used here) eliminates this loss by biasing the B2 electrode at the same potential as the TUBE after the protons are injected into the outer well.

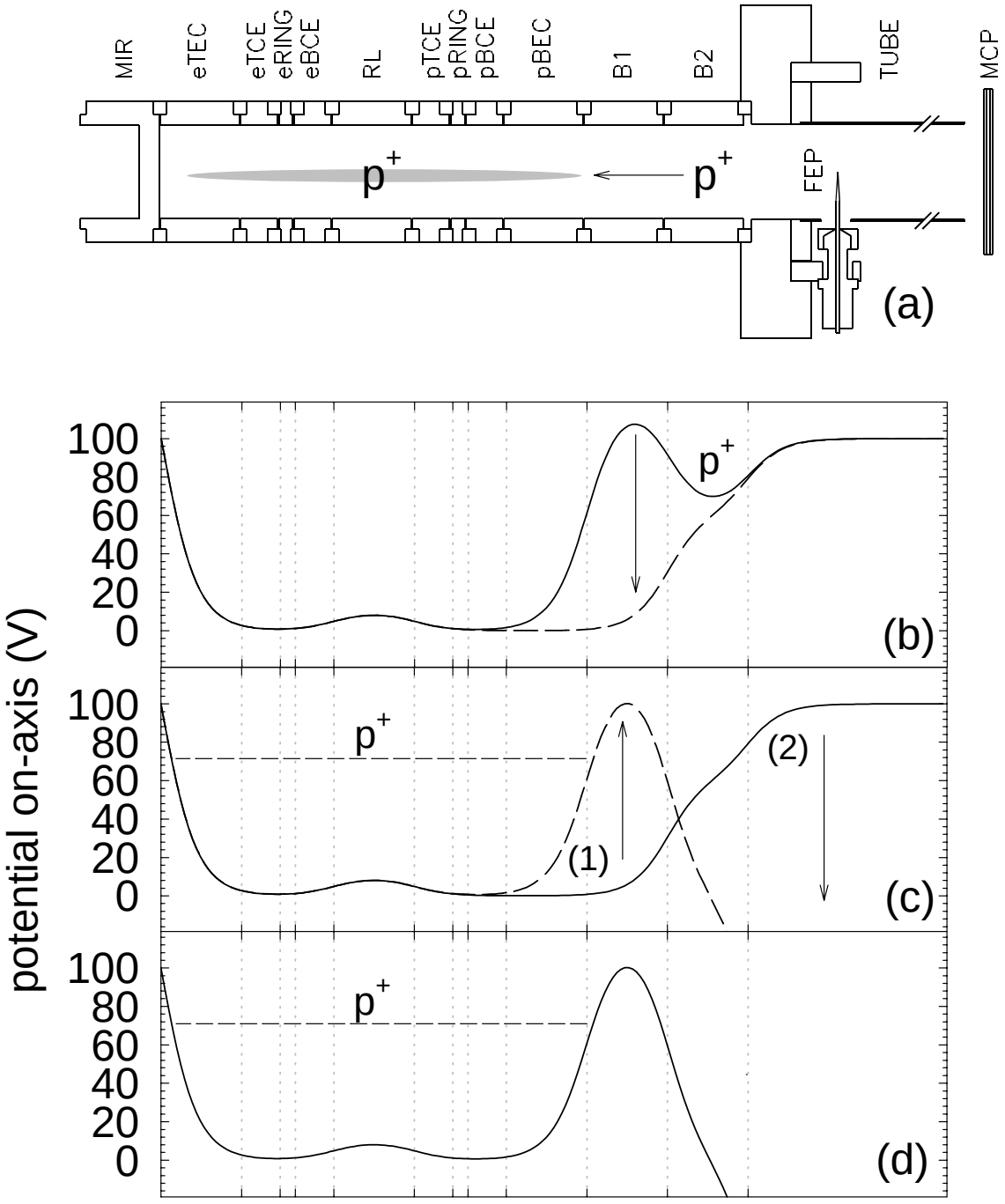

Figure 4.7: Nested Penning trap realization. (a) Trap electrodes. (b) Protons start in the upper well (centered on B2), and are admitted into the nested trap by lowering the potential on B1. The potential on B1 is restored (c1) and the original proton well eliminated (c2), leaving the protons as shown in (d).

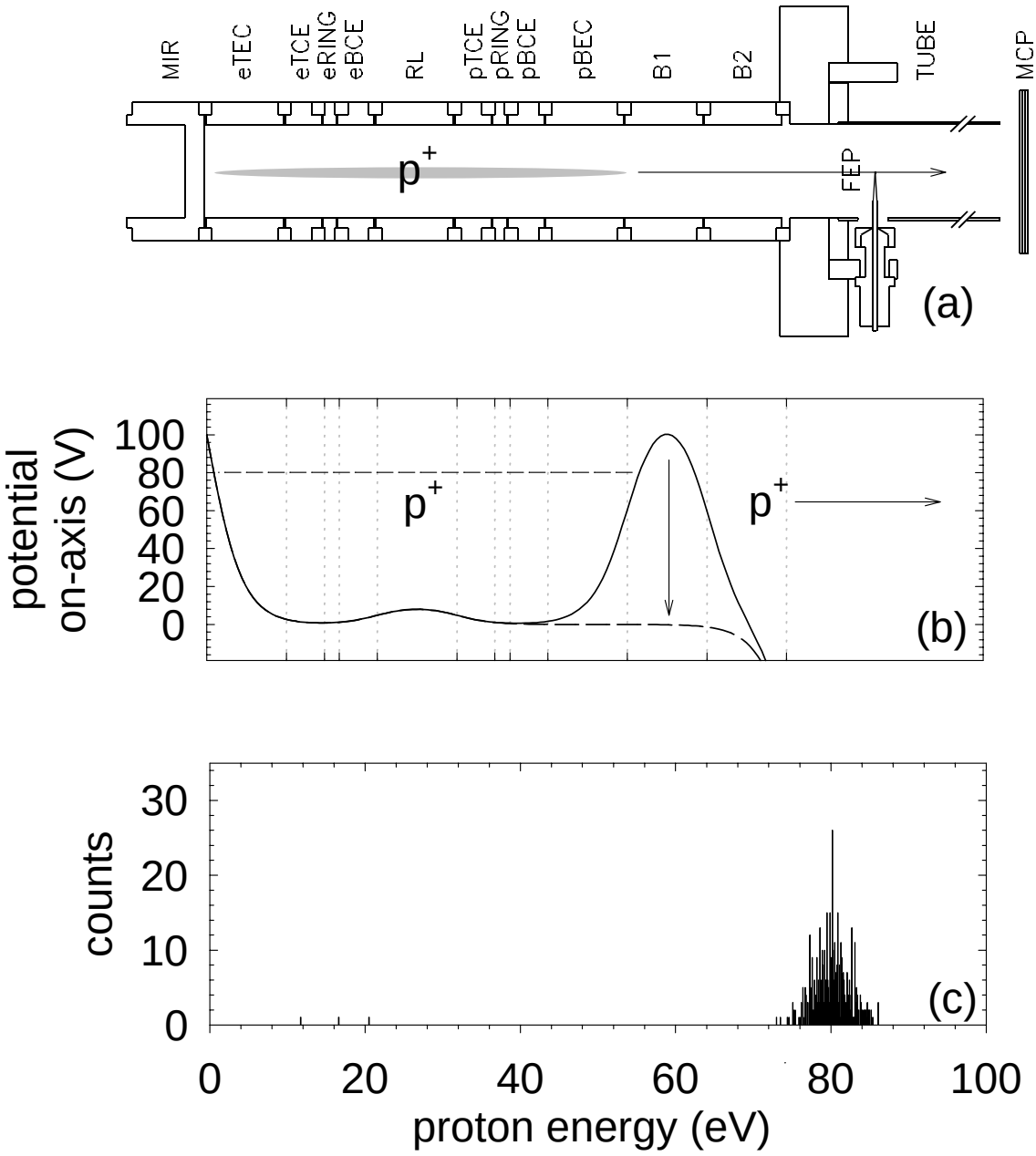

Figure 4.8: Detection of protons in the nested trap. (a) Trap electrodes. (b) The protons (initial energy indicated by the dashed line) are released to the microchannel plates by ramping down the potential on B1. The proton energy in the well is reconstructed in (c), taking into account adiabatic cooling (see text). No electrons are trapped in the inner well.

near the axis of the trap are (generally) not the same. The effects of adiabatic cooling, experienced by the protons as one (or both) of their confining walls is reduced, also changes the potential at which they are detected. The adiabatic cooling is most easily understood by considering the effect of reducing the well depth produced by an ideal quadrupole potential (Eq. 2.2). The charged particle executes harmonic motion in z at a frequency ω_z, and the condition for the existence of an adiabatic invariant is [75]

$$T\frac{d}{dt}V_0(t) \ll V_0(t) \tag{4.1}$$

where $V_0(t)$ is the time-dependent trapping potential and $T = 2\pi/\omega_z$ is the orbital period. If condition 4.1 is met, the energy divided by the frequency,

$$I = \frac{E}{\omega_z}, \tag{4.2}$$

is an adiabatic invariant (*i.e.*, it is approximately a constant of the motion). Since the axial frequency ω_z varies with trapping potential as $\sqrt{V_0(t)}$, both it and the axial energy E decrease as the trapping potential is reduced.

A similar analysis obtains when protons are released from the nested trap when only one of the confining potentials (B1 electrode) is reduced, although in this case the complicated well structure defies a simple analytic solution. The effect of the adiabatic cooling is determined by numerically integrating the (axial) differential equations of motion for a proton in the trap (with energy E) as the confining wall is reduced. A calibration curve is constructed by this process which inverts the calculated relation to give the initial energy E of the proton in the well (relative to an arbitrary zero of potential energy) as a function of the potential applied to the

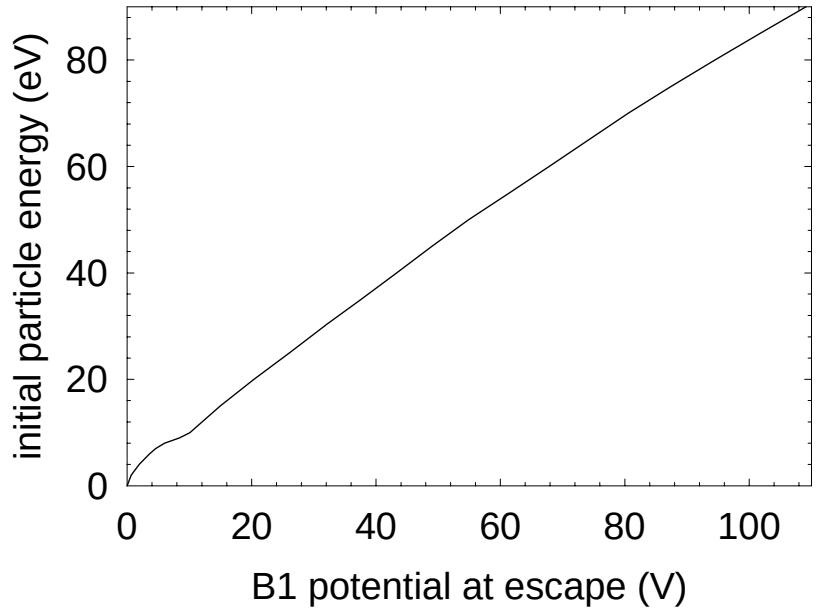

Figure 4.9: Calculated calibration relates the initial energy of protons in the outer well to the potential (on B1) which allows them to escape the trap (for an exponential ramp with time constant 0.1 sec and 10 V applied to the RL).

electrode at the moment the particle escapes the trap (Fig. 4.9).

The integration routine used here is an implementation of the Runge-Kutta algorithm with adaptive step size [76]. Only the axial equation of motion is integrated, reducing the problem to that of a particle in a one-dimensional potential, which is calculated by analytic solution of Laplace's equation (on the axis of the trap) from the electrode geometry and the applied trapping potentials (Eqs. 2.6 *et. seq.*). Due to rounding and other calculational errors, the accuracy of the calibration is estimated to be no better than .05 eV. The curve permits the energy spectrum of the particles to be expressed in terms of their energies with respect to the bottom of the well prior to the start of the ramp [see, for instance, Fig. 4.8(c)].

In another set of experiments, the voltage applied to the B2 electrode prior admitting the protons into the outer well is varied. In Fig. 4.10, four separate proton

spectra (corresponding to four different B2 "injection" potentials) are combined to illustrate the effect of the variation: the protons are detected in four discrete peaks at energies corresponding to those at which they were injected into the trap. The width of the peaks is not understood, but may be an indication of the starting energy distribution of the protons trapped on the B2 electrode before they are released into the outer well.

The nested trap becomes an even more interesting tool when electrons are trapped in the inner well so that the two (oppositely-charged) particle species overlap. The previous experiment is repeated (as described above) for the four B2 injection potentials, each with a cloud of approximately 300,000 sideband-cooled electrons trapped on the RL electrode. The effect is unmistakable (Fig. 4.11): the four (high-energy) peaks collapse into a single peak at a lower energy as the electrons cool the protons [1]. Such sympathetic cooling has been previously demonstrated in ion traps with particles of the same sign of charge, such as $^{198}Hg^{+}$ and $^{9}Be^{+}$ ions [77] and electrons and antiprotons [3]. This experiment is the first demonstration of cooling by particles of *opposite* signs of charge in an ion trap [1].

Figure 4.12 summarizes the results of this electron-cooling experiment. The proton numbers are normalized such that the number of "hot" counts is equal to number of "cold" counts, weighted by the relative numbers in each of the uncooled spectra at the four injection energies. This normalization is conducted to account for load-to-load variations in the number of protons, as well as to account for the $(40 \pm 8\%)$ of the protons which have cooled out of contact with the electron cloud and become trapped between the MIR and the RL electrodes.

To understand the proton endpoint energy E, a set of experiments is conducted to determine its dependence on the "depth" W of the inner trap [Fig. 4.13(b)]. Both E and W are determined with respect to the bottom of the well between the B1 and

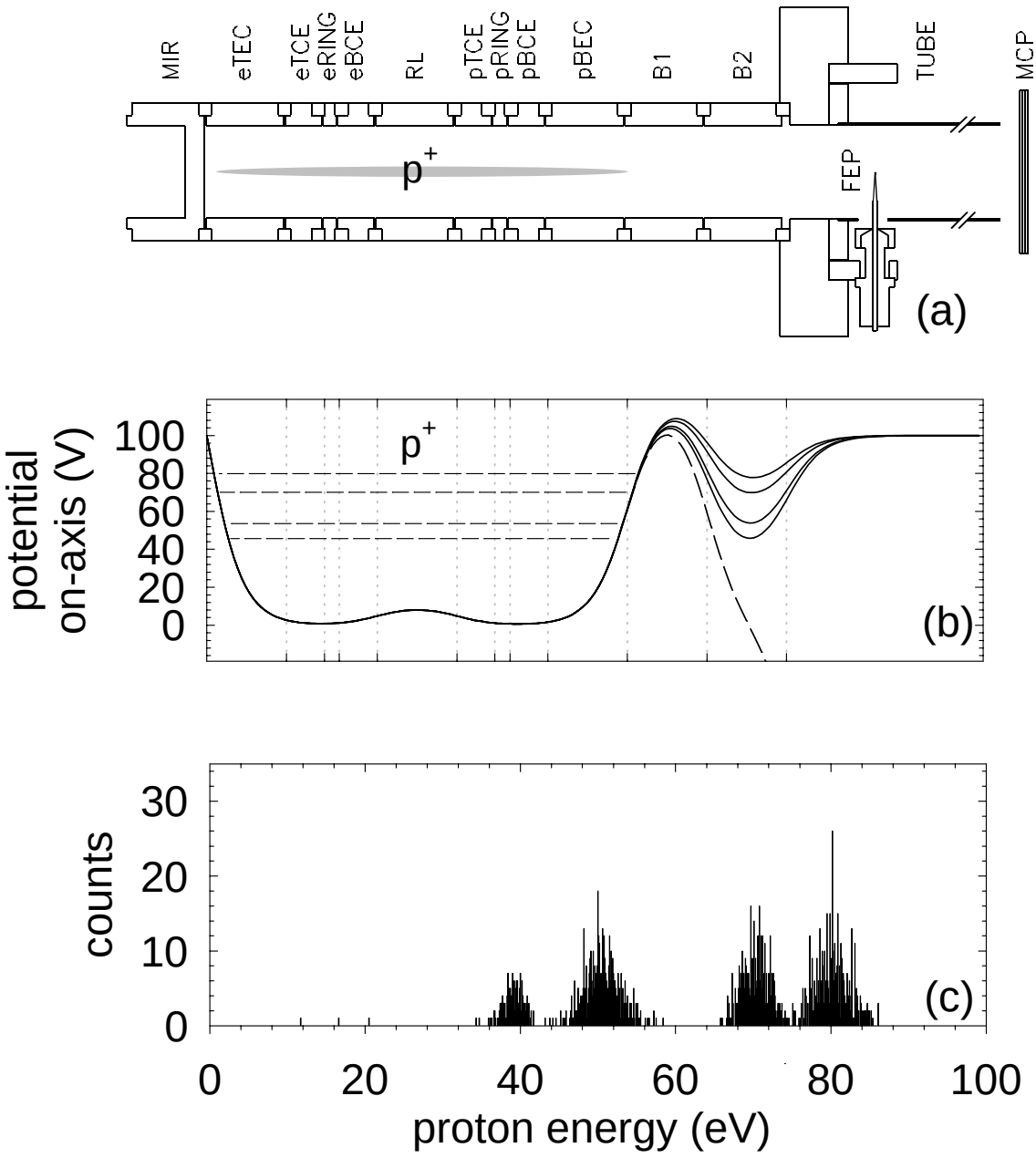

Figure 4.10: Energy spectra of four (uncooled) proton loads, injected at different energies. (a) Trap electrodes. The four different injection energies are given by the varying potential applied to B2 as shown in (b). The resulting spectra (c) show these four peaks. (Exponential ramp from +125 V to −10 V with 0.1 sec time constant, ≈ 30 sec in well.)

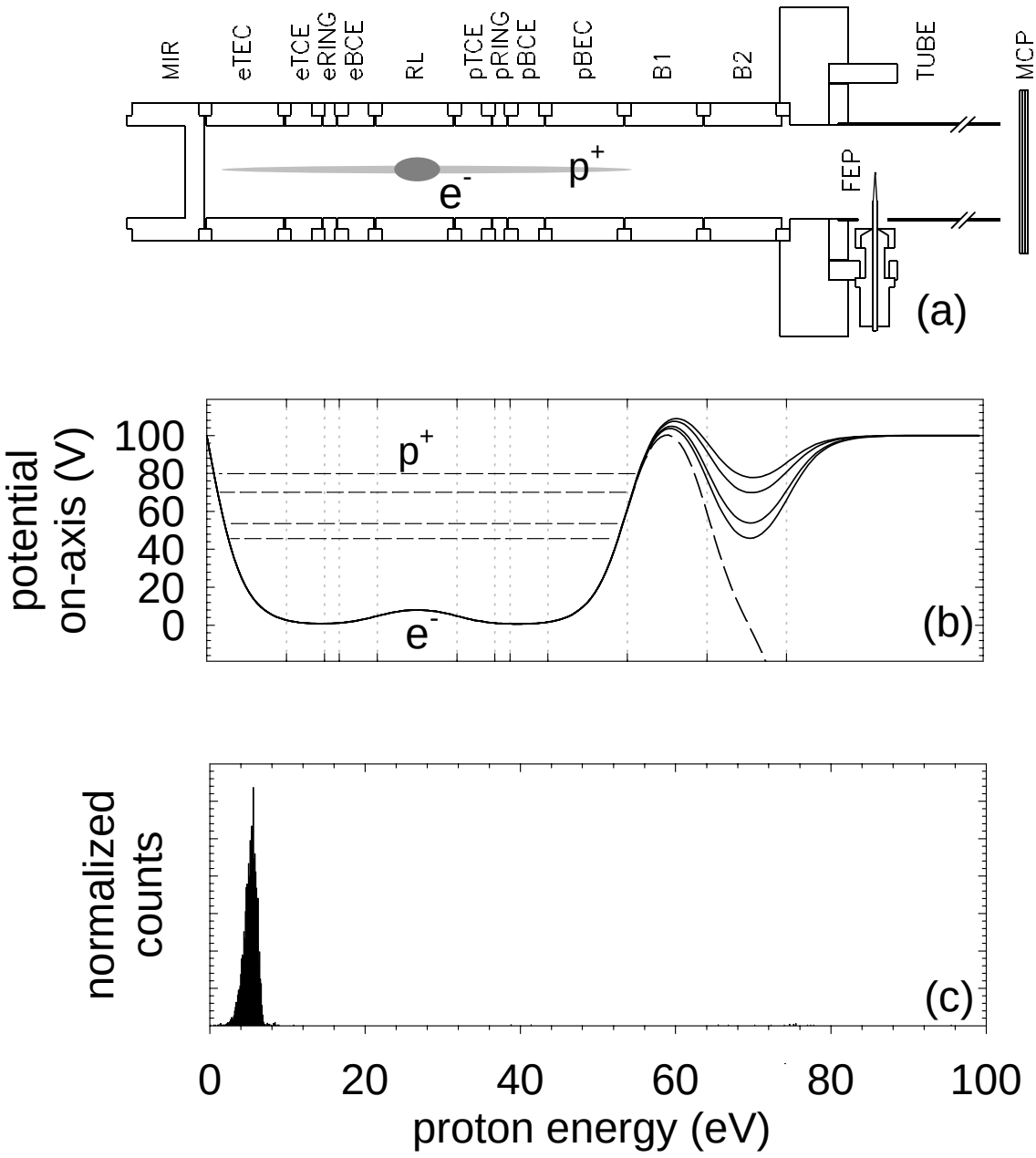

Figure 4.11: Electrons cool protons. (a) Trap electrodes. Protons are injected at the four distinct energies shown in (b); approximately 3×10^5 electrons are trapped on the RL. The electrons cool the protons to a single peak at low energy (c). (Exponential ramp from +125 V to −10 V with 0.1 sec time constant, $\approx$ 30 sec in well.)

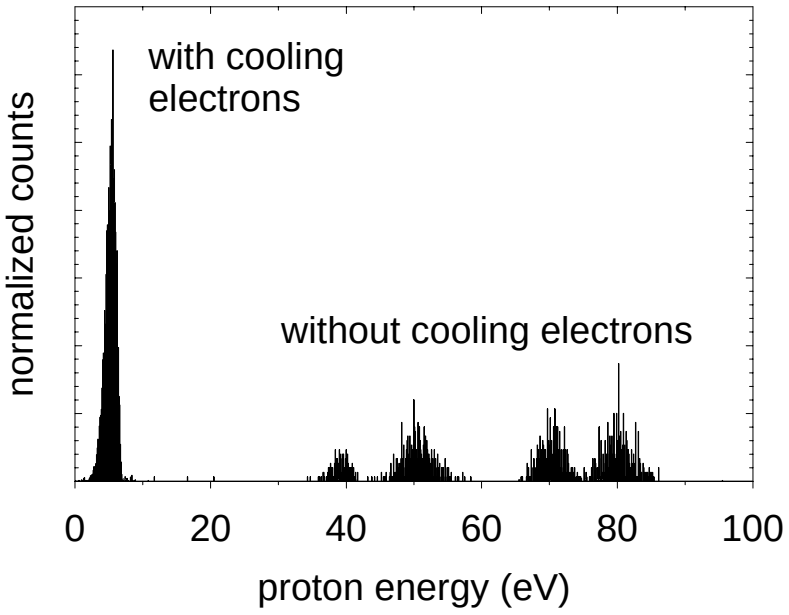

Figure 4.12: Electron cooling of protons.

RL electrodes *before* the ramp releases the protons to the microchannel plates.[4] The proton energy is measured at five different well depths; the results from Gaussian fits to the resulting spectra are plotted in Fig. 4.13(c), where the error bars denote the FWHM and a line at $E = W$ is included for reference. The proton energy closely tracks the well depth, indicating that the protons are cooled to a point at which they have a low relative velocity with respect to the electrons — the critical point at which recombination is expected to be most effective.

Recent analysis reveals an initially unrecognized difference between the proton endpoint energies measured with the linear and exponential ramps. The earlier data (Fig. 4.13) were taken with fast (but relatively noisy) linear ramps (100 V in 3.5 ms) rather than exponential ramps (0.1 sec time constant), involved fewer protons (hun-

[4]This is a slightly different convention than that used in Fig. 3 of Ref. [1], which determines the proton energy with respect to the bottom of the well at the moment the protons escape to the microchannel plates. The difference amounts to shifting the points along the line $E = W$.

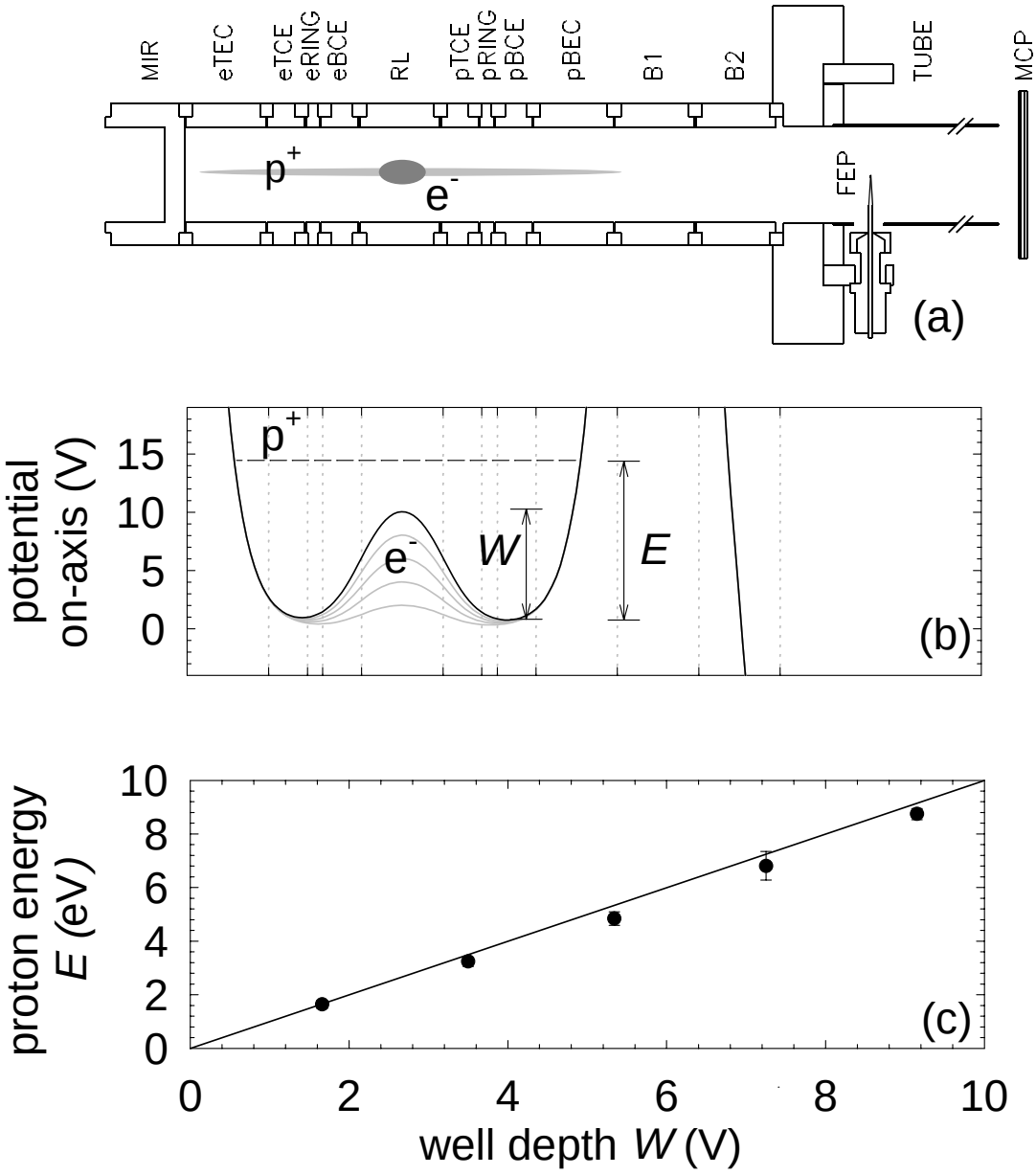

Figure 4.13: Proton endpoint energy E as a function of electron well depth W. (a) Trap electrodes. (b) Magnified view of the potential on-axis, showing the definition of E and W. The proton endpoint is closely related to the electron well depth, as can be seen in (c); this indicates that the protons cool to a low relative velocity with respect to the electrons. The points and error bars represent the central value and FWHM of Gaussian fits to the data. (Linear ramp in 3.5 ms, +125 V to −10 V, $\approx$ 10 sec in well.

dreds rather than thousands), and had a shorter proton-electron interaction time (10 sec rather than 30 sec). The majority of the data reported here were measured with the improved exponential ramps. The proton endpoint energy for a well depth $W = 7.4$ V is found to be $E = 6.8$ eV with the linear ramp, whereas it drops to $E \approx 5.1$ eV for the exponential ramp. (These points are shown in Fig. 4.14.) The procedural variations between the two data sets make the primary contributor to this difference difficult to identify, and a complete understanding awaits future study.

The relatively long time constants in the electrode filters do not permit the study of cooling at times below ≈ 1.5 sec; this is unfortunate, since almost all of the cooling is expected to take place on this order (Sec. 4.4.2). Data were taken at only a few longer time intervals; the (very preliminary) results are shown in Fig. 4.14, and suggests that a slow process extracts energy from the protons after the electron-cooling is complete.

The presence of cooled protons trapped between the MIR and RL electrodes confirms that many (if not all) of the protons eventually lose enough axial energy to become decoupled from the electron cloud. Moreover, the width of the cooled spectra is much wider than would be expected for a cloud of protons cooled by 4 K electrons (even accounting for effects due to the space charge of the electron cloud and a slightly larger magnetron orbit, both expected to decrease the measured energy on the order of 10^{-1} V). These effects are not understood, although there are some intriguing possibilities. For instance, the protons may evolve towards a thermal distribution through collisions with one another at some slow rate; for 5 eV protons, the equilibration timescale is on the order of 10^2 sec [78], which is not so much greater than the observed times. Higher-energy protons of the distribution are quickly cooled through contact with the electron cloud, reducing the net axial

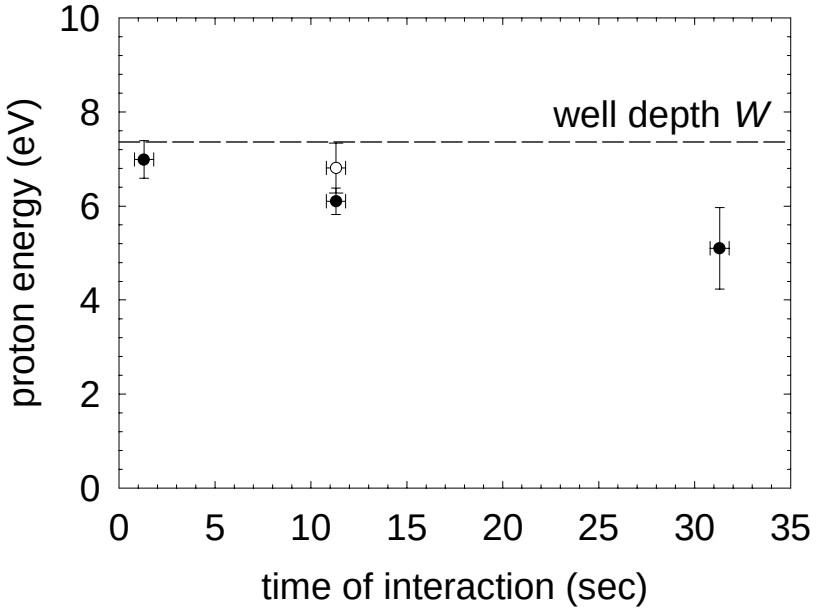

Figure 4.14: Proton energy as a function of time (very preliminary). A slower process appears to extract energy from the protons in addition to the rapid cooling which brings the proton energy to that of the well depth. The points and error bars represent the central value and FWHM of Gaussian fits to the data, and the dashed line represents the well depth $W = 7.4$ V. (Exponential ramp, time constant 0.1 sec, +125 V to −10 V, except for the hollow point: linear ramp in 3.5 ms, +125 V to −10 V.)

energy of the protons. Such a process could continue to extract axial energy from the protons even after a majority has cooled out of direct contact with the electrons.

A more tantalizing explanation arises in the context of recombination. In the three-body collisional-radiative recombination process (Eq. 1.12), the recombined hydrogen atoms would be in high Rydberg states which are easily field-ionized by the trapping potentials (a field of 7 V/cm is sufficient to ionize levels $n > 100$), possibly retrapping the protons at energies $E < W$. (Those protons retrapped at energies $E > W$ are again electron-cooled, possibly getting another chance). This process could not, however, explain a time-dependent decrease in the proton

energy once the protons are cooled out of contact with the electron plasma, unless it occurred in connection with a rethermalization process such as that suggested above.

The proton-electron interaction is easily restarted by reducing the potential on the RL electrode (W); the protons once again pass through the electron cloud and can be detected by repeating the B1 ramp after reducing the potential on the RL electrode to detect the protons which cool to the microchannel plate side of the electron well. An additional fraction (roughly 40–50%) of the protons is retrapped between the MIR and RL electrodes.

The interaction could be also maintained by supplying additional axial energy to the protons with radiofrequency drives, tailored to become resonant with the axial motion of only those protons which have dropped into the side wells. A less subtle recoupling method recovers the protons from the side wells and repeats the entire electron-cooling cycle. In this procedure, the inner well depth W is reduced until the protons have only a few eV of energy above the bottom of the side wells, at which point they are coupled to the proton axial tuned circuit, cooled to 4 K, sideband-cooled (if necessary), and returned to the outer well of the nested trap. The beautiful lineshapes of Fig. 3.5 are from protons recovered from one of the side wells after having been electron-cooled.

4.4 Theory of Electron Cooling

Electron cooling is most easily described as a plasma process. This section evaluates the experimental parameters (*e.g.*, density, spatial extent, space-charge potential, and Debye length) for an electron plasma, and reviews the theory for calculating the expected cooling rates.

4.4.1 Electrons as a Nonneutral Plasma

The electrons in the trap are assumed to form a sphere of uniform charge density n_e and radius r. The radius of the cloud is determined by the condition that the restoring force at the surface of the sphere (due to the external trapping potential) is equal to the repulsive force exerted by other electrons in the plasma. This condition is most easily matched on the axis of the trap, yielding an electron density

$$n_e = \frac{3C_2V_0}{4\pi d^2 e} = 3.44 \times 10^6 \ V_0[\text{Volts}] \ \text{cm}^{-3} \tag{4.3}$$

where C_2 and d are characteristic trap values (Eq. 2.15) and V_0 is the (applied) trapping potential. For typical electron trapping potentials ($\sim 10\ V$) the electron density is on the order of 10^7–10^8 cm^{-3}.

The space charge potential at the surface of the electron plasma is found by calculating the electric potential at the surface of the sphere. The radius of the plasma is given by

$$r = \left(\frac{3N_e}{4\pi n_e}\right)^{1/3} = .620 \left(\frac{N_e}{n_e[\text{cm}^{-3}]}\right)^{1/3} \ \text{cm} \tag{4.4}$$

where N_e is the number of trapped electrons. For $N_e \approx 3 \times 10^5$ electrons, r is on the order of 1 mm, and the space charge potential is

$$V_{sc} = \left(\frac{4}{3}\pi n_e N_e^2 e^3\right)^{1/3} = 2.32 \times 10^{-7} (n_e[\text{cm}^{-3}] N_e^2)^{1/3} \ \text{Volt.} \tag{4.5}$$

For typical numbers of electrons and trapping potentials, the space charge potential is on the order of 0.1–1 V.

The most important characteristic of a plasma is its Debye length λ_D, which

determines the length beyond which interparticle forces are screened by the other charges in the plasma. The Debye length is defined to be [79]

$$\lambda_D \equiv \left(\frac{k_B T_e}{4\pi e^2 n_e}\right)^{1/2} = 143 \left(\frac{T_e[\mathrm{K}]}{n_e[\mathrm{cm}^{-3}]}\right)^{1/2} \text{ cm.} \tag{4.6}$$

For these electron plasmas, λ_D is on the order of 10^{-2} cm, which is less than the spatial extent of the cloud for $N_e > 10^5$ electrons at a trapping potential of 10 V.

4.4.2 Electron Cooling Rate Equations

The process by which the protons cool in the electron cloud is modeled in terms of rate equations [80]. The protons are assumed to transfer their energy to the electrons with some characteristic time constant τ_{eq} in the equation [78]

$$\frac{dT_p}{dt} = -\frac{1}{\tau_{\mathrm{eq}}}(T_p - T_e) \tag{4.7}$$

where

$$\tau_{\mathrm{eq}} = \frac{3 m_p m_e}{8(2\pi)^{\frac{1}{2}} n_e e^4 \ln \Lambda} \left(\frac{k_B T_p}{m_p} + \frac{k_B T_e}{m_e}\right)^{3/2}. \tag{4.8}$$

The Coulomb logarithm ($\ln \Lambda$) is familiar from scattering theory, and is typically on the order of 10^1. The parameter Λ is the ratio of the maximum and minimum impact parameters $b_{\max}$ and $b_{\min}$ [39], and may be expressed [80]

$$\Lambda = \frac{4.130 \times 10^3}{\sqrt{n_e[\mathrm{cm}^{-3}]}} \sqrt{T_e[\mathrm{K}]} \left(T_e[\mathrm{K}] + \frac{T_p[\mathrm{K}]}{1836} + \frac{\sqrt{T_p[\mathrm{K}] T_e[\mathrm{K}]}}{21.43}\right). \tag{4.9}$$

Due to charge screening effects, the maximum impact parameter is the Debye length λ_D, and the minimum impact parameter is the distance of closest approach for particles of temperatures T_e and T_p.

Equation 4.7 would be sufficient to describe the cooling process if the number of cooling electrons were infinitely large; the temperature of a finite number of electrons, however, will increase as they are heated by the protons. A second rate equation is introduced under the assumption that this energy is equally distributed between all of the electrons [80]:

$$\frac{dT_e}{dt} = \frac{N_p}{N_e}\frac{1}{\tau_{\mathrm{eq}}}(T_p - T_e) - \frac{1}{\tau_c}(T_e - T_b) \tag{4.10}$$

where N_p and N_e refer to the numbers of protons and electrons, respectively, τ_c is the time constant for electron synchrotron radiation (0.1 sec), and T_b is the temperature of the environment (4.2 K).

A final modification to both Eqs. 4.7 and 4.10 takes into account the fact that the two clouds are not in constant contact with one another; for instance, an 80 eV proton will spend only $\approx 1\%$ of its orbital period within the electron cloud. Numerical integration of the coupled rate equations with this "duty" factor [43] yields a theoretical cooling time on the order of 1 sec for $N_e/N_p \sim 10^2$ (Fig. 4.15).

The model summarized here does not include the effect of an externally applied magnetic field, which (at low temperatures) is expected to decrease the coupling between the electron cyclotron and axial motions [70]. Moreover, the distribution of proton energies within the trap is unlikely to be Maxwellian, although this analysis has been used with some success to predict cooling behavior in other decidedly non-Maxwellian distributions [80, 81].

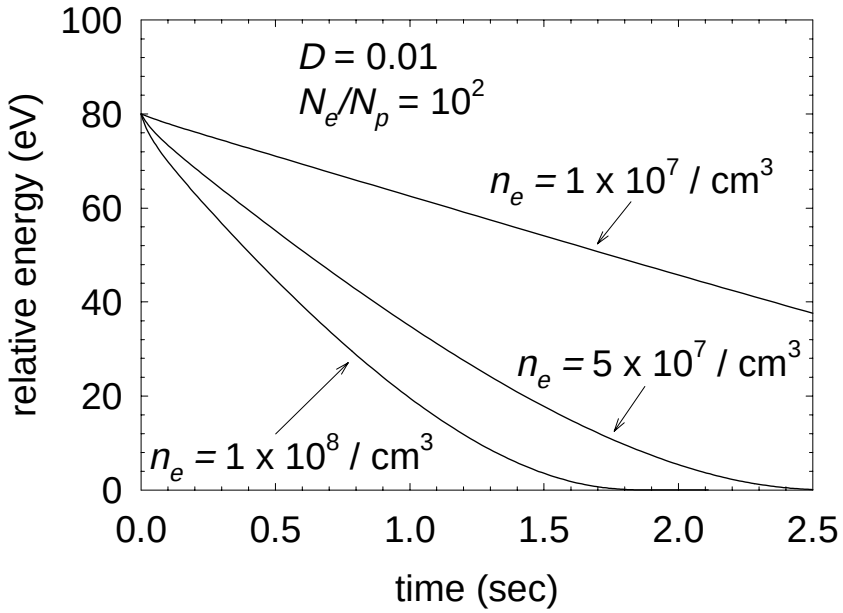

Figure 4.15: Calculated proton cooling as a function of time. The curves are for varying densities of electron clouds, with a fixed duty cycle (1%) and $N_e/N_p \sim 10^2$.

4.5 Conclusions and Future Directions

Electron cooling of protons is an encouraging step towards recombination. The nested Penning trap may also be used to study recombination and opposite-charge interactions in other systems, *e.g.*, in positive and negative ions, protonium, or positronium. The last may prove more difficult than the experiments reported here, primarily because the ability of the electrons to cool themselves into the side wells of the nested trap may prevent sufficiently long periods of plasma overlap for recombination to take place.

Experiments to pin down several features of the electron-cooling will reveal more about the role of the nested Penning trap as a vehicle for such recombination studies. Most critical is to understand the endpoint energy and width of the cooled protons in order to identify the contributing processes (such as high-Rydberg recombina-

tion and subsequent field-ionization, or collisional energy redistribution among the protons). Another important parameter is the electron cooling rate, particularly at short times ($t < 1$ sec), which may be measured by reducing the filter time constants and changing the injection procedure (*e.g.*, the injection and detection barriers need not be produced by the same electrode). By reducing the electrostatic trapping fields, high-Rydberg hydrogen produced during the proton-electron interaction may survive long enough to de-excite and be detected; a loss in the number of detected protons might provide a clue to the occurrence of this process. The apparatus has been designed to detect the Lyman photons from such recombination events; advantage has not yet been taken of these features. Finally, adding a laser to stimulate recombination will permit additional experiments to determine the optimum conditions for recombination. Such studies are already in progress.

Chapter 5

Positrons

Using merged plasmas to produce cold antihydrogen requires the accumulation of large numbers of cryogenic positrons under the extremely high vacuum conditions compatible with the trapping and storage of antiprotons. The accumulation technique described in this chapter improves upon an electronic damping method [4], in which 3.5×10^4 positrons were captured at rates up to 0.2 e^+/sec from a 10 mCi ^{22}Na source, by a factor of $\approx$ 150 (per unit of source activity). The new accumulator has captured one million positrons directly into a cylindrical, open-access Penning trap [38] at rates as high as 16 e^+/sec from a 5 mCi source. This trapping configuration is currently the most promising for the production of cold antihydrogen, and has already made possible the first simultaneous capture of positrons and antiprotons (Ch. 6).

5.1 Positrons: Source to Moderator

Positrons are emitted from a 5 mCi (185 MBq) ^{22}Na salt sealed within a titanium and tungsten capsule (Fig. 5.2) mounted above the trap vacuum enclosure (Fig. 5.3)

in the cold electronics region of the apparatus. [The apparatus (Fig. 5.1) is similar to that of Ch. 2, and some details are therefore deferred to Sec. 5.9.] ^{22}Na decays with a half-life of 2.6 years, emitting positrons in 90% of its disintegrations with kinetic energies up to 546 keV. An estimated 50% of the positrons are absorbed within the source material [82], and only 50–75% of the remainder (depending on the fraction scattered into the forward direction by the tungsten backing material in the source capsule) are expected to travel along the magnetic field lines in the direction of the trap vacuum enclosure. Up to 66% of the remaining positrons emerge from the source capsule through its 5 μm titanium exit window [83, 84].[1] The source capsule emits $(34 \pm 7) \times 10^6$ e^+/sec, therefore, corresponding to a positron current of 5.5 ± 1.5 pA.

The positron current leaving the capsule is measured with an electrometer as it strikes a brass chopper wheel located just above the trap vacuum enclosure. The wheel is rotated by a stepping motor (mounted at the brass hat, Fig. 5.4) to either block or admit the beam. A small fraction of the measured 5 pA current is expected to be due to the difference in secondary electron currents liberated from the source window and the chopper wheel by the incident positrons. (The secondary currents could not be easily measured due to the inability to prevent passage of low-energy electrons between the source and the wheel.)

A small additional reduction in the positron current occurs as the positrons approach the magnetic field center (where $B = 5.51$ Tesla) from their starting point at the source (where $B = 5.46$ Tesla). The positron cyclotron frequency is fast (154 GHz) compared to the rate of change of the magnetic field it experiences, and as a consequence the ratio $p_\perp^2/B$ is an adiabatic invariant (where $p_\perp$ is the momentum perpendicular to the magnetic field). Since the total momentum of an

[1] This effect was ignored in estimations of the positron current in the previous experiment [55].

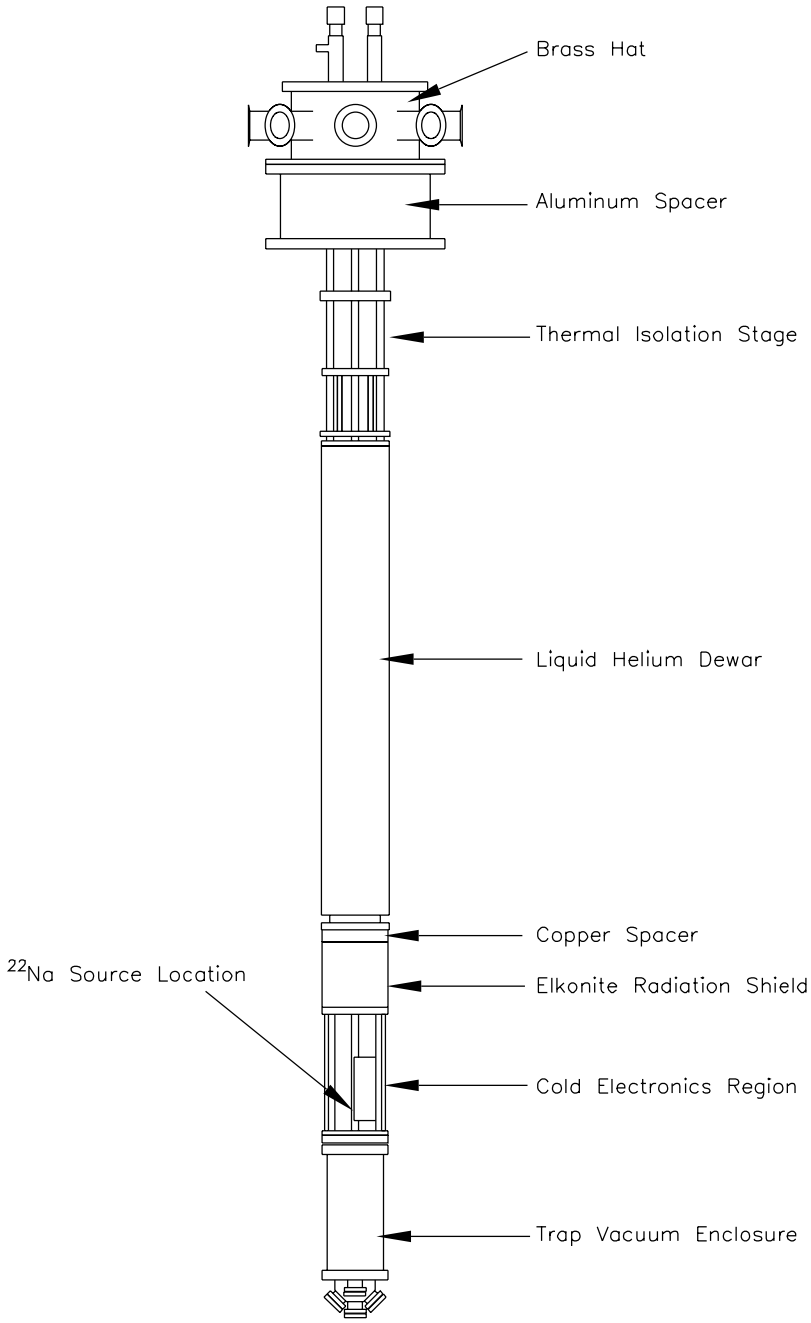

Figure 5.1: Positron trap apparatus. Note the similarities to Fig. 2.7.

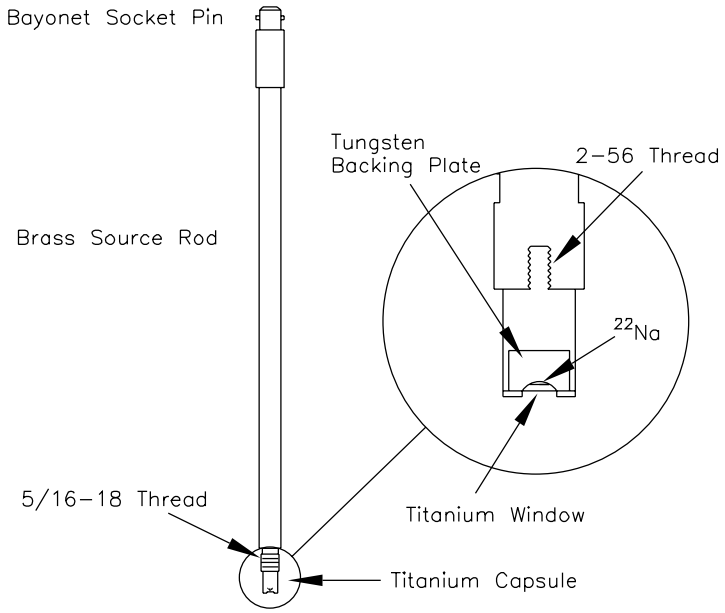

Figure 5.2: ^{22}Na source capsule. Inset: detail of capsule.

incident positron is conserved, its momentum parallel to the magnetic field ($p_{\|}$) must therefore decrease as B increases. A positron emitted at an angle greater than the critical angle θ_c, defined with respect to the magnetic field by

$$\sin\theta_c = \frac{p_{\|}}{p_{\perp}} = \sqrt{\frac{5.46}{5.51}}, \tag{5.1}$$

does not have enough $p_{\|}$ to supply the requisite increase in $p_{\perp}$ and is "bounced" back to the source — an effect which reduces the number of positrons which strike the moderator by a factor of $(1 - \cos\theta_c)$. For the field magnitudes considered here, at least 90% of the positrons emerging from the source capsule can attain the field maximum. (This is actually a lower limit, since positrons emitted at larger angles are preferentially absorbed in the source material and the titanium exit window and do not survive to be bounced.)

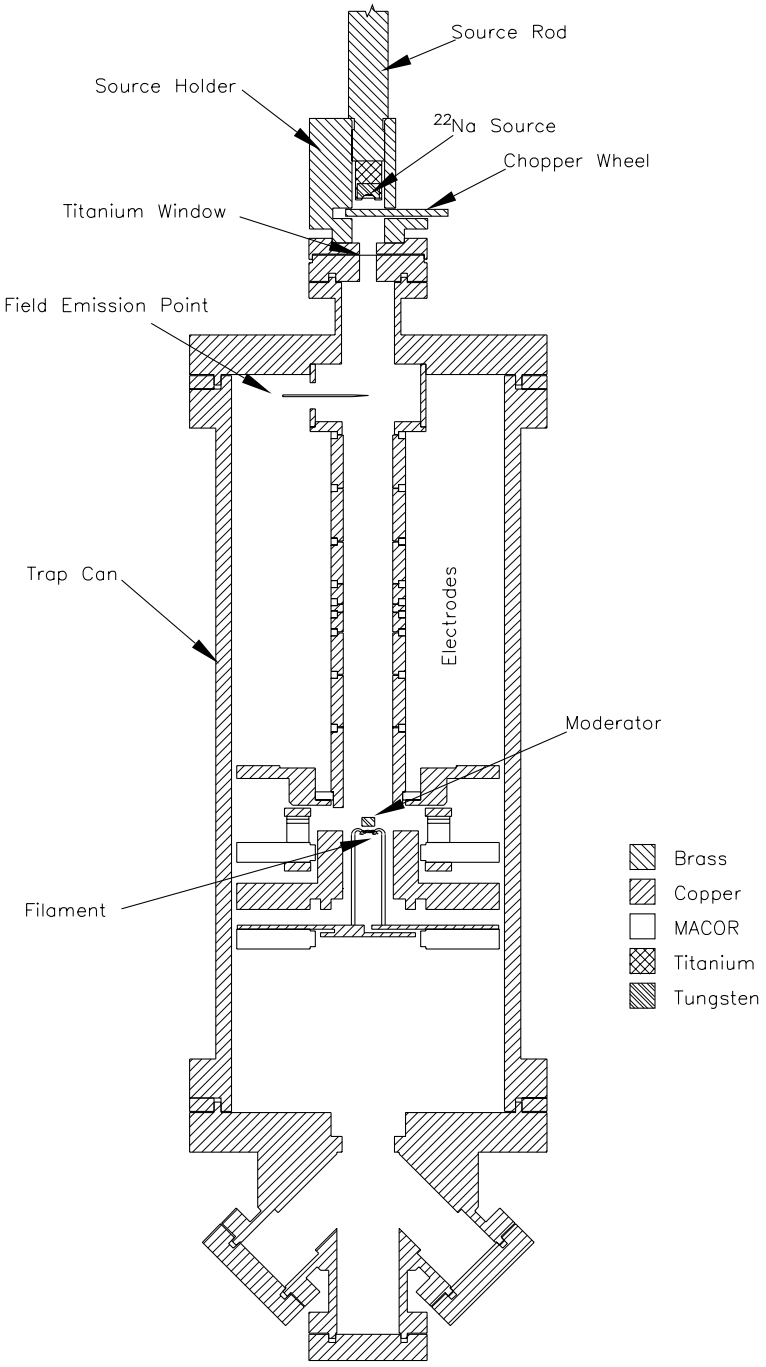

Figure 5.3: Trap vacuum enclosure for the reflection-moderated positron accumulator. Positrons travel from the ^{22}Na source to the moderator along the axis of the trap.

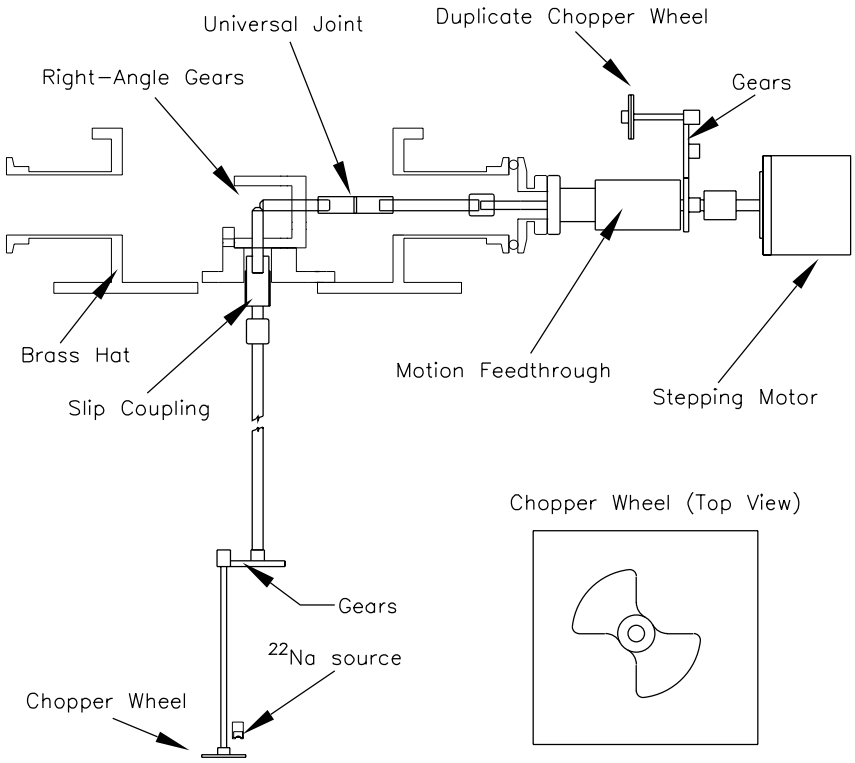

Figure 5.4: Positron beam chopper system (not to scale).

Approximately 34% of the positrons which survive the magnetic bounce are absorbed in the 10 μm titanium entrance window at the top of the trap vacuum enclosure (neglecting shifts in the kinetic energy spectrum resulting from their passage through the source exit window). A positron current of only 3 pA is therefore expected to pass into the trap enclosure to strike the moderator — or about 1 of every 10 positrons created in the decay of the ^{22}Na source.

The positron current on the moderator is measured directly with an electrometer, or by rotating the chopper wheel at ≈ 1 Hz and detecting the resulting time-dependent signal with an FFT spectrum analyzer or lockin amplifier. All three techniques agree to within 10%. By appropriately biasing the trap electrodes, the measured current is further distinguished into an incident positron current from

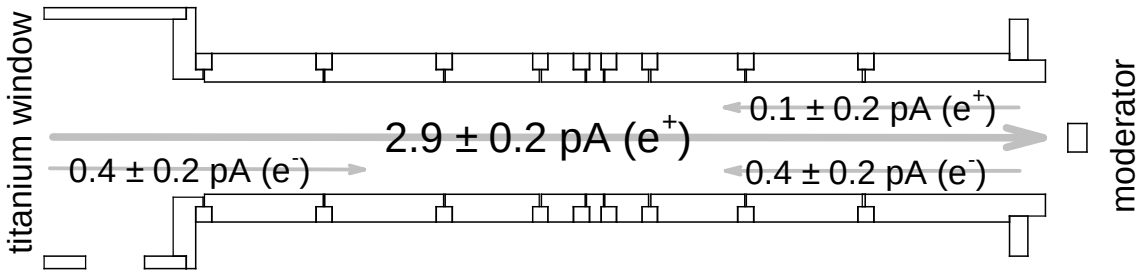

Figure 5.5: Measured positron and electron currents inside the trapping region (schematic). The secondary currents shown are for particles with energy below ≈ 8 eV.

the source, a backscattered/moderated positron current from the moderator (at energies below ≈ 8 eV), and two secondary electron currents from the moderator and the titanium entrance window, respectively (also at energies below ≈ 8 eV). These currents are summarized (schematically) in Fig. 5.5. The primary positron beam current (2.9 ± 0.2 pA) is in good agreement with the estimates of this section. Smaller secondary electron currents that nearly cancel are liberated from both the moderator and the titanium window, but a backscattered positron current cannot be resolved.

5.2 Trapping Positrons: Reflection Moderator

A tungsten (100) positron moderator is used to slow the high-energy positrons from the radioactive source and emit a fraction ($< 1\%$) back into the vacuum [85] with a narrow distribution of energies centered about the positron workfunction of the material (typically a few eV) [86]. Positronium (Ps) atoms are also formed as escaping positrons pick up electrons from the moderator surface [87, 88]. Once free of the surface, the positrons (and positronium atoms) encounter the electrostatic fields produced by the open-access, cylindrical trap electrodes [38], shown in

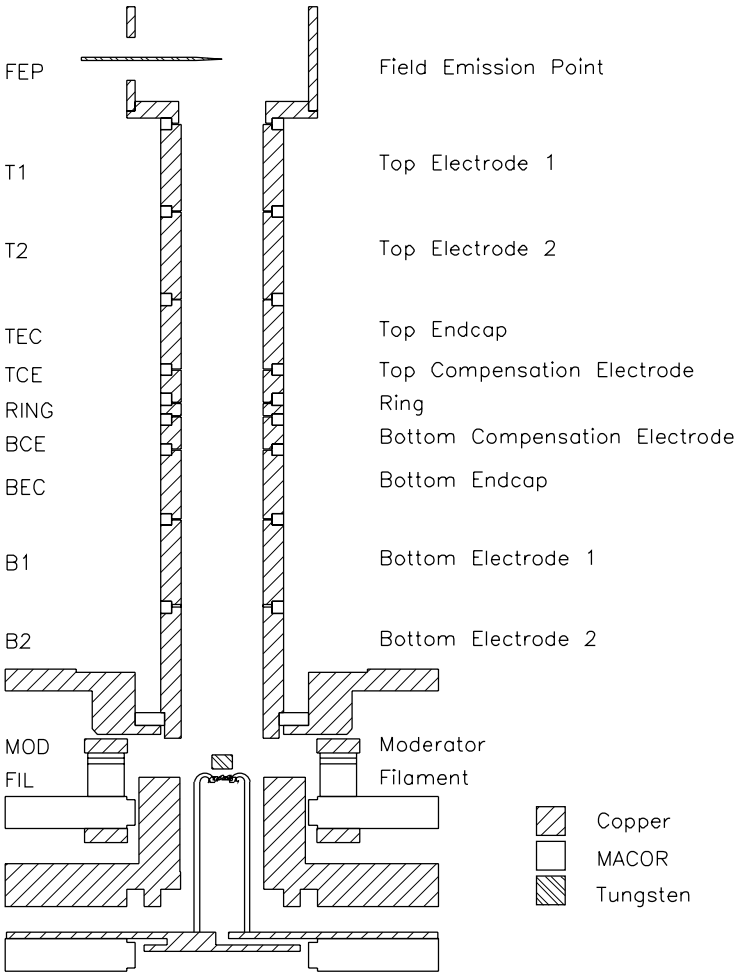

Figure 5.6: Electrodes for the reflection-moderated positron accumulator.

Fig. 5.6. Unlike the closed-surface hyperbolic electrodes of the previous accumulator [4], this electrode configuration is particularly well-suited to opposite-charge interaction studies [1] and antiproton trapping [2].

The accumulator was originally designed to trap moderated positrons as they collided with (and transferred their axial energy to) an electron plasma stored on one of the trap electrodes. The observed trapping occurred at rates exceeding the expected 0.7 e^+/sec by more than a factor of 10, however, and continued with-

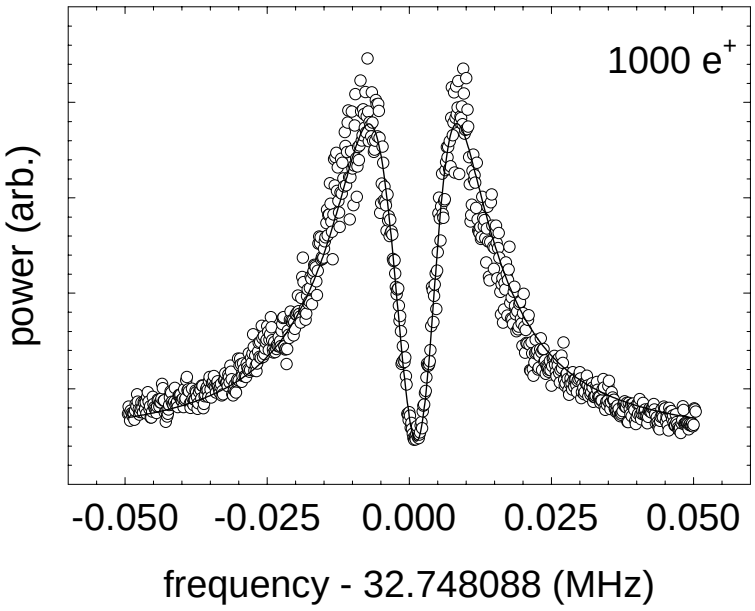

Figure 5.7: First positrons trapped in the accumulator. The initial trapping rate exceeded that of the earlier cryogenic accumulator [4] by more than an order of magnitude.

out noticeable decrease in the *absence* of cooling electrons. Investigations of the actual trapping mechanism were abbreviated in the race to bring a combined positron/antiproton trap online before the permanent closing of the low-energy antiproton facility (LEAR) at the end of 1996. Nevertheless, an understanding has emerged which points towards positron trapping through field-ionization of highly-excited positronium atoms produced at or near the moderator surface.

The positron accumulation rate is measured as a function of the applied electrode voltages in order to characterize the trapping mechanism. The procedure begins by blocking the positron beam and emptying the trap of all charged particles. The electrode voltages at which the trapping rate is to be measured are then established and the positron beam unblocked for a short time (typically 300 sec). Noise (from DC to 1 MHz) is applied to one of the trap electrodes to drive the axial frequencies

of positive ions, preventing them from becoming trapped with the positrons. At the end of the accumulation time the beam is once again blocked, the noise drive turned off, and the trapped positrons transferred to the harmonic trapping region for magnetron cooling and counting. The process is subsequently repeated under computer control for various configurations of the electrode potentials.

An example of this procedure is shown in Fig. 5.8. The electrode potentials are illustrated in Fig. 5.8(b), where the range of moderator (MOD) potentials examined (0–12 V) is indicated by the diverging lines at the right edge of the graph. Positrons collected on the B1 electrode are moved to the harmonic trapping region, cooled, and counted, yielding the trapping rate as a function of the MOD bias [Fig. 5.8(c)]. The variation implies that positrons slowed by the moderator are essential to the loading process. (Error bars are approximately the size of the points, as discussed in Sec. 5.9.4 on p. 165.)

A remarkable symmetry exists between the trapping rates for electrons (liberated by the positron beam) and positrons when the electrode potentials are inverted (*i.e.*, $V \rightarrow -V$). Figure 5.9 shows that the peak electron trapping rates are nearly identical to those for positrons. The observed phenomena suggest a trapping mechanism involving the inherent electron-positron symmetry of (highly-excited) positronium, ionized by the electrostatic trapping fields with subsequent capture of the positron (or electron) by the trap.

Figure 5.10 depicts a trajectory calculation for an excited positronium atom which yields its positron to the trap after being field-ionized. (The small radial component of the electric field is omitted from these calculations.) The simulation demonstrates that such a process *could* yield trapped positrons, and also reveals that the trapping occurs over a wide range of excited Ps states.

Positrons liberated by the field-ionization of excited positronium will not be

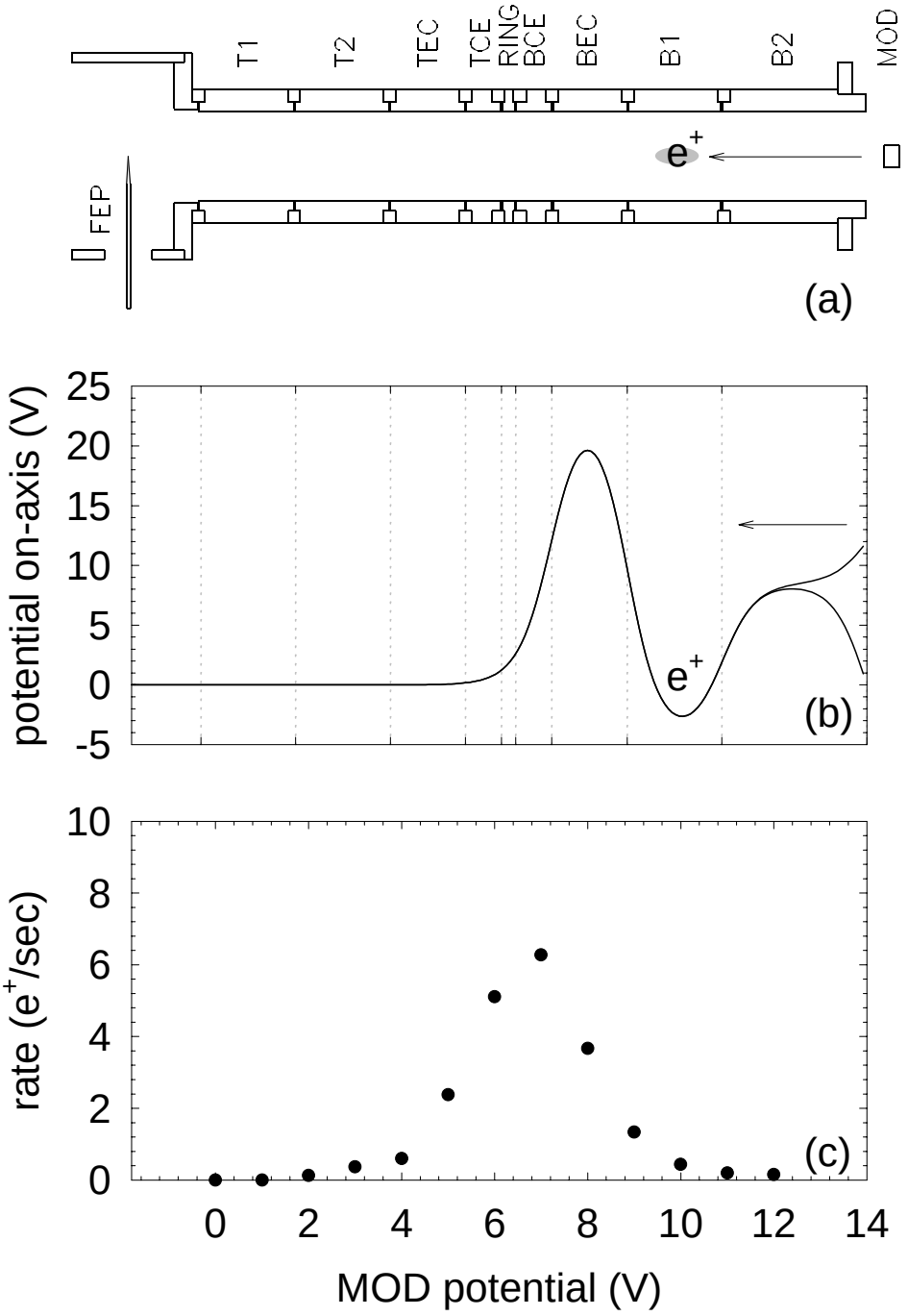

Figure 5.8: Positron trapping rate as a function of the MOD bias. (a) Trap electrodes. The MOD bias is varied between the limits indicated in (b), and the trapping rate is shown in (c). Error bars are approximately the size of the points.

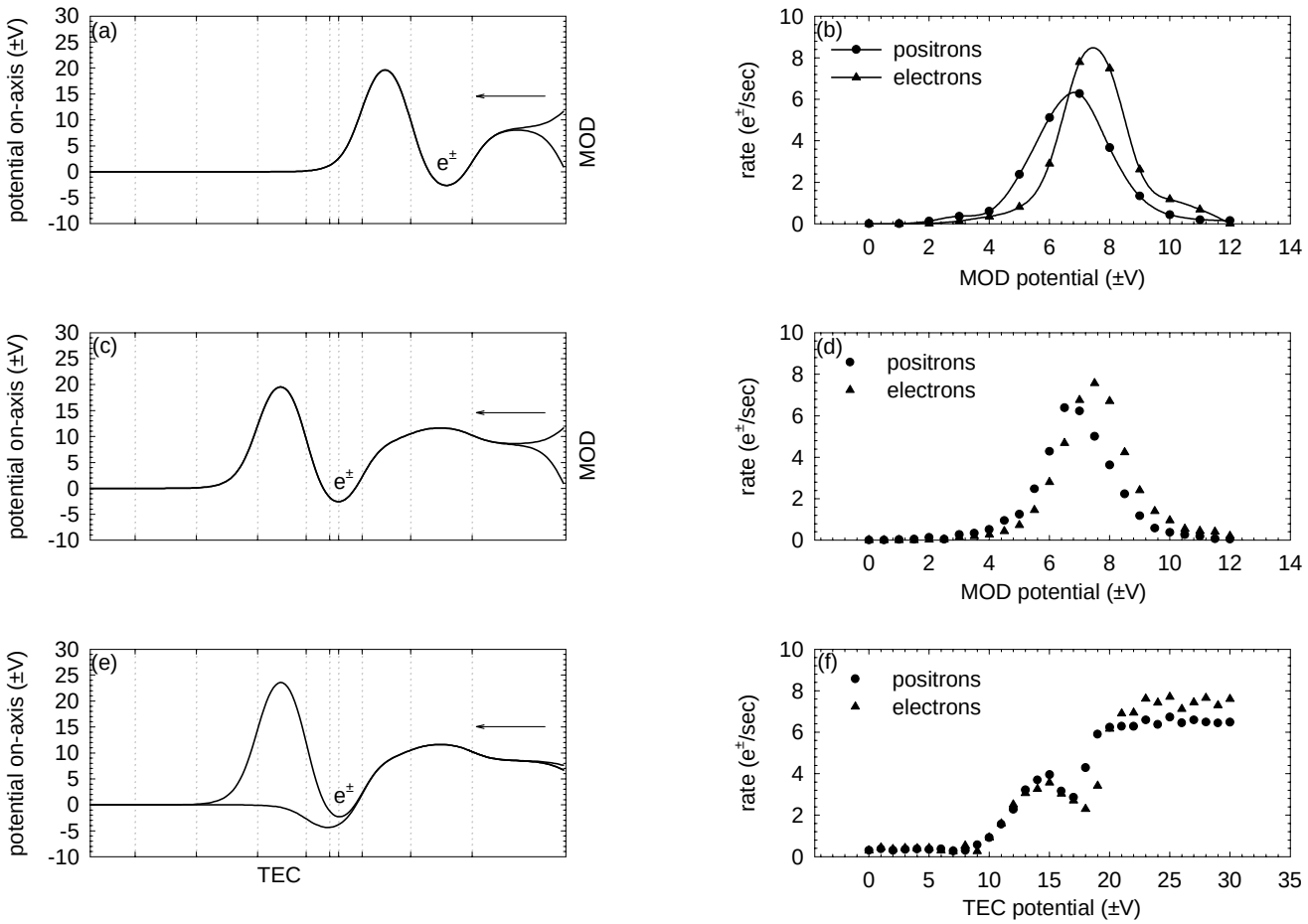

Figure 5.9: Symmetry in trapping rates for electrons and positrons suggests a process involving positronium. [In (e)–(f), the map is taken at the moderator potential with the highest trapping rate, *i.e.*, $V_{\mathrm{MOD}} = -7.5$ V. The curves in (b) are intended to aid the eye.]

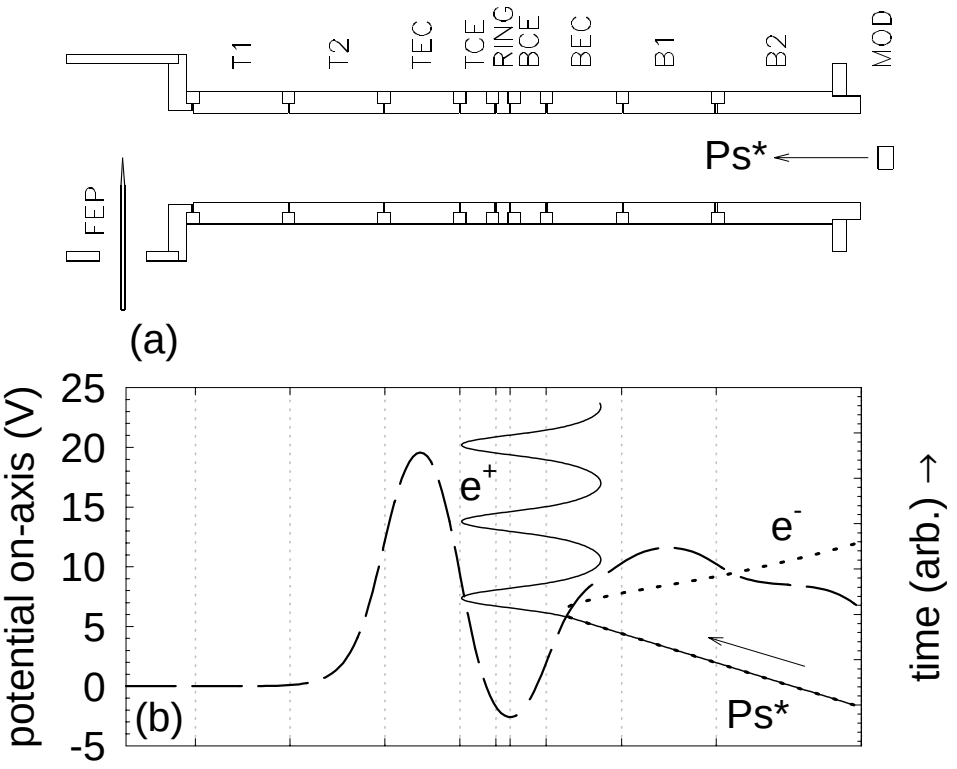

Figure 5.10: A numerical simulation of the field-ionization of a positronium atom, leading to a trapped positron. (a) Trap electrodes. (b) The highly-excited positronium is field-ionized as it reaches the relatively high fields inside the trapping region. Inverting the trapping potentials ($V \rightarrow -V$) leads to a trapped electron. (The pair is started with a separation of 7×10^{-5} cm, and each has 2 eV of kinetic energy along the axis of the trap.)

trapped if the atom is ionized outside of the trapping region. The trapping rate is therefore expected to decline if the moderator bias is significantly different from that of the adjoining (B2) electrode ($V_{\mathrm{B2}} \approx 8$ V), qualitatively matching the observed dependence in Fig. 5.8. The peak trapping rate does not occur precisely as the local field vanishes (*i.e.*, for $V_{\mathrm{MOD}} \approx V_{\mathrm{B2}}$), however, suggesting that a small field near the moderator may serve to enhance the production of highly-excited positronium. (Positronium production possibilities are discussed below.)

Additional experiments confirm that the highest trapping rates occur when the MOD potential tracks the potential on the adjacent B2 electrode, rather than the height of a potential barrier interposed between the moderator and the trapping region (Fig. 5.11). The barrier height is varied over a range exceeding 5 V, whereas the highest trapping rate remains unchanged at $V_{\mathrm{MOD}} \approx 6.5$ V. This behavior is rather surprising if charged particles alone are responsible for the trapping, since it is unlikely that a process leading to trapped positrons which involves charged particles (such as positron-electron or positron-atom collisions) is sensitive to the potentials near the moderator but not to the potentials near the trapping region.

A close examination of Figs. 5.11(c) and (e) reveals that positrons are trapped at high rates even if the barrier prevents all workfunction-emitted positrons (below ≈ 4 eV from an oxidized tungsten surface [89]) from entering the trapping region! Since positrons which cannot enter the trapping region cannot be trapped, this observation supports a trapping mechanism which does not explicitly involve moderated positrons.

The positronium field-ionization hypothesis explains the reduction in the trapping rate which occurs in the potential configuration shown in Fig. 5.11(e) compared to that of Fig. 5.11(c). The key lies in the magnitude of the electric field at the entrance to the trapping region (Fig. 5.12), not in the height of the barrier (as might

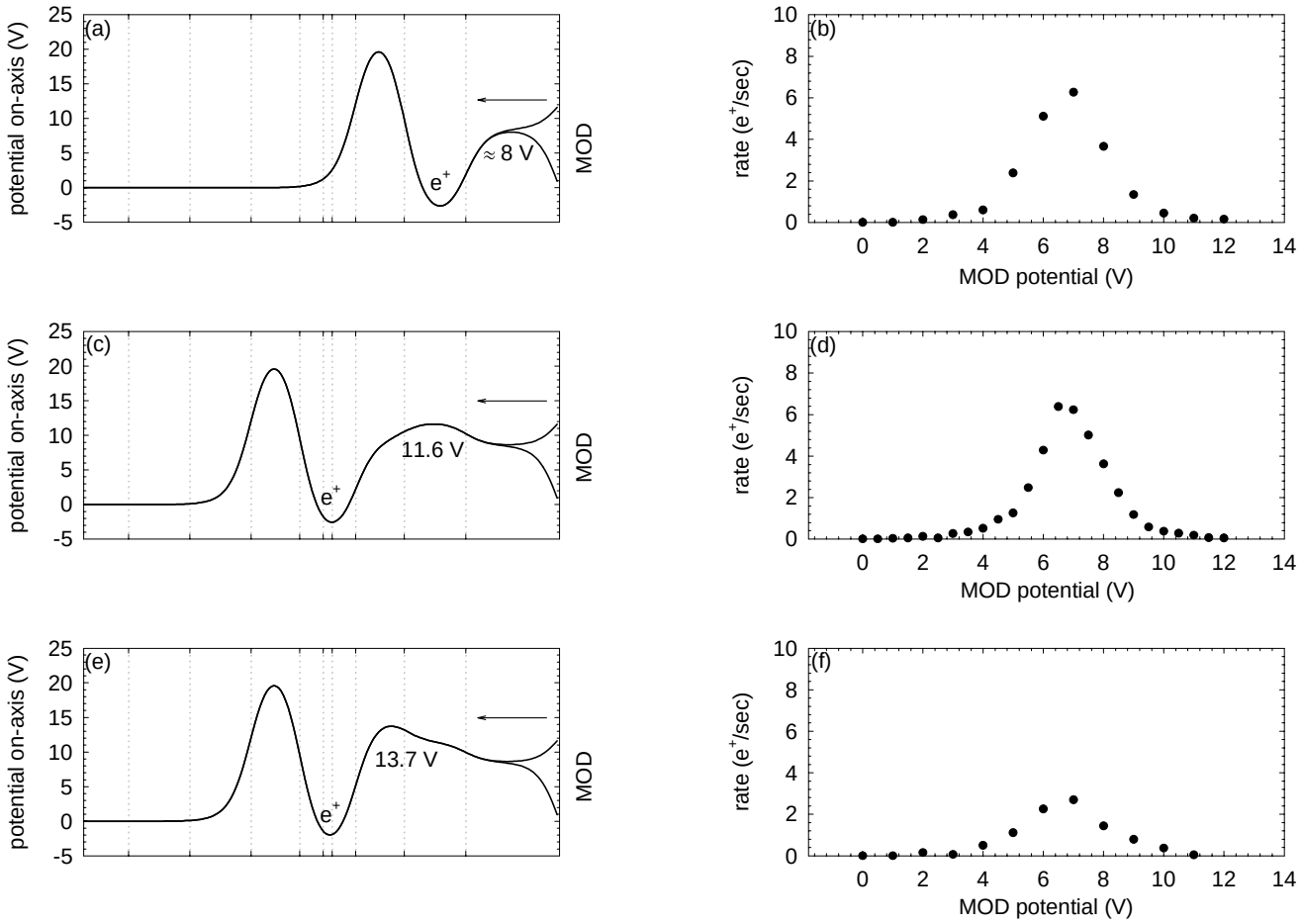

Figure 5.11: The moderator bias which produces the peak trapping rate is independent of the height of the potential barrier between the moderator and the trapping region. This lack of dependence suggests that charged particles are not exclusively responsible for the trapping mechanism.

be imagined for charged particles). The electric fields produced by the electrodes are higher at the entrance of the trap in (e) as opposed to (c), and thus positrons stripped from their parent atoms by these fields will be less tightly bound in the potential wells. If the kinetic energy of the liberated positron is greater than the depth of the well at which the atom is ionized, the positron will not be trapped at all. To trap more higher-energy positrons, therefore, the fields must be minimized at the entrance of the trapping region and increased only after the depth of the well is greater than the kinetic energies of the liberated positrons.

A "phase space" summarizing the ability of the potentials and fields of the trapping region to ionize and capture highly-excited positronium atoms is identified by plotting the depth of the trapping well as a function of the first instance of the increasing electric field magnitude encountered by an atom incident from the moderator surface. The phase space for the the two trapping configurations considered above is shown in Fig. 5.13; the plots reveal the space of (c) is larger than that of (e), and includes a region corresponding to excited positronium atoms with higher kinetic energies (denoted by the arrows). A distribution of atoms from the moderator corresponding to this region explains the reduced trapping rate of configuration (e). Figure 5.14 illustrates this point in a trajectory calculation of a positronium atom which, under the same initial conditions as Fig. 5.10, does not yield a bound positron in the trapping configuration of Fig. 5.11(e).

Information about the distribution of excited positronium atoms emitted from the moderator is obtained by varying the depth of the trapping region (Fig. 5.15). The largest phase space is occupied by the deepest well configuration [Fig. 5.16(a)], which possesses a reduced trapping rate. Sections of the remaining trapping configurations project into the region unclaimed by (a) and have much higher trapping rates [with the exception of (e), which occupies a very small region and has a dra-

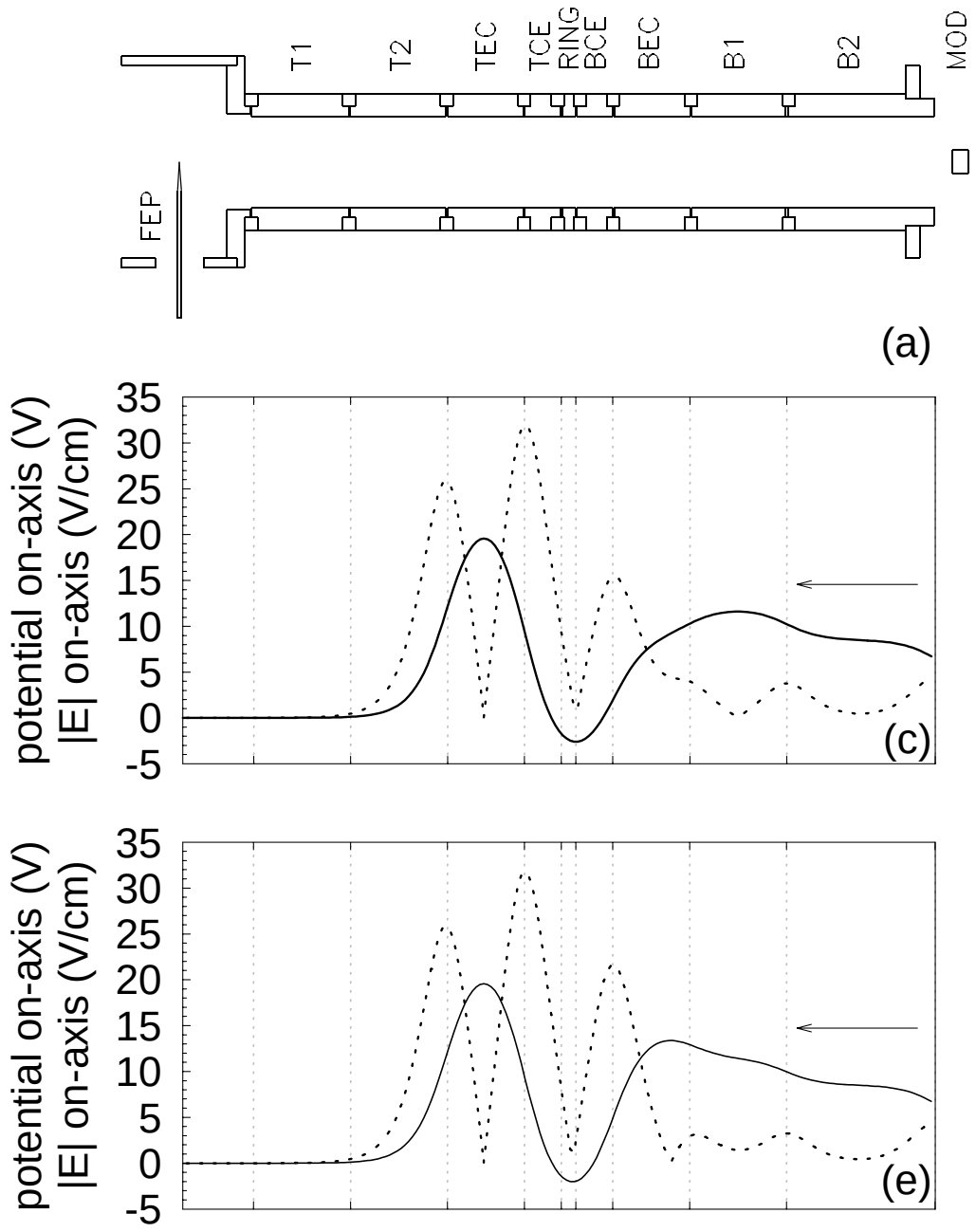

Figure 5.12: Electric potentials (solid lines) and field magnitudes (dashed lines) for two trapping configurations. The configuration shown in (c) accumulates positrons at a higher rate than (e) by reducing the ionizing fields at the entrance to the trapping region, ionizing positronium deeper within the well.

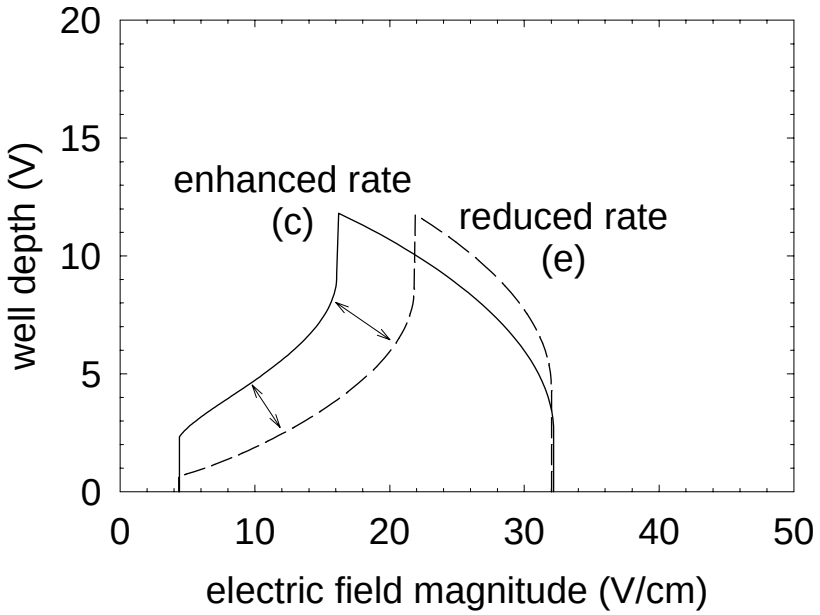

Figure 5.13: Depth of the potential well in which positrons are captured as a function of the first instance of each field magnitude experienced by a positronium atom originating at the moderator. These two plots correspond to the moderator potentials at which the trapping rate is highest in Figs. 5.11(c) and (e). Configuration (c) can trap more highly-excited, higher-energy positronium (region indicated by double arrows) than (e), which has a reduced trapping rate.

matically reduced trapping rate]. The trapping dependences are consistent with a distribution of positronium atoms which inhabits in the region indicated in Fig. 5.16.

In certain circumstances the electron trapping rate is much higher than the positron trapping rate under voltage inversion. For example, electrons are also trapped in the potential "hill" produced by the B2 electrode potential (Fig. 5.17). Positrons are not observed to trap at these high rates when the potentials are inverted, indicating that here (at least) a different mechanism — probably electron-electron collisions, since all secondaries are energetically capable of entering the B2 trapping region — is at work. (The positron trapping rate on the B1 electrode does not change appreciably when the electrons accumulated on the B2 electrode are dumped

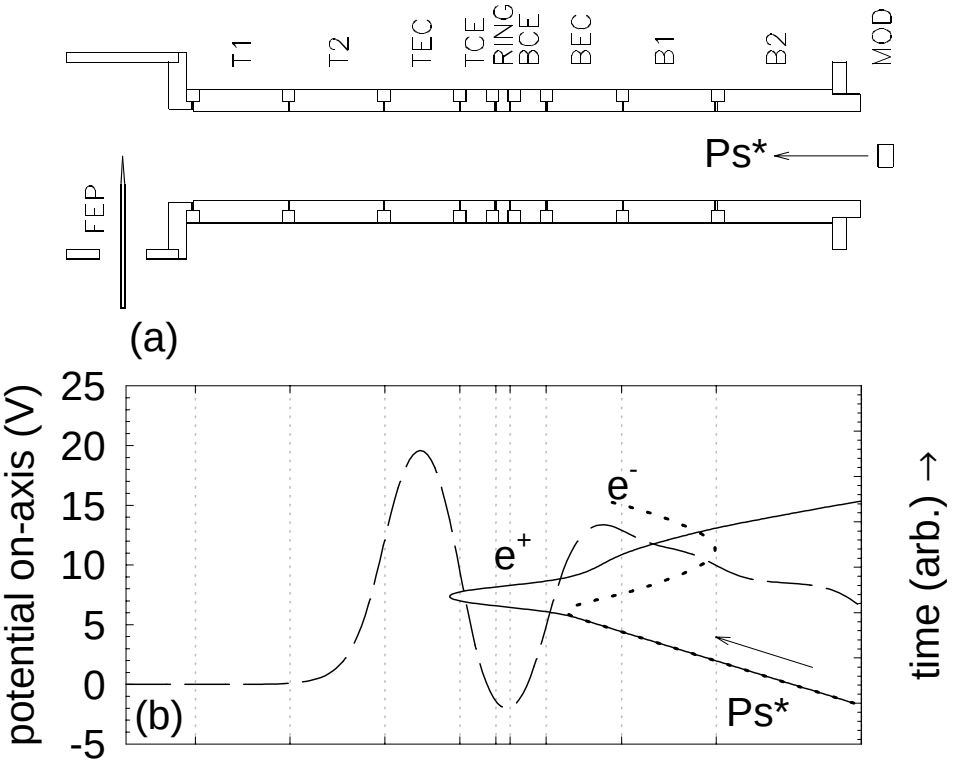

Figure 5.14: A numerical simulation of a field-ionized positronium atom in which the positron is not trapped. The positronium atom is started with the same initial conditions as that in Fig. 5.10; in this case, the trapping field ionizes the atom too high in the well for the $\approx$ 2 eV positron to remain bound. (Notice that in this case the electron remains trapped in the nearby well.)

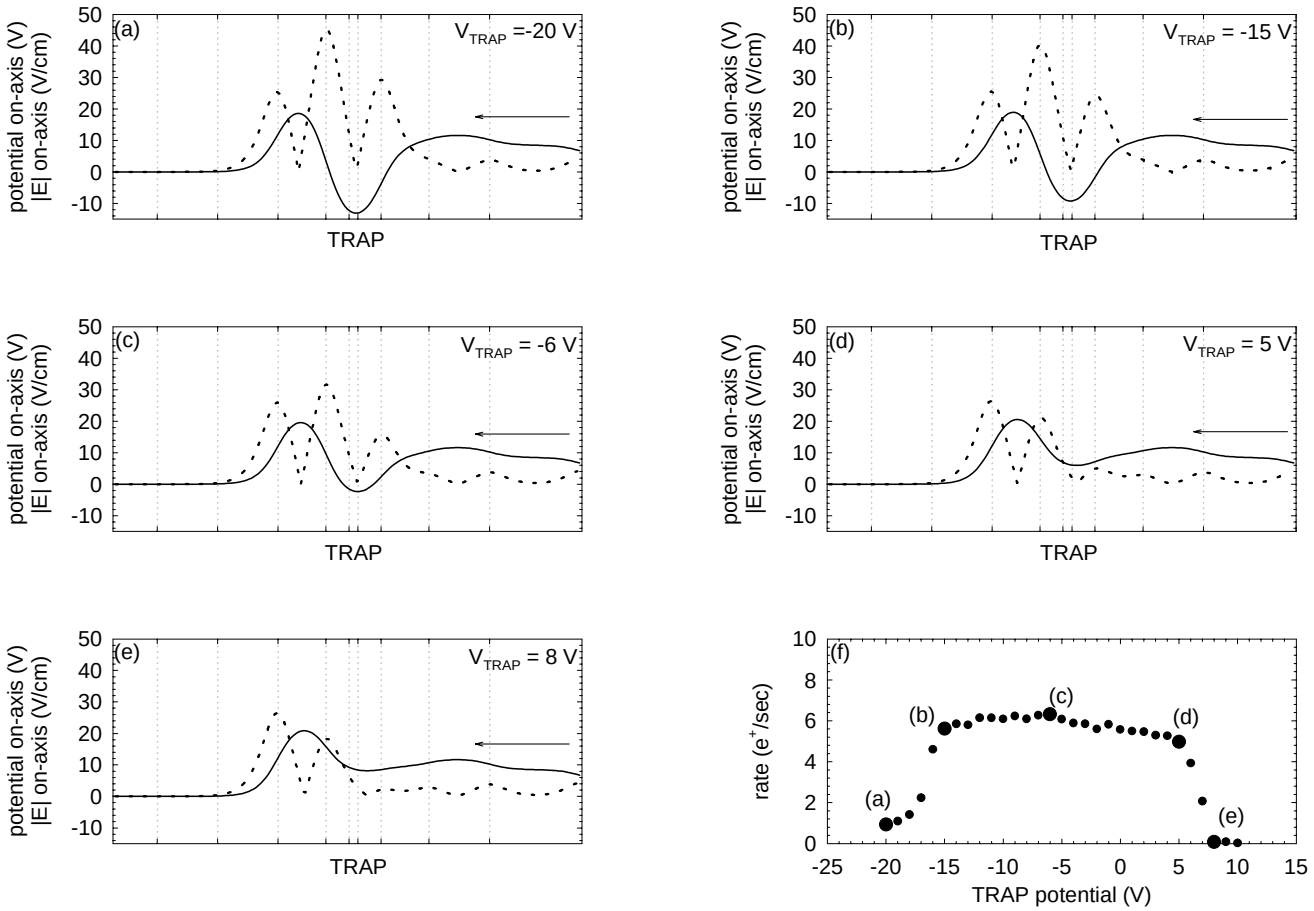

Figure 5.15: Positron trapping rate as a function of the depth of the trap. The map is shown in (f), and the potentials (solid lines) and the magnitudes of the electric field (dashed lines) at the highlighted points are shown in (a)-(e). The trapping rate diminishes for both very shallow and very deep wells, and is insensitive to well depth in between.

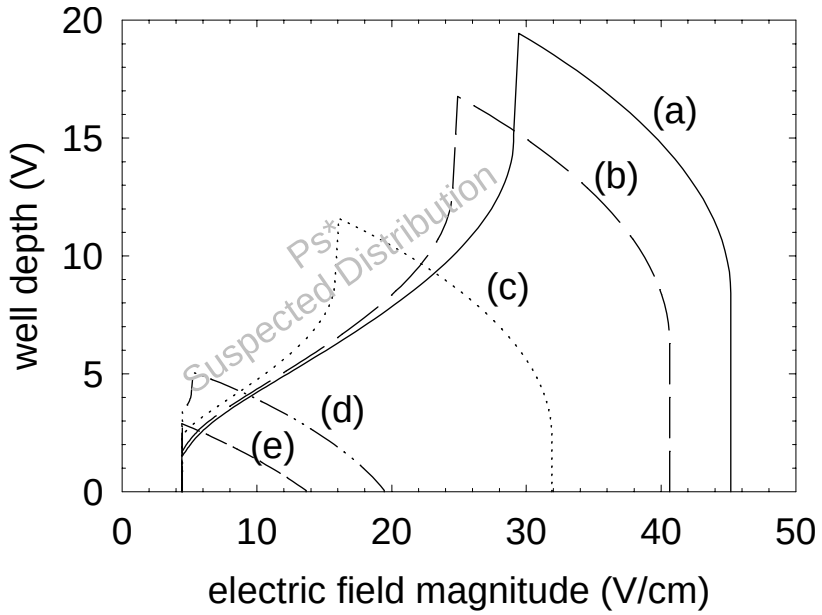

Figure 5.16: Trappable positronium phase as a function of the depth of the trap. These plots accompany Fig. 5.15.

to the moderator at periodic intervals.)

Other rate dependences present puzzling features which appear to be superimposed upon the general dependences predicted by the field-ionization hypothesis, such as that seen illustrated in Fig. 5.18(f) and its accompanying phase space plot, Fig. 5.19. As the potential on the TEC electrode is increased from 0 V, both the phase space and the trapping rate increase. Between (c) and (d), however, the phase space increases but the trapping rate declines, suggesting that a competing process is preventing the positrons from becoming (or remaining) trapped. Other dependences in different electrode configurations demonstrate similar anomalies [*e.g.*, Fig. 5.28(b)], indicating that there remain subtleties which are not addressed by the positronium field-ionization hypothesis.

A less well-understood aspect of the field-ionization hypothesis is its unusual

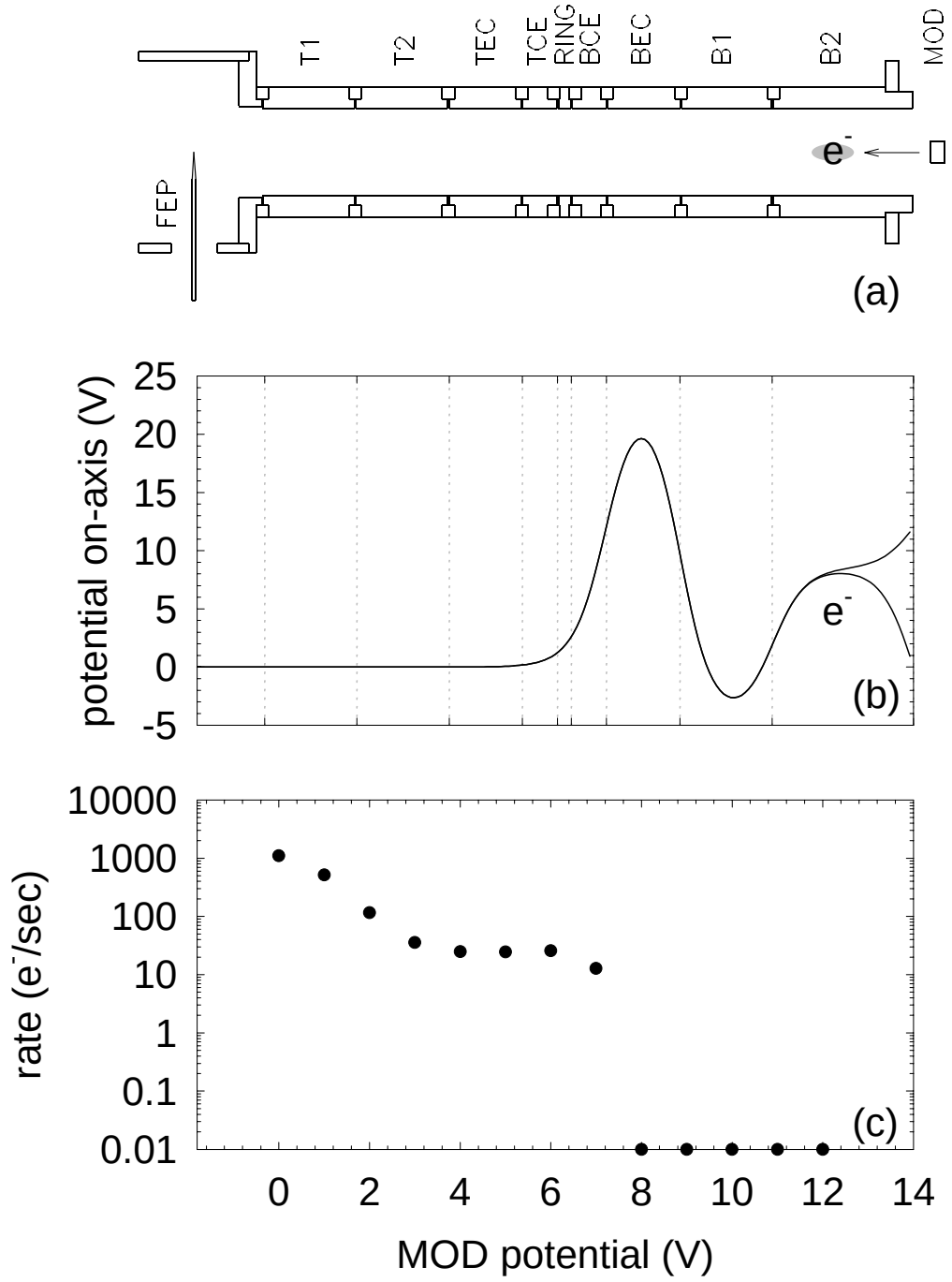

Figure 5.17: Electron trapping rate on the B2 electrode as a function of moderator bias. Positrons are *not* observed to trap at these high rates when the potentials are inverted.

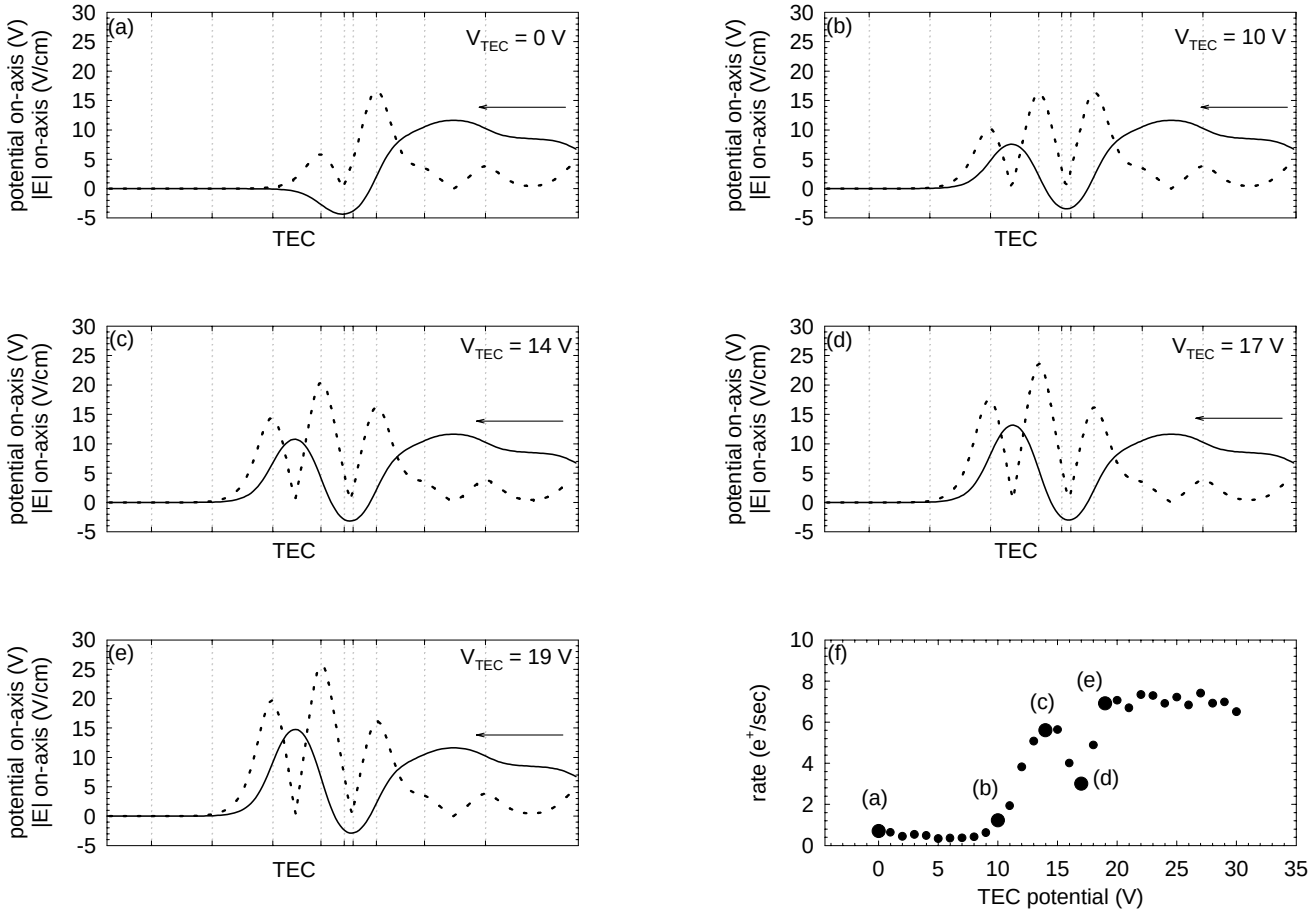

Figure 5.18: Positron trapping rate as a function of the potential applied to the TEC electrode (f). The potentials (solid lines) and the magnitudes of the electric field (dashed lines) at the highlighted points are shown in (a)-(e). Note the reduction in the trapping rate at (d).

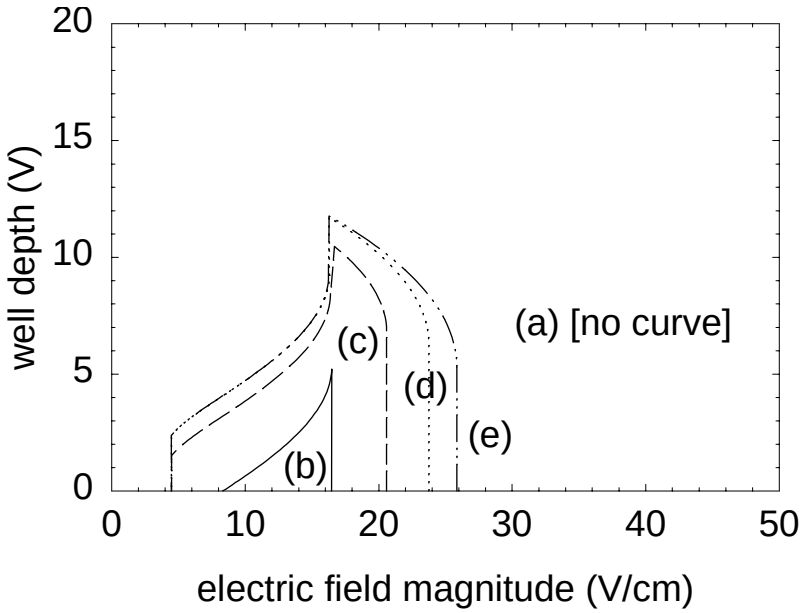

Figure 5.19: Trappable positronium phase as a function of the potential applied to the TEC electrode. Although the phase space increases monotonically with the TEC potential, at point (d) the trapping rate declines. (These plots accompany Fig. 5.18.)

requirement of a source of highly-excited positronium atoms. One possibility is that positronium is produced away from the surface of the moderator by recombination of a (workfunction- or epithermally-emitted) positron and its associated secondary electrons. The particles are correlated in both time and space, and the magnetic field maintains this proximity by constraining the particles to orbits about field lines. Recombination (or pickup) may be assisted by the electrostatic fields produced by the electrodes or by a three-body process, if permitted by the density of the field-correlated electron swarm.

Positronium is known to be produced by thermal positrons at the moderator

surface if its formation potential $\epsilon_{\rm Ps}$, defined by [86]

$$\epsilon_{\rm Ps} = \varphi_+ + \varphi_- - \frac{E_{\rm Ps}}{n^2}, \tag{5.2}$$

is negative (where φ_+ and φ_- are the positron and electron workfunctions, respectively, $E_{\rm Ps} = 6.8$ eV is the positronium Rydberg, and n is the quantum level at which the positronium is produced). Highly-excited Ps from thermal positrons is excluded since no material has been conclusively identified for which $\epsilon_{\rm Ps} < 0$ when $n > 1$ [90]. Epithermal or backscattered positrons [91], however, may pick up an electron to form an excited state of positronium, in which case φ_+ in Eq. 5.2 is replaced with the kinetic energy of the positron. Excited-state ($n = 2$) positronium has been observed from both uncleaned [92] and cleaned [93] surfaces at fractions near 10^{-2}–10^{-4} of the number of incident low-energy positrons [92]. States higher than $n = 2$ have not been observed but are expected at rates which scale as n^{-3} [94], becoming almost vanishingly small for the easily-ionizable $n > 100$.

Other mechanisms which account for the observed trapping dependences are difficult to identify. The most obvious of these, a bad vacuum, is easily ruled out. Under the extreme assumption that *every* collision between a positron and a background gas atom (*e.g.*, helium) results in a trapped positron, the background gas pressure required is

$$P = 1.02 \times 10^{-18}\ \frac{R[e^+/\text{sec}]\, T[\text{K}]}{I[e^+/\text{sec}]\, \sigma_{\rm tot}[\text{cm}^2]\, \ell[\text{cm}]}\ \text{Torr} \tag{5.3}$$

where $R = 10\ e^+$/sec is the trapping rate, $I \approx 2 \times 10^4\ e^+$/sec is an estimate of the low-energy positron current entering the trapping region, $\sigma_{\rm tot} \approx 5 \times 10^{-16}$ cm^2 is the maximum *total* cross-section for positrons on helium at low energies [95],

and $\ell \approx 4$ cm is the length of the interaction region. Inserting these values gives $P \approx 10^{-6}$ Torr — certainly much higher than the pressure inside the trap vacuum enclosure (measured in a similar apparatus to be less than 5×10^{-17} Torr [42, 43]). Moreover, the lifetime of trapped positrons (at 4 K) in 10^{-6} Torr of helium is only a few minutes (Sec. 5.5.3), contradicting the observed lifetime (with the positron beam on) of at least several days (Sec. 5.5.1).

A high background gas pressure is also expected to lead to the trapping of ions inside the positron plasma. The sensitivity of positron clouds to ions has not yet been thoroughly studied, but the intentional addition of 10 protons to a cloud of several hundred positrons is observed to disrupt the positron axial signal entirely. The telltale signs of ion contamination (*e.g.*, weak or nonexistent "dip," and erratic sideband cooling responses) are rarely observed (even when the anti-ion drive is not applied), suggesting that ions are not a major contributor to the loading mechanism.

Even though positronium could be collisionally-ionized inside the trapping region (presumably by a secondary electron or positron), the particle densities and energies suggest that this would be an uncommon occurrence. The synchrotron-radiation time constant $\tau_c \approx 0.1$ sec is much longer than the time it takes a positron to pass through the trapping region, and it is therefore unlikely that the particle could become bound even if axial energy could be freely exchanged with cyclotron energy and radiated away. Similarly, the positron axial damping rate, even if well-coupled to the electron axial tuned circuit, could not permit significant energy losses in a single pass through the trapping region. (Trapping also occurs at equally high rates in regions far from any tuned circuit.)

The field-ionization of positronium and subsequent capture of the liberated positron by the trap is currently the best candidate for the trapping mechanism. The source of the excited positronium atoms, and additional subtleties in the trapping

dependences, remain to be explained. The present understanding permits some optimizations, however, which will be discussed in subsequent sections.

5.3 Heating the Moderator

Another set of experiments attempted to determine the trapping dependence on the conditions of the moderator surface. In order to clean the moderator surface of adsorbed gases it must be heated to high temperatures — a demanding technical challenge in the 4 K, 6 Tesla environment of the trap. Use of an expensive field-emission point array heated the moderator effectively but had a lifetime too short to be practical [55], so a cheaper alternative was identified: a light-bulb filament.[2] The filament is driven by a 6 kHz current since the strong magnetic field exerts powerful torques on the current loop which cause it to fracture at lower frequencies.

In a first test, the moderator was heated to approximately 550 K (as measured by a thermocouple junction) and held there for 30 sec; it was then allowed to cool back to 4 K. As a result, the positron trapping rate decreases and shifts slightly (Fig. 5.20). These changes could be explained by a removal of some of the adsorbed gases critical to the production of highly-excited positronium, or the charging of an insulating overlayer on the moderator surface by the electrons from the filament (although the filament is on the wrong side of the moderator to effectively charge the front surface). The surface was not likely to have been appreciably cleaned at the low temperatures achieved. (Heating to higher temperatures to desorb additional contaminants was prevented by the failure of the filament.)

The trapping rate and dependences are, to a large degree, restored after thermally cycling the apparatus to room temperature and back to 4 K (without re-

[2] Best results were found with a 100 W light-bulb.

pumping the trap vacuum enclosure), as seen in the third trace of these figures. The surface changes induced by the filament (*e.g.*, reduction of surface contaminants or surface charging) are apparently undone in the poor vacuum of the trap enclosure at room temperature.

5.4 Trapping Positrons: Transmission Moderator

The reflection-moderated positron accumulator is not fully compatible with antiproton trapping, since the moderator and source each block one end of the trapping region and leave no access for antiprotons. Fortunately, thin tungsten crystal films may also be used as moderators [96]. Unlike reflection moderators, the slow positrons (and positronium atoms) are emitted from the moderator surface in the direction opposite to positron source, permitting the moderator to be mounted above the electrodes (Fig. 5.21).

The trapping rates in the first transmission-moderated accumulator depend on the electrode potentials in a similar fashion to those of the reflection moderator (*e.g.*, Fig. 5.22), suggesting that the positron trapping mechanism is the same in both moderator geometries. Since the fast- to slow-positron conversion efficiencies of transmission moderators are typically lower than those of reflection moderators [96], it is somewhat surprising that the *absolute* trapping rates are also almost identical.

Another similarity to the reflection-moderated accumulator is that the highest trapping rates result from reducing the fields at the entrance of the trapping region, ionizing the excited positronium atoms deeper within the potential well. The configuration shown (Fig. 5.23) yields a trapping rate of 12 e^+/sec. (The trapping rate with this set of applied electrode potentials was not measured with the reflection-moderated accumulator.)

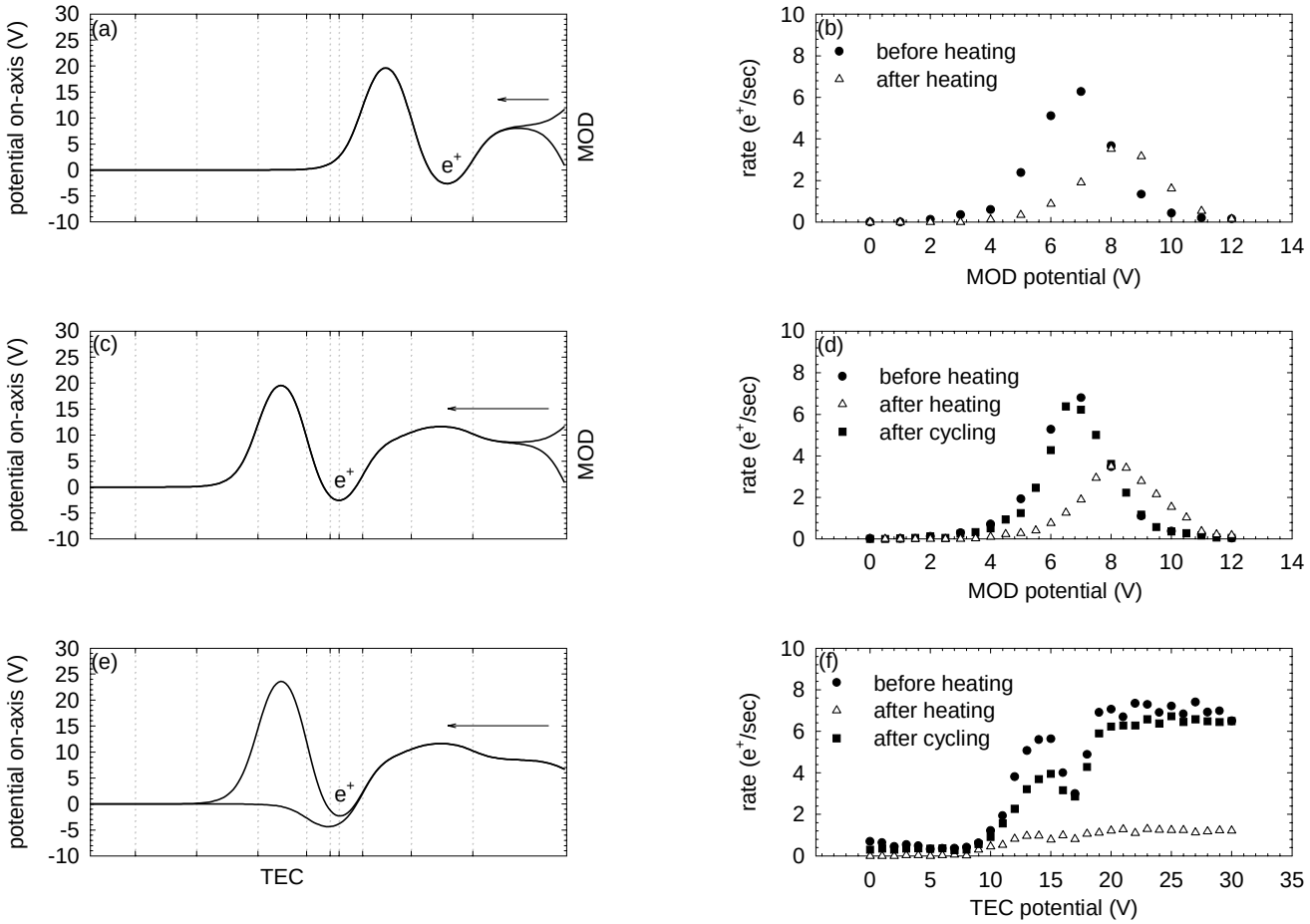

Figure 5.20: The effect of heating the moderator to 550 K. The heating reduces the trapping rate and shifts the dependence on the MOD bias. The trapping rates and dependences are (mostly) restored upon thermal cycling of the apparatus.

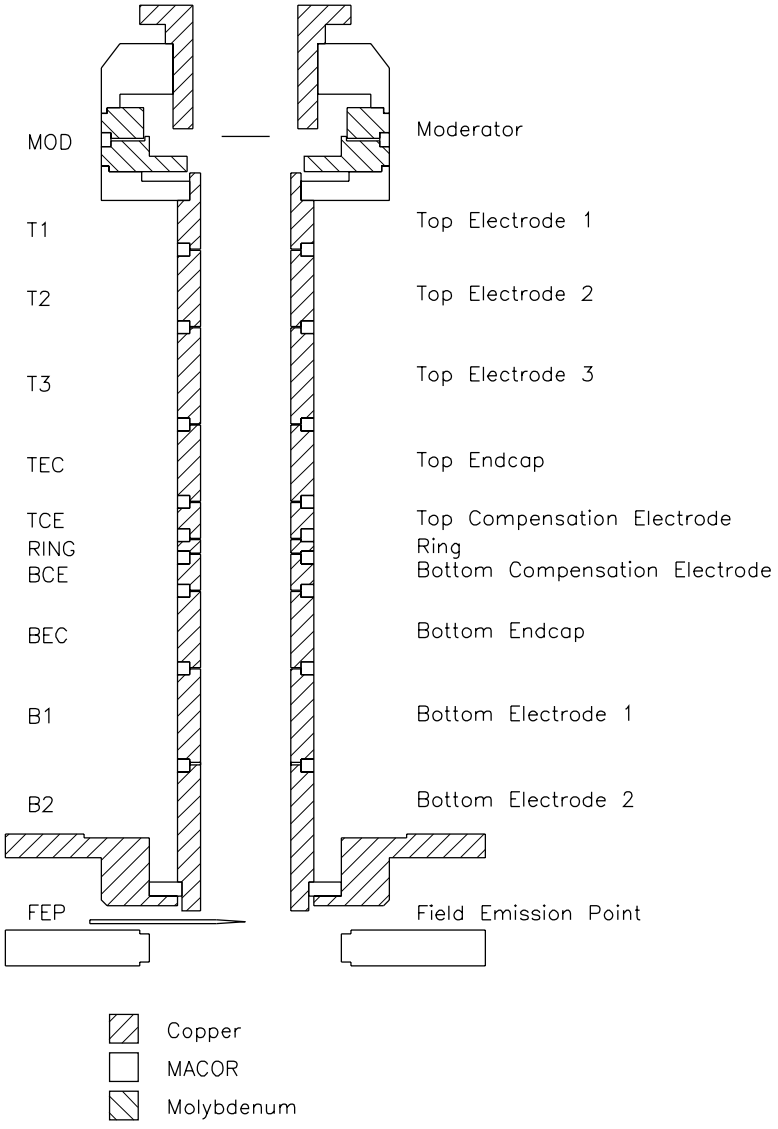

Figure 5.21: Electrodes for the first transmission-moderated positron accumulator.

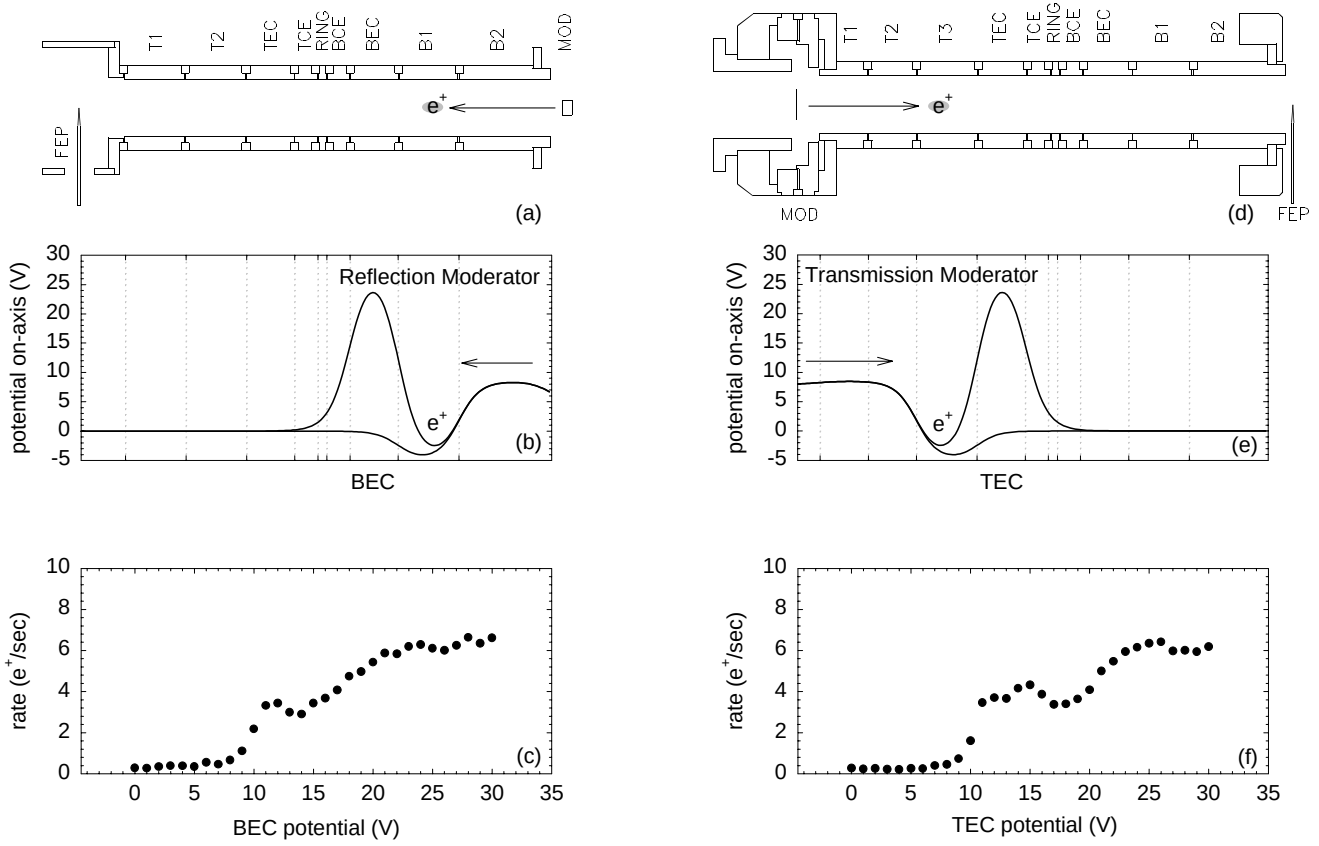

Figure 5.22: A comparison of trapping rate dependences from the reflection and transmission moderators. The similarity suggest that identical processes are responsible for trapping positrons in both moderator configurations.

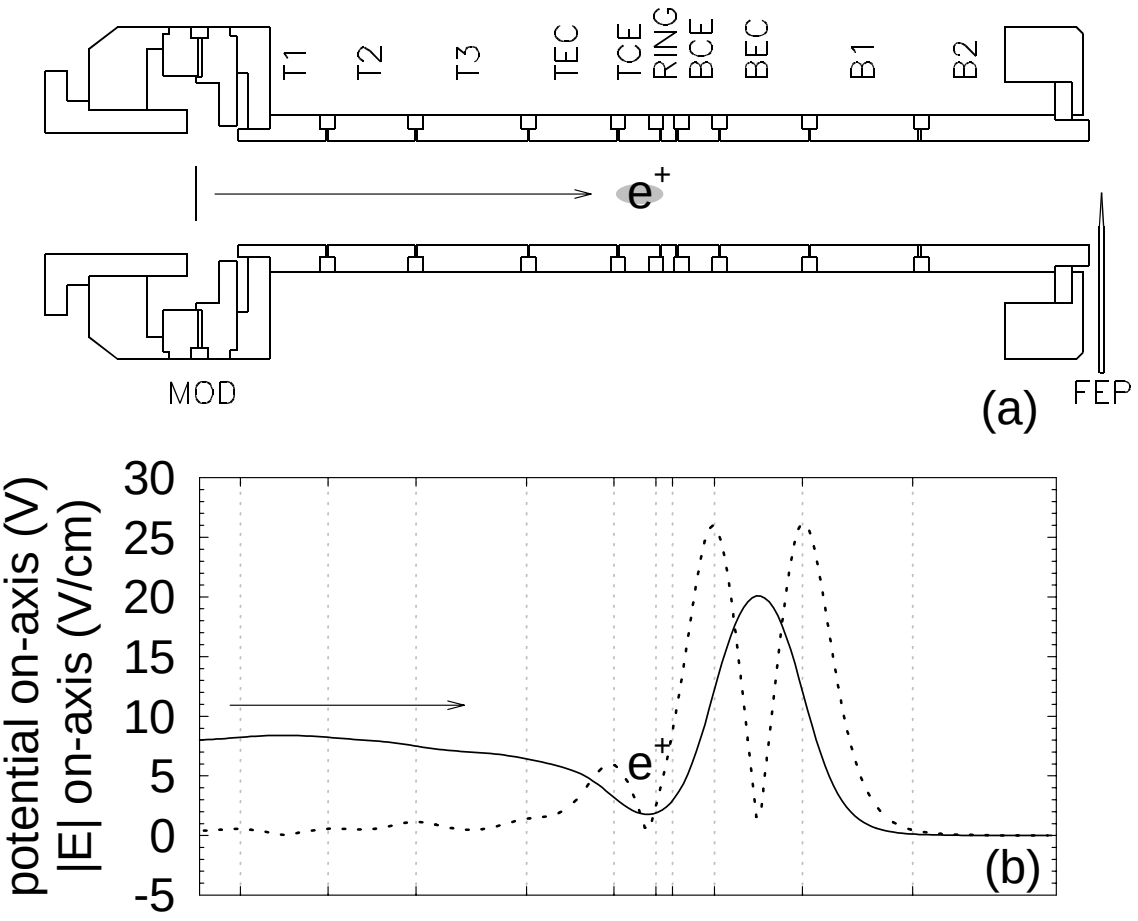

Figure 5.23: Trapping potential configuration which yields the highest trapping rate with the transmission moderator (12 e^+/sec). The positronium field-ionization occurs deeper within the trapping region by reducing the fields near the entrance of the well.

A second transmission-moderated positron accumulator (the positron/antiproton trap) incorporates a set of additional electrodes for trapping and detecting antiprotons (Fig. 6.3), including an unusually-shaped electrode just below the moderator and a gold-plated aluminum degrader mounted just below the electrodes. (Additional details on this apparatus are given in Ch. 6).

The positron/antiproton trap also demonstrates the enhancement of the trapping rate as the field magnitude is minimized at the entrance of the trapping well, providing one of the clearest connections between the trapping rate and the phase space. Superimposed on the broad hump on the left-hand side of Fig. 5.25(f) is a narrow spike in the trapping rate, which occurs precisely as the electric field vanishes at the entrance to the trapping well [Fig. 5.25(d)]. The phase space expands at precisely the same potentials at which the narrow peak is observed (Fig. 5.26).

As the B1 potential is increased above 10 V in Fig. 5.25(f), the trapping rate grows again as positrons are trapped from the surface of the degrader. This is a surprising development in the positron/antiproton trap which makes it possible to simultaneously load positrons from both surfaces at once (Fig. 5.27). The configuration shown trapped 12 e^+/sec, which could have been further optimized by reducing the electric fields at the entrances to the trapping regions (as done in Fig. 5.23). By replacing the aluminum degrader with a tungsten crystal which is simultaneously an antiproton degrader and a positron reflection moderator, it may be possible to obtain even higher yields of trapped positrons.

The trapping rate from the degrader grows to 6 e^+/sec by biasing the moderator to +100 V, presumably increasing the number of low-energy positrons incident on the its surface. Low-energy positrons are not deeply implanted into the bulk of the degrader material and thus do not have time to thermalize before being re-emitted (epithermally) from the surface, preferably as positronium [91].

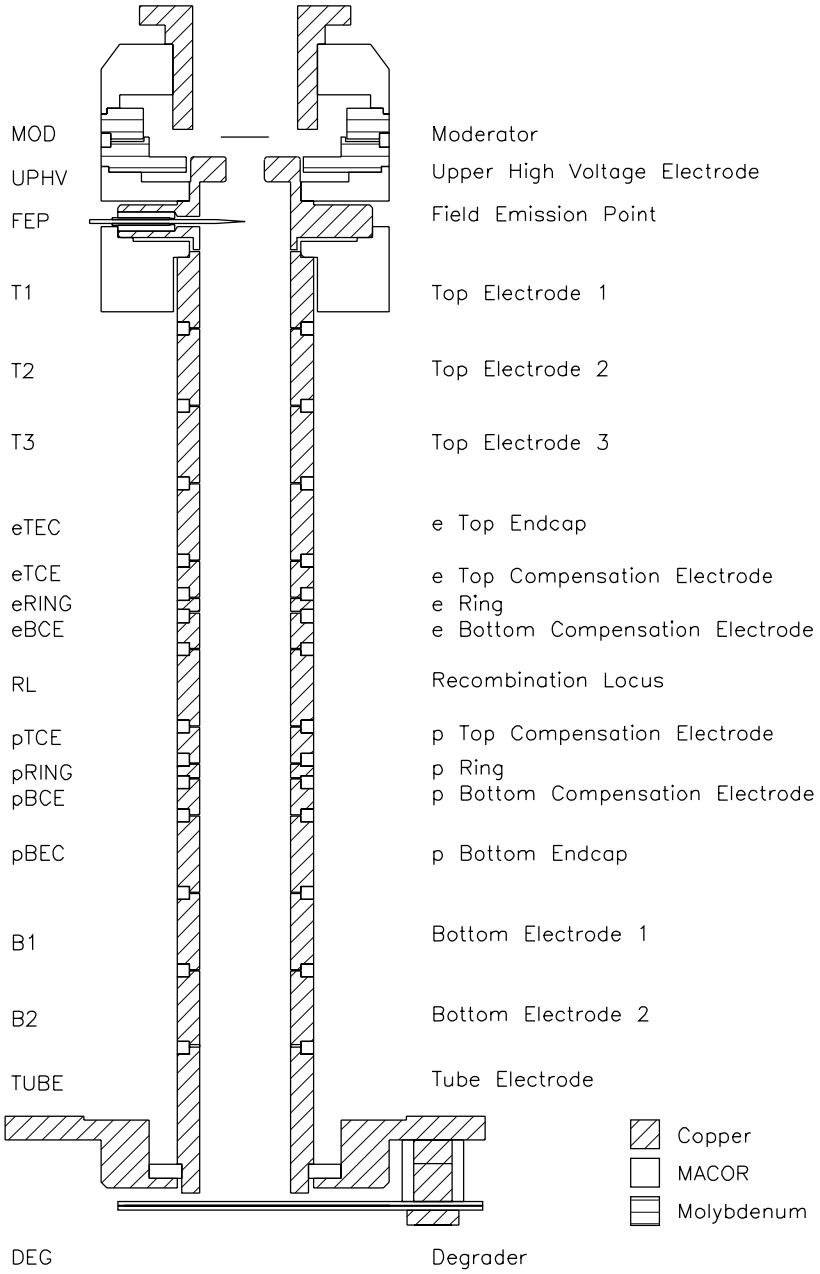

Figure 5.24: Electrodes for the positron-antiproton trap.

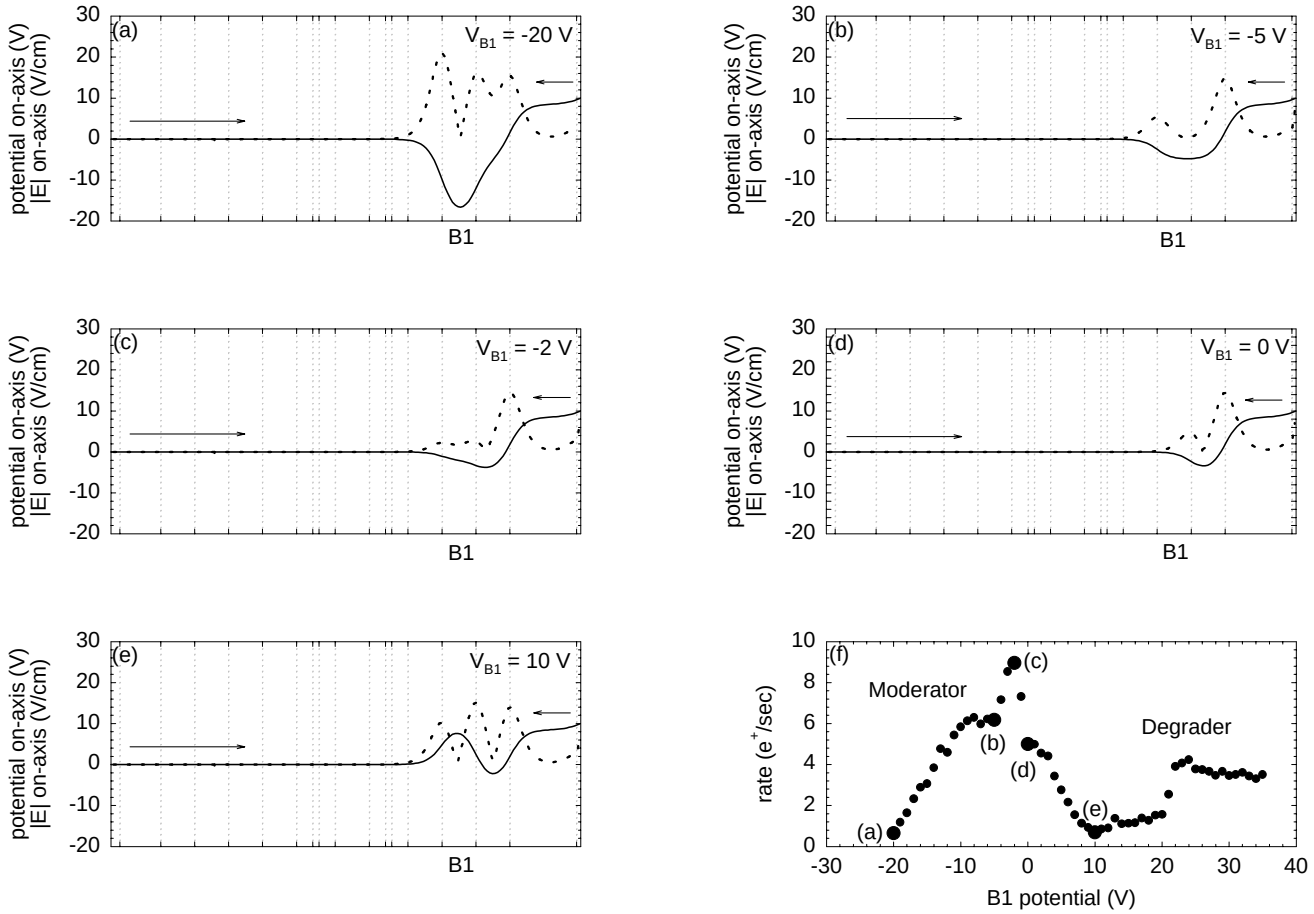

Figure 5.25: Positron trapping from both the transmission moderator and the degrader (f). At the most negative B1 potentials, positrons originating at the moderator are trapped. As the B1 potential increases, trapping occurs for positrons from the degrader. Note the sharp peak (c) as the fields at the entrance of the trapping region nearly vanish for particles incident from the moderator.

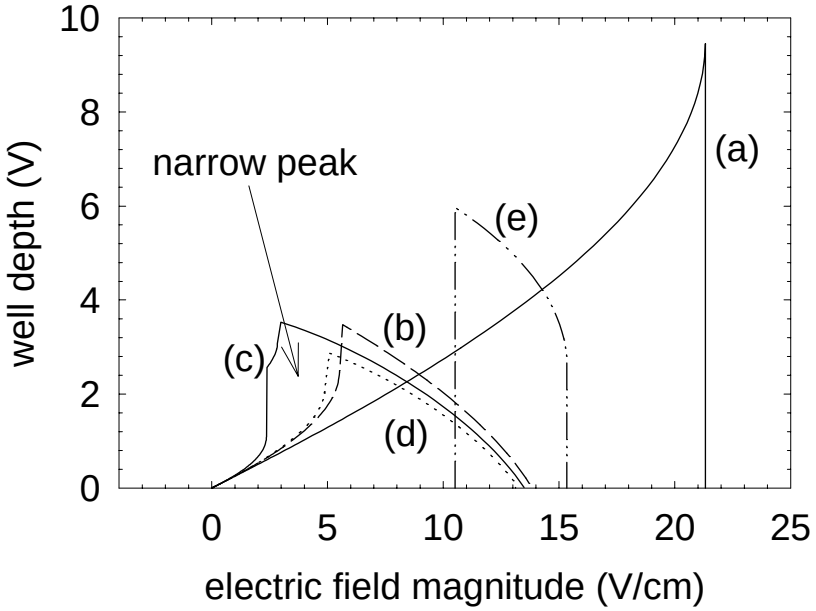

Figure 5.26: Trappable phase space for positronium incident from the moderator plot. The highest trapping rate occurs as the phase space grows into the region indicated by the arrow. (This figure accompanies Fig. 5.25.)

The trapping rates as a function of the bias on the various surfaces (relative to the adjoining electrodes) are compared in Fig. 5.28. All share the same general features, but the trapping rates from the degrader and the first transmission-moderated accumulator depend more weakly on the potential between the moderator and the adjacent electrode than do the other two geometries. It is tempting to ascribe the widths of these peaks to the diameter of the effective surface, since both the reflection moderator and the transmission moderator in the positron/antiproton trap subtend smaller angles of the trap than do the flat plates of the other configurations. No connection between the geometry and the trapping rate is yet understood, although the presence of stronger radial fields in the narrower moderator geometries may play a role in selecting a narrower distribution of emitted positronium.

Another notable difference is that the degrader peak trapping rate occurs at

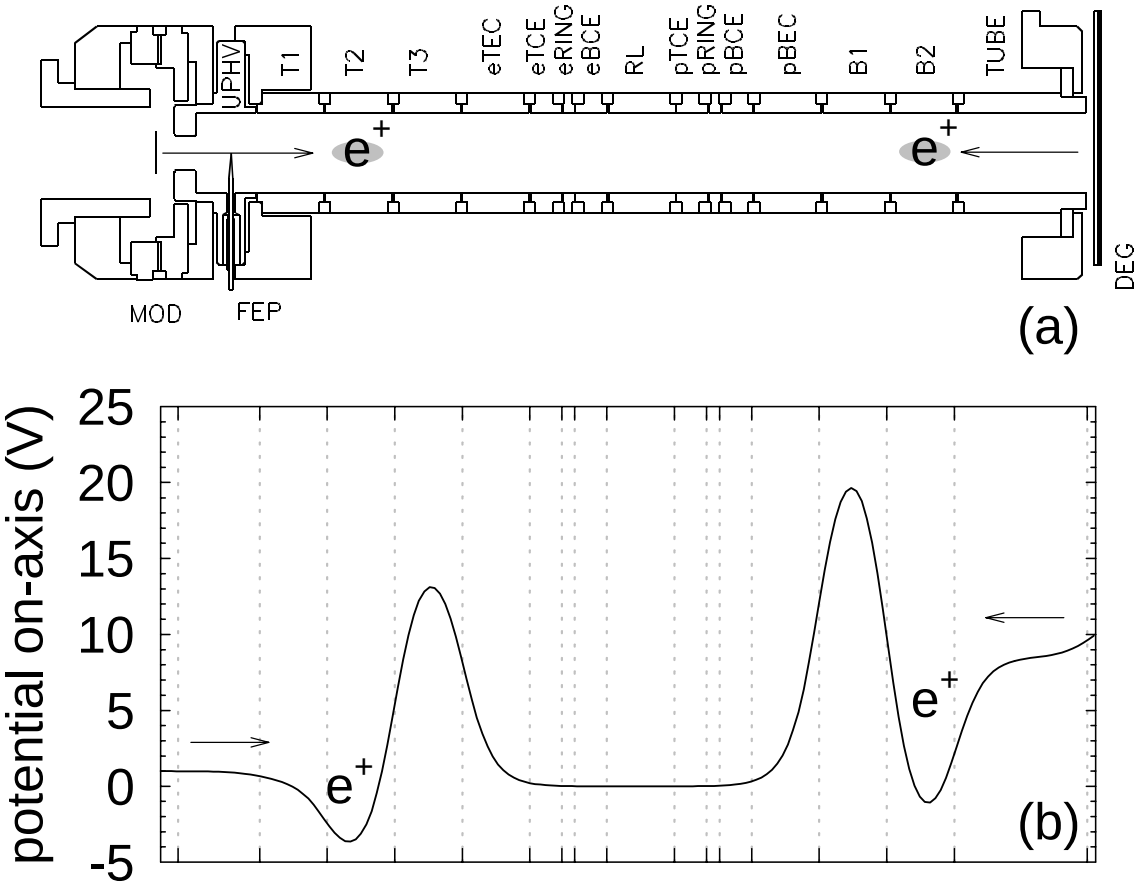

Figure 5.27: Trapping from the transmission moderator and the degrader simultaneously. The configuration shown yielded a net trapping rate of 12 e^+/sec, and could have been further optimized by reducing the fields at the entrances of the potential wells.

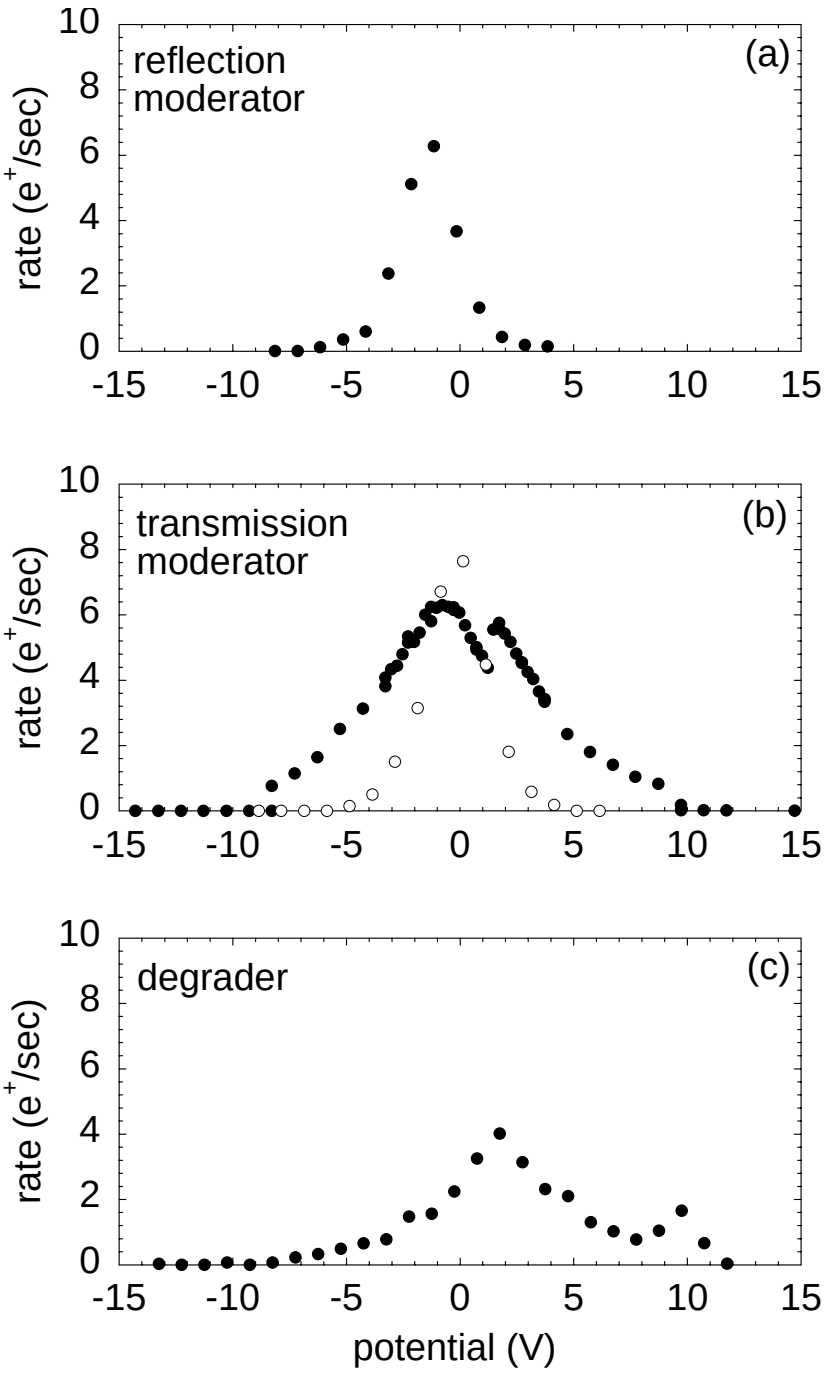

Figure 5.28: Trapping rates as a function of surface bias relative to the potential produced by the adjoining electrode. (a) Reflection moderator. (b) Transmission moderators, in the first accumulator (solid circles) and positron/antiproton trap (hollow circles). (c) Degrader.

a positive (relative) voltage, whereas the highest trapping rates for the tungsten moderators are negative. Curiously, the positron workfunction for gold is also positive [97], which should prevent all thermalized positrons from leaving the degrader surface. It is not yet known if there is a connection between these observations.

Finally, as observed under similar circumstances with the reflection moderator, the symmetry between electron and positron trapping rate dependences under voltage inversion is broken with the transmission moderator (Fig. 5.29). The rates and dependences are similar until the MOD potential rises above the barrier resulting from the T1 and T2 electrodes (at roughly 8.5 V), at which point the electron trapping rate climbs slightly. For much higher MOD potentials, the electron trapping rate seems to have a much higher peak, and appears not to depend smoothly on the MOD potential (although this has not yet been explored extensively). Since all electrons emitted from the moderator are capable of entering the trapping region at these higher potentials, an electron-electron collision mechanism is the most likely explanation for the asymmetry.

5.5 Accumulation of Positrons

5.5.1 One Million Positrons

Antihydrogen recombination rates depend directly on the density of the positron plasma (Ch. 1) and indirectly on the volume it occupies. The largest number of positrons is desired to maximize both quantities simultaneously, requiring continuous accumulation over longer times. In the initial accumulation studies, positrons were trapped directly into the harmonic trapping region, and the plasma automatically sideband-cooled every 10–30 minutes to counter the magnetron heating caused

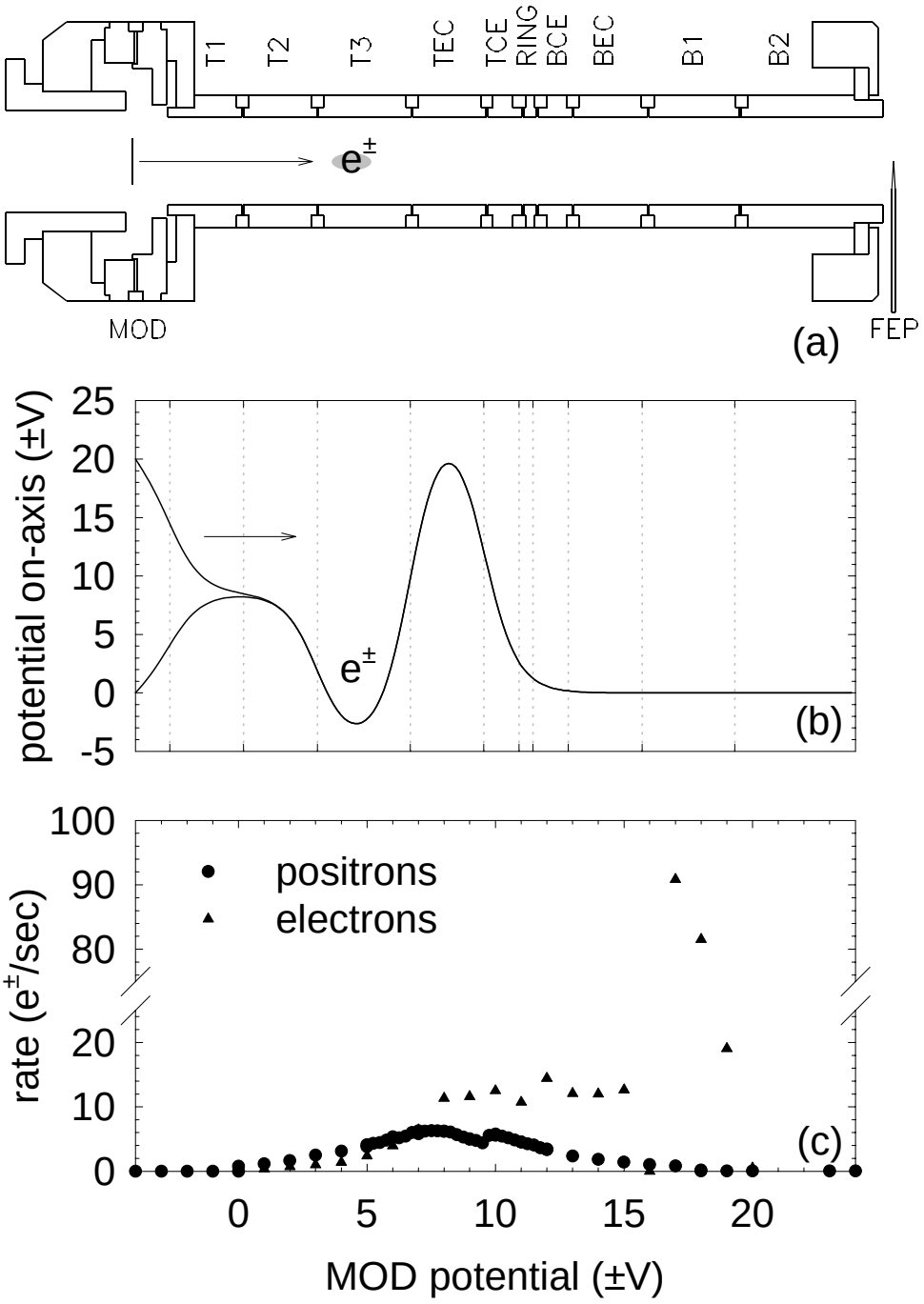

Figure 5.29: Electron trapping rate under the voltage inversion $V \rightarrow -V$. The symmetry between positron and electron trapping rates as a function of the trapping potentials is broken under these conditions with the transmission moderator.

by the passage of the positron beam through the trapped cloud. For smaller numbers of positrons the sideband-cooling was effective, but as the cloud grew the automatic procedure was unable to sufficiently cool or accurately count the positrons, and the curve deteriorated [Fig. 5.30(a)]. The difficulties encountered in the early long-term accumulation attempts have since been resolved by separating the trapping and storage regions (Ch. 6).

The signal from one million positrons stored in the accumulator at the end of the accumulation run is shown in Fig. 5.30(b). A weak signal from a nearby radio transmitter enhances the low-frequency peak of the axial motion, preventing a particularly good fit to the theoretical lineshape (Eq. 3.13). The number of particles N may still be measured from the spacing between the peaks, however, since this spacing is proportional to $\sqrt{N}$ if $N\gamma_z \gg \Gamma$ (Sec. 3.2). For this detection circuit, a peak separation of ≈ 500 kHz corresponds to one million positrons.

5.5.2 Limits on Positron Accumulation

More than one million positrons can be stored by accumulating for longer periods of time.[3] Aside from loss mechanisms (detailed in the following section), there are two limits which, in concert, define the maximum number of positrons which can be stored in this Penning trap. The first is due to the space charge potential of the positron cloud, which, for large numbers of trapped particles, can exceed the trap depth. This limit is expressed

$$\frac{V_0}{V_{\rm sc}} \geq 1 \tag{5.4}$$

where V_0 is the trapping potential, $V_{\rm sc}$ is the space-charge potential on the axis of the trap (Eq. 4.5), and a spherical distribution of positrons in the trap is assumed.

[3]The race to beat the LEAR shutdown enforced rather strict limits on how much time the accumulator could be devoted to accumulation rather than to other studies.

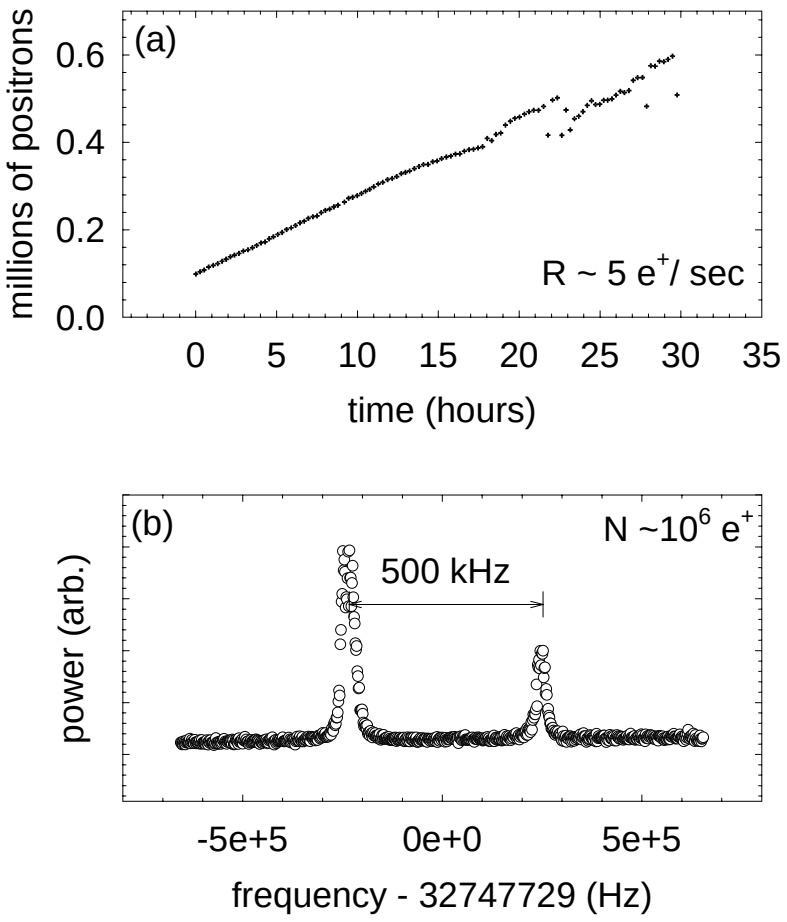

Figure 5.30: Accumulating positrons. (a) Number of positrons as a function of time. The net rate R is lower than the peak rate due to the time spent magnetron-cooling the cloud. The curve is also truncated due to difficulties associated with automatic handling of so many positrons. (The automatic run began with approximately 100,000 e^+in the trap.) Approximately one million positrons are shown in (b), at the end of the accumulation run. (See text.)

The maximum number of positrons N_e which can be trapped is, therefore,

$$N_e \leq \frac{V_0 d}{\sqrt{C_2} e} = 4.82 \times 10^6 \ V_0[\text{Volt}]. \tag{5.5}$$

This is only an order of magnitude more than has already been accumulated in a 10 V trapping potential. To store more positrons, the trap depth must be increased, which simultaneously increases the density of the trapped particles.

The Brillouin density limit [98] constrains the maximum density of a trapped nonneutral plasma. This limit is reached when the radial electric force due to the trapped positrons exceeds the radial confinement provided by the magnetic field, *i.e.*,

$$2\frac{\omega_p^2}{\omega_c^2} \geq 1 \tag{5.6}$$

where

$$\omega_p = \left(\frac{4\pi n_e e^2}{m_e} \right)^{1/2} \tag{5.7}$$

is the positron plasma frequency and ω_c is the cyclotron frequency. The critical density n_e is, therefore,

$$n_e = \frac{B^2}{8\pi m_e c^2} = 4.85 \times 10^{12} \ B[T]^2 \ \text{cm}^{-3}. \tag{5.8}$$

For a magnetic field $B = 6$ T, this critical density is many orders of magnitude larger than the typical cloud density $n_e \approx 5 \times 10^7$ cm^{-3} (Sec. 4.4.1). The Brillouin density limit is important for cold positron plasmas stored at very large trapping potentials, and cannot be achieved with the trapping potentials accessible to this apparatus (< 300 V).

5.5.3 Positron Loss Mechanisms

Three mechanisms contribute to positron loss from the accumulator. The most important is radial loss due to magnetron heating of the plasma, which results from collisions between the plasma and untrapped particles, as well as from azimuthal inhomogeneities in the trapping fields (due to the presence of charge-patches on the electrode surfaces). In most situations these effects are not particularly severe, and can be countered with a sideband cooling drive (Sec. 3.3). The sensitivity to charge-patches can also be inhibited by avoiding long, shallow trapping configurations (Sec. 4.1).

Positrons may also be lost from the trap through annihilations with the electrons of background gas atoms. The largest cross-sections are for positronium formation (and subsequent annihilation), which occurs if the positron energy is greater than the positronium formation threshold [99]

$$E_0 = E_I - E_{\mathrm{Ps}} \tag{5.9}$$

where E_I is the ionization energy of the atom, and $E_{\mathrm{Ps}} = R_\infty/2$ is the positronium Rydberg. Positronium formation is the dominant inelastic process in the Öre gap [99],

$$E_0 < E < E_{\mathrm{ex}} \tag{5.10}$$

where E_{ex} is the minimum energy required to electronically excite the atom. Trapped positrons at 4 K have energies well below typical Ps formation thresholds, insuring that this is not a significant loss mechanism from the accumulator.

Direct electron-positron annihilation takes place in the absence of positronium

Table 5.1: Some values of Z_{eff} for common gases.

gas	Z_{eff}	Ref.
He	3.94	[100]
Ne	5.99	[100]
H_2	14.6	[101]
O_2	30.5	[102]
Ar	33.8	[103]
N_2	36.7	[103]
CO_2	54.7	[104]
H_2O	319	[103]

formation with an effective cross section σ_a, given by [99]

$$\sigma_a = \frac{\pi r_e^2 c Z_{\text{eff}}}{v} \tag{5.11}$$

where ($r_e \approx 2.8 \times 10^{-13}$ cm) is the classical electron radius and Z_{eff} is a measure of the effective number of electrons associated with each atom or molecule. (Some typical values for Z_{eff} for common gases are given in Table 5.1.) The positron lifetime against direct annihilation is

$$\tau = \frac{1}{nv\sigma_a} = 1.4 \times 10^{-4} \, \frac{T[\text{K}]}{Z_{\text{eff}} P[\text{Torr}]} \text{ sec.} \tag{5.12}$$

At $T = 4$ K and $P = 5 \times 10^{-17}$ Torr of helium, the positron lifetime is extremely long (10^{12} sec), and direct annihilation is also not a significant loss mechanism.

A rough measurement of the positron lifetime in the trap τ can be determined from the accumulation curve [Fig. 5.30a] by fitting it to a function of the form [105]

$$N(t) = R\tau(1 - e^{-t/\tau}) \tag{5.13}$$

where the R is the trapping rate. A best fit to the data yields a lifetime $\tau \approx 60$ hours, which is interpreted as a lower bound resulting from the problems associated with magnetron-cooling the large positron cloud.

5.6 Comparison with Other Methods

A variety of trapping methods has been developed to accumulate positrons since they were first trapped in a hyperbolic Penning trap in 1979 [106]. The previous cryogenic accumulator [4] used a hyperbolic trap with a tuned LCr circuit to extract the axial energy of moderated positrons from a 10 mCi ^{22}Na source. The positrons entered the trapping region through an off-axis hole, preventing many from escaping until they completed one magnetron orbit. The positrons were captured as a tuned LCr circuit extracted their axial energy during this slow orbit. Although the cryogenic vacuum was sufficient for antiproton storage, the closed-surface electrode configuration was inconvenient for interaction studies and antiproton trapping. Moreover, the modest 0.2 e^+/sec trapping rate required long accumulation times to obtain large positron plasmas. The new cryogenic accumulator is a significant improvement over its predecessor in both electrode configuration and trapping rate.

Another accumulator [107, 108] uses positrons from a tungsten vane-moderated ^{22}Na source which are confined in a cylindrical Penning trap by quickly ramping the potential on the entrance endcap. Assisted by a mechanism of chaotic transport [109], about 25% of the moderated positrons are captured and subsequently ejected from the trap in a bunch at repetition rates near 250 Hz. Although better suited to bunching, this trapping method could be adapted to accumulation in a cryogenic apparatus (at a concomitantly reduced rate) by permitting the positrons to cool between cycles.

A similar approach [110] makes use of electron-positron pair production at a pulsed electron LINAC. The entrance endcap of the cylindrical trap is quickly ramped after each pulse to confine the positrons. Designed to quickly accumulate 2.4×10^9 e^+ at densities exceeding $10^8/\mathrm{cm}^3$ in a cryogenic vacuum, this sort of trap would be a serious contender if a high-intensity pulsed positron source were available at the antiproton site.

A final positron accumulator [105, 111] uses a solid neon moderator to slow positrons from a 50 mCi ^{22}Na source. The positrons enter a multistage cylindrical Penning trap, where up to 10^8 e^+ are trapped in a few minutes through collisions with a nitrogen buffer gas. The nitrogen is subsequently pumped away, permitting positron lifetimes on the order of an hour at a base pressure of $\approx 4 \times 10^{-10}$ Torr. This device is clearly a powerful tool for the rapid accumulation of large numbers of positrons, since in a few minutes it accumulates more positrons than can be trapped in a day using the cryogenic accumulator developed in this work (assuming identical source strengths).

One of the principal technical challenges which must be overcome before the positrons trapped using the buffer-gas technique can be applied to antihydrogen production is how to deliver them into the cryogenic vacuum required for the storage of antiprotons. One possibility is to fabricate a valve which can be opened briefly to admit the positrons [112]. Even very small leaks in the trap vacuum enclosure are observed to decrease the antiproton lifetime, so the valve would have to be reliable and entirely leak-free. In place of the valve, a thin remoderator crystal film could be used to separate the cryogenic vacuum from the trapping vacuum, provided it is never exposed to a large differential pressure. The cryogenic accumulator, of course, avoids these challenges by accumulating positrons directly into the cryogenic vacuum.

5.7 Other Applications

Highly-charged high-Z ions are produced at high energies in facilities such as an EBIT. A variety of experiments [113] (*e.g.*, precision mass spectroscopy, and production of Coulomb crystals) become possible as these ions are cooled to 4 K and stored in the extremely high vacuum of a cryogenic Penning trap. Cooling highly-stripped ions to 4 K is a difficult task, since gas-assisted cooling results in charge-transfer and ion loss, and the readily-available light ions can be difficult maintain at cold temperatures. A cold positron plasma, however, cools itself to 4 K through synchrotron radiation, and does not participate in charge-exchange processes with the ions; consequently, it is nearly ideal for cooling highly-stripped ions [113], just as an electron plasma has been successfully used to cool keV-energy antiprotons to 4 K [3].

The cryogenic positron plasma may permit recombination studies with a cryogenic electron plasma, possibly in a nested trap configuration [1]. The positronium produced could be easily detected by its annihilation radiation. Other positron-electron plasma experiments also become possible [114].

5.8 Conclusions

A new and efficient positron accumulation technique is demonstrated, with strong evidence favoring a mechanism involving the field-ionization of highly-excited positronium atoms produced at or near the surface of a tungsten positron moderator. One million positrons are trapped at rates exceeding 10 e^+/sec — a factor of 50 improvement over the earlier method of cryogenic positron accumulation [4]. The accumulation occurs in both reflection- and transmission-moderator geometries, as

Table 5.2: Peak trapping rates in various moderator configurations. The peak trapping rate for the transmission moderator is in a configuration that was not tested in the reflection-moderated trap.

Moderator	Rate (e^+/sec)
Reflection	7.4 ± 0.2
Transmission	12.1 ± 0.2
Transmission[a]	16 ± 3
Degrader	4.0 ± 0.8
Degrader[b]	6.1 ± 1.2

[a]At CERN, uncalibrated detector.
[b]With transmission moderator at +100 V.

well as from materials not traditionally considered "moderators." The open-access cylindrical electrode geometry of the accumulator, and its extremely high cryogenic vacuum, are well-suited to the simultaneous confinement of antiprotons and positrons (Ch. 6).

Additional experiments will add to the understanding of the trapping mechanism. Measuring the trapping rate as a function of the magnetic field may help determine whether the production of the highly-excited positronium is peculiar to the high magnetic fields used in these experiments. The moderator material, temperature, and surface conditions should be varied systematically to identify any dependences. Most importantly, the electron and positron trapping rates should be compared in all trapping configurations to determine at what points the symmetry in loading rates exists. Extensive examination should also be made of the trapping rate dependences which do not make sense under the positronium field-ionization hypothesis.

The trapping rate is likely to increase with the activity of the source. For example, a more efficient 150 mCi ^{22}Na source would permit the trapping of one million

Table 5.3: Possible improvements to enhance the trapping rate.

improvement	factor
150 mCi ^{22}Na source	30
more efficient or enlarged ^{22}Na source	2
two moderators	2
optimized trapping potentials	2
improved moderator (*e.g.*, solid Ne)	? 30

positrons in about 25 minutes. This time could be cut in half again if positrons were collected from both sides of the trap at once (*e.g.*, by using a transmission moderator on one end of the trap and a reflection moderator which is also an antiproton degrader on the other). Additional gains result from further optimization of the trapping potentials or, possibly, by identification of a better moderator material (*e.g.*, solid neon or diamond). These possibilities are summarized in Table 5.3.

5.9 Appendix: Details

5.9.1 Positron Sources

Two additional radioactive positron sources were considered in place of the ^{22}Na source used in these experiments: ^{58}Co, and ^{19}Ne. ^{58}Co has a half-life of 71.3 days and a relatively small fraction (15%) of decays which result in a positron; large activities may be obtained, however, and a 1 Ci ^{58}Co source was ordered for the antiproton/positron experiments at CERN.[4] The other radioactive source considered, ^{19}Ne, emits a positron in virtually all of its decays at energies up to 2.2 MeV. ^{19}Ne is produced at a proton accelerator in the reaction $^{19}\mathrm{F}(p,n)^{19}\mathrm{Ne}$ [115], after which the inert (but radioactive) gas can be piped to the experimental area and

[4]This source was not delivered.

frozen onto a cold surface inside the accumulator (*e.g.*, a surface located just above the trap vacuum enclosure). This scheme was considered seriously for a time due to the proximity of the proton LINAC-2 to the CERN antiproton accelerator site. The half-life of ^{19}Ne is only 17.2 sec, which permits a large activity (1 Ci or greater) to be effectively switched off by terminating production of the gas at the target. Preliminary experiments conducted at the Harvard Cyclotron [116] demonstrated the feasibility of this scheme by producing ^{19}Ne and plating it onto a cryogenic surface.

5.9.2 Moderator Treatments

The reflection moderator is a tungsten (110) crystal [117] in the shape of a cylinder with a diameter of 0.12" and a height of 0.08". The crystal was originally used in the previous cryogenic accumulator, before which it was mechanically polished, electrochemically etched, and annealed.

The moderator is suspended by two .003" diameter wires which pass through small holes electron-beam drilled through the sides of the crystal to form a tungsten–3% rhenium/tungsten–25% rhenium (type D) thermocouple [118]. In a procedure to eliminate the carbon from the crystal [119], the moderator was heated to $\approx$ 1500 K by 1 keV electron bombardment from a filament for 41 hours in 3.5×10^{-5} Torr of oxygen. Six times during this process the oxygen was pumped out and the moderator temperature increased to 2500 K to desorb the carbon monoxide (and other surface contaminants).

After this treatment the moderator/filament assembly was carried in air to the apparatus, where it was mounted below the electrodes in the trap vacuum enclosure (Fig. 5.6). The enclosure was evacuated to $\approx 10^{-7}$ Torr, the moderator briefly heated to 2500 K, and treated at 1500 K in 3×10^{-5} Torr of oxygen for about

an hour. Finally, the oxygen was pumped out and the temperature brought to 2500 K for 30 sec. The crystal was then allowed to cool slowly, the trap can sealed, and the apparatus lowered into the magnet. This *in situ* moderator treatment also contaminated the trap electrodes, so the apparatus was removed and the electrodes replated and repolished. This final moderator preparation was subsequently omitted after having left the moderator in air for about a week.

The tungsten (100) transmission moderator is suspended by two pairs of tungsten alloy wires, each crossing the other at a right angle on opposite sides of the crystal. The crystal had been damaged in a vacuum breach while being treated to remove carbon, causing one of its two faces to become severely discolored. A small section of the discolored face was restored after two hours of heating to 1200 K in 4.7×10^5 Torr of oxygen, and a brief heating in high vacuum to almost 2400 K. (Several "pinholes" could be seen through the crystal at the high temperature.) After cooling, the moderator was carried in air to the apparatus, where it was mounted in the apparatus with its less-damaged (shiny) side toward the trap electrodes.

5.9.3 Wiring

The cold electronics and electrode wiring diagram for the reflection-moderated accumulator is shown in Fig. 5.31. The circuits are similar to those of Fig. 2.8 with a few notable changes. For instance, the B2 electrode is fitted with a copper-constantan (type T) thermocouple [118] for monitoring its temperature as the moderator is heated. The filament current is delivered on 20 AWG enameled copper wire with the exception of brief "thermal breaks" fashioned of the outer (shield) conductors of stainless-steel microcoaxial cables. The lines are thermally anchored to one of the gas-cooled copper plates in the thermal isolation stage, reducing the heat load

on the helium dewar. The total resistance of the filament circuit (including that contributed by the transmission lines) is 5 Ω.

The remainder of the trap wiring is similar to that of the apparatus described in Ch. 2. The bias potentials for the ring and compensation electrodes of the single harmonic trapping region are derived from a Fluke Direct Volts Calibrator (Sec. 2.4.1). The remaining electrodes are biased by DAC channels. A single FET amplifier circuit is connected to monitor the electron (positron) axial motion (Sec. 2.4.3). Five RF drive lines are included, three of which (electron sideband, electron modulation, and electron axial) are for electron (positron) sideband cooling and detection (Sec. 2.4.2). White noise (DC–1 MHz) is applied to the remaining "anti-ion" drives (on the B1 and T2 electrodes) to drive the axial motions of positive ions, preventing them from becoming trapped along with the positrons.

The first transmission-moderated trap is wired almost identically, with the exception that it has no provision for heating the moderator. The positron/antiproton trap includes many additional electrodes and detectors, and is discussed further in Ch. 6.

5.9.4 Counting Trapped Positrons

In order to determine the absolute number of positrons in the trap, the damping rate γ_z is measured for a single electron in the trap.[5] The technique is identical to that used in Sec. 3.4 with the exception that the dip width is measured directly, rather than with a coherent drive — a technique made possible by a helical resonator with

[5]Loading a single electron is in many respects easier than loading a single positron, and the damping rate is independent of the *sign* of the charged particle.

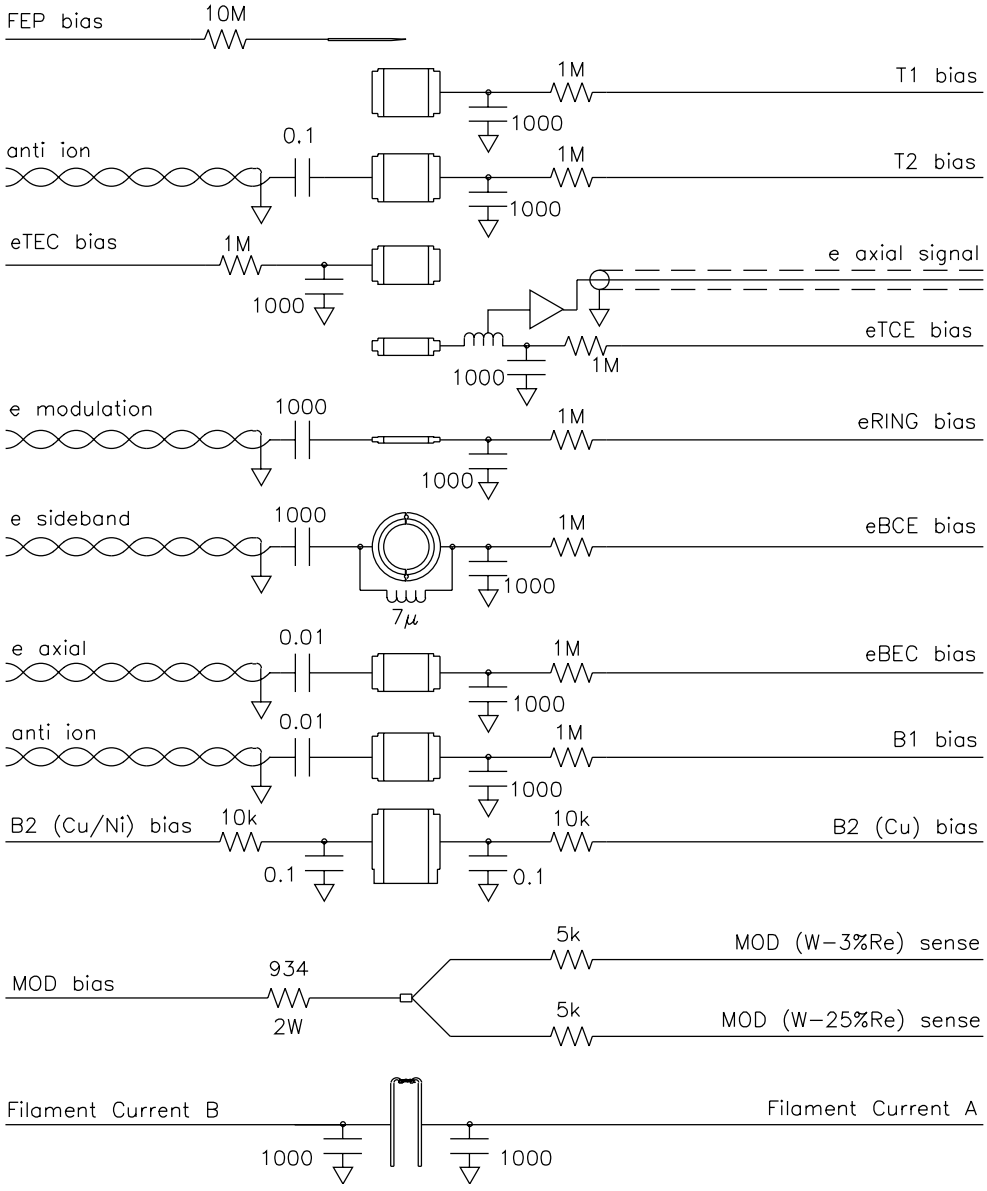

Figure 5.31: Trap wiring diagram for the reflection-moderated positron accumulator. Note the similarities to Fig. 2.8. Circuits are also added for a filament and monitoring the temperature of the moderator and the B2 electrode.

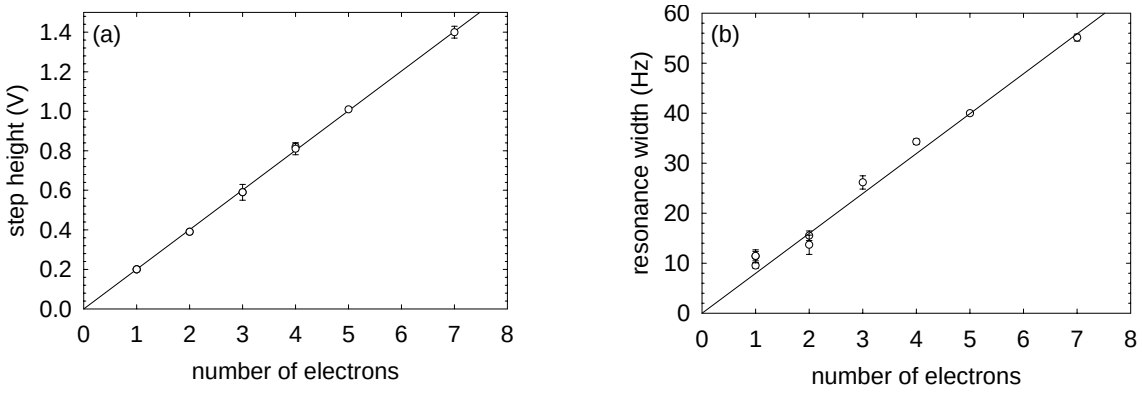

Figure 5.32: Calibration of the single particle resonance width for the positron trap. Electrons are used to calibrate the detector, since the loading of small numbers of positrons was difficult to control at the time these measurements were made. (a) Measured "step height" for various cloud sizes. (b) Resonance widths for various cloud sizes. A constrained straight-line fit to the data yields the single particle width: $\gamma_z(e^-) = 2\pi \cdot (7.98 \pm .05)$ Hz. (The single electron data are not included in the fit; see text.)

a quality factor $Q \approx 1100$. The measured damping width γ_z is

$$\gamma_z(e^-) = 2\pi \cdot (7.98 \ \pm \ 0.05) \text{ Hz}. \tag{5.14}$$

The measured "step" heights and resonance widths are shown in Fig. 5.32a and 5.32b. The relatively large single-particle width permits single particles to be easily resolved by their undriven axial motion, or "dip" (Fig. 5.33). As with all measured single particle widths, however, the trapping potential is insufficiently stable to permit a direct determination of the damping width from measurements on a single particle. (The measured width of the highly-averaged single electron dip shown here is almost twice the natural linewidth.)

The first accumulator also used this electron axial tuned circuit, but the value of γ_z changes slightly when the detector is attached in a different electrode configuration. The width-per-particle is proportional to the effective parallel resistance

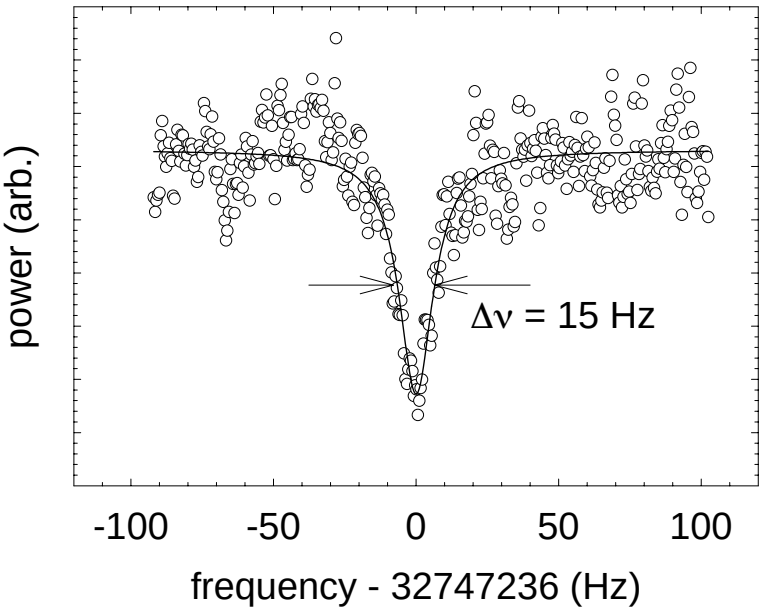

Figure 5.33: Single electron "dip," observed by averaging for several minutes. Instabilities in the trapping potential and the long averaging time make the measured linewidth nearly twice the natural linewidth.

$R = Q^2 r$ of the circuit on resonance (Eq. 3.14), *i.e.*,

$$\gamma_z \propto R = Q\omega_{LC}L, \tag{5.15}$$

where Q and ω_{LC} are the circuit quality factor and resonant frequency of the tuned circuit, and L is the inductance of the helical resonator. Since L is a property of the coil (and is not changed between the two apparatus), measurement of Q and ω_{LC} are sufficient to scale γ_z.

The positron/antiproton trap, however, used an entirely different (and uncalibrated) helical resonator. Its geometry was similar to that of the electron axial detector of the recombination apparatus, however, which was measured in Ch. 3. Scaling this value by the circuit Q and resonant frequency suggests a value for

$\gamma_z \approx 2\pi \cdot 4$ Hz. Comparison of the positron trapping rates from the transmission moderator measured by it and the calibrated resonator circuit under similar potential configurations indicates a value closer to 6 Hz. The width-per-particle is therefore taken as the average of these two values, or $\gamma_z = 2\pi \cdot (5.1 \pm 1.0)$ Hz, for the antiproton/positron trap.

In addition to the absolute uncertainty in γ_z, there is an uncertainty associated with the error in the fit to the lineshape. As with the previous accumulator [55], this is typically on the order of 1% for clouds larger than $N \approx 3000$, rising to about 10% at $N \approx 100$, and remaining at ± 10 for smaller clouds. The final uncertainty arises from shot noise, requiring a factor of $\sqrt{N}$ to be added in quadrature. Altogether, the error bars are approximately the size of the points throughout the maps in this chapter.

5.9.5 Effects of the Positron Beam at Higher Trap Temperatures

The apparatus is precooled to 77 K by filling its liquid helium dewar with liquid nitrogen. When the temperature is near 77 K and the positron beam turned on, electrons load into positively-biased regions of the trap (Fig. 5.34). The electrons are presumably trapped as the incident positron beam strips electrons from background gas atoms, since biasing the trap electrodes to prevent secondary electrons (below 100 eV) from entering the trapping region does not appreciably inhibit the loading. (A leak in the trap vacuum enclosure at 4 K also results in large electron clouds.) The lifetime of the electrons in the trap at 77 K depends on the length of time the trap vacuum enclosure has been at room temperature after having been evacuated and sealed, and can be as long as an hour if the evacuation occurs just prior to

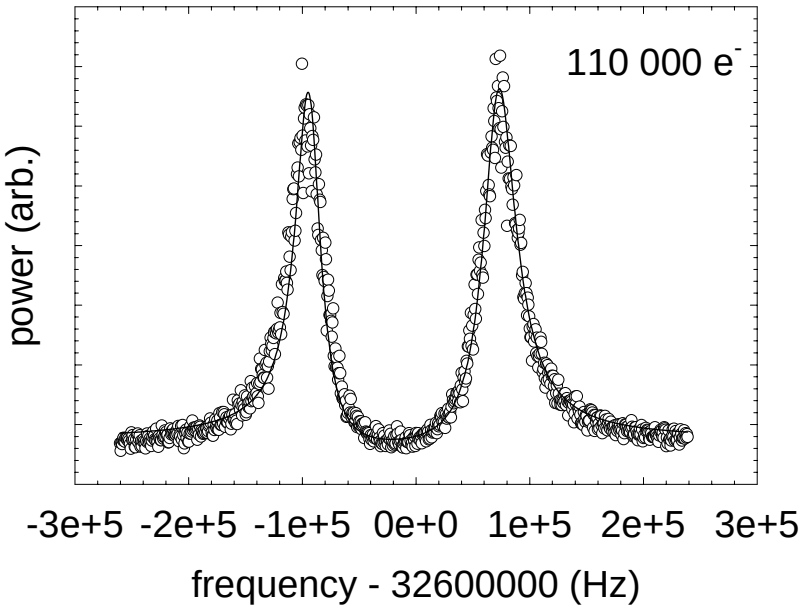

Figure 5.34: Electrons loaded at 77 K by action of the positron beam. The particles have a lifetime in the trap of up to an hour, even at this high temperature.

cooldown. Electrons will also load (at a reduced rate) if the positron beam is entirely blocked, which may be the result of ionization due to the 1.2 MeV gamma-radiation from the ^{22}Na source. Neither electrons nor positrons are observed to trap at room temperature (with the e^+ beam on or off) or at 4 K (with the e^+ beam off). Positrons have not yet been observed to trap at 77 K, although this has not yet been thoroughly studied.

Chapter 6

Positrons and Antiprotons

Cold plasmas of antiprotons and positrons have been trapped separately for several years [2, 4]. This chapter describes the first simultaneous confinement of antiproton and positron plasmas, and the first interaction between the two in a nested Penning trap. A trap for both antiprotons and positrons was realized at Harvard after the success of the new positron trapping method in mid-1996. The only site in the world which provided antiprotons at energies suitable for trapping was the Low Energy Antiproton Ring (LEAR), however, situated on the Franco-Swiss border outside Geneva at the European Center for Particle Physics (CERN). The TRAP collaboration (PS196) had there for a decade performed experiments on antiproton trapping [2] and cooling [3], culminating in the impressive proton-antiproton mass comparisons [120, 15, 47]. The last nine days of LEAR antiproton beam (9–18 December 1996) were made available to the collaboration for an attempt to produce cold antihydrogen before the accelerator was permanently closed.

In early September the apparatus was disassembled and shipped by plane to CERN, where it was reassembled and improved in the following months. Although unforeseen difficulties and limited accelerator time prevented antihydrogen produc-

tion from the trapped plasmas, the apparatus separately stored record numbers of antiparticles — one million positrons over a twenty-four hour period in late November (before the antiproton beam was available), and 0.6 million antiprotons in a single intense pulse of antiprotons from LEAR. The experience gained in these preliminary experiments will prove invaluable with the advent of a new low-energy antiproton source early in the next century.

6.1 Experiments with Positrons and Antiprotons

The positron-antiproton apparatus is shown in Fig. 6.2. Its open-access cylindrical electrode configuration (Figs. 6.3 and 6.4) permits positrons to enter the trapping vacuum enclosure from a 5 mCi ^{22}Na source positioned above the trap and antiprotons from the LEAR beamline below. A set of six scintillators surrounds the superconducting magnet to detect the pions produced by antiproton-proton annihilations. Since the scintillators are also sensitive to the 1.2 MeV γ-radiation from the decay of ^{22}Na, the positron source is lifted into a lead blockhouse at the top of the apparatus when not in use. (Further apparatus details are found in Sec. 6.3, Chs. 2 and 5, and Ref. [40].)

One million positrons were trapped, using the trapping mechanism described in Ch. 5, while the apparatus was being readied to receive the antiproton beam (Fig. 6.5). The difficulties experienced in the earlier long-term accumulation experiments (Ch. 5) were reduced by accumulating positrons into one trapping region (the T2 electrode) and subsequently relocating them into a separate trapping region in which they were continuously magnetron-cooled. At occasional intervals additional positrons trapped on the T2 electrode were added to the stored cloud (Fig. 6.6). An average trapping rate of 10 e^+/sec was maintained despite frequent interruptions

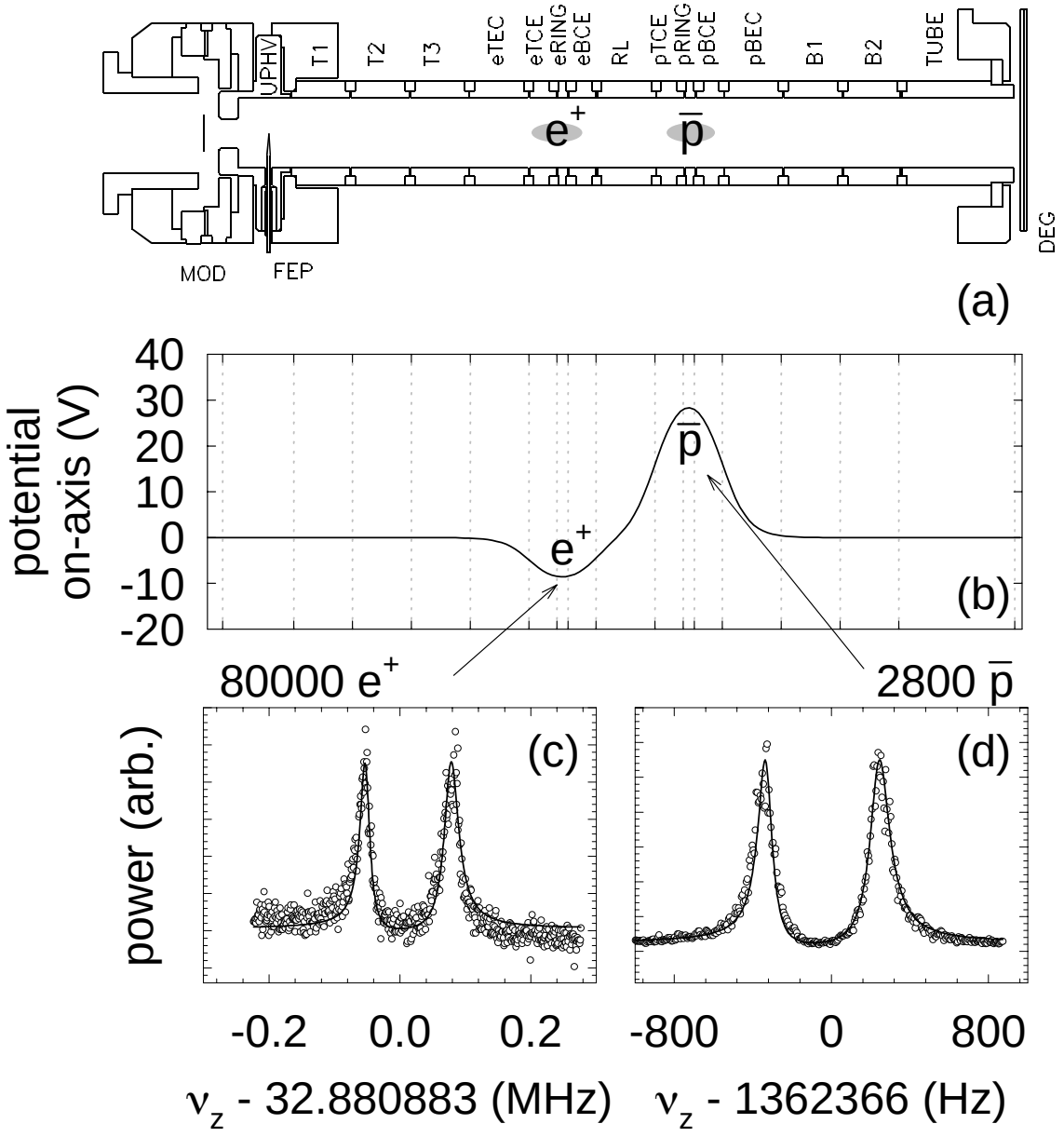

Figure 6.1: Positrons and antiprotons trapped simultaneously. (a) Trap electrodes. (b) Potential on the axis of the trap. The positrons (c) and antiprotons (d) are confined in adjacent trapping regions. This is the first time that the constituents of antihydrogen have been confined together in the same apparatus.

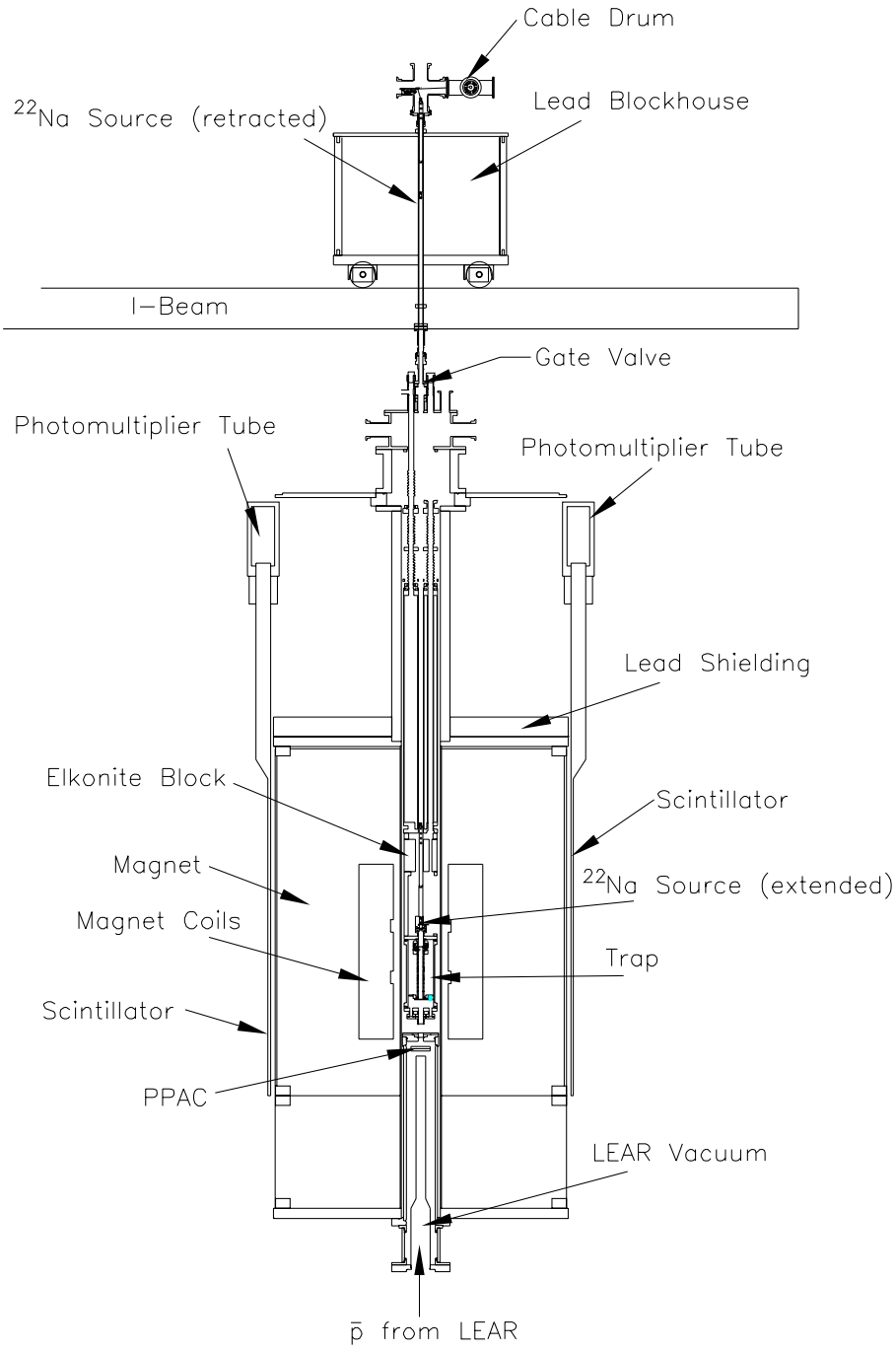

Figure 6.2: Overview of the antiproton/positron apparatus. A lead blockhouse houses the radioactive positron source when it is not in use. Antiprotons are delivered from the accelerator through the beamline attached to the bottom of the magnet.

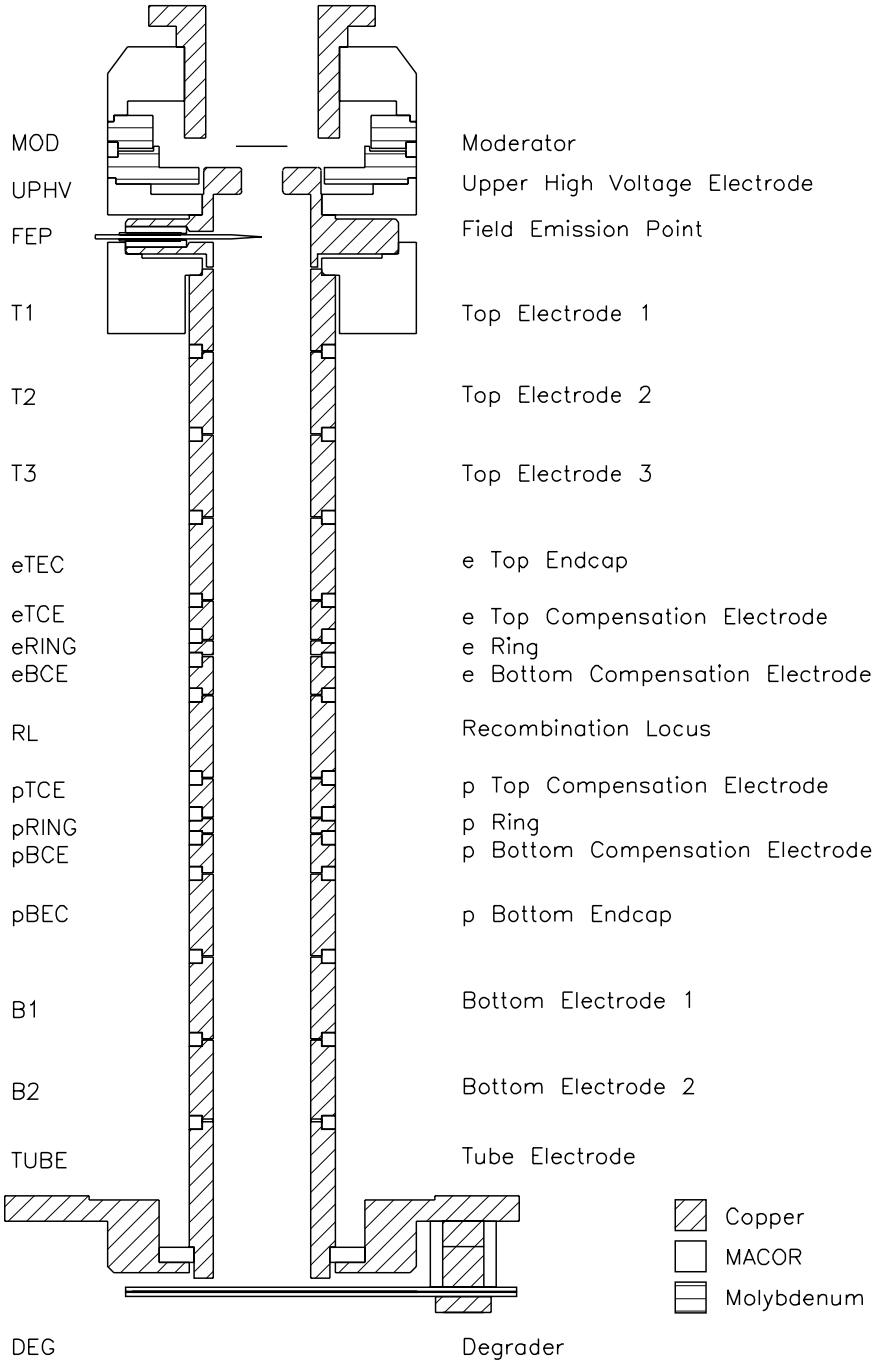

Figure 6.3: Electrodes for the positron/antiproton trap.

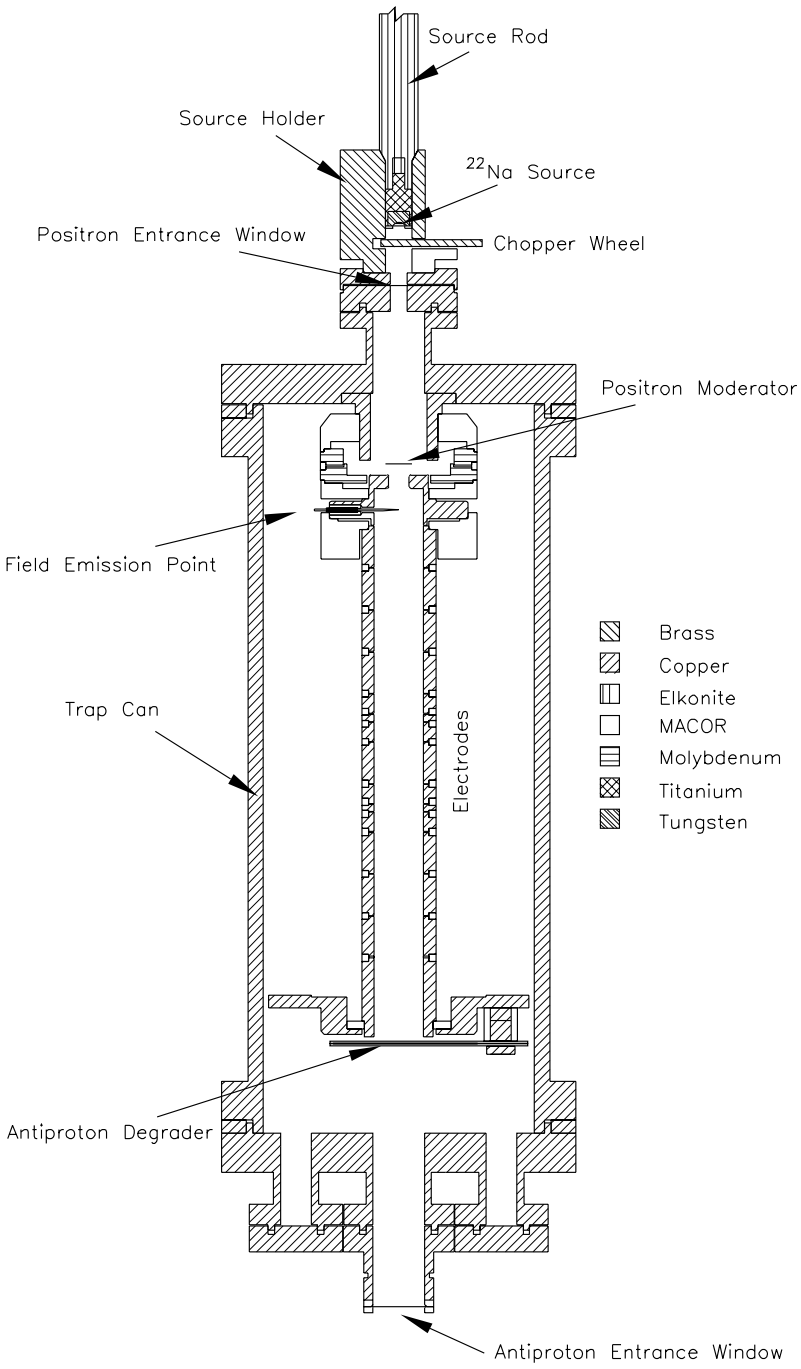

Figure 6.4: Antiproton/positron trap vacuum enclosure. The antiprotons enter through the Ti window at the bottom of the enclosure, and the positrons enter through a corresponding window at the top.

as the various systems of the apparatus were being tested and adjusted. (Trapping rates as high as 16 ± 3 e^+/sec were observed from the moderator, and 3.9 ± 0.8 e^+/sec from the degrader.) The axial signal from the 10^6 positrons is shown in Fig. 6.5(b), where the asymmetry originates from the pi-network matching circuit of the electron axial amplifier (Sec. 2.4.3).

Antiprotons are produced when a 26 GeV proton beam from the CERN proton synchrotron (PS) collides with an iridium target [121, 43]. (The PS accelerator complex is shown in Fig. 6.7). After being magnetically collected and stochastically cooled in the antiproton collector ring (AC), up to 10^{12} $\bar{p}$ are stacked in the antiproton accumulator ring (AA) [121]. The antiprotons are subsequently slowed to 180 MeV in the PS [121] on their way to LEAR, where they are further slowed to 5.9 MeV and resonantly bunched for extraction to the trap. As many as 3×10^9 antiprotons to the trap in a single 250 ns pulse, although numbers on the order of 10^8 were more typical.

The antiprotons enter the trap vacuum enclosure through a 10 μm titanium window (Fig. 6.4) and pass through a 116 μm gold-plated aluminum degrader. The degrader stops about half of the antiprotons, and approximately 1 in 10^4 escape into the trapping region with an energy below 3 keV [2]. These antiprotons reflect from the -3 kV potential applied to the UPHV electrode and are captured by suddenly dropping the degrader potential to -3 kV which completes the trap [2, 122]. After a brief hold time (typically 100 sec) the antiprotons are released from the trap by ramping down the potential on the degrader, and the scintillators detect the pions produced as the antiprotons annihilate on the degrader surface (Fig. 6.8).

A record 0.6×10^6 $\bar{p}$ were trapped in a single pulse from LEAR (Fig. 6.10), the most ever captured in a trap of this size and only 40% less than the maximum number captured in a trap 4 times larger and 4 times deeper [123]. After a 100 sec

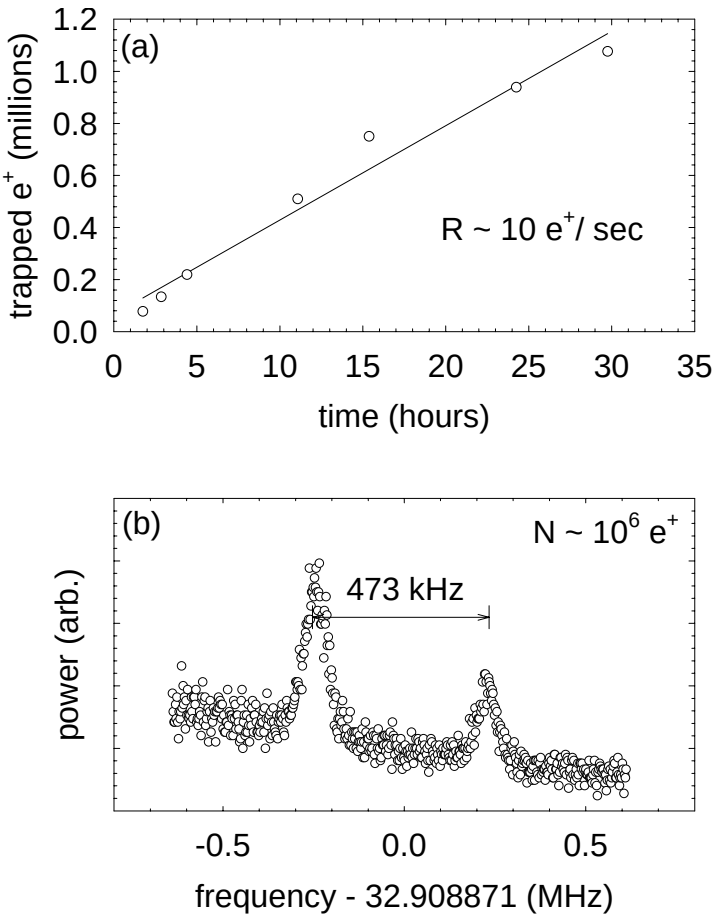

Figure 6.5: Accumulation of one million positrons in the same apparatus used to capture antiprotons. (a) This accumulation curve was taken while other adjustments were being made to the apparatus. Despite the frequent interruptions, an average rate of 10 e^+/sec was maintained. (b) Electrical signal from $1.0 \pm 0.2 \times 10^6$ stored positrons. The absolute numbers are only known to within 20% due to the uncertainty in the detector calibration (see Sec. 6.3).

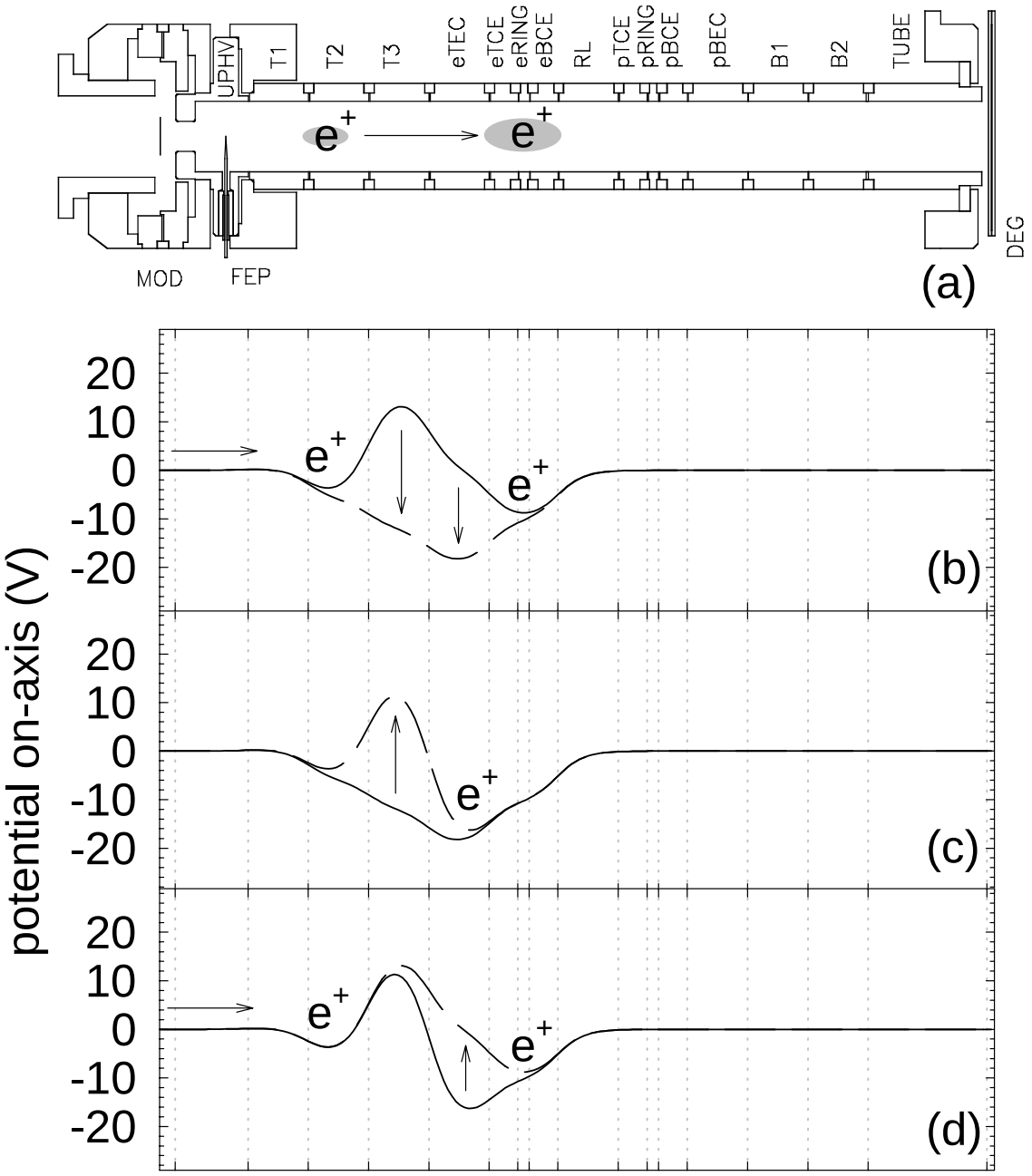

Figure 6.6: Positron accumulation procedure. Positrons are continuously trapped on the T2 electrode and then occasionally added to the larger cloud, maintained under a constant sideband cooling drive, in the electron trap (b)–(d).

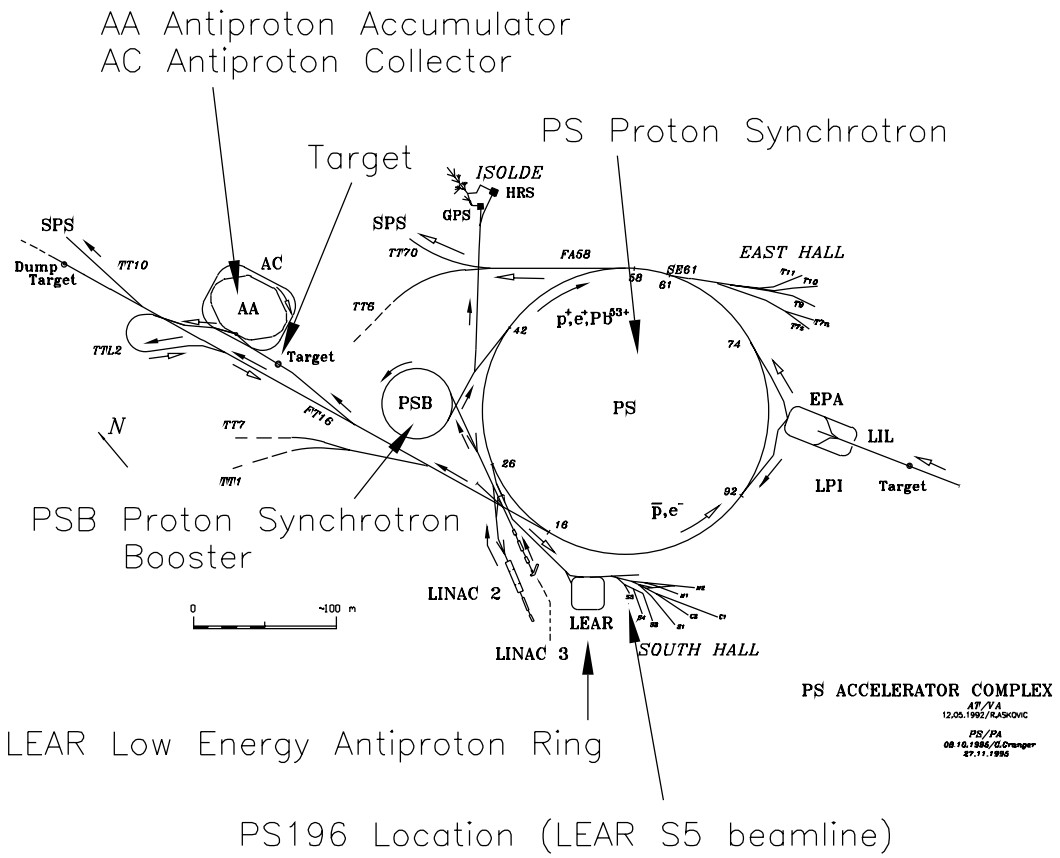

Figure 6.7: The CERN antiproton complex. Antiprotons are formed at the target, collected in the AC, stored in the AA, and transferred to LEAR for further cooling before extraction to the PS196 site.

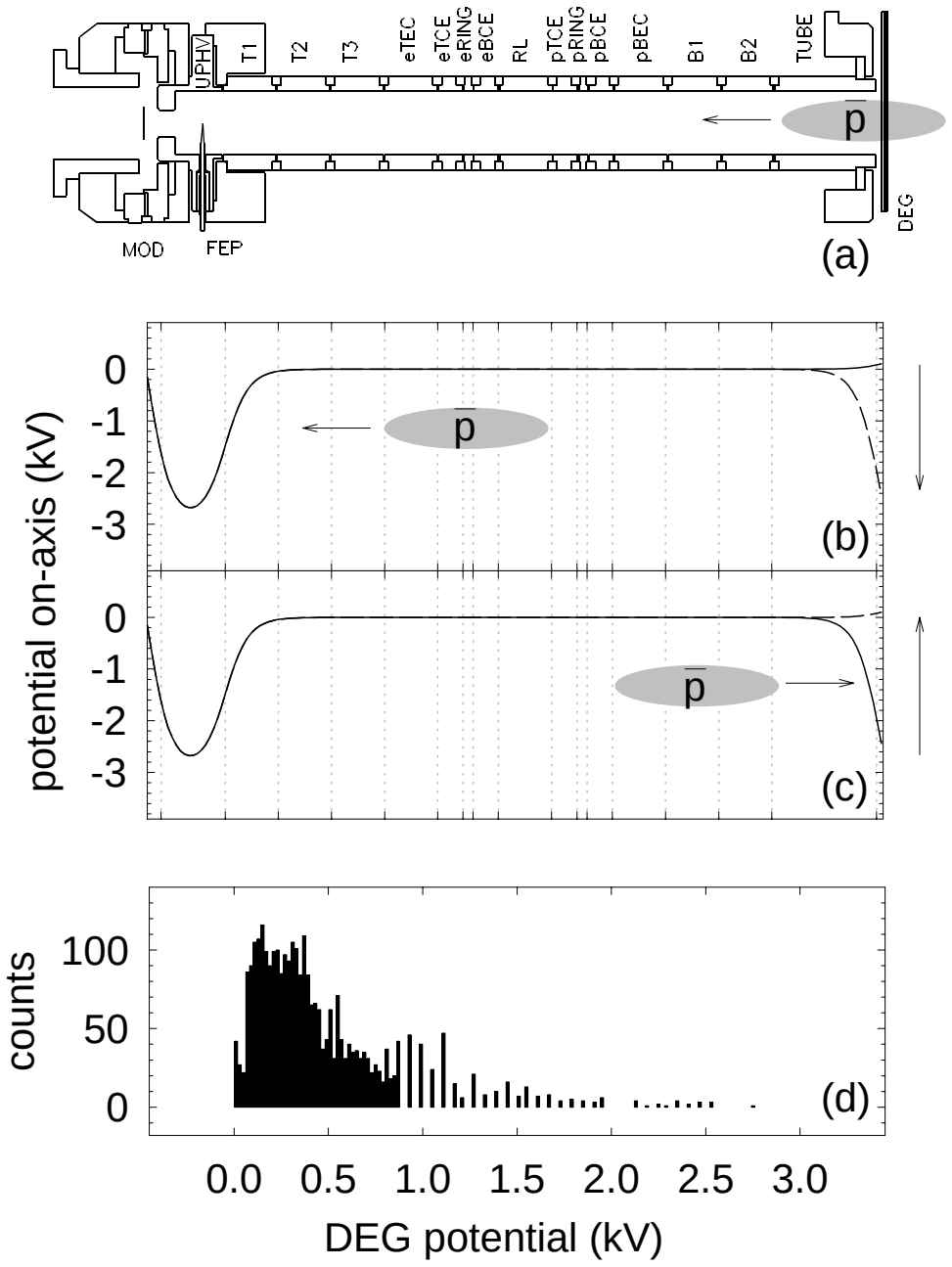

Figure 6.8: Trapping antiprotons. Antiprotons enter the trap through the degrader. Those with energies below 3 keV are caught by dropping the potential on the degrader (b). When the degrader potential is reduced, protons to spill out (c) and are detected by the scintillators (d).

hold time, about two-thirds[1] of the trapped antiprotons were cooled [3] through collisions with $\approx$ 4 million electrons preloaded into the electron trap (Fig. 6.9). Once the electron-cooling is complete (typically within 100 sec), the electrons can be ejected from the trap by quickly pulsing the potential on one electrode [15], leaving the slower antiprotons behind.

Positrons are clearly heated by the antiprotons when they are used in place of the cooling electrons in a nested trap configuration. In Fig. 6.11, approximately 57,000 e^+ are shown before (a) and during (b) the antiproton injection. The large enhancement in the signal occurs as the tuned circuit extracts the axial energy from the antiproton-heated positrons, and implies that the positrons are cooling the antiprotons.

The antiprotons are expected to cool until they have a low relative velocity with respect to the positrons, just as protons are cooled by electrons [1]. In an analysis of the antiproton energies, the cooled antiprotons were discovered at the bottom of the nested trap, rather than at the height of the positron well. This suggests that the positron-cooling process was augmented by the presence of contaminant *electrons*, loaded into the trap during the antiproton pulse. In this scenario, the electrons continued to cool the antiprotons into the bottom of the trap after the positron-cooling was completed.

In addition to contaminant electrons, the antiproton pulse causes contaminant ions to become lodged in the positron cloud, the resulting signal from the trapped positrons becomes quite feeble after the antiprotons are ejected to the degrader. These spectator ions can be avoided by accumulating the positrons *after* the antiprotons have been trapped and electron-cooled, although this introduces an addi-

[1]It is suspected that these cold antiprotons effectively filled the trap, and the remaining hot antiprotons could not be further cooled.

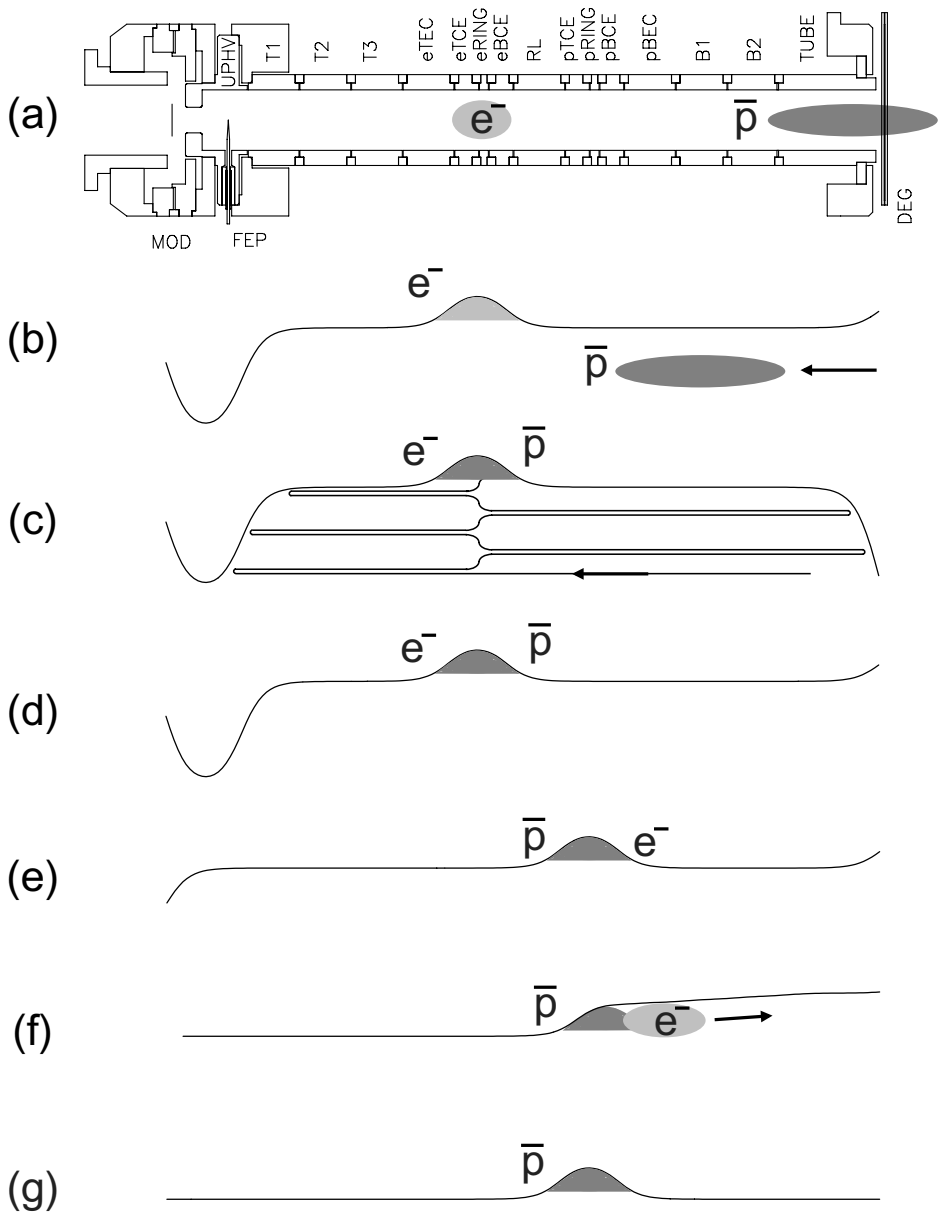

Figure 6.9: Electron cooling of antiprotons (schematic). The antiprotons enter the trap through the aluminum degrader (a). After the antiprotons are in the trap (b), the high-voltage is quickly raised on the degrader (c). The trapped antiprotons are cooled by the electrons, and ultimately fall into the harmonic trapping region (d). The particles are then moved to the proton trap (e) and the electrons are ejected from the trap (f), leaving behind a clean, cold plasma of antiprotons (g).

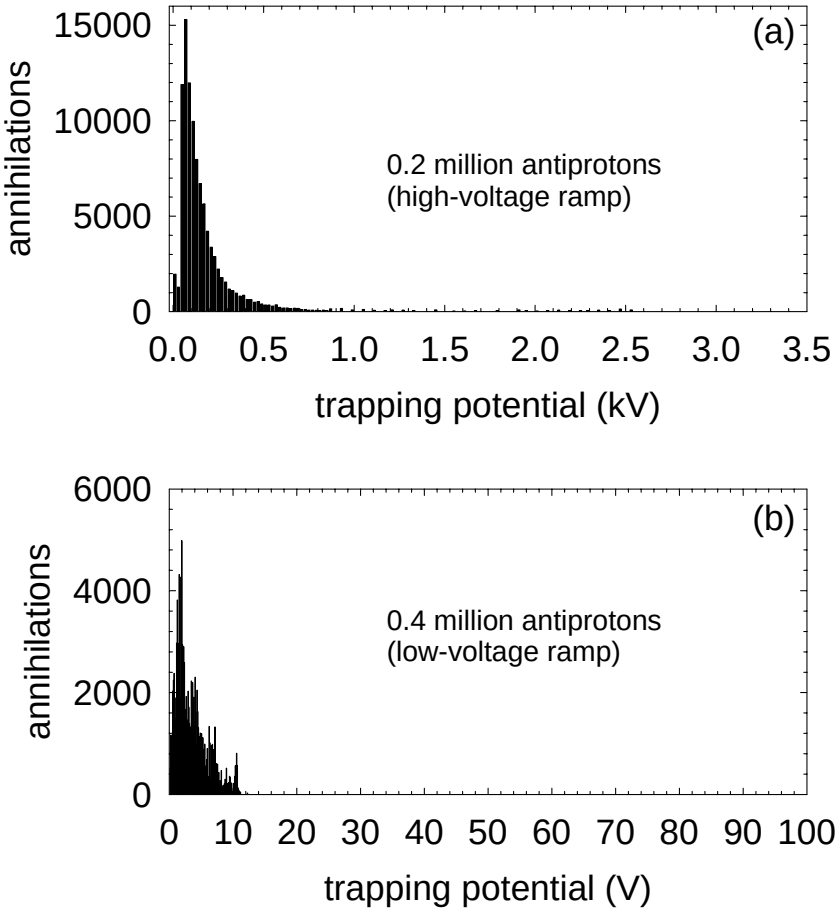

Figure 6.10: Antiprotons captured in a single shot from LEAR. The annihilations detected from the higher-energy antiprotons are shown in (a). The electron-cooled antiprotons are ramped to the degrader separately (b). The total number of counts corresponds to approximately 0.6 million trapped antiprotons.

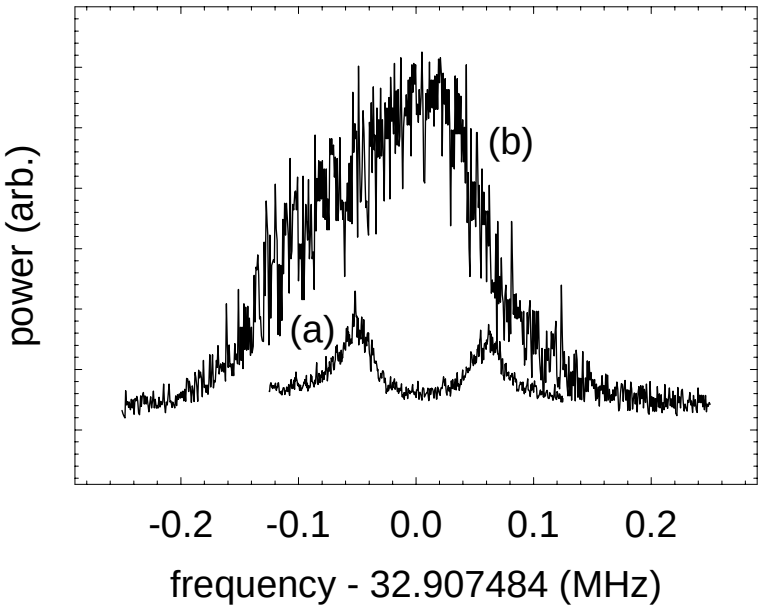

Figure 6.11: Hot antiprotons interact with cold positrons. (a) Electrical signal from 57,000 e^+ stored in an 11 V well prior to antiproton injection. After injection of hot antiprotons (b) the signal is enhanced as the tuned circuit damps the axial energy of the antiproton-heated positrons.

tional level of complexity to the procedure. The positron beam is itself a source of contaminating electrons which become trapped among the antiprotons, but these can be ejected by rapidly pulsing an endcap potential. The contamination of the antiproton cloud can also be reduced by preventing secondary electrons (or highly-excited positronium) from leaving the degrader surface by applying to it a bias of $\approx +50$ V width respect to the TUBE.

Once both plasmas are confined, cleaned, and centered, they may be nondestructively detected and counted using the radiofrequency detection circuits. The axial signals from simultaneously trapped antiprotons and positrons, separated by a mere centimeter, are shown in Fig. 6.1. This was a triumphant moment, involving the synthesis of many different techniques and procedures developed over the a decade

of research towards the production of antihydrogen through the merging of cryogenic plasmas.

The plasmas were subsequently merged in a nested Penning trap configuration [1], as shown in Fig. 6.12. The antiprotons were observed at the energy at which they were injected into the nested trap (≈ 70 eV), not at the reduced energies expected after positron-cooling. The detected signal is probably from antiprotons in large magnetron orbits which oscillate back and forth around (but not through) the relatively modest-sized ($\rho \approx 1$ mm) positron plasma. Sideband-cooling the antiproton cloud shown in Fig. 6.1 proved to be quite challenging, and the cloud often showed signs of axial heating after slightly shifting the potentials applied to the ring and/or the compensation electrodes. It seems that there was a significant population of antiprotons in magnetron orbits too large to be effectively detected by the radiofrequency techniques (see Sec. 6.3, below).

Antiproton trapping had an extremely unfortunate effect on positron trapping which prevented further trials of the antiproton-positron interaction. After having taken some rather intense antiproton shots from LEAR on the first day of antiproton beam, the positron trapping from the moderator stopped. Positrons could still be trapped from the degrader, however, although the rate was reduced to $\approx 2\ e^+$/sec. Since the positron trapping rate had once been reduced by heating the moderator in the cryogenic vacuum and subsequently restored by warming the entire apparatus to room temperature and cooling back to 4 K (Ch. 5), the decision was made to thermally cycle the apparatus — a process which takes almost 24 hours. The thermal cycling successfully restored the trapping rate, suggesting that the antiprotons altered the moderator surface (*e.g.*, scrubbed it clean of a contaminant required for the production of highly-excited positronium, or charged it up). After this experience, care was taken not to eject low-energy antiprotons to the moderator surface.

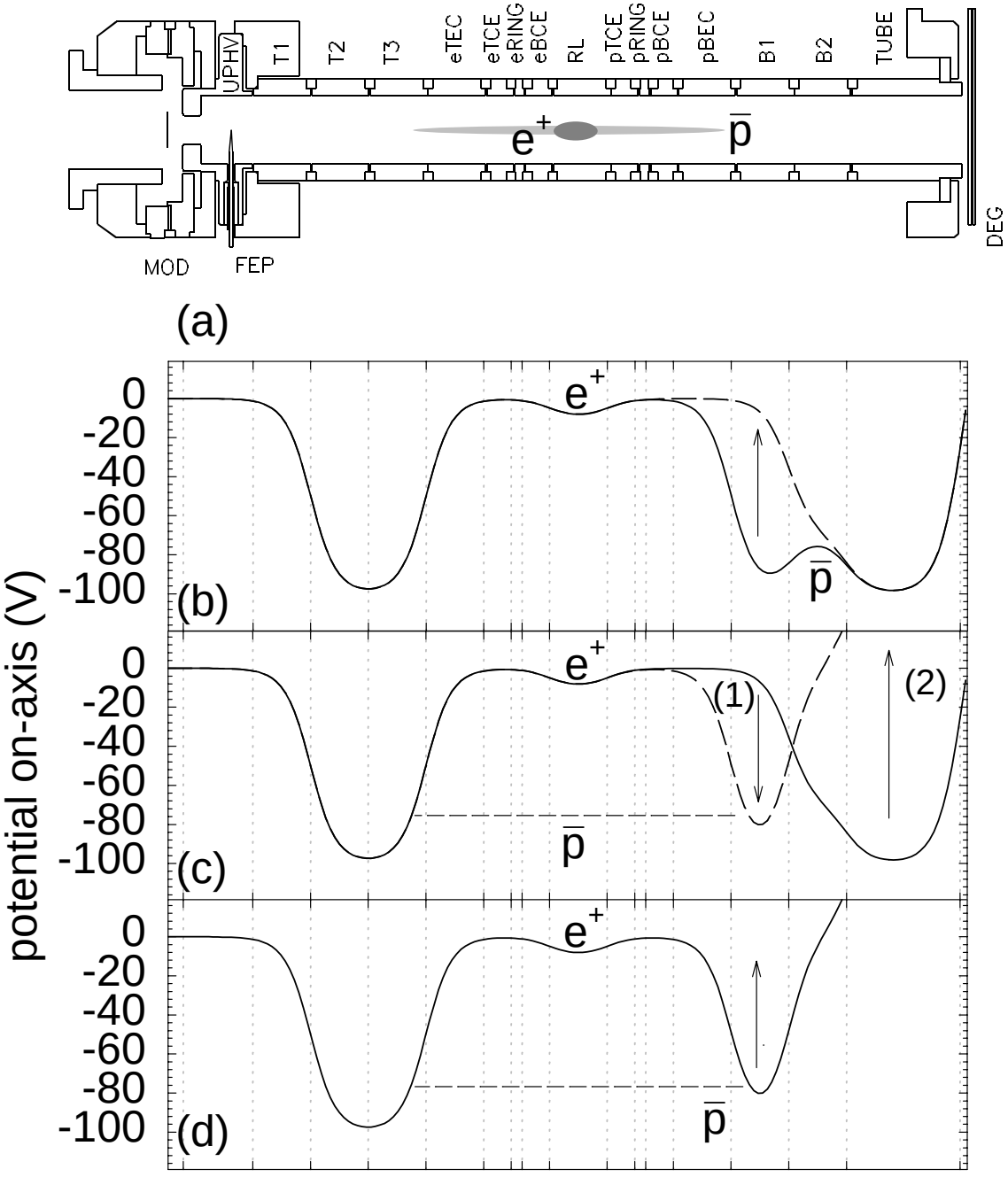

Figure 6.12: Nested trap scheme for interaction studies between positrons and antiprotons. (a) Trap electrodes. The antiprotons are moved to a well on the B2 electrode, whence they are injected into the nested trap (b). The trapping potentials are then restored as shown in (c) to prepare for the detection of the antiprotons as the barrier is eliminated in (d). Results are discussed in the text.

Antiprotons could not be prevented from striking the moderator during the loading sequence, however, and the positron trapping once again stopped after another ≈ 50 antiproton shots. A second thermal cycling restored the trapping, but after a third loss the apparatus was not cycled and other complementary antiproton studies were conducted instead.

One long-term solution to this problem would be to separate the positron and antiproton trapping regions, and other solutions will be sought. The positron trapping mechanism is otherwise quite robust, and the accumulator operated for months with no appreciable reduction in the trapping rate due to the action of the *positron* beam on the moderator surface.

6.2 Conclusions

Positrons and antiprotons are, for the first time, simultaneously confined at 4 K in a Penning trap. An interaction is observed when high-energy antiprotons are injected into a cloud of cold positrons. These are significant steps toward the production of cold antihydrogen.

A number of technical problems were revealed during the nine days of antiproton beam. Contaminants figure prominently, in that positron plasmas subjected to pulses of antiprotons are susceptible to ion contamination, and antiproton plasmas subjected to the positron beam are susceptible to electron contamination. Most challenging is the loss (and return) of the positron trapping mechanism after bombarding the moderator with antiprotons, which might be solved by separating the antiproton and positron trapping regions or by other means.

6.3 Appendix: Details

The three ancestral lines of this apparatus are best seen in its electrode arrangement. The core electrodes, with separate trapping regions for antiprotons and positrons, are arranged in the manner of the recombination apparatus. At the top of the electrode stack is the transmission moderator, familiar from the earlier positron trapping studies (Ch. 5). Just below the moderator is an unusually-shaped electrode (UPHV) designed to be biased to -3 kV to confine antiprotons. The UPHV electrode is surrounded by a set of large MACOR spacers to stand off the high voltage (the dielectric strength of MACOR is observed to decline precipitously at low temperatures, enforcing a design with a minimum of 1/4" of MACOR between points at high potential with respect to one another). Two field emission points (FEPs) poke through small holes to provide electrons for diagnostics. The FEPs are insulated from the UPHV by thin alumina sleeves, and can therefore be independently biased from the UPHV electrode. At the bottom of the electrode stack is a 116 μm thick gold-plated aluminum disk used to slow antiprotons to energies at which they can be trapped. The degrader is mounted with alumina standoffs so that it, too, can be biased to -3 kV.

In order not to saturate the six scintillators which surround the superconducting magnet with gamma radiation from the ^{22}Na positron source, and to permit experimenters to work in the experimental zone when positrons are not being trapped, an elevator and lead blockhouse system was constructed to house the radioactive positron source (Fig. 6.13). The source rests in a 1/2" diameter stainless-steel tube which passes through $\approx$ 40 lead blocks stacked in an aluminum frame. A set of aluminum wheels permit the blockhouse to roll out of position along two aluminum I-beam rails (Fig. 6.14), enabling removal of the lower part of the apparatus from

the bore of the superconducting magnet for servicing.

A set of small vacuum chambers atop the blockhouse houses the source elevator system, which consists of a source rod, cable, cable drum, and motor. The source rod is very similar to the one used in the earlier positron experiments (Fig. 5.2), except that the lower half of the rod is machined of Elkonite (rather than brass) to provide additional radiation shielding, and is tapered (rather than threaded) to settle smoothly into the brass source holder. The cable is braided DACRON fly line, 30 lb test [124] which retains its strength and flexibility at 4 K. It is tied through a hole in the top of the source rod and secured with a drop of epoxy to insure that the knot does not come undone. A computer-controlled stepping motor winds the cable on its drum.

To trap positrons, the blockhouse is rolled into position above the magnet and the stainless-steel source tube attached (with a VCO fitting) to a gate valve on the brass hat. The blockhouse/elevator vacuum system is pumped down to a few mTorr, after which the gate valve is opened and the helium dewar cryopumps the blockhouse. The source can then be lowered down the central axis of the apparatus until it settles into the source holder in the cold electronics region. With the source in the magnet bore, the experimenters are well-shielded from the source by the concrete blocks which surround the experimental zone. A layer of lead blocks was placed on the upper surface of the magnet to shield the crane drivers who occasionally work overhead.

The elevator system is controlled through a computer interface which simultaneously monitors the position of the source, the tension in the cable, and the background radiation level in the zone. Either the computer or the experimenters (by means of a "panic button" on the console) can arrest the source motion if anything goes awry, and the motor will cut out on its own if the cable tension exceeds

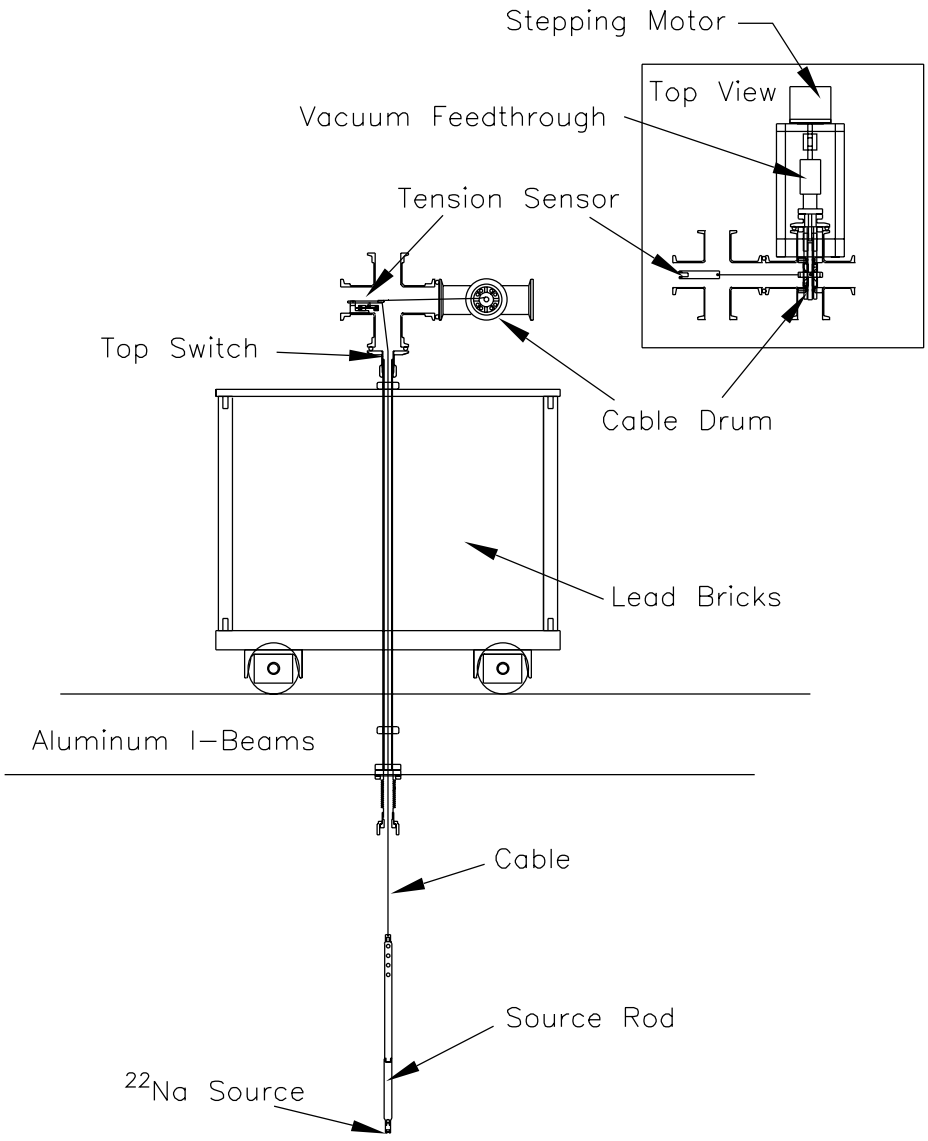

Figure 6.13: Lead blockhouse and elevator assembly. The source is retracted into the blockhouse for safekeeping, and can be lowered into the apparatus to load positrons.

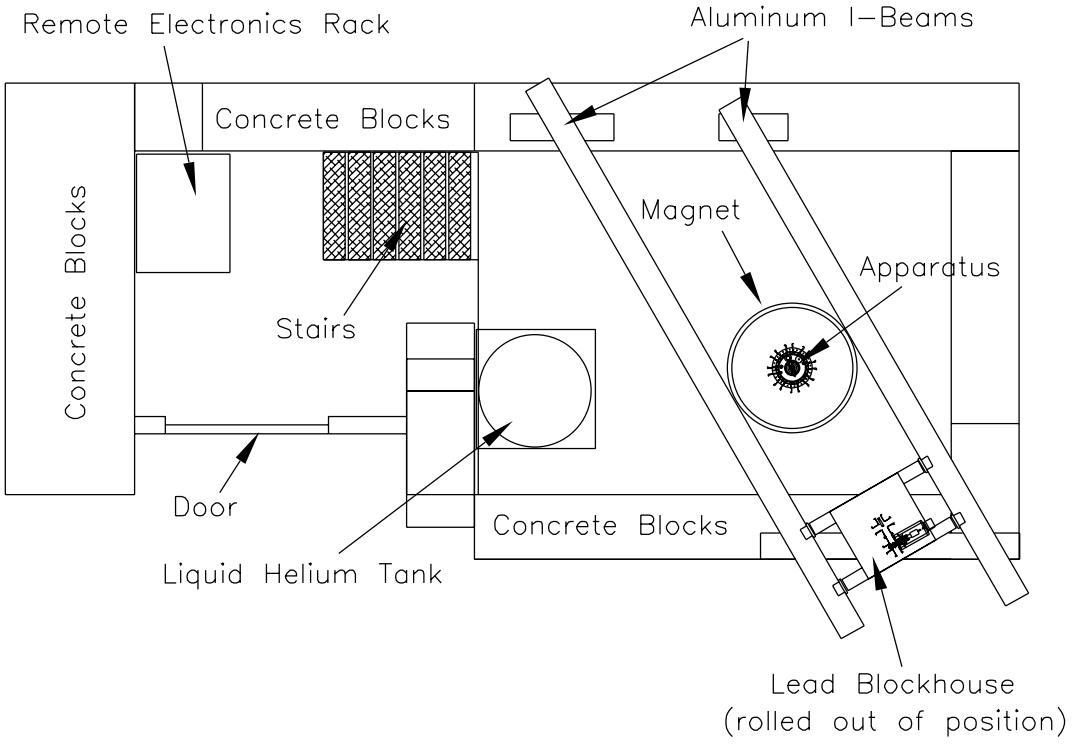

Figure 6.14: Crane driver's eye view of the experimental zone. The lead blockhouse is shown rolled out of position as it would be if the lower section of the apparatus were being serviced.

a predefined limit. A video camera is aimed at the cable through a plexiglass port, permitting direct inspection of the cable speed and tension as the source is raised and lowered.

Two mechanical switches define the limits of the source motion. One switch is tripped when the source is fully retracted into the blockhouse, causing the computer to cut power to the motor. (The video camera and background radiation monitors are always used to verify that the source is safely in the blockhouse before people enter the zone.) The second switch is tripped when the source reaches the cold electronics region, and is verified by the slack in the cable as it is unreeled further.

The source rod tends to rapidly boil off helium from the liquid helium reservoir

when it is lowered into the apparatus, and has enough thermal mass to entirely empty the helium dewar before cooling to 4 K. For safety reasons, the source must be retracted into the (room-temperature) lead blockhouse during the ≈ 10 minutes it takes to refill the reservoir, warming slightly and making iterative cooling something of a Sisyphean endeavor. By reducing the thermal contact between the rod and the source holder (*e.g.*, by lifting it slightly from the source holder), however, the hot source rod can stay in place for several hours *without* additional helium fills. A better long-term approach may be to pre-cool the source with liquid nitrogen (or cold helium exhaust gas) to further minimize the heat load on the system.

The apparatus wiring is very similar to those of the previous traps [Figs. 2.8 (p. 31) and 5.31 (p. 162)]. The only major change is the addition of "pulser" lines (stainless-steel microcoaxial cables) which are AC-coupled to the eTEC and pBEC electrodes (Fig. 6.15) to permit the fast endcap pulses necessary to remove electrons or positrons from the trap while retaining the heavier particles (protons or antiprotons).

The proton axial resonant circuit was calibrated as described in Ch. 3, but later moved from the original electron-proton apparatus to the positron-antiproton apparatus. Since the coil inductance is not expected to change appreciably, its value of γ_z (the damping width per proton) is scaled by its center frequency ω_z and quality factor Q, as described in Sec. 5.9.4 (p. 164), giving $\gamma_z/2\pi \approx 0.6$ Hz. By dumping the nondestructively-counted antiprotons to the scintillators, a calibration curve may be constructed (Fig. 6.16) which relates γ_z to the detection efficiency ϵ. An earlier calibration of the antiproton detection efficiency gives $(47\pm3)\%$ [43], yielding a value $\gamma_z/2\pi \approx 0.2$ Hz. Since it is difficult to imagine either calibration being off by a factor of 3, it is suspected that additional antiprotons (occupying large magnetron orbits within the trap) are not seen by the radiofrequency detector but are nonetheless

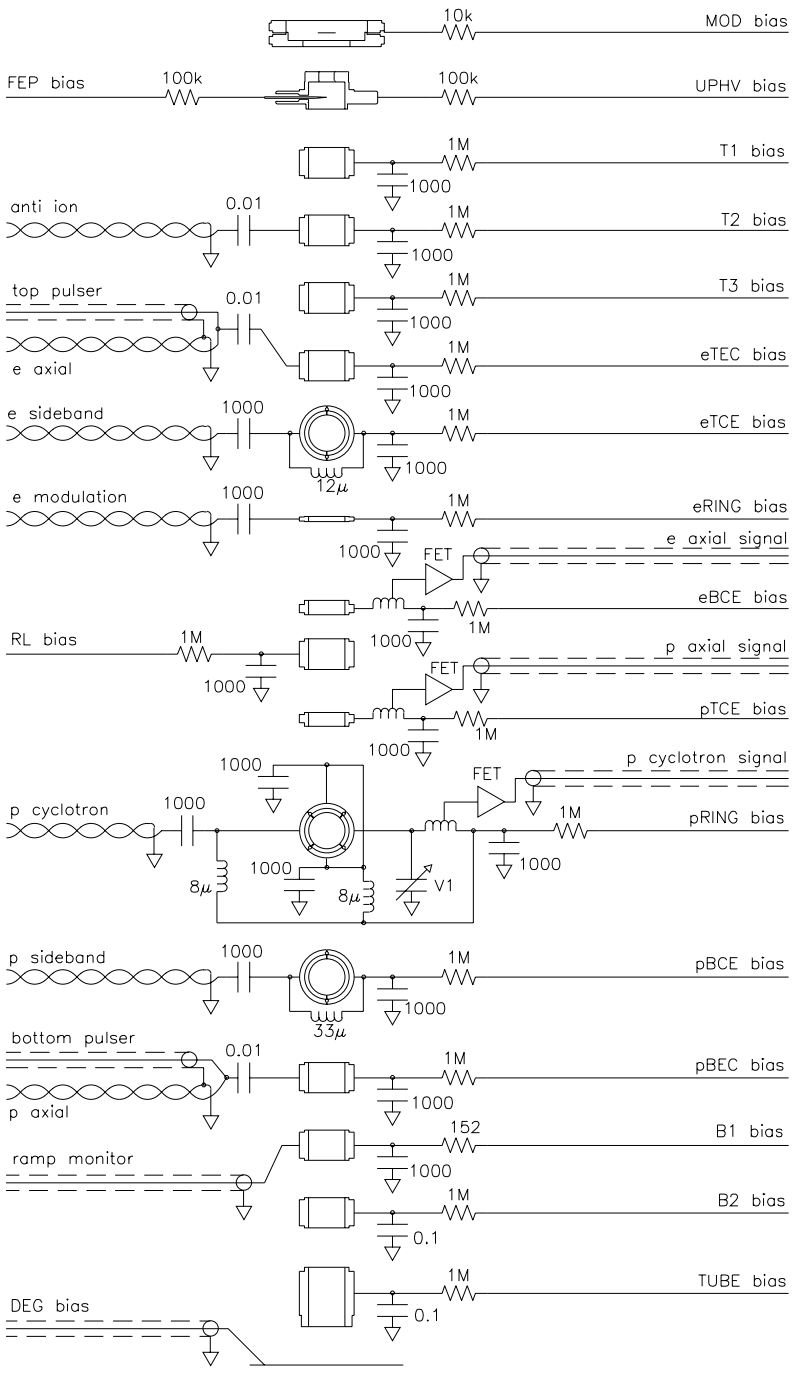

Figure 6.15: Wiring diagram for the positron/antiproton trap.

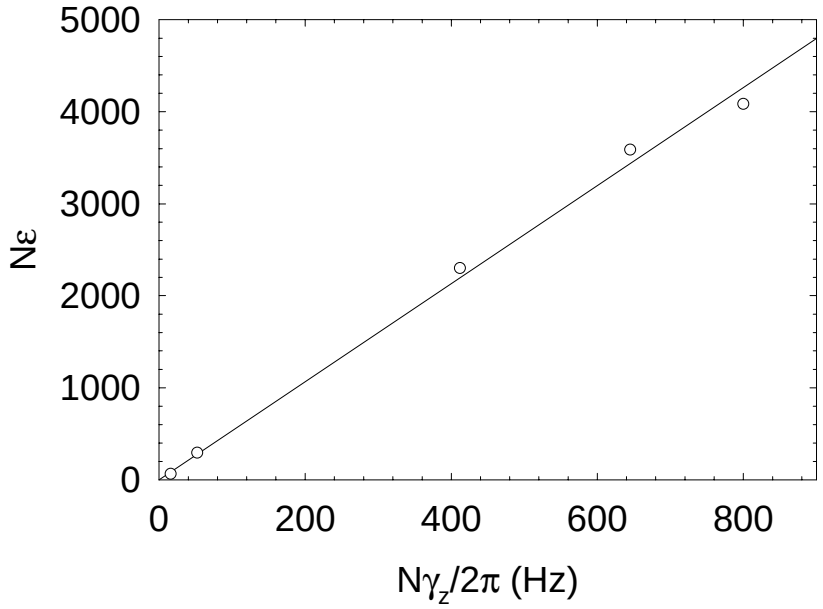

Figure 6.16: Scintillator detection efficiency $N\epsilon$ as a function of dip width $N\gamma_z/2\pi$ for varying numbers of antiprotons N. A similar technique (counting protons via their cyclotron motion) will be used in the future to calibrate the efficiency of the destructive antiproton detectors.

detected by the scintillators when they strike the degrader surface and annihilate. This is also consistent with the difficulties experienced in magnetron-cooling the antiprotons, as described in Sec. 6.1.

There was little opportunity to load small electron (or positron) clouds to extensively calibrate the electron axial amplifier, so the calibration of Sec. 5.9.4 was retained (*i.e.*, $\gamma_z = 2\pi \cdot (5.1 \pm 1.0)$ Hz), adjusted for the new values of the resonance center frequency and Q.

Chapter 7

Conclusions

Much progress has been made towards producing cold (anti)hydrogen through the merging of cryogenic trapped plasmas. Clean clouds of protons and electrons are now routinely loaded, centered, made to interact, and counted using both nondestructive and destructive detection techniques. The particles are easily moved about the interior of the trapping region, and an interaction in which electrons cool protons has been observed in the context of a nested Penning trap [1], suggesting that recombination is not far away. For the corresponding experiments with antimatter, a new accumulation technique traps more than one million cryogenic positrons at rates up to 150 times higher than those observed in a previous cryogenic accumulator (per unit of source activity). A positron/antiproton trap makes use of this trapping mechanism in an open-access electrode geometry for the first demonstration of simultaneous confining and merging of cryogenic positron and antiproton plasmas.

Several issues remain. Most importantly, (anti)hydrogen recombination must be demonstrated using the merged-plasma approach. Reduction of the trapping fields will permit highly-excited antihydrogen to survive long enough to reach an electrode

surface, annihilate, and be detected by coincident observation of the annihilation pions and 511 keV photons. A laser tuned to de-excite atoms to a low-lying quantum level may assist the recombination rates. Depletion of the number of trapped particles, and possibly detection of the photons accompanying de-excitation of the resulting atoms, may provide further evidence of recombination.

The positron trapping mechanism must be better understood in order to be further optimized. A larger source activity will certainly yield higher trapping rates, and it is possible that other improvements may follow. Of course, the difficulties associated with antiproton bombardment of the moderator must be resolved. Finally, the contaminants in the antiproton and positron clouds must be eliminated. Many reliable anti-contaminant routines have been developed for these experiments, not all of which were fully brought to bear on the problem during the 9 days available.

Once recombination is demonstrated, the neutral anti-atoms will be magnetically trapped and interrogated for the test of CPT and gravity. These experiments will undoubtedly prove to be extremely challenging, and numerous technical issues remain to be solved. These challenges make the experiments exciting, and promise even greater rewards in the years to come.

Bibliography

[1] D. S. Hall and G. Gabrielse, Phys. Rev. Lett. **77**, 1962 (1996).

[2] G. Gabrielse, X. Fei, S. L. Rolston, R. Tjoelker, T. A. Trainor, H. Kalinowsky, J. Haas, and W. Kells, Phys. Rev. Lett. **57**, 2504 (1986).

[3] G. Gabrielse, X. Fei, L. A. Orozco, R. L. Tjoelker, J. Haas, H. Kalinowsky, T. A. Trainor, and W. Kells, Phys. Rev. Lett. **63**, 1360 (1989).

[4] L. H. Haarsma, K. Abdullah, and G. Gabrielse, Phys. Rev. Lett. **75**, 806 (1995).

[5] W. Quint, R. Kaiser, D. Hall, and G. Gabrielse, Hyperfine Interact. **76**, 181 (1993).

[6] G. Baur *et al.*, Phys. Lett. B **368**, 251 (1996).

[7] T. D. Lee and C. N. Yang, Phys. Rev. **104**, 254 (1956).

[8] C. S. Wu, E. Ambler, R. W. Hayward, D. D. Hoppes, and R. P. Hudson, Phys. Rev. **105**, 1413 (1957).

[9] L. Landau, Nucl. Phys. **3**, 127 (1957).

[10] M. Gell-Mann and A. Pais, Phys. Rev. **97**, 1387 (1955).

[11] J. H. Christenson, J. W. Cronin, V. L. Fitch, and R. Turlay, Phys. Rev. Lett. **13**, 138 (1964).

[12] Claude Itzykson and Jean-Bernard Zuber, *Quantum Field Theory* (McGraw-Hill Book Company, New York, 1980), p. 157.

[13] R. Carosi *et al.*, Phys. Lett. B **237**, 303 (1990).

[14] Robert S. Van Dyck, Jr., Paul B. Schwinberg, and Hans G. Dehmelt, Phys. Rev. Lett. **59**, 26 (1987).

[15] G. Gabrielse, D. Phillips, W. Quint, H. Kalinowsky, G. Rouleau, and W. Jhe, Phys. Rev. Lett. **74**, 3544 (1995).

[16] F. Schmidt-Kaler, D. Leibfried, S. Seel, C. Zimmermann, W. König, M. Weitz, and T. W. Hänsch, Phys. Rev. A **51**, 2789 (1995).

[17] J. Scherk, Phys. Lett. B **88**, 265 (1979).

[18] T. Goldman, Richard J. Hughes, and Michael Martin Nieto, Phys. Lett. B **171**, 217 (1986).

[19] F. C. Witteborn and W. M. Fairbank, Phys. Rev. Lett. **19**, 1049 (1967).

[20] Ronald E. Brown, J. B. Camp, and T. W. Darling, Nucl. Instrum. Meth. B **56/57**, 480 (1991).

[21] G. Gabrielse, Hyperfine Interact. **44**, 349 (1988).

[22] D. S. Weiss, M. Kasevich, B. Young, and S. Chu, in *Atomic Physics 13: Thirteenth International Conference on Atomic Physics*, AIP Conference Proceedings No. 275, edited by H. Walther, T. W. Hänsch, and B. Neizert (American Institute of Physics, New York, 1992), p. 132.

[23] E. G. Adelberger, B. R. Heckel, C. W. Stubbs, and Y. Su, Phys. Rev. Lett. **66**, 850 (1991).

[24] G. Gabrielse, S. L. Rolston, L. Haarsma, and W. Kells, Phys. Lett. A **129**, 38 (1988).

[25] D. R. Bates and A. Dalgarno, *Atomic and Molecular Processes* (Academic Press, New York, 1962), p. 245.

[26] J. Stevefelt, J. Boulmer, and J.-F. Delpech, Phys. Rev. A **12**, 1248 (1975).

[27] R. Neumann, H. Poth, A. Winnacker, and A. Wolf, Z. Phys. A **313**, 253 (1983).

[28] G. Gabrielse, S. Rolston, L. Haarsma, and W. Kells, Phys. Lett. A **129**, 38 (1988).

[29] Michael E. Glinsky and Thomas M. O'Neil, Phys. Fluids B **3**, 1279 (1991).

[30] P. O. Fedichev, Phys. Lett. A **226**, 289 (1997).

[31] J. P. Schermann and F. G. Major, Ann. Phys. **16**, 225 (1978).

[32] J. Walz, S. B. Ross, C. Zimmermann, L. Ricci, M. Prevedelli, and T. W. Hänsch, Phys. Rev. Lett. **75**, 3257 (1995).

[33] B. I. Deutch, F. M. Jacobsen, L. H. Andersen, P. Hvelplund, and H. Knudsen, Phys. Scr. **T22**, 248 (1988).

[34] J. W. Humberston, M. Charlton, F. M. Jacobsen, and B. I. Deutch, J. Phys. B **20**, L25 (1987).

[35] J. P. Merrison, H. Bluhme, J. Chevallier, B. I. Deutch, P. Hvelplund, L. V. Jørgensen, H. Knudsen, M. R. Poulsen, and M. Charlton, Phys. Rev. Lett. **78**, 2728 (1997).

[36] M. Charlton, Phys. Lett. A **143**, 143 (1990).

[37] L. S. Brown and G. Gabrielse, Rev. Mod. Phys. **58**, 233 (1986).

[38] G. Gabrielse, L. Haarsma, and S. L. Rolston, Int. J. Mass. Spectrom. Ion Proc. **88**, 319 (1989).

[39] John David Jackson, *Classical Electrodynamics*, 2nd ed. (John Wiley and Sons, New York, 1975).

[40] Robert Lee Tjoelker, Ph.D. thesis, Harvard University, Cambridge, Massachusetts, 1990.

[41] Acton Research Corporation, Acton, Massachusetts 01720.

[42] G. Gabrielse, X. Fei, L. A. Orozco, R. L. Tjoelker, J. Haas, H. Kalinowsky, T. A. Trainor, and W. Kells, Phys. Rev. Lett. **65**, 1317 (1990).

[43] Xiang Fei, Ph.D. thesis, Harvard University, Cambridge, Massachusetts, 1990.

[44] W. W. Macalpine and R. O. Schildknecht, Proc. IRE **57**, 2099 (1959).

[45] David Forrest Phillips, Ph.D. thesis, Harvard University, Cambridge, Massachusetts, 1996.

[46] G. Gabrielse, J. Grobner, W. Jhe, H. Kalinowsky, D. Phillips, and W. Quint, Nucl. Phys. A **558**, 701c (1993).

[47] Anton Nabil Khabbaz, Ph.D. thesis, Harvard University, Cambridge, Massachusetts, (in progress).

[48] Microwave Device Technologies Corporation, Westford, Massachusetts 01886.

[49] 2850FT Blue, from Emerson & Cuming, Inc., Woburn, Massachusetts 01888.

[50] Joseph Ladislas Wiza, Nucl. Instrum. Meth. **162**, 587 (1979).

[51] G. W. Fraser, J. F. Pearson, G. C. Smith, M. Lewis, and M. A. Barstow, IEEE Trans. Nucl. Sci. **NS-30**, 455 (1983).

[52] E. Morenzoni, K. Oba, E. Pedroni, and D. Taqqu, Nucl. Instrum. Meth. A **263**, 397 (1991).

[53] G. W. Fraser, M. T. Pain, J. E. Lees, and J. F. Pearson, Nucl. Instrum. Meth. A **306**, 247 (1991).

[54] National Instruments, Austin, Texas 78730.

[55] Loren Dean Haarsma, Ph.D. thesis, Harvard University, Cambridge, Massachusetts, 1994.

[56] W. Thompson and S. Hanrahan, J. Vac. Sci. Tech. **14**, 643 (1977).

[57] *The ARRL Handbook for the Radio Amateur*, 67th ed., edited by Kirk A. Kleinschmidt (American Radio Relay League, Newington, Connecticut, 1990).

[58] D. J. Wineland and H. G. Dehmelt, J. Appl. Phys. **46**, 919 (1975).

[59] W. Shockley, J. Appl. Phys. **9**, 635 (1938).

[60] Murray D. Sirkis and Nick Holonyak, Jr., Am. J. Phys. **34**, 943 (1966).

[61] Joseph Ngai Tan, Ph.D. thesis, Harvard University, Cambridge, Massachusetts, 1992.

[62] Ching-Hua Tseng, Ph.D. thesis, Harvard University, Cambridge, Massachusetts, 1995.

[63] R. R. Goruganthu and W. G. Wilson, Rev. Sci. Instrum. **55**, 2030 (1984).

[64] A. Müller, N. Djurić, G. H. Dunn, and D. S. Belić, Rev. Sci. Instrum. **57**, 349 (1986).

[65] G. W. Fraser, Nucl. Instrum. Meth. **206**, 445 (1983).

[66] B. Brehm, J. Grosser, T. Ruscheinski, and M. Zimmer, Meas. Sci. Tech. **6**, 953 (1995).

[67] J. A. Schecker, M. M. Schauer, K. Holzscheiter, and M. Holzscheiter, Nucl. Instrum. Meth. A **320**, 556 (1992).

[68] C. F. Driscoll and J. H. Malmberg, Phys. Rev. Lett. **50**, 167 (1983).

[69] C. F. Driscoll, K. S. Fine, and J. H. Malmberg, Phys. Fluids **29**, 2015 (1996).

[70] Michael E. Glinsky, Thomas M. O'Neil, and Marshall N. Rosenbluth, Phys. Fluids B **4**, 1156 (1992).

[71] B. R. Beck, J. Fajans, and J. H. Malmberg, Phys. Rev. Lett. **68**, 317 (1992).

[72] J. Tan and G. Gabrielse, Phys. Rev. A **48**, 3105 (1993).

[73] Y. Wang and K. P. Wanczek, Rev. Sci. Instrum. **64**, 883 (1993).

[74] V. H. Vartanian and D. A. Laude, Org. Mass. Spec. **29**, 692 (1994).

[75] L. D. Landau and E.M. Lifshitz, *Mechanics*, 3rd ed. (Pergamon Press, New York, 1976), p. 154.

[76] William H. Press, Saul A. Teukolsky, William T. Vetterling, and Brian P. Flannery, *Numerical Recipes in C: The Art of Scientific Computing*, 2nd ed. (Cambridge University Press, New York, 1992).

[77] D. J. Larson, J. C. Bergquist, J. J. Bollinger, Wayne M. Itano, and D. J. Wineland, Phys. Rev. Lett. **57**, 70 (1986).

[78] Lyman Spitzer, *Physics of Fully Ionized Gases* (Interscience Publishers, New York, 1952).

[79] Wulf B. Kunkel and Marshall N. Rosenbluth, in *Plasma Physics in Theory and Application*, edited by Wulf B. Kunkel (McGraw-Hill, New York, 1966), Chap. 1.

[80] S. L. Rolston and G. Gabrielse, Hyperfine Interact. **44**, 233 (1988).

[81] A. Wolf, H. Poth, W. Schwab, B. Seligmann, M. Wörtge, H. Haseroth, C. E. Hill, and J.-L. Vallet, Hyperfine Interact. **44**, 217 (1988).

[82] New England Nuclear Corp., Boston, Massachusetts 02118.

[83] L. D. Hulett, J. M. Dale, and S. Pendyala, Surf. Interf. Anal. **2**, 204 (1980).

[84] G. R. Massoumi, Peter J. Schultz, W. N. Lennard, and J. Ociepa, Nucl. Instrum. Meth. B **30**, 592 (1988).

[85] A. P. Mills, Jr., P. M. Platzman, and B. L. Brown, Phys. Rev. Lett. **41**, 1076 (1978).

[86] Peter J. Schultz and K. G. Lynn, Rev. Mod. Phys. **60**, 701 (1988).

[87] K. F. Canter, A. P. Mills, Jr., and S. Berko, Phys. Rev. Lett. **33**, 7 (1974).

[88] Allen P. Mills, Jr., Phys. Rev. Lett. **41**, 1828 (1978).

[89] D. A. Fischer, K. G. Lynn, and D. W. Gidley, Phys. Rev. B **33**, 4479 (1986).

[90] M. Charlton and G. Laricchia, Hyperfine Interact. **76**, 97 (1993).

[91] R. H. Howell, I. J. Rosenberg, and M. J. Fluss, Phys. Rev. B **34**, 3069 (1986).

[92] T. D. Steiger and R. S. Conti, Phys. Rev. A **45**, 2744 (1992).

[93] D. C. Schoepf, S. Berko, K. F. Canter, and P. Sferlazzo, Phys. Rev. A **45**, 1407 (1992).

[94] Kazem Omidvar, Phys. Rev. A **12**, 911 (1975).

[95] K. F. Canter, P. G. Coleman, T. C. Griffith, and G. R. Heyland, J. Phys. B **5**, L167 (1972).

[96] K. G. Lynn, B. Nielsen, and J. H. Quateman, Appl. Phys. Lett. **47**, 239 (1985).

[97] R. M. Nieminen and C. H. Hodges, Solid State Comm. **18**, 1115 (1976).

[98] Ronald C. Davidson, *An Introduction to the Physics of Nonneutral Plasmas*, 2nd ed. (Addison-Wesley Publishing Company, Reading, Massachusetts, 1989), p. 42.

[99] T. C. Griffith and G. R. Heyland, Phys. Rev. **39C**, 171 (1978).

[100] P. G. Coleman, T. C. Griffith, G. R. Heyland, and T. L. Killeen, J. Phys. B **8**, 1734 (1975).

[101] G. Laricchia, M. Charlton, T. C. Griffith, and G. R. Heyland, J. Phys. B **20**, 1865 (1987).

[102] G. R. Heyland, M. Charlton, T. C. Griffith, and G. L. Wright, Can. J. Phys. **60**, 503 (1982).

[103] K. Iwata, R. G. Greaves, T. J. Murphy, M. D. Tinkle, and C. M. Surko, Phys. Rev. A **51**, 473 (1995).

[104] G. L. Wright, M. Charlton, T. C. Griffith, and G. R. Heyland, J. Phys. B **18**, 4327 (1985).

[105] T. J. Murphy and C. M. Surko, Phys. Rev. A **46**, 5696 (1992).

[106] P. B. Schwinberg, R. S. Van Dyck, Jr., and H. G. Dehmelt, Phys. Lett. **81A**, 119 (1981).

[107] R. S. Conti, B. Ghaffari, and T. D. Steiger, Nucl. Instrum. Meth. A **299**, 420 (1990).

[108] R. S. Conti, B. Ghaffari, and T. D. Steiger, Hyperfine Interact. **76**, 127 (1993).

[109] B. Ghaffari and R. S. Conti, Phys. Rev. Lett. **75**, 3118 (1995).

[110] T. E. Cowan, B. R. Beck, J. H. Hartley, R. H. Howell, R. R. Rohatgi, J. Fajans, and R. Gopalan, Hyperfine Interact. **76**, 135 (1993).

[111] C. Kurz, R. G. Greaves, and C. M. Surko, Phys. Rev. Lett. **77**, 2929 (1996).

[112] C. M. Surko, R. G. Greaves, and M. Charlton, Hyperfine Interact. **109**, 181 (1997).

[113] D. A. Church, Nucl. Instrum. Meth. B **53**, 504 (1991).

[114] R. G. Greaves and C. M. Surko, Phys. Rev. Lett. **75**, 3846 (1995).

[115] Sindano wa Kitwanga, P. Leleux, P. Lipnik, and J. Vanhorenbeeck, Phys. Rev. C **42**, 748 (1990).

[116] M. Schneider, T. Roach, D. S. Hall, and G. Gabrielse (unpublished).

[117] Goodfellow Corporation, Berwyn, Pennsylvania 19312.

[118] Omega Engineering Inc., Stamford, Connecticut 06907.

[119] R. G. Musket, W. McLean, C. A. Colmenares, D. M. Makowiecki, and W. J. Siekhaus, Appl. Surf. Sci. **10**, 143 (1982).

[120] G. Gabrielse, X. Fei, L. A. Orozco, R. L. Tjoelker, J. Haas, H. Kalinowsky, T. A. Trainor, and W. Kells, Phys. Rev. Lett. **65**, 1317 (1990).

[121] S. Baird, J. Bosser, M. Chanel, P. Lefèvre, R. Ley, D. Manglunki, S. Maury, D. Möl, and G. Tranquille, Hyperfine Interact. **76**, 61 (1993).

[122] X. Fei, R. Davisson, and G. Gabrielse, Rev. Sci. Instrum. **58**, 2197 (1986).

[123] M. H. Holzscheiter, X. Feng, T. Goldman, N. S. P. King, R. A. Lewis, and G. A. Smith, Phys. Lett. A **214**, 279 (1996).

[124] U.S. Line Company, Westfield, Massachusetts 01085.